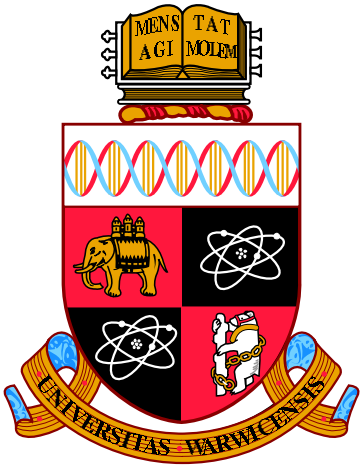

Active and Passive Nematic Multipoles

by

Alexander James Hamilton Houston

Thesis

Submitted to the University of Warwick

for the degree of

Doctor of Philosophy

Department of Physics

January 2022

Contents

List of Figures iii

Acknowledgments v

Declarations vi

Abstract vii

1 Introduction 1

2 Overview of Passive and Active Nematics 7

2.1 An introduction to liquid crystals 9

2.2 Nematic elasticity 11

2.3 Active nematic hydrodynamics 15

2.4 Topological defects in passive and active nematics 20

2.4.1 Two dimensions 20

2.4.2 Three dimensions 27

2.5 Colloids in nematics 32

3 Active Nematic Multipoles 37

3.1 Hydrodynamics of active nematics 38

3.2 Multipole director distortions 39

3.3 Flows from multipole distortions 46

3.4 Active forces and torques 54

3.5 Two-dimensional systems and ratchets 57

3.5.1 Multipoles as topological defects 57

3.5.2 Flows from multipole distortions 59

3.6 Discussion 65

4 Active Defect Loops as Active Multipoles **68**
4.1 Multipole description of nematic defect loops 69
4.1.1 Generic perturbations of a circular loop 73
4.2 Active forces and torques 76
4.3 Active flows 80
4.4 Discussion 83

5 Polygonal Colloids in Two-Dimensional Nematics **84**
5.1 The Dirichlet problem and conformal mapping 88
5.1.1 The Riemann mapping theorem 89
5.1.2 The Dirichlet problem on the disc 90
5.1.3 Schwarz-Christoffel maps 94
5.2 Regular polygons 101
5.2.1 Even-sided polygons 102
5.2.2 Odd-sided polygons 111
5.3 Principles of polygonal colloids in nematics 116
5.4 Star Polygons 118
5.5 Cog Polygons 128
5.6 High-order multipoles 136
5.7 Discussion 140

6 Envoi **143**

Bibliography **145**

List of Figures

2.1 Liquid crystalline phases. 10
2.2 The modes of nematic deformation. 13
2.3 Hydrodynamics of bulk active nematics. 19
2.4 Nematic topological point defects in two dimensions. 21
2.5 Illustration of the fundamental homotopy group of $\mathbb{R}P^2$. 24
2.6 Active flows of two-dimensional nematic point defects. 25
2.7 Representative nematic point defects in three dimensions. 28
2.8 Nematic line and loop defects. 30
2.9 Colloids in nematics. 34

3.1 The multipolar director distortions up to quadrupole order. 43
3.2 The connection between spherical harmonics and nematic topological defects. 45
3.3 The active flows due to three-dimensional nematic multipole distortions up to quadrupole order. 51
3.4 Additional flow solutions induced by spin-1 nematic multipoles. 53
3.5 Representative defect configurations for nematic multipoles in two dimensions. 60
3.6 Monopole and dipole distortions in two-dimensional active nematics. . . . 62
3.7 Quadrupole distortions in two-dimensional active nematics. 65

4.1 Defect loops of splay, bend, and twist type. 71
4.2 Active forces and torques experienced by generic splay, bend and twist defect loops. 78
4.3 The asymptotic flows induced by defect loops. 81

5.1 Shape-controlled nematic distortions with polygonal colloids. 87
5.2 A two-dimensional nematic with varying anchoring conditions on a disc. . 92

5.3 The notation for labelling polygons. 95
5.4 The argument for analyticity of the Schwarz-Christoffel map. 96
5.5 Representative examples of some of the families of polygonal colloids considered in this thesis. 98
5.6 The Pochhammer integration contour. 99
5.7 Geometric frustration due to symmetry of colloids. 103
5.8 Numerical simulations of squares in a two-dimensional nematic. 106
5.9 Analytic solutions for even-sided regular polygons in a two-dimensional nematic. 109
5.10 The dependence of quadrupole strength on side number for even-sided regular polygons. 110
5.11 Numerical simulations of triangles in a two-dimensional nematic. 111
5.12 Analytic solutions for odd-sided regular polygons in a two-dimensional nematic. 115
5.13 The dependence of multipole strengths on side number for odd-sided regular polygons. 116
5.14 Local picture for director winding at a vertex. 117
5.15 Square-based stars in a two-dimensional nematic. 121
5.16 Hexagon-based stars in a two-dimensional nematic. 122
5.17 Triangle-based stars in a two-dimensional nematic. 125
5.18 Pentagon-based stars in a two-dimensional nematic. 126
5.19 Numerical simulations of square-based cogs in a two-dimensional nematic. 129
5.20 Analytical solutions for cog polygons in a two-dimensional nematic. 130
5.21 The phase space of the chirality of distortions induced by cogs in two-dimensional nematics. 132
5.22 Further analytical solutions for cog polygons in a two-dimensional nematic. 134
5.23 A one-parameter family of polygonal colloids based on a triangular motif. 137
5.24 A two-parameter family of polygonal ‘flower’ colloids based on a ‘petal’ motif from even-sided regular polygons. 139
5.25 The second iteration of the Koch snowflake in a two-dimensional nematic. 141

Acknowledgments

First and foremost, I am indebted to my supervisor Gareth Alexander for his invaluable guidance and insight. Throughout my time at Warwick he has achieved the delicate balance of always steering the research in fruitful directions, while also allowing me the freedom to find my own questions. It is an impressive feat and one I'm sincerely grateful for.

I would like to thank Lewis, Ollie, Steve and indeed all the fellow occupants of PS 151 for helping to make life in a poorly-lit office a little brighter. In a different building but the same group, I similarly appreciate my many interactions with Jack and Joe.

I have been unreasonably fortunate in the friendships I formed these past years, including, but by no means limited to, Ben, the other Ben (I'll leave you to sort out which is which), Darion, Tom, Kat, Hollie and George. Whether it be through tea, the pub, a quiz, climbing, running, hiking or just doing nothing much at all, you have all contributed to the moments which have made Warwick a special place to be. Some of you have also been adequate housemates.

Finally, to my parents, for all your love and support I can only say thank you. I do not have the words to truly describe all that you have done for me, nor to express my gratitude.

Declarations

This thesis is submitted to the University of Warwick in support of my application for the degree of Doctor of Philosophy. It has been composed by myself and has not been submitted in any previous application for any degree.

Chapter 4 has been published as
A.J.H. Houston, G.P. Alexander. Defect Loops in Three-Dimensional Active Nematics as Active Multipoles. *Phys. Rev. E* **105**, L062601, 2022.

Material from Chapters 4 and 5 is being prepared for publication.

Abstract

Active matter seeks to bring a physical understanding to bear on biological systems. These systems are rendered 'active' by self-driven constituents which break time-reversal symmetry on the local scale and induce striking non-equilibrium effects such as persistent currents. The particular focus of this thesis is active nematics, in which this activity is paired with the orientational order that characterises the nematic liquid crystalline phase. One of the signature features of passive nematics is their topological defects and these also play a defining rôle in the dynamics of their active counterparts. The equilibrium state of a nematic is provided by harmonic functions and this thesis is a three-fold investigation of the insight these can provide into the behaviour of active nematics.

This is initiated by introducing a novel multipole approach to characterise the far-field active response to distortions of the nematic. We identify those distortions which result in actively-driven phenomena forbidden in equilibrium, such as spontaneous propulsion or rotation and also how such distortions could result from colloids or topological defect configurations.

Applying this approach to the solid angle function, appropriate to describe the distortions originating from a defect loop, reveals the part played by the loop's geometry in its dynamics, in particular rotational effects due to non-planarity. These offer an explanation for the recent experimental observation that activity results in an uneven distribution of loop geometries.

Lastly, we use conformal mappings to investigate in two dimensions how the multipole character of a nematic may be influenced by colloidal geometry. This fulfills the initial motivation of showing how to controllably induce all the distortions we identified as producing striking active phenomenology, but also provides methods for analytic determination of the equilibrium director, applicable to a generic colloid, and shows how colloids can be designed which generate arbitrarily intricate nematic multipoles.

The results of this thesis provide a framework for understanding the basic responses of active nematics, along with the dynamics of their fundamental, topological, excitations as well as how geometry interacts with nematic order. They open up pathways to novel nematic metamaterials as well as the design of bio-inspired micromachines.

By mathematics we shall come to heaven.
This page the door of God's academy
for the geometer.

Rowan Williams, Bach for the Cello

1 Introduction

UNDERSTANDING the processes of life is surely one of the great challenges of science. While we are used to the notion that inanimate matter should succumb to a physical description, living creatures have an ineffable quality that seems to set them apart. However, this distinction is eroding. Much as one of the crowning achievements of 20th century science was quantum mechanics providing a physical basis for the rules of chemistry, there is increasing effort to gain similar physical insight into the behaviour of biological systems. Indeed, in the wake of the quantum revolution it was Schrödinger's hope that understanding the chemistry of organic molecules might lead to a physical theory of life [1]. Nonetheless, the quest to understand life from physical principles did not end with the discovery of the structure of DNA, contrary to Crick's supposed exclamation that he and Watson had 'found the secret of life' [2]. The difficulties inherent in establishing the rules that govern the smallest scales notwithstanding, they can still be insufficient to explain the collective phenomena that emerge at larger ones. This is familiar in physics as the phrase 'more is different', introduced by Anderson in his 1972 article of the same name [3] – the standard model does not render redundant the study of large-scale condensed matter systems in their own right and their behaviour is often best described by formulating theories in terms of macroscopic collective properties, rather than in the most basic constituents. This shortcoming of a bottom-up

approach is eloquently encapsulated by Berry, who observes that the behaviour of living organisms is not easily understood by 'writing down the Schrödinger equation and gazing at it' [4].

Understanding the collective behaviour of biological systems from a condensed matter viewpoint is the goal of the field known as active matter. It has its origins in the work on fish schools by Aoki [5] and Partridge [6] and in Reynold's 1986 agent-based simulation of bird flocks known as Boids (this being 'Birds' in a Brooklyn accent [7]), which was used to model flying bats for the 1992 film Batman Returns [8]. The field garnered increased attention within the physics community when in 1995 Vicsek showed that a phase transition from random motion to collective flocking could occur in a model of 'flying magnets' – agents that moved in their direction of alignment and updated this alignment in order to match that of their neighbours, subject to noise [9]. Shortly afterwards Toner and Tu formulated Vicsek's model as a continuum field theory with the Toner-Tu flocking equations [10]. In the subsequent years unifying principles have been revealed behind phenomena in disparate systems over a vast array of scales, from the murmurations of starlings at dusk [11; 12] to the swarming of bacterial populations [13; 14; 15].

The domain of active matter is any system which is composed of constituent elements capable of converting energy into directed motion or stresses exerted on their environment. Living organisms provide the prototypical example, but there are also synthetic realisations in the form of agitated rods [16; 17] and colloidal particles driven by chemical reactions [18; 19]. That they are driven out of equilibrium by the injection of energy on the local level makes them fundamentally different from more traditional forms of non-equilibrium systems in which the input of energy is global, for example by applying a shear to the sides of a container. The local breaking of time-reversal symmetry means that active matter is not subject to the law of detailed balance and is able to display persistent currents in its steady state. The aim of the field then is to determine how to formulate theories of active systems in light of the symmetries that are both broken and maintained, to draw out the underlying principles that lead from self-driven agents to emergent collective phenomena and understand how these principles might be applied to control biological matter and design bio-inspired materials.

This thesis is concerned with a particular class of active matter known as active nematics [20], comprised of an ambient fluid containing anisotropic rod-shaped agents which exhibit orientational ordering. This ordering invites a description by means of analogy with nematic liquid crystals [21], a quintessential example of an ordered fluid phase. Before discussing this active nematic class further we present a striking example

of the non-equilibrium phenomena that can occur in active systems that will motivate much of the work of this thesis.

An asymmetric cog placed in a population of bacteria can spontaneously and consistently rotate [22; 23]. The incoherent run-and-tumble movement of the bacteria is reminiscent of Brownian motion but the presence of the cog rectifies this motion causing the bacteria to preferentially move along its edges and exert a sustained torque. This ability to extract the energy inherent in active systems in the form of useful work is of direct relevance for the design of biological micromachines. It also stands in stark contrast to the inability to extract such work from equilibrium systems, as exemplified by Feynman's ratchet-and-pawl thought experiment [24]. The bacterial systems in which these ratchet effects have been realised lack the orientational ordering which characterises active nematics, and achieving similar rectification of the dynamics in these ordered systems is an on-going challenge. In Chapter 3 we show how rotational flows may be induced in active nematics and in Chapter 5 we demonstrate that suitably designed cogs may allow for analogous ratchet behaviour to be achieved.

In considering active nematics we work within the framework of a phenomenological hydrodynamical theory introduced by Simha and Ramaswamy in 2002 [25]. While attempts have been made to derive theories of active hydrodynamics from the coarse-graining of a microscopic description [26; 27] we do not engage with this here and instead accept as our starting point Simha and Ramaswamy's continuum theory derived from pure thought on the basis of permitting in the equations all terms allowable by the symmetries of the system. The resulting equations have been used to describe the behaviour of many systems, including eukaryotic cells [28; 29], certain bacterial colonies [13; 14] and epithelial cells [30]. The spirit of our work will be to trade specificity for generality, ignoring the details of particular biological systems in favour of approximations that allow us to bring to bear the powerful machinery of algebraic topology and complex analysis while still capturing the essential qualitative phenomena.

Condensed matter systems are often best described not in terms of their constituent particles, but in terms of the 'quasiparticle' fundamental excitations of the collective, and active matter is no exception. In ordered media these excitations often take the form of topological defects, singular structures where the ordering breaks down that encode some non-trivial winding. The study of topological defects can be traced back to the 1830s with Whewell's studies of amphidromic points [31; 32], places in the sea where lines of high tide meet and at which no tide can be defined. Another example is given by the winding of time zones around the poles of the Earth, making the specification of the time at these points impossible. Topological defects have since found application across

a wide array of ordered phases, including but not limited to cosmic strings [33], vortices in superfluids [34], phase singularities of quantum wavefunctions [35; 36], 'threads of darkness' in light fields [37] and in the molecular alignment of liquid crystals [21]. The non-equilibrium stresses that define active matter elevate their topological defects to the status of driving the system dynamics, leading to a quasiparticle description of their behaviour in terms of that of their defects [38]. This formulation is well-advanced in the case of two-dimensional active nematics [39; 40; 41; 42], but is still being developed in three-dimensions due to the more complicated form that the topological defects take [43; 44]. The fundamental role that these topological defects play in three-dimensional active nematics will be the subject of Chapter 4.

A unifying theme running through this thesis stems from the theoretical description of active nematics that we employ. We consider the flows that result from an active nematic in which the energy due to elastic deformations is minimised. These energy minimisers are harmonic functions, that is solutions of Laplace's equation, and this thesis may therefore be viewed as harmonics three ways. Chapter 3 rests on the fact that the asymptotic distortions of a uniformly aligned nematic are described by the spherical harmonics. In Chapter 4 we apply this multipole analysis to defect loops, utilising the fact that the unique harmonic function with winding around a singular loop is, up to an additive constant, given by the solid angle function of Maxwell [45; 46]. Lastly, our two-dimensional work in Chapter 5 relies on the one-to-one correspondence between harmonic functions and meromorphic functions.

The near-ubiquitous nature of Laplace's equation therefore lends the methods used in this thesis applicability in a broader context than we consider here. The potential of any conservative force bound by Gauss's law will, in free space, obey the Laplace equation, making it fundamental to the study of electrostatics and gravity. Additionally, it appears as the time-independent form of the heat and wave equations, as well as the free-space Schrödinger equation. Lastly, it is a foundational principle of physics that the equilibrium states of systems can be described as minimising some functional. The Dirichlet, squared-norm functional is among the simplest and its minimisers are again solutions of the Laplacian. This is the source of its relevance to the study of nematics but also applies to the description of minimal surfaces.

The remainder of this thesis is organised as follows. Chapter 2 contains a brief survey of the theory of passive and active nematics, with a focus on those parts pertinent to our later studies, in particular the role played by topological defects.

In Chapter 3 we employ a multipole analysis of nematic distortions to characterise the generic response to deformations of an active nematic. A similar multipole approach

has been successfully used to understand the behaviour of passive nematics, for example in the context of interactions between colloidal inclusions, but their application to active systems as what we term 'active nematic multipoles' is novel. It provides a hierarchical framework for understanding the behaviour of active nematics in which a generic active flow may be derived from a fundamental response. We identify those distortions for which the active stresses produce a net active force or torque, as determined by the nature of the dipole and quadrupole term respectively. These distortions are associated with striking self-propulsive and rotational behaviour and their understanding opens up avenues for the control of active nematics and the ability to extract useful work from them. As a global description of the response of an active nematic to distortions, the work of this chapter is applicable to those distortions that arise due to colloids or singular structures such as defect loops. Much of the remainder of the thesis is an unpacking of the ideas in this chapter with regard to these specific applications.

In Chapter 4 we apply this multipole expansion to the solid angle function to develop a description of defect loops in three-dimensional active nematics. These defect loops have been shown in a recent experiment to be the key driver of the dynamics in these systems [43]. Our work provides a global description which complements a previous local analysis [44] and also extends it to consider non-planar loops and loops with a generic orientation. This leads to a self-dynamics dependent on the loop's geometric type. The dipole term leads to active stresses that generate a global self-propulsion for splay and bend loops. The quadrupole moment is non-zero only for non-planar loops and generates a net 'active torque', such that defect loops are both self-motile and self-orienting. Our analysis identifies right- and left-handed twist loops as the only force- and torque-free geometries, suggesting a mechanism for generating an excess of twist loops, as observed experimentally [43]. Finally, we determine the Stokesian flows created by defect loops and describe qualitatively their hydrodynamics.

In Chapter 5 we use conformal methods to construct the harmonic functions appropriate for a given polygonal colloid in a two-dimensional nematic and understand the connection between the geometry the colloid and the distortion it induces, paying particular attention to the form of the dominant multipole. This is motivated by the work of Chapter 3 which identified certain multipoles as generating non-equilibrium effects in active nematics, but also by multipole-based description of colloidal interactions in passive nematics. In this context it is a goal to achieve high-order distortions which lead to intricate interactions and, in the sense of the colloidal atom paradigm, exceed the complexity of the periodic table. We begin by using our construction to provide a quantitative description of experimental observations of the diversity of distortions that

can be induced by regular polygons. We then investigate the effects of concavity and chirality through classes of star- and asymmetric cog-shaped polygons. This identifies subtle orientation-dependency in both cases. In the latter case this would seem to confound the ability of a cog to produce a sustained active rotation, since the coefficient of the chiral quadrupole which is associated with a net active torque varies as the cog rotates. However, we show how suitably designed cogs can avoid this issue and produce ratchet effects of the same kind as observed in bacterial systems, with the same potential for work extraction and micromachine design. Lastly, we demonstrate how the techniques we have developed may be used to design colloids which induce a distortion with a leading multipole of arbitrarily high order.

Finally, in Chapter 6 we reflect on the work of this thesis, draw a few conclusions based on its main findings and offer some promising avenues for future investigations.

My heart is in a world of water and crystal
Du Fu, In Abbot Zan's Room at Dayun Temple

2

Overview of Passive and Active Nematics

To reiterate, the defining, unifying property of active matter is that the individual constituent entities are able to convert energy into motion or the exertion of stresses, constituting a breaking on time-reversal symmetry on the local level. However, within this umbrella term many distinctions can be made. The focus of this thesis is the class of wet active nematics. To unpack what is meant by this we now briefly lay out some of the features which characterise and differentiate active systems.

The distinction between living and synthetic active systems notwithstanding, let us begin with the particles that comprise the active system. These may be spherical, lacking any orientational order and described by a scalar order parameter: the density. This has applicability for example as a simplified model of the run-and-tumble motion of certain bacteria such as *E. coli* [47] and predicts a liquid-gas 'motility induced phase separation' [48]. The description can be in terms of self-propelled agents or continuum fields, through an adaptation of the Cahn-Hilliard model [48]. The description of chiral fluids composed of self-spinning fluids, such as colloidal suspension of spinning magnets [49], requires a second scalar field, the rotation frequency. The combined breaking of both parity and time-reversal symmetry leads to topologically-protected edge currents [50; 51; 52], analogous to those that appear in the quantum Hall effect [53].

Alternatively, the particles may be anisotropic and hence capable of displaying

orientational order. In polar systems the particle's anisotropy leads to self-propulsion in a particular direction, described by a vector order parameter. This is the class of flocking models such as the Toner-Tu equations [10; 54] in which the coupling of broken spatial symmetry with the breaking of time-reversal symmetry results in net currents and is applicable to the description the collective behaviour on scales ranging from animal herds [55] to migrating cells [56]. Other systems possess what is known as nematic symmetry; the orientational ordering is not in a given direction but rather along a given line, with no preference for aligning parallel or antiparallel. This apolarity can originate from the particles themselves if they have nothing to distinguish a 'head' from a 'tail' or from the interactions, for example if they are purely steric [57]. This more subtle form of orientational order is familiar from nematic liquid crystal and is described by a tensorial order parameter [21]. The head-tail symmetry of active nematics precludes the generation of net currents, but complex dynamics can emerge nonetheless [20] and topological defects with polar orientation can exhibit active motility [40].

A second partition can be made according to the role played by friction. Dry systems are those in which the collection of active particles can be viewed as following an overdamped dynamics, with no momentum transfer through the fluid, while in wet systems there is momentum conservation through the fluid and hydrodynamic interactions play a key role [57]. It should be noted that this is less a distinction of the system than it is of the model used to describe it, as ultimately whether a system behaves as wet or dry will depend on the length scales being considered [57]. The flocking examples given in the previous paragraph belong to the class of dry polar active matter; systems that may be described by wet polar models include cytoskeletal suspensions [58], swimming bacteria [59] and platinum-coated colloids driven by catalytic reactions [19]. Dry nematic models can be applied to collections of melanocytes [60] and agitated granular rods [16].

This returns us to the primary focus of this thesis: wet active nematics; nematically ordered systems driven from equilibrium by the motility of their individual elements which experience long-range hydrodynamic interactions mediated by an ambient fluid. We discuss the biological relevance of active nematics to the behaviour of bacteria and cells in Section 2.4.1. Their quintessential experimental realisation is a two-dimensional in vitro assembly of microtubules and kinesin motors lying at an oil-water interface, introduced by the Dogic lab in 2012 [61]. The typical length of the microtubules is 1.5μm and so this suspension provides a synthetic testing ground for models of micro-scale active nematics. Many of the developments in the theory of active nematics have been fueled by this system and the ability to both synthesise and measure with light-sheet

microscopy three-dimensional analogues, only achieved in 2019 [43], is driving interest in the theoretical description of three-dimensional active nematics [62; 44; 63].

Although understanding the dynamics of active nematics provides the principle motivation for the work of this thesis, this leads us in Chapter 5 to results which are applicable to traditional, passive nematic liquid crystals. In the remainder of this chapter we therefore present an overview of the theory of both passive and active nematics, proceeding in concert as much as possible. Even with focusing our attention on a subclass of liquid crystal physics and active matter respectively this still constitutes a very broad area and what follows is not intended to provide a complete review, only to lay the groundwork for the results that follow.

2.1 An introduction to liquid crystals

Liquid crystals, with a name that seems a discordant contradiction, are a mesophase of matter intermediate between crystals and liquids and combining properties of both. The translational order that typifies crystals is lost but long-ranged orientational order remains, meaning they can both flow and respond elastically; supporting shears and torques [21]. Of course, for orientational order to be a meaningful concept the molecules that exhibit liquid crystalline phases must be anisotropic, a classic example being MBBA, shown in Figure 2.1, which at atmospheric pressure transitions from the crystalline to liquid crystalline state at 20°C before entering the isotropic phase at 47°C, in which there is no preferred molecular alignment. The transition is first-order, allowing co-existence between the ordered and isotropic phases and in general may be either thermotropic, governed by temperature, or lyotropic, brought on by changes in concentration. There is also not a single liquid crystalline phase. What we have described is known as a nematic; when there is a degree of positional ordering such that the molecules are organised into layers the material is termed a smectic and in a cholesteric the molecules have a preference to twist about an axis. Schematics of these liquid crystalline phases are shown in Figure 2.1. The chemistry of what phases are exhibited by a given molecule can be subtle; 5CB forms a nematic while the similar 8CB displays a smectic phase.

Such molecular details are not our concern. The key feature for us is the orientational ordering of nematics, which makes them a fruitful basis for modelling certain forms of active matter, and this may be captured through a continuum director field $\mathbf{n}$ whose direction corresponds to a coarse-grained average of the local molecular orientation. The director $\mathbf{n}$ should not be thought of as a vector but rather a line field, having head-tail symmetry such that the system is invariant under the transformation $\mathbf{n} \to -\mathbf{n}$. As is

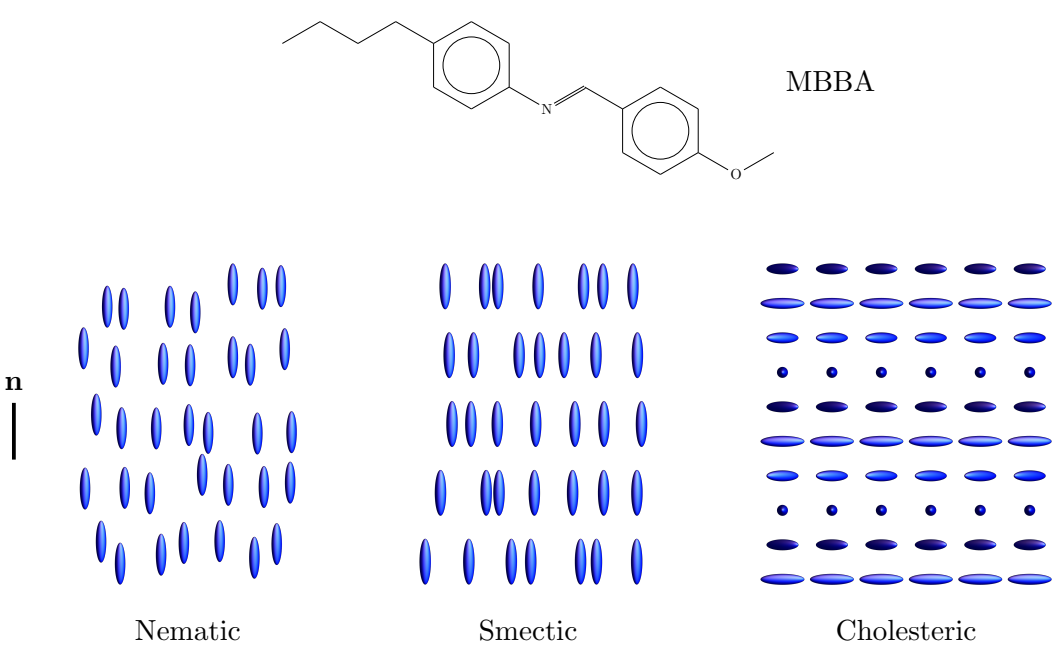

Figure 2.1: Liquid crystalline phases. Above: the molecular structure for N-4-Methoxybenzylidene-4-butylaniline (MBBA), which forms a nematic phase at room temperature. Below: schematic representations of the nematic, smectic and cholesteric phases. The director $\mathbf{n}$ corresponding to the average local molecular orientation in the nematic is also shown.

clear from Figure 2.1, this symmetry need not be present in the nematogens themselves (that it, the molecules which exhibit nematic ordering), rather we should think that as many molecules point 'up' as 'down', the nematic symmetry of $\mathbf{n}$ emerging as a consequence of our 'zoomed out' description. It will however be constructive at times to treat $\mathbf{n}$ as though it were a vector by choosing a consistent orientation, but any conclusions we draw should be independent of this choice. As $\mathbf{n}$ simply encodes a line of preferential alignment its magnitude carries no information and it will always be taken to be unit length.

In light of this symmetry $\mathbf{n}$ is ill-equipped to act as an order parameter, but a suitable choice is provided by the Q-tensor [64]

$$Q_{ij} = s\left[n_i n_j - \frac{1}{d}\delta_{ij}\right], \tag{2.1}$$

a traceless tensorial order parameter of rank 2, with d the number of spatial dimensions. This tensor corresponds to the anisotropic part of the dielectric tensor and is non-zero

in the nematic phase while vanishing in the isotropic phase, allowing the isotropic to nematic transition to be described by Landau-de Gennes theory [21]. The direction of nematic ordering corresponds to the non-degenerate eigenvalue of $\mathbf{Q}$ and the scalar s quantifies the degree of this ordering. While Q is well-suited to numerical simulations, $\mathbf{n}$ is typically more useful in revealing the rôle of geometry in analytic calculations and we use it throughout this thesis.

2.2 Nematic elasticity

The fundamental elastic distortion energy governing the equilibrium behaviour of nematics, along with its geometric interpretation, was put forward by Frank in his seminal paper of 1958 [65], building on earlier work by Oseen [66]. In what is largely the standard presentation the free energy takes the form

$$\begin{aligned} F = \int \mathrm{d}^3\mathbf{r} \frac{K_1}{2}(\mathbf{n}(\nabla\cdot\mathbf{n}))^2 + \frac{K_2}{2}(\mathbf{n}\cdot\nabla\times\mathbf{n})^2 + \frac{K_3}{2}((\mathbf{n}\cdot\nabla)\mathbf{n})^2 \\ - K_{24}\left[\mathbf{n}(\nabla\cdot\mathbf{n}) - (\mathbf{n}\cdot\nabla)\mathbf{n}\right], \end{aligned} \tag{2.2}$$

where the K_i are elastic constants.

Each term in (2.2) represents a distinct mode of deformation for the nematic, with its own geometric significance. Taking them in turn, $\mathbf{n}(\nabla\cdot\mathbf{n})$ is the splay vector. The reasons for our departure from the standard representation of splay as the scalar $\nabla\cdot\mathbf{n}$ are twofold. Unlike the scalar, the splay vector is invariant under $\mathbf{n}\to-\mathbf{n}$ and since $\mathbf{n}^2=1$ the contribution to the energy in (2.2) is unchanged. As we shall see in Section 2.3 it also captures part of the force that arises due to the presence of active stresses in nematically aligned systems. The twist $\mathbf{n}\cdot\nabla\times\mathbf{n}$ is a pseudoscalar; it has a handedness and its sign is reversed by inversion of the spatial coordinates. Via the Frobenius integrability condition [67] it determines whether the director field provides a foliation, meaning it may be viewed as the normal vector field to a family of continuous system-spanning surfaces. This is only possible when $\mathbf{n}\cdot\nabla\times\mathbf{n}=0$ and so this vanishing of twist is a requirement for the layer structure of smectics. The failure to form a foliation caused by the twist inherent in the cholesteric ground state is naturally described by contact topology [68]. The third term of (2.2) is sometimes written as $(\mathbf{n}\times(\nabla\times\mathbf{n}))^2$ [69], but the form given above makes its geometric origin clearer. In measuring the gradients of $\mathbf{n}$ in the direction of $\mathbf{n}$, $(\mathbf{n}\cdot\nabla)\mathbf{n}$ is equivalent to the normal curvature of the integral curves of $\mathbf{n}$. The final term is known as the saddle-splay. If the director field does constitute a foliation then this measures the Gaussian curvature [70] of the

corresponding surfaces [71], although this description can be applied more generally by viewing the director as sitting in a curved space [72]. As a total derivative it will not play a role in the work of this thesis but can be important in systems with complex anchoring conditions [73] or with a proliferation of defects [71; 74].

Although this formulation of the Frank free energy is sufficient for our purposes, we give here a brief overview of a treatment of the nematic distortions that is more firmly rooted in the geometry of vector fields [75; 76]. The gradients of $\mathbf{n}$ at any point are a section of $T^*(\mathbb{R}^3) \times T(\mathbb{R}^3)$. The director acts as a preferred direction at each point and provides a canonical splitting of the tangent bundle into a line bundle L and a bundle of orthogonal 2-planes ξ [77]. Correspondingly, the gradients of $\mathbf{n}$ may be decomposed into those parallel and perpendicular to $\mathbf{n}$. Due to the uniaxial nature of the director the perpendicular gradients can be further decomposed according to the action of a rotation group, isomorphic to $SO(2)$, which generates rotations around the local director orientation, giving [77]

$$\partial_i n_j = n_i(n_k\partial_k)n_j + \frac{\nabla\cdot\mathbf{n}}{2}(\delta_{ij} - n_i n_j) + \frac{\mathbf{n}\cdot\nabla\times\mathbf{n}}{2}\epsilon_{ijk}n_k + \Delta_{ij}, \tag{2.3}$$

$$\Delta_{ij} = \frac{1}{2}(\delta_{ik} - n_i n_k)\partial_k n_j + \frac{1}{2}(\delta_{jk} - n_j n_k)\partial_k n_i - \frac{\nabla\cdot\mathbf{n}}{2}(\delta_{ij} - n_i n_j), \tag{2.4}$$

with the resulting four distinct modes of deformation shown in Figure 2.2. The first term of $\partial_i n_j$ is the bend. As it is always normal to $\mathbf{n}$ it is a section of ξ [77], affording it unusual geometric and topological properties for a vector field [78]. The remaining three terms, taken as an operator, comprise the shape operator [70]. The first of these is the isotropic part, with its magnitude given by the splay. The next, with magnitude equal to the twist, is the antisymmetric part. It acts on the planes of ξ as a complex structure, providing rotations of $\pi/2$ about $\mathbf{n}$. Lastly, Δ_{ij} is a spin-2 object which, owing to its structure, has been termed the anisotropic orthogonal gradients [79] and the biaxial splay [76]. Its eigenvectors correspond to the directions of principal curvature of the director; the geometry of the umbilic lines where it is degenerate is considered in [79]. This decomposition of gradients according to a preferred direction and associated rotation group is mirrored in our treatment of nematic multipoles in Chapter 3, only there the splitting is not local but global, provided by the far-field alignment.

One feature that distinguishes the free energy of nematics from that for magnetic systems [80], in which the same distortions contribute to the energy, is that each distinct deformation mode has a separate elastic constant K_i. Despite this elastic anisotropy and the variation of these parameters with temperature we can estimate their value through

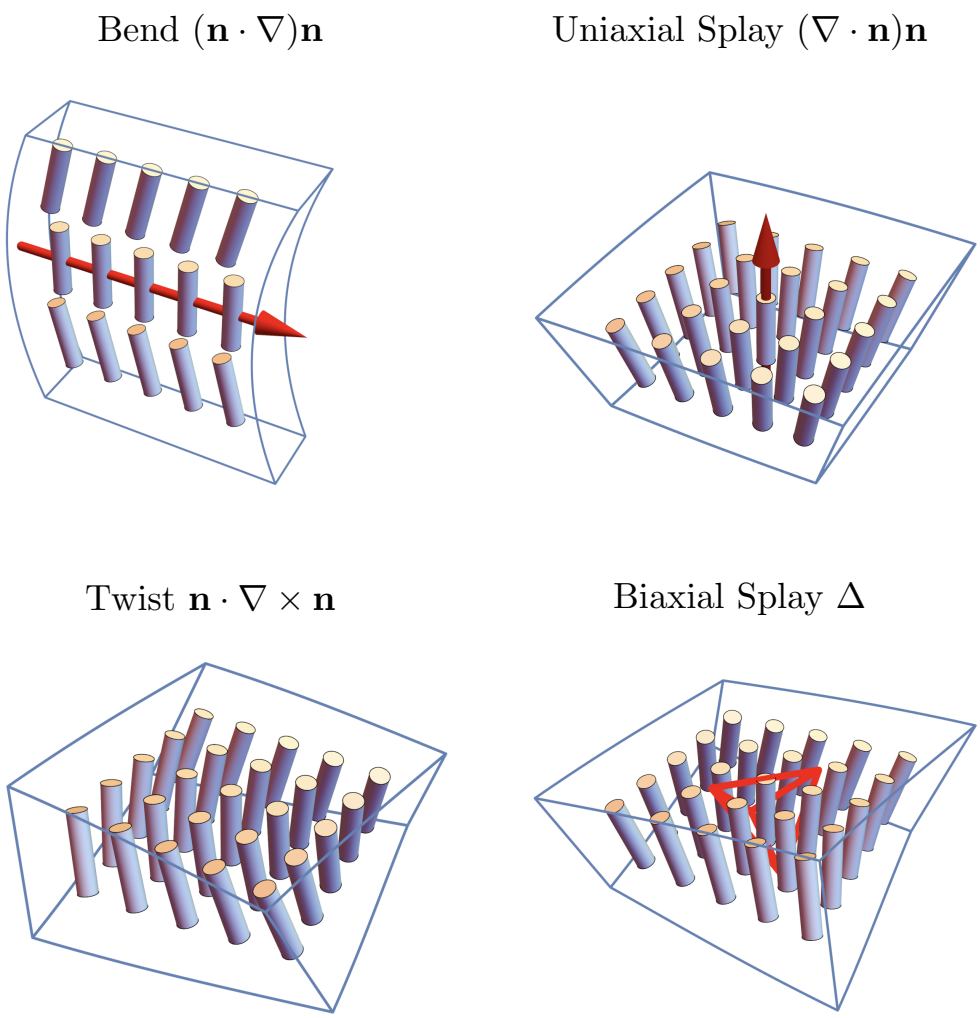

Figure 2.2: The modes of nematic deformation. Bend and uniaxial splay are vectors, the twist a scalar and the biaxial splay Δ a spin-2 tensor. The red tetrahedron represents the tensor $\Delta_{ij}n_k$. Figures reproduced from [76].

the following argument [21]. As $\mathbf{n}$ is dimensionless each of the K_i must have dimensions of energy per length. The only relevant length is that of the nematogen molecules, approximately 1nm. For the energy we use the interaction energy of the molecules, taken to be k_BT with $T \sim 300$K, after all it is the very property of not being tightly bound at room temperature that makes liquid crystals, and all of soft matter, soft. This gives $K_i \sim 4 \times 10^{-12}$J, in remarkably good comparison with the measured values [21].

We do not retain this elastic anisotropy in our treatment of nematics, instead adopting a one-elastic-constant approximation, $K_i = K$ for all i, under which the Frank free energy takes the form

$$F = \frac{K}{2} \int \mathrm{d}^3\mathbf{r} |\nabla \mathbf{n}|^2. \tag{2.5}$$

One reason for this is practicality. The minimisers of (2.5) are harmonic functions and so exact solutions can be provided in many contexts. By contrast, with distinct elastic constants the only analytic solution is that provided by Dzyaloshinskii for a scale-free two-dimensional system with at most one disclination [81; 69], for which the director angle is given by an elliptic integral of the third kind [82]. We cannot claim that this approximation captures all aspects of the nematic system. There are elastic torques that only arise due to a discrepancy in the elastic constants [83; 84] and active nematics can display morphologies indicative of strong elastic anisotropy [85; 86; 87], perhaps due to a hydrodynamic coupling between flows and director alignment producing modified effective elastic constants. At the same time, it is not a spurious simplification. It has been used to describe the salient features of defect dynamics in active nematics in both two and three dimensions [40; 88; 89] and it underpins both the simulation and theoretical description of colloidal inclusions in nematics [90].

As already mentioned, each chapter of this thesis revolves around a distinct form of the minimisers of (2.5). Chapter 3 utilises that in the far-field limit the director distortions can be linearised as $\mathbf{n} = \mathbf{e}_z + \delta n_x \mathbf{e}_x + \delta n_y \mathbf{e}_y$ and applying the Euler-Lagrange equations to (2.5) shows that both δn_x and δn_y are harmonic and may be given as a multipole expansion

$$n_i = \sum_{l=0}^{\infty} \sum_{m=-l}^{l} q_{lm}^i \left(\frac{a}{r}\right)^{l+1} Y_l^m(\theta, \phi). \tag{2.6}$$

Chapter 4 rests on the status of the solid angle function [45; 46]

$$\omega(\mathbf{x}) = \int_K \frac{\mathbf{p}_\infty \times \mathbf{p}}{1 + \mathbf{p}_\infty \cdot \mathbf{p}} \cdot \mathrm{d}\mathbf{p} \mod 4\pi, \tag{2.7}$$

as the unique minimiser of (2.5) with winding around a singular loop K. Here $\mathbf{p}$ labels

the points of K and the vector $\mathbf{p}_\infty$ is arbitrary. Lastly, our two-dimensional work in Chapter 3 and Chapter 5 uses the fact that solutions of (2.5) have a director angle that may be expressed as the imaginary part of a meromorphic function

$$\phi = \Im \ln \Phi = \Im \ln \prod_j (z - z_j)^{s_j}, \tag{2.8}$$

such that the s_j characterise the winding of the director at the locations z_j.

2.3 Active nematic hydrodynamics

From the equilibrium states of nematics, we now turn to the hydrodynamical theory that governs their dynamics, and by extension the dynamics of active nematic systems. Such theories are constructed in terms of a discrete set of fields, termed hydrodynamic or slow variables, whose relaxation time grows unboundedly with wavelength [80]. These are typically provided by conserved quantities and the Goldstone modes [91] arising from the breaking of continuous symmetries. Of the former type we have the density $\rho(\mathbf{r}, t)$ and momentum $\rho(\mathbf{r}, t)\mathbf{u}(\mathbf{r}, t)$, with $\mathbf{u}(\mathbf{r}, t)$ the fluid velocity, while the deformations of $\mathbf{n}$ belong to the latter case. The equations that result were first formulated for a suspension of self-propelled particles by Simha and Ramaswamy [25] and are a modification of those for passive nematics [92; 21]. Their derivation can also be found along with a discussion of other aspects of active hydrodynamics in several reviews of the subject [57; 93]. In our presentation we restrict attention to a single-component active material and take the concentration to be constant, rather than including it as an additional slow variable as in [25].

The equations of active nematohydrodynamics are the conservation of mass density

$$\partial_t \rho + \partial_i(\rho u_i) = 0 \tag{2.9}$$

and the force-balance equation

$$\rho(\partial_t + u_j \partial_j) u_i = \partial_j \sigma_{ij}, \tag{2.10}$$

where σ_{ij} is the stress tensor

$$\sigma_{ij} = -p\delta_{ij} + 2\mu D_{ij} + \frac{\nu}{2}(n_i h_j + h_i n_j) + \frac{1}{2}(n_i h_j - h_i n_j) + \sigma^E_{ij} - \zeta n_i n_j \tag{2.11}$$

along with the relaxational equation governing the director dynamics

$$\partial_t n_i + u_j \partial_j n_i + \Omega_{ij} n_j = \frac{1}{\gamma} h_i - \nu \left[D_{ij} n_j - n_i \left(n_j D_{jk} n_k \right) \right]. \tag{2.12}$$

Here p is the pressure, μ the viscosity, γ a rotational viscosity and $D_{ij} = 1/2(\partial_i u_j + \partial_j u_i)$ and $\Omega_{ij} = 1/2(\partial_i u_j - \partial_j u_i)$ the symmetric and antisymmetric parts of the velocity gradients. The flow alignment parameter ν determines the behaviour of anisotropic particles in flow according to their shape; flow-tumbling for $-1 < \nu < 1$ and flow-aligning otherwise. The molecular field $h_i = -\delta F / \delta n_i$ acts to relax $\mathbf{n}$ to a minimiser of the Frank free energy (2.2). In a one-elastic-constant approximation with the Frank energy given by (2.5) the molecular field is $h_i = K(\nabla^2 n_i - n_i n_j \nabla^2 n_j)$ and the Ericksen stress is $\sigma^E_{ij} = -K \partial_i n_k \partial_j n_k$. In addition to equations (2.9)-(2.12) we have the conditions that $\mathbf{u}$ vanishes on all boundaries with Dirichlet boundary conditions imposed on $\mathbf{n}$. At infinity $\mathbf{u}$ vanishes while $\mathbf{n}$, p and ρ tend to constants, although we shall shortly take the fluid to be incompressible such that ρ is constant everywhere. The only departure from the hydrodynamics of passive nematics comes in the final term of (2.12), $-\zeta n_i n_j$, introduced in [25]. Such a term is precluded in equilibrium systems as it does not derive from a free energy but it must be included here as there is no symmetry to rule it out [25]. We defer a discussion of this term and its consequences for a moment.

The above equations represent a generalisation of the Navier-Stokes equations [94; 95], required to capture the two-way coupling between flows and particle orientation brought about by the nematogen's anisotropy. Owing to their shape the particles are responsive to flow gradients and also induce flows when they reorient. A welcome simplification is that the foreboding nonlinearities in (2.10) need not be retained. To see this we introduce characteristic length and velocity scales l_0 and u_0 such that (2.10) may be expressed in terms of dimensionless variables. The relative significance of the inertial and viscous terms is then given by a dimensionless number, the Reynolds number $\mathrm{Re} = \frac{\rho l_0 u_0}{\mu}$ [94]. The material properties may be approximated by those for water, for which $\rho/\mu \sim 10^6$ [94] and the microscale applications that we have in mind result in $\mathrm{Re} \sim 10^{-6}$ [96; 61]. We are therefore able to neglect the inertial terms in (2.10) and, taking the density to be constant such that the continuity equation (2.9) reduces to the condition of fluid incompressibility, are left with the linear Stokes equations

$$\begin{aligned} \nabla \cdot \mathbf{u} &= 0, \\ \nabla \cdot \sigma &= 0. \end{aligned} \tag{2.13}$$

Given our experience of inertia-dominated flows, the behaviour that results from these equations is counter-intuitive and deserves some discussion. They are time-reversible, as can be dramatically demonstrated by the mixing together of ink drops, followed by their 'unmixing' back into separate drops [97]. It also has a profound impact on the swimming of microorganisms as any time-reversible stroke cannot result in a net displacement, as encapsulated in Purcell's scallop theorem [98]. The response to a point force is given by the Stokeslet [99; 100]

$$u_i = G_{ij} f_j = \frac{f_j}{8\pi\mu}\left(\frac{1}{r}\delta_{ij} + \frac{r_i r_j}{r^3}\right), \tag{2.14}$$

with G_{ij} the Green's function, known as the Oseen tensor, several derivations of which are given in [101]. By Newton's third law any self-propelled particle must be net force- and torque-free. The flows induced by microswimmers are therefore typically dominated by the flow response to a force dipole, the stresslet, given by the traceless symmetric part of (2.14). Microswimmers may be classified according to the sign of the stresslet term as either a pusher if fluid is drawn in from the sides and expelled at the ends or a puller if the reverse holds.

Returning to the active contribution to the stress tensor, we can now see that its form can be justified as resulting from a coarse-graining of a dense distribution of force dipoles. The activity ζ is a phenomenological parameter whose magnitude captures the strength of these stresses and whose sign denotes the nature as extensile when $\zeta > 0$ and contractile when $\zeta < 0$, corresponding to pusher and puller dipoles respectively. A striking consequence of these active stresses, identified in the paper of Simha and Ramaswamy [25], is that the orientationally-ordered flow-free bulk system is unstable to long-wavelength splay or bend deformations of the director, according to the sign of ζ. This instability can be established through a linear stability analysis [25] but an intuition for it is provided by the pictorial argument of Figure 2.3(a) and (b) [93]. When the stresses are contractile splay deformations induce shear flows that exacerbate the original distortion, with the same applying to bend deformations in extensile systems. This mechanism also gives rise to novel instabilities in thin active films [102], where perturbations of the free surface couple to splay modes of the director.

A linear analysis can only tell us that the ordered state is unstable, not what results from this instability, but numerical simulations predict a state of active turbulence [103; 104; 105; 106], which has also been seen experimentally, for example in suspensions of bacteria [107], as shown in Figure 2.3(c). It is characterised by regions of vortical flow, born out of the instability of nematic order to vorticity illustrated in Figure 2.3(a)

and b), and is so named because these cause a resemblance to turbulent flows [1]. The dynamics is complicated but can be understood as stemming from a four-stage cycle [108], in which the nematic order succumbs to the hydrodynamic instability, leading to the formation of 'walls' of high director distortion. These walls release elastic energy by focusing the distortion into singular structures called topological defects [2], which annihilate in pairs, restoring nematic order and starting the cycle anew. The vorticity correlations decay over a characteristic length scale defined by the competition between the elastic forces seeking to maintain order and the active stresses as $l_A \sim \sqrt{K/|\zeta|}$.

A major challenge is to tame active turbulence to produce oriented and controllable dynamics. The active length scale suggests that one route to this is via confinement. Indeed, confinement to a channel is able to suppress the active nematic instability, provided the channel width h is less than $\sqrt{K/|\zeta|}$. For channels wider than this or, for fixed channel geometry, when $|\zeta| > K/h^2$ a spontaneous flow transition occurs [109], with a defined profile for both the director angle and the flow velocity. This is similar in form to the Fredericks transition [21], except now the director is being reoriented not by an external field but by internal stresses and the transition is associated with a dynamic, flowing state. Many methods of controlling the dynamics of active nematics hinge on the behaviour of their topological defects and so we shall delay their discussion until 2.4.1, after first describing the defects of two-dimensional nematics.

We conclude this section by stating the approach to analysing the dynamics of active nematics that is employed in this thesis. The full equations as laid out in (2.9)-(2.12) are only solvable analytically in a one-dimensional geometry [109]. We instead employ a minimal description in which only the active contribution to the stress tensor (2.11) is retained and consider the active flow induced by an equilibrium director field. This approach has been utilised previously [40; 110; 44; 89; 111] and will be discussed further at the start of Chapter 3. This amounts to solving the Stokes equation

$$-\nabla p + \mu \nabla^2 \mathbf{u} = \zeta \nabla \cdot (\mathbf{nn}) = \zeta \left[\mathbf{n} \nabla \cdot \mathbf{n} + (\mathbf{n} \cdot \nabla)\mathbf{n} \right], \tag{2.15}$$

where we see that the active force is comprised of the splay and bend vectors introduced in Section 2.2. We will discuss the associated boundary conditions in Chapter 3.

[1] It should be noted though that turbulence is associated with high Reynolds number and we are dealing with the opposite regime here.

[2] These are the subject of the following section.

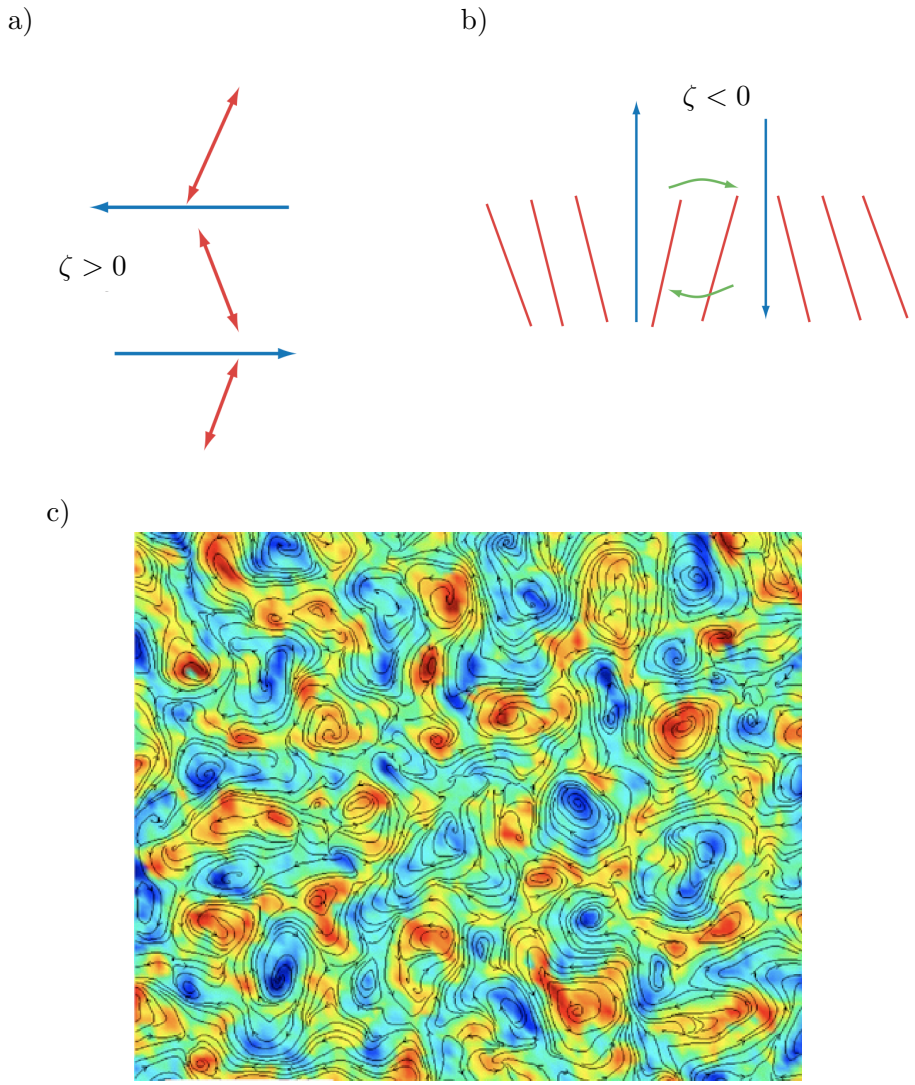

Figure 2.3: Hydrodynamics of bulk active nematics. (a) and (b) The bulk ordered state is unstable to long wavelength bend deformations in extensile systems ($\zeta > 0$) and splay deformations in contractile ones ($\zeta < 0$). Figures from [93]. (c) These instabilities lead to a bulk state of active turbulence, shown in a quasi-two-dimensional suspension of the bacteria *B. subtilis*. The black streamlines of the flow velocity are superposed on the vorticity field. Figure from [107].

2.4 Topological defects in passive and active nematics

2.4.1 Two dimensions

As already mentioned, nematic liquid crystals display dielectric anisotropy described by the tensor Q_{ij}. Consequently when light is shined through a thin sample viewed between crossed polarisers none emerges whenever the director is aligned with either polariser direction, which for concreteness we take to be the vertical and horizontal. This leads to a network of dark brushes called a Schlieren texture, shown in Figure 2.4. If we consider a point where four brushes meet we see that in its neighbourhood the director is twice vertical and twice horizontal, such that it winds through a full turn as we circle this point. Taking the director to be confined in the plane of the sample we write $\mathbf{n} = (\cos\theta, \sin\theta)$ and with γ a path enclosing the point we have $\oint_\gamma \nabla\theta \cdot \mathrm{d}\mathbf{l} = 2\pi$. Applying Stokes' theorem we see that at the place where the brushes meet $\nabla\theta$ must be singular. It is the points where only two brushes meet, around which the director winds by π, that demonstrate the aforementioned nematic symmetry that $\mathbf{n}$ and $-\mathbf{n}$ are equivalent. In general one of these singular points may be associated with a half-integer winding number $q = \oint_\gamma \nabla\theta \cdot \mathrm{d}\mathbf{l} \in \frac{1}{2}\mathbb{Z}$, such that $\mathbf{n}$ winds by $q\pi$ on a small path around the singularity and in its neighbourhood has the form $\mathbf{n} = (\cos q\theta, \sin q\theta)$, in a one-elastic-constant approximation. This winding is a topological property of the system in that any smooth deformation of the director cannot change the number of singularities or their windings, only shift their locations. Consequently these singularities are known as topological defects and the winding numbers as their topological strength or charge. The term defect refers to the fact that at these places the nematic orientation is undefined and so the system melts into the isotropic phase. The picture of this occurring at points is an idealisation, in reality each singularity is associated with a defect core, characterised by the correlation length of the nematic order, over which the ordering falls to zero.

The geometric description of the continuous deformations of a nematic is therefore complemented by a topological description of the locations where the nematic ordering breaks down. The two are not fully distinct of course, as topological defects naturally induce large deformations in the surrounding nematic, indeed it was by considering gradients of $\mathbf{n}$ that we established their existence. We shall see in 2.4.1 that this role as foci of distortions lends them a leading part in the dynamics of active nematics.

It is natural to seek to reduce one's description of a physical system down to one in terms of a discrete set of quasi-particle excitations. In a nematic these are the topological defects described above, in terms of which the theory of nematic elasticity

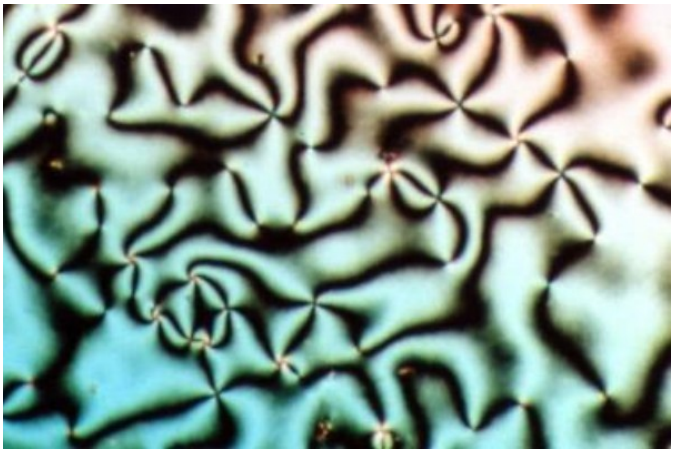

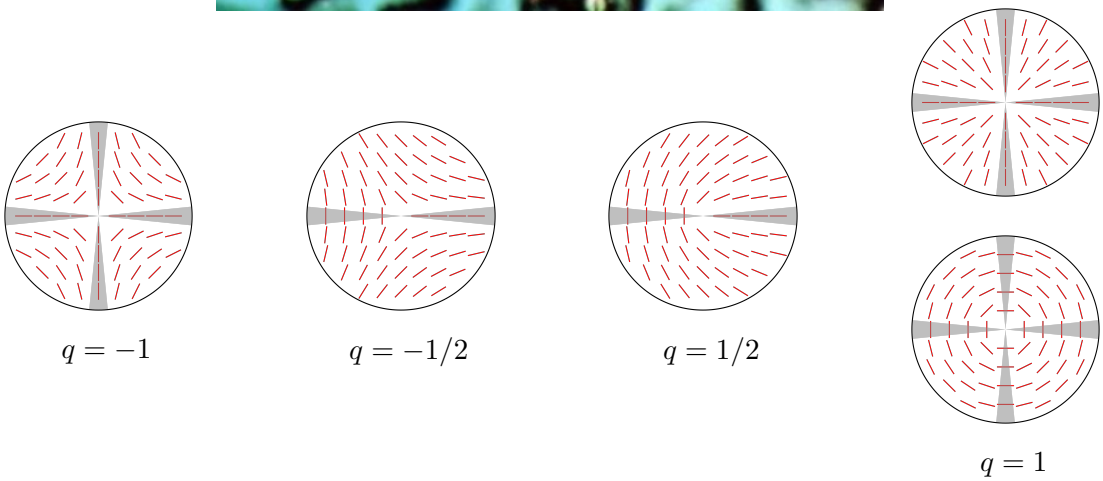

Figure 2.4: Nematic topological point defects in two dimensions. Above: a Schlieren texture formed by viewing an illuminated thin sample of nematic through cross polarisers. The dark 'brushes' arise whenever the director is aligned with either polariser. From [112]. Below: two-dimensional nematic point defects of various indexes with profiles that minimise the one-elastic-constant free energy and the brushes that would be observed in a Schlieren texture overlaid. Note that the pattern of brushes only distinguishes $|q|$, but cannot be used to infer its sign. Note also the two distinct $q = 1$ defects, which result from these defects being spin 0.

may be reformulated as a Coulomb gas of defects [113] interacting via an energy [21]

$$E = q_1 q_2 K \ln\left(\frac{r}{a}\right), \tag{2.16}$$

where r is the defect separation, a is the size of the defect core and we are working in a one-elastic-constant approximation. There are two points to draw from this. Firstly, defects of opposite sign experience an elastic attraction, rendering them meta-stable. Though defects may arise through rapid quenching to the nematic phase, those not maintained through boundary conditions or external fields are expected to pair-wise annihilate as the system equilibrates. Secondly, there is an energetic cost associated with high-index defects. Setting $q_1 = q_2 = q$ in (2.16) and redefining r as a characteristic next-defect distance we see that defects have a self-energy that grows as q^2. In particular, the energy of a single $+1$ defect is double that for two $+1/2$ defects and in general only the lowest-index topological defects are observed, although higher-charge defects can be stabilised under certain conditions [114]. The nematic to isotropic transition is then seen as originating from the unbinding of pairs of $\pm 1/2$ defects [115] in a manner akin to the Berezinskii-Kosterlitz-Thouless transition [116; 80].

Defects may also be maintained through curvature of the substrate. The interaction between defects and curvature is two-fold. On the global, topological, level the integrated Gaussian curvature G of a manifold is related to its genus g via the Gauss-Bonnet theorem [71]

$$\int_M G \mathrm{d}A = \chi, \tag{2.17}$$

with $\chi = 2(1-g)$ the Euler characteristic. The Poincaré-Hopf theorem [117] then states that for a tangential vector field the sum of indices of its singularities must be equal to the Euler characteristic. On the local, geometrical, level defects in elastic systems have a proclivity to reside at points where the sign of their topological index matches that of the underlying Gaussian curvature in order to alleviate geometrical frustration [118; 8; 119]. This has consequences for the morphology of vesicles with orientational order [120] and nematic textures in spherical geometries [121] where defects are required, but can also lead to a meta-stable many-defect state on the torus, for which $\chi = 0$, due to defects of opposing sign being separated into regions of positive and negative Gaussian curvature [122].

Homotopy theory of defects

We now briefly recapitulate the above description of director winding in the more formal language of algebraic topology [123] that will aid us when we come to generalising to three dimensions. This treatment of defects was developed in the 1970s [124] and serves as an extension of Landau's theory of phase transitions, in which the symmetry group G of a high-temperature isotropic phase is reduced to a subgroup H in the low-temperature ordered phase. The order parameter that characterises the ordered phase resides in a topological space called the ground state manifold (GSM), given by the coset space G/H. Defects may be classified via the behaviour of the order parameter in the neighbourhood of the defect, that is by maps $S^n \to \text{GSM}$, where the sphere S^n is a measuring surface that encloses the defect and the dimension n is one less than the codimension of the singular structure. The set of equivalence classes of these maps up to homotopy (continuous deformation), with a common base point $x \in \text{GSM}$ fixed, form a group, the homotopy group $\pi_n(\text{GSM})$. Returning to the case of a two-dimensional nematic the GSM is, owing to the nematic symmetry, a circle with antipodal points identified, that is the real projective line $\mathbb{R}P^1$. Calculating the homotopy group $\pi_1(\mathbb{R}P^1) \cong \mathbb{Z} \cong \frac{1}{2}\mathbb{Z}$ we recover our previous identification of an infinite set of distinct point defects.

In anticipation of our upcoming discussion of the topological defects of three-dimensional nematics we now present the relevant homotopy groups. To find the GSM we take G as $SO(3)$, the rotation group of Euclidean space, and H as the group D_∞ of symmetries of the nematic director. Hence the GSM is $SO(3)/D_\infty \cong \mathbb{R}P^2$ [124; 77] and the homotopy groups $\pi_1(\mathbb{R}P^2)$ and $\pi_2(\mathbb{R}P^2)$ classify the local structures of line and point defects respectively. For the first of these we find $\pi_1(\mathbb{R}P^2) \cong \mathbb{Z}_2$, as illustrated in Figure 2.5, which shows $\mathbb{R}P^2$ as a hemisphere with antipodal points on the boundary identified. In the latter case the fact that S^n is the covering space of $\mathbb{R}P^n$ with fiber S^0 can be used to show that $\pi_2(\mathbb{R}P^2) \cong \pi_2(S^2) \cong \mathbb{Z}$ [123].

The power of this approach is that it determines the nature of the possible defects purely from the topology of the order parameter space, divorced from any specifics of the physical system[3], although the defect morphology may be affected by instance-dependent properties such as an energy functional. This gives the construction a universality and the same defects that arise in two-dimensional nematics can be found in any line field, such as the polarisation patterns of light [127], the singularities in the principal curvature of surfaces, known as umbilic points [128] and fingerprints [129]. The last of these

[3]Cautionary examples exist where a naïve application of homotopy theory leads to an erroneous prediction for the defects of a system such as in the classification of defects in a two-dimensional smectic [125] and the combination laws for C points in polarisation fields [126].

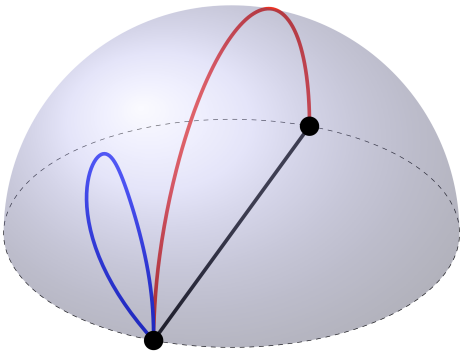

Figure 2.5: Illustration of the fundamental homotopy group of $\mathbb{R}P^2$. The real projective plane is depicted as a hemisphere with antipodal points identified. There are two distinct classes of loops, those that are contractable (blue) and those than span to the antipode. The latter corresponds to the only non-trivial element which squares to the identity such that $\pi_1(\mathbb{R}P^2) \cong \mathbb{Z}_2$.

examples leads us in the direction of considering the impact of these defects in biological contexts.

Topological defects in two-dimensional active nematics

Insight into the impact that topological defects have on the dynamics of active nematics can be attained by following the approach laid out in Section 2.3 and solving Stokes' equations for a single disclination with the director minimising (2.5), that is $\mathbf{n} = (\cos q\theta, \sin q\theta)$ with q the charge of the defect [39; 40]. The flow solutions were calculated in [40] by integrating the active force against the two-dimensional Oseen tensor [100] and are illustrated in Figure 2.6 for $\pm 1/2$ defects. The key distinction between the flows is that the flow is non-zero at the location of the $+1/2$ defect while at the $-1/2$ defect it vanishes. This is readily understood by noting that the $+1/2$ defect breaks fore-aft symmetry, allowing a choice of propulsion direction which is not possible for the $-1/2$ defect as it possesses three-fold symmetry. This difference in the motility of these defects in active nematics due to their symmetry predates the calculation of their active flows, being contained in the supplementary material of [16]. This means that $+1/2$ defects behave as self-propelled polar particles, with the defect being advected by the flows it induces and moving along its orientation vector [130; 131] at a speed proportional to the activity. The direction of propulsion therefore serves as an indicator of the nature of activity present in the system, with the defect moving head first in extensile systems and tail first in contractile ones.

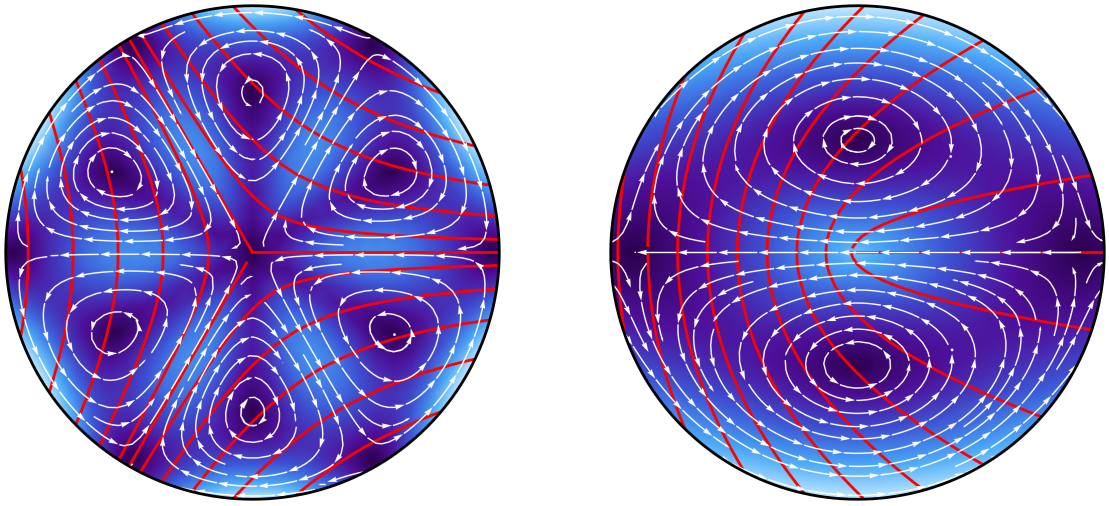

Figure 2.6: Active Flows of two-dimensional nematic point defects. The streamlines of the flow are shown in white with the background colour indicating its magnitude and the red lines are integral curves of the director field. A no-slip boundary condition is applied on the black circle. After [40].

The Coulomb gas picture of passive nematics is therefore replaced by one of a gas of self-motile $+1/2$ defects accompanied by passive $-1/2$ defects [41; 113]. In addition to the elastic forces the $+1/2$ defects experience active torques [42], with defect interactions generically being non-reciprocal [132]. This non-reciprocity of interactions is something of a hallmark of active systems [113] and will reemerge in Chapter 3. The defect unbinding now arises through competition between elastic attraction and the active motility of $+1/2$ defects, transitioning the bulk system from the ordered phase to the state of active turbulence described earlier. Due to the torques that $+1/2$ defects experience their motion is not purely ballistic and by considering the persistence length of this motion a criterion for active defect separation can be established [41; 38]. This significance of the orientation of the $+1/2$ defects leads to an 'order-through-disorder' effect with rotational noise confounding their ability to actively separate from their $-1/2$ partners and stabilising the nematic phase [41; 38; 113].

Half-integer defects are a hallmark of nematic symmetry and their observation has enabled the identification of many biological systems as active nematics. The distinct local environment of topological defects makes them natural foci for functionality and the impact they can have on the behaviour of biological matter is remarkable [20; 38; 113]. The recognition of biological nematic defects dates back to the 1960s, when they were

observed in the orientation of fibroblast cells [133]. Work beginning in the 1990s showed that the so-called 'pinwheel' patterns in the cells that make up the visual cortex of cats are in fact also $\pm 1/2$ defects [134; 135; 136]. Further examples have subsequently been found in both eukaryotic [28; 29] and prokaryotic cells [137; 138; 139], with bacterial colonies exhibiting an isotropic-nematic phase transition as they grow [137] and even displaying micro-domains of distinct nematic alignment which tile the colony like a mosaic [139; 20].

Instances of nematic defects being tied to biological function are provided by monolayers of neural progenitor cells and epithelial Madin-Darby Canine Kidney cells. In the former cells are found to be depleted at $-1/2$ defects and accumulate at $+1/2$ ones, forming three-dimensional mounds [140]. In the latter $+1/2$ defects act as centres for apoptosis, that is cell death and extrusion from the monolayer [30]. In growing biofilms vertical lift-off and mound formation has been instead found to occur at $-1/2$ defects [141]. The motility that $+1/2$ defects acquire in active systems allows them to overcome the elastic repulsion that would keep them separate in passive nematics to form $+1$ defects. These integer defects have been shown to play a crucial role in developmental morphogenesis [142; 143; 144], for example in *Hydra* [145], where in the early development two $+1$ defects define what is to become the body axis and protrusions driven by the self-propulsion of $+1/2$ defects are linked to the formation of later structure. Similar defect-driven dynamic morphology occurs in deformable active shells [146; 147; 148]. The formation of topological defects also plays a pivotal role in the expansion of bacterial colonies [138; 13], with $+1$ asters appearing to support verticalisation of bacteria [15]. This leads to a tortoise-and-hare scenario, in which populations of *P. aeruginosa* that were individually less motile than mutant strains were able to outperform their faster rivals as the latter become frozen by the formation of $+1$ defects [149].

Having discussed the role of defects in the dynamics of active nematics, we now return to the issue of how this dynamics may be controlled. Numerical simulations of laterally confined active nematics have revealed an additional 'Ceilidh dance' state [150], intermediate to the spontaneous flow state and active turbulence and arising when the characteristic vortex size is commensurate with the channel height. This state is characterised by two columns of $+1/2$ defects that weave sinusoidally along the channel in opposing directions. As the activity is increased patches of active turbulence form, with the transition to the turbulent phase belonging to the directed percolation universality class [151]. Similar confinement effects driven by the motility of $+1/2$ defects have been observed for confinement to the disc [150; 152; 153; 154], where the Euler characteristic

requires a total defect charge of +1. Recent experiments on mouse fibroblast cells have observed both the spontaneous flow transition [155] and a dynamical state with two +1/2 defects under circular confinement [156].

The state of active turbulence can also be tamed by effects that screen the hydrodynamic interactions. One route is to increase the substrate friction [157; 158; 159; 160]. The length scale of hydrodynamic screening is determined by the friction f as $l_{sc} \sim \sqrt{\mu/\rho f}$ [20] and has much the same effect as a confinement scale; when $l_{sc} \sim l_A$ a defect-free state is achieved [157] and for intermediate friction the defects arrange into a regular lattice [158].

An additional method is to couple the active nematic to a soft interface. Hydrodynamic screening can be tuned by varying the viscosity of an oil layer [161], with higher viscosity resulting in more defects by reducing their motility and hence impeding their ability to annihilate [20]. Spatial structure can be induced via a passive smectic [162; 163], with the active nematic organising into circular regions corresponding to the toroidal focal conic domains in the smectic substrate [163]. On applying a magnetic field the response of the smectic causes alternating lamellar flows to be established in the active nematic [162].

The influence of curvature on topological defects has been investigated on the sphere where the four requisite +1/2 defects display quasi-periodic motion between tetrahedral and coplanar configurations [164; 165; 89]. Additional effects, including defect localisation, arise on prolate or oblate spheroids [166]. The ability of the distinct regions of Gaussian curvature on a torus to separate topological defects persists in active nematics and has been confirmed experimentally [167].

2.4.2 Three dimensions

Point defects

To reiterate, in three dimensions the nematic GSM is $S^2/\{\mathbf{p} \sim -\mathbf{p}\} \equiv \mathbb{R}P^2$. Accordingly, point defects in three-dimensional nematics are classified by the homotopy classes of maps $S^2 \to \mathbb{R}P^2$. As $\pi_2(\mathbb{R}P^2) \equiv \mathbb{Z}$ there are an infinite number of distinct point defects in three-dimensional nematics, some of which are shown in Figure 2.7, using the representative field for a degree q defect [77]

$$\mathbf{n}_q(\mathbf{r}, \theta, \phi) = \sin\theta\,[\cos(q\phi)\mathbf{e}_x + \sin(q\phi)\mathbf{e}_y] + \cos\theta\mathbf{e}_z. \tag{2.18}$$

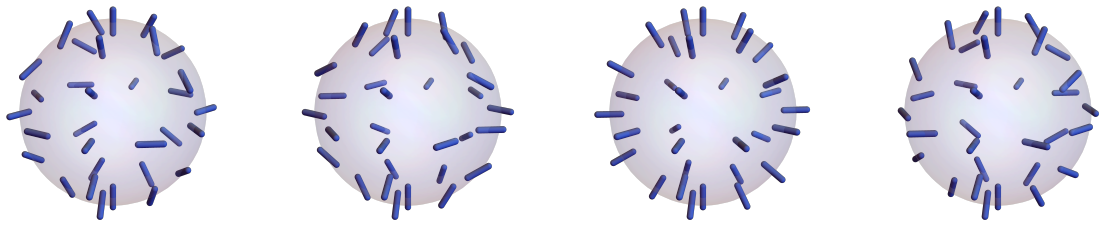

$q = -2$ $q = -1$ $q = 1$ $q = 2$

Figure 2.7: Representative nematic point defects in three dimensions. The director field is given by (2.18) and is shown on a spherical surface centred on the defect.

The case $q = 1$, for which $\mathbf{n} = \frac{\mathbf{r}}{|\mathbf{r}|}$, serves as a quintessential example of all three-dimensional nematic point defects and gives them the name hedgehog defects. In particular the $q = 1$ defect is known as a radial hedgehog and the $q = -1$ one a hyperbolic hedgehog. The degree of a defect is most easily calculated by orienting the director, lifting the GSM from $\mathbb{R}P^2$ to S^2. The degree of maps $S^2 \to S^2$ can be found by pulling back the area form on the image sphere to the measuring surface and integrating to give

$$q = \frac{1}{4\pi} \int \mathrm{d}x\mathrm{d}y \mathbf{n} \cdot (\partial_x \mathbf{n} \times \partial_y \mathbf{n}) \,. \tag{2.19}$$

The resulting integral is not invariant under the nematic symmetry $\mathbf{n} \to -\mathbf{n}$, but rather changes its sign. This is indicative of the inability to assign an unambiguous degree to point defects in three-dimensional nematics [77; 168].

Line defects

Three dimensions allows the existence of not just point but also line defects. These are classified according to $\pi_1(\mathbb{R}P^2) \equiv \mathbb{Z}_2$. The two elements of this group mean that there is not an array of topologically distinguished line defects, rather the only topological distinction that can be made is between a defect being present or not. This may seem surprising, as naively one might expect that each of the point defects in two dimensions could be extruded to give a topologically distinct line defect. To see why this is not so, consider the director field [77]

$$\mathbf{n}_\beta = \cos(\phi/2)\mathbf{e}_x + \cos\beta \sin(\phi/2)\mathbf{e}_y + \sin\beta \sin(\phi/2)\mathbf{e}_z. \tag{2.20}$$

This provides a homotopy between the $+1/2$ ($\beta = 0$) and $-1/2$ ($\beta = \pi$) defect profiles. A similar homotopy allows the removal of $+1$ defects through 'escape into the third

dimension' and arises when normal anchoring is applied to cylindrically confined nematics [169; 170; 171]. It should be noted the above classification only captures the local topology of a line defect. The question of how the director may be consistently extended to provide a complete texture gives rise to more subtle global topology [172; 173; 75].

As in two dimensions, minimisation of the one-elastic-constant Frank free energy (2.5) results in rotation of the director in a single plane. Unlike the two-dimensional case, this plane is not restricted to being the plane normal to the defect line but can be any plane in $\mathbb{R}^2$. We may define this winding plane by its unit normal vector $\mathbf{\Omega} \in S^2$ and a different defect profile results according to the angle that $\mathbf{\Omega}$ makes to the defect line unit tangent vector $\mathbf{t}$. The resulting minimal director fields can be given explicitly as [43; 44]

$$\mathbf{n} = \cos(\phi/2)\mathbf{m} + \sin(\phi/2)\mathbf{\Omega} \times \mathbf{m}, \tag{2.21}$$

with ϕ the azimuthal angle around the defect line and $\mathbf{m}$ is a unit vector normal to both $\mathbf{\Omega}$ and $\mathbf{t}$. When $\mathbf{\Omega}$ is parallel or antiparallel to $\mathbf{t}$ (2.21) reduces to the profile of $+1/2$ and $-1/2$ two-dimensional point defects respectively, with these profiles being known as wedge type. When $\mathbf{\Omega}$ is orthogonal to $\mathbf{t}$ the resulting defect profiles are termed twist type. Figure 2.8(a) illustrates (2.21) for different $\mathbf{\Omega}$ with $\mathbf{m}$ fixed. This collection of local profiles also displays the homotopy given in (2.20) between the two wedge type profiles via a twist profile. There is a circle's worth of local twist profiles, which may be further categorised as radial or azimuth twist according to the direction of the director along $\phi = 0$. For the homotopy in (2.20) the director is always radial along this line and so the twist profile in Figure 2.8 is of radial twist type.

Restriction of the director rotation to a single plane may also be used to provide a global director texture around a closed defect loop, as first introduced by Friedel & de Gennes [174]. Taking $\mathbf{e}_1, \mathbf{e}_2$ as an orthonormal basis for the plane, with $\mathbf{e}_1$ the asymptotic director orientation we have

$$\mathbf{n} = \cos(\omega/4)\mathbf{e}_1 + \sin(\omega/4)\mathbf{e}_2, \tag{2.22}$$

with ω the solid angle function [45; 46] of the defect loop. This serves as a minimiser of the Frank free energy (under the approximation of one elastic constant) regardless of the shape of the defect loop or the orientation of $\mathbf{\Omega}$ and so is able to capture much of the geometric complexity that nematic defect loops can display. Representative examples of this geometric diversity are shown in Figure 2.8(b) for planar circular loops with uniform $\mathbf{\Omega} = \mathbf{e}_1 \times \mathbf{e}_2$. They are termed splay, bend and twist loops according to the predominant

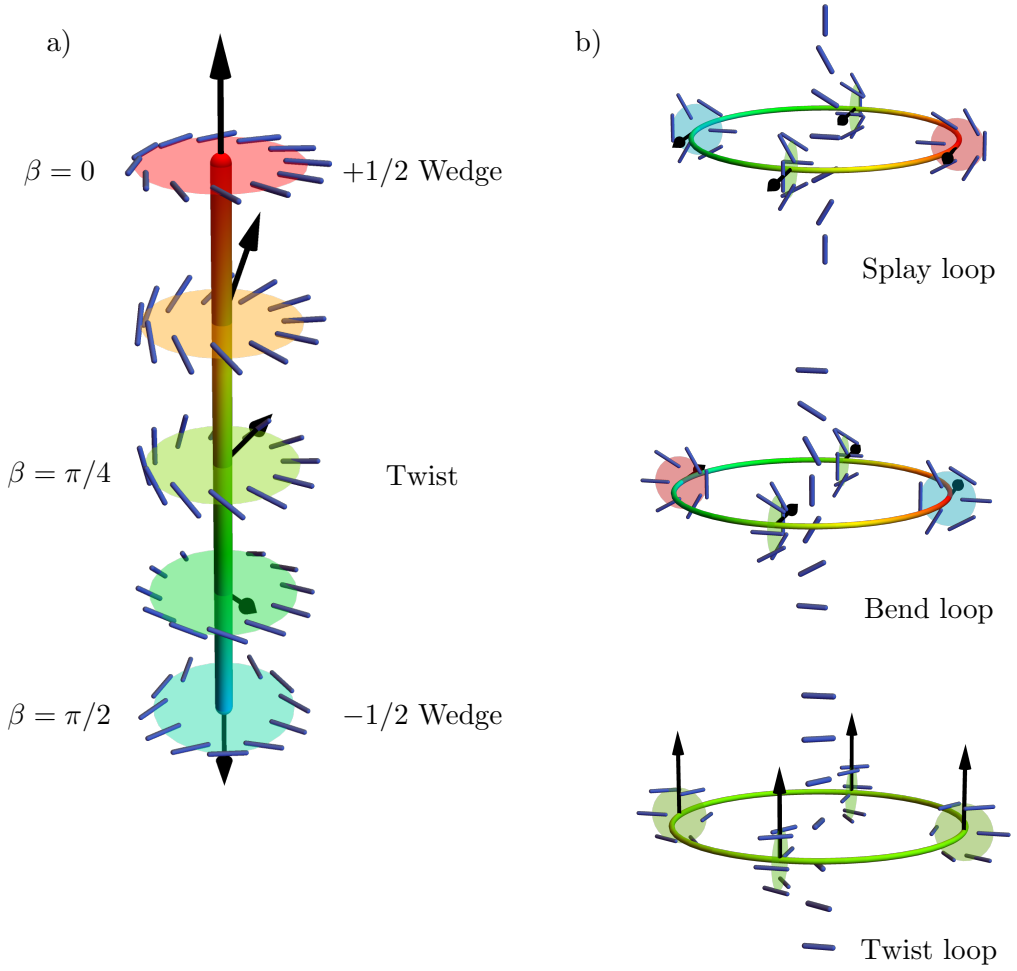

Figure 2.8: Nematic line and loop defects. (a) Local profiles of defect lines. The director is shown as blue rods in planes orthogonal to a defect line along which the local profile varies according to the homotopy in (2.20). The director rotation is confined to the plane normal to a winding vector $\mathbf{\Omega}$, shown as a black arrow. (b) Representative examples of planar nematic defect loops. Their names stem from the dominant nature of the director distortion through the centre of the loop. The local director profile is shown in certain cross-sections of the loop and the loop is coloured according to the nature of this winding, as in (a).

nature of the nematic distortion on a line through the loop [4]. We have chosen to keep the plane of the defect loop fixed and hence $(\mathbf{e}_1, \mathbf{e}_2)$ changes, being $(\mathbf{e}_z, \mathbf{e}_x)$ for the splay loop, $(\mathbf{e}_x, \mathbf{e}_z)$ for the bend loop and $(\mathbf{e}_x, \mathbf{e}_y)$ for the twist loop.

Topological defects in three-dimensional active nematics

The description of the active dynamics of three-dimensional active nematics in terms of their topological defects is less developed than in two dimensions, in part due to the greater geometrical complexity the defects can display and in part because until recently an experimental realisation was lacking. Recent experiments have revealed the dynamics to be dominated by charge-neutral defect loops [43], with charge-neutral here referring to the vanishing of the hedgehog charge. The defect loops shown in Figure 2.8(b) are all charge-neutral and, within the one-elastic-constant approximation used for simulations, are energetically equivalent. However, a bias towards those of twist type has been found both experimentally and in numerical simulations [43], an observation that currently lacks a complete explanation. Simulations of three-dimensional active nematics confined to droplets have demonstrated that the dynamics of defect loops, along with the topological changes they can undergo such as intersection and break-up, are key to the understanding of active nematic turbulence [62]. The pivotal role of twist was identified in a quasi-two-dimensional channel geometry where the onset of twist in defect lines was found to initiate the transition from two-dimensional to three-dimensional active turbulence [175].

Initial analytical work on the active dynamics of nematic defect loops has provided a local description of the active flow at each point on the defect loop [44], resulting from solving Stokes' equations with the director distortions captured by Maxwell's solid angle function [46; 77]. By considering certain canonical orientations of planar defect loops as shown in Figure 2.8(b) it was found that splay and bend defect loops self-propel. In Chapter 4 we present a complementary global description of active nematic defect loops based on a multipole expansion of the solid angle. Through this we are able to describe loops with arbitrary alignment with respect to the far field and include the effects of non-planarity, which we show leads to self-orientation of defect loops and a mechanism to produce the observed bias towards loops of pure-twist type.

[4] We stress that this nomenclature should not be taken to mean that such defect loops are associated only with these specific distortions of the director.

2.5 Colloids in nematics

Colloidal inclusions transform the physics of nematics and their description requires the synthesis of many of the concepts we have met so far. Reviews of their modelling, properties and applications can be found in [176; 177; 90]. They typically result in the formation of topological defects and so provide a fertile setting for the exploration of global nematic topology [178] and the application of knot theory [179] to liquid crystalline systems [180; 173]. They experience anisotropic elastic interactions mediated by the nematic environment which may be understood from a multipole description of the far-field distortions they induce [90]. This multipole description invites analogies with electrostatics [181; 182] and a colloidal atom paradigm [183; 184] dating back to the work of Einstein and Perrin [185]. In this vein colloids have been designed to induce dominant multipole distortions that exceed the multipoles found in the atomic orbitals of the periodic table [90; 186; 187; 188]. The 'chemistry' of nematic colloids has also been investigated, with crystals formed from one species of colloid [189; 190] or binary mixtures [191; 192]. This opens up applications for self-assembled metamaterials and photonics [193].

To understand the response of the director to colloidal inclusions we add a surface term, known as the Rapini-Papoular surface energy [194], to the bulk free energy discussed earlier (2.5), giving

$$F = \frac{K}{2}\int \mathrm{d}^3\mathbf{r}|\nabla\mathbf{n}|^2 - \frac{W}{2}\int \mathrm{d}^2\mathbf{r}(\mathbf{n}\cdot\mathbf{v})^2, \tag{2.23}$$

where $\mathbf{v}$ is an easy axis of director alignment and the coefficient W typically has a value of $10^{-7} - 10^{-3}\mathrm{Jm}^{-2}$ [177]. Through appropriate treatment of the colloid surface the preferred director anchoring may be normal, tangential or conical [90]. The competition between the surface anchoring and the bulk elasticity defines a length known as the extrapolation length [90] or Kleman-de Gennes length [177] as $\xi_e = K/W$. Recalling that $K \sim 10^{-11}$ N, we have $\xi_e \sim 100$ nm-10 μm. For colloids smaller than ξ_e the distortion of the director is negligible. Minimisation of the total energy may favour deviating from the surface anchoring condition and an interpretation of the extrapolation length is then that the boundary condition is satisfied virtually at a distance ξ_e within the colloid [177]. Colloids larger than ξ_e will result in topological defects being formed in the bulk nematic, with the total defect charge compensating the degree of the boundary condition so as to allow for a uniform asymptotic alignment.

Surfaces may be classified, up to homeomorphism, by their genus, orientability

and number of boundary components [90; 195] and varying these properties for colloids results in a great richness of topological phenomena. This has been demonstrated for generic handlebodies [196; 197], knotted colloids [198; 199] and in the use of colloids to form knotted defect lines [200; 201], in an explicit illustration of global nematic topology [173; 178]. The distortions induced by a trefoil knot are shown in Figure 2.9(a), with the colour representing the orientation of the director when projected into a plane orthogonal to the far-field alignment [198]. The points where the colours meet correspond to surface defects known as boojums [5]. In fact even for a fixed colloidal topology there can be many ways for the boundary degree to be cancelled by a configuration of topological defects. Taking the sphere with normal anchoring as an example the colloid may induce either a hyperbolic hedgehog point defect or a defect loop with a cross-sectional profile of $-1/2$ winding [176], shown in a schematic two-dimensional cross-section in Figure 2.9(b) and (c) respectively. This faculty for the point defect to 'open up' into a loop serves as an explicit demonstration that line defects can carry a hedgehog charge. The defect configuration that arises is dependent on the colloid size as well as the type and strength of the anchoring [176]. In particular, tangential anchoring results in a pair of surface boojum defects at the poles [176].

There is generally an energetic benefit from overlapping of regions of director distortion, leading to anisotropic elastic interactions [177]. The distinct distortions associated with the above arrangements of topological defects lead to distinct elastic interactions. A phenomenological description of these interactions was introduced by Lubensky et al. in 1998 [181] utilising the asymptotic form of the minimisers of the bulk elastic energy (2.6) and an analogy with electrostatics. The resulting elastic interaction potential for axially symmetric particles is [204]

$$U_{\text{int}} = 4\pi K \sum_{l=0}^{\infty} q_l q_{l'} (-1)^{l'} (l+l')! \, \frac{a^{l+l'+2}}{r^{l+l'+1}} P_{l+l'}(\cos\theta), \tag{2.24}$$

where the $P_{l+l'}(\cos\theta)$ are the Legendre polynomials.

The hedgehog defect configuration is rotationally symmetric but has no horizontal plane of mirror symmetry and so the far-field distortion has dipole character; it is known as the UPenn dipole. Just as for charge configurations this dipole can be viewed

[5] It is customary to note that this terminology was introduced by David Mermin to describe surface defects in ^{3}He-A, inspired by the action of the Snark in Lewis Carroll's The Hunting of the Snark [202]. He found the motion of a bulk vortex to the surface reminiscent of the poem's closing lines 'He had softly and suddenly vanished away - For the Snark *was* a boojum, you see.' Mermin's own account may be found in [203].

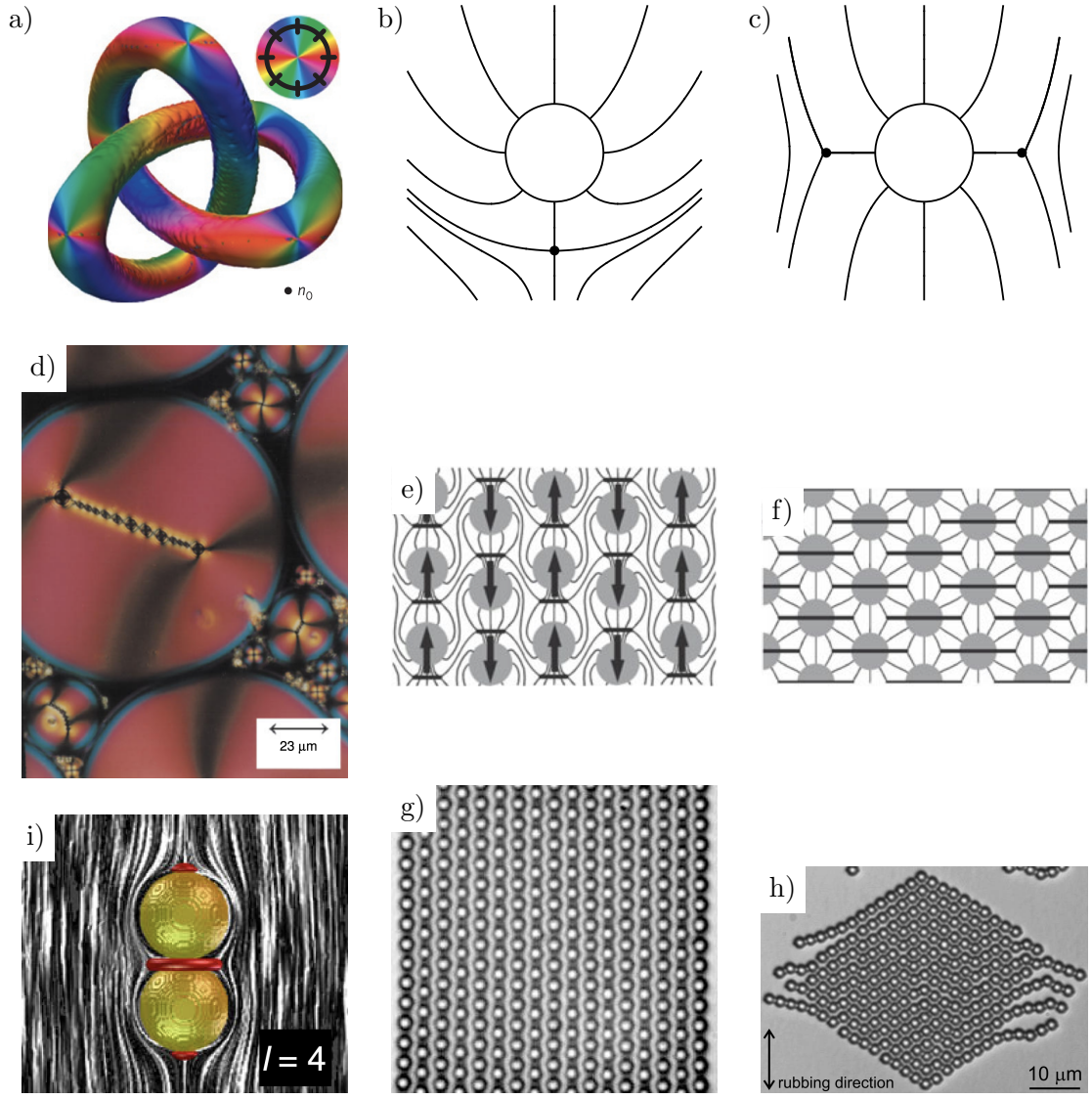

Figure 2.9: Colloids in nematics. (a) A nematic distortion induced by a trefoil knot. The colour indicates the orientation of the director in a plane orthogonal to the far-field alignment according to the inset. From [198]. (b) and (c) Schematic representations of the director distortions around a spherical colloid for the dipolar hyperbolic hedgehog defect arrangement and quadrupolar Saturn ring defect loop configuration respectively. The director is axially symmetric and is shown in a cross-section, with the black dots indicating the location of the point or line defects. (d) Chains of dipolar colloids formed in an emulsion of water droplets in a nematic, from [205]. (e) and (f) Schematics illustrating the formation of colloidal lattices for dipolar and quadrupolar colloids respectively, from [177]. Their experimental realisations are shown in (g), from [189] and (h), from [190]. (i) A hexadecapolar distortion induced in a nematic by a 'gourd colloid' with the red lines indicating the locations of defect loops and boojum defects, from [186].

as arising due to the separation of the index -1 hyperbolic hedgehog and a virtual index $+1$ radial hedgehog located at the centre of the colloid [177]. These dipolar distortions, along with their anisotropic interactions, were first observed in the experiments of Poulin et al. in 1997 [205; 206] in which small water droplets were dispersed in a nematic, shown in Figure 2.9(d). The resulting interaction has two lobes of attraction and causes colloids to primarily form long chains of parallel dipoles along the far-field direction with weak perpendicular interactions between antiparallel dipoles allowing the formation of two-dimensional [189] or even three-dimensional [207] crystals. A schematic illustration of the dipolar alignment in the colloidal crystal is shown in Figure 2.9(e) and an experimental realisation in Figure 2.9(g). The point defect shown in Figure 2.9(b) has been opened into a ring defect in Figure 2.9(e) due to the effects of confinement [177]. The far-field distortion around the defect loop is quadrupolar and given the colloid-loop arrangement is called the Saturn ring quadrupole. This defect configuration was first predicted by Terentjev in 1995 [208] and subsequently observed for colloids with weak anchoring [209], small diameter [210] and under confinement to thin planar cells [211]. The elastic interaction between such colloids has four regions of attraction and leads to the formation of either kinked chains or two-dimensional lattices [190], again illustrated schematically in Figure 2.9(f) and experimentally in Figure 2.9(h). As can be seen from (2.24) the quadrupole elastic interaction is much weaker than that between dipoles, decaying as r^{-5} rather than r^{-3}. Accordingly the structures formed can be disrupted by fluctuations in temperature or flows in the liquid crystal and deteriorate over a timescale of about a month [190], whereas dipolar crystals can be stable for over a year in laboratory conditions [189]. There has been a drive to design colloids that result in high-order multipole distortions [187; 186; 188], motivated partly by the ensuing intricacy of interactions which allows for the design of novel metamaterials and also by a more fundamental study of multipole structure beyond that observed in the periodic table [186]. To this end axisymmetric dominant multipoles up to order 6 have been induced in a nematic environment by forming colloids from stacked spheres and tuning the director anchoring on the surface. This is illustrated in Figure 2.9(i) for a hexadecapole.

Both the directionality of the pair-wise elastic interactions and their power-law nature can be probed by releasing a particle from an optical trap and tracking the direction of the elastic forces through video microscopy [90]. In this way the use of the multipole expansion for the director distortions to explain the physics of nematic colloids has been robustly tested for dipolar distortions [212; 213; 214; 215; 216], quadrupolar interactions [217; 190], octupoles [218; 187] and hexadecapoles [187], in addition to being

confirmed numerically [219; 190].

In the following chapter we demonstrate how a multipole analysis can also be usefully applied to understand the response to distortions of active nematics. The character of nematic distortions is not determined simply by the topology of the colloidal inclusion, but also by its geometry. This nuance, in a two-dimensional context, will be the subject of Chapter 5 and we a defer a review of work in this area until then.

The principle, I said
is leverage. Not quite
the Gunslinger rejoined,
that is the mechanism
I asked for the principle

Ed Dorn, Gunslinger I

3

Active Nematic Multipoles

Active matter encompasses a wide array of systems across many length scales in which the constituent elements input energy, driving the system out of equilibrium [220; 93; 57; 221]. An issue of fundamental importance is how to harness the energy inherent in these non-equilibrium systems into useful work, for example by transforming their often apparently random or chaotic dynamics into persistent motion. Among the most striking experimental realisations of this are active ratchets [22; 23; 222; 223; 224] - persistent rotation of gears in bacterial baths - the separation of bacteria by asymmetric barriers [225] and the rectification of the motion of microswimmers by an anisotropic medium [226; 227; 228].

We focus here on a particular class of active matter in which the individual elements exhibit the orientational ordering associated with nematic liquid crystals [20]. Such active nematics include cell monolayers [156], tissues [30], bacteria in liquid crystalline environments [229] and suspensions of both bacteria [107] and synthetic microtubules [61] and have been shown to be well-modelled by the addition of an active stress to the hydrodynamics of nematics [40; 44].

The significant features of nematics are reflected in their active counterparts. They exhibit hydrodynamic instabilities [93; 102] and spontaneous flow transitions [109; 155] and topological defects play a decisive role in their dynamics, possessing self-motility

in both two [38; 40] and three dimensions [43; 62; 44].

The equilibrium response of the nematic director to perturbations can, when linearised, be described in terms of multipoles [230; 231; 205; 181]. This has proved a powerful tool in understanding the physics of colloidal inclusions [176; 186] and their applications in metamaterials and soft photonics [193].

We find this an equally fruitful paradigm in active nematics. Utilising the same multipole distortions we characterise the far-field active response to perturbations. This allows us to identify those distortions which produce directed or rotational flows and show that such responses may be naturally induced by colloids. The understanding this gives of the relation between non-equilibrium responses and local manipulations and molecular fields in active nematics will bring both fundamental insights and the potential for control of active metamaterials.

3.1 Hydrodynamics of active nematics

The hydrodynamical equations of active nematics were presented in Section 2.3. An often-used approximation is to consider the active flows generated by an equilibrium director field. This approximation has been used previously in the theoretical description of the active flows generated by defects in both two [40; 110] and three dimensions [44], including on curved surfaces [89], and in active turbulence [111]. The equations can then be taken to be $\mathbf{h} = 0$ for the director field and the Stokes equation

$$-\nabla p + \mu \nabla^2 \mathbf{u} = \zeta \nabla \cdot \big(\mathbf{nn}\big), \tag{3.1}$$

for the active flow. Although one of the key applications of the work in this chapter is to colloids, in our approach we only impose asymptotic conditions on the solutions, namely that $\mathbf{u}$ vanishes with p and $\mathbf{n}$ tending to constant values. We do not include any short scale conditions to explicitly handle the presence of a colloid, such as a no-slip condition on $\mathbf{u}$ or Dirichlet conditions on $\mathbf{n}$. In (3.1) we have neglected the Ericksen stress since for an equilibrium director field it can be balanced by a contribution to the pressure (representing nematic hydrostatic equilibrium). The neglect of the nematic stresses may be further justified by observing that they are two powers of gradients higher order than the retained active stress.

We limit our analysis to director fields that can be linearised around a (locally)

uniformly aligned state, $\mathbf{n} = \mathbf{e}_z + \delta\mathbf{n}$, for which the equations reduce to

$$\nabla^2 \delta\mathbf{n} = 0, \tag{3.2}$$

$$\nabla \cdot \mathbf{u} = 0, \tag{3.3}$$

$$-\nabla p + \mu\nabla^2 \mathbf{u} = \zeta\big[\mathbf{e}_z\big(\nabla \cdot \delta\mathbf{n}\big) + \partial_z \delta\mathbf{n}\big], \tag{3.4}$$

with the same boundary conditions as discussed for (3.1), meaning that $\delta\mathbf{n}$ vanishes at large distances. These nematic distortions correspond to elastic multipole states in the director field, which are often thought of as an asymptotic description, however, they provide a close approximation even at only moderate distances outside a 'core' region that is the source of the multipole (and which we do not describe explicitly here, although see the following chapter on disclination loops). This is relevant to the active system as it is well-known that the uniformly aligned active nematic state is fundamentally unstable [25] and active nematics are turbulent on large enough scales. Our solutions should be interpreted as describing the behaviour on intermediate scales, larger than the core structure of the source but smaller than the scale on which turbulence takes over.

3.2 Multipole director distortions

As outlined above, we take the director to be $\mathbf{n} = \mathbf{e}_z + \delta\mathbf{n}$, where $\delta\mathbf{n}$ is a two-component vector of transverse distortions, both components of which are harmonic, meaning that at order l they may be expressed as $1/r^{l+1}Y_m^l$ or as l derivatives of $1/r$. Since we are considering perturbations around a uniformly aligned state, there is significance to the symmetries of this ground state, namely an $SO(2)$ subgroup of the full rotation group corresponding to rotations around $\mathbf{e}_z$. As $\delta\mathbf{n}$ is comprised of two independent harmonic functions the distortions at order l form a $2(2l+1)$-dimensional vector space and a natural basis is provided by the irreducible representations under the action of $SO(2)$. This gives immediate insight into the nature of the active response that harmonic distortions might induce, for just as the presence or lack of active motility in nematic point defects is a consequence of their respective symmetries [40], the spin of multipoles under the action of $SO(2)$ has consequences for their active flows. The spin denotes the number of equivalent symmetry states in a full rotation, with the sign indicating whether a local director rotation results in a global rotation of the same (positive) or opposing (negative) sense. In particular, spin ± 1 distortions may lead to translations along or rotations about transverse directions and only spin 0 ones can do so along or about $\mathbf{e}_z$.

Before calculating the active response to elastic multipole states, we first expand upon their structure as differentials of $1/r$. This apparent diversion is worthwhile as it sets up the derivative-based perspective of harmonics we take throughout this chapter, which is also mirrored in our calculation of their active responses.

As a prelude, let us consider some aspects of complex geometry. A complex manifold has a complex structure which provides a splitting of the complexified tangent bundle into a holomorphic and anti-holomorphic bundle [232]. A similar splitting of the derivative allows a decomposition at order l into $l+1$ distinct bundles, see the discussion in [75]. Vector fields are sections of these bundles and the winding of their zeros can be inferred from the bundle they belong to [75].

Inspired by these points, and in light of the natural distinction with the far-field direction, we complexify the transverse plane, making the decomposition $\mathbb{R}^3 \cong \mathbb{C} \oplus \mathbb{R}$ and describing the transverse distortions via the complex function $\delta n = \delta n_x + i\delta n_y$. The natural choice for the derivatives on $\mathbb{C}$ is the Wirtinger derivatives

$$\begin{aligned} \partial_w &= \frac{1}{2}(\partial_x - i\partial_y), \\ \partial_{\bar{w}} &= \frac{1}{2}(\partial_x + i\partial_y), \end{aligned} \tag{3.5}$$

with the Laplacian given by $\partial_z^2 + 4\partial_{w\bar{w}}$. This brings us to two equivalent expressions for the harmonic director distortions

$$\begin{aligned} \delta n = \delta n_x + i\delta n_y &= \sum_{l=0}^{\infty} \sum_{m=-l}^{l} q_{lm} \left(\frac{a}{r}\right)^{l+1} Y_l^m(\theta, \phi), \\ &= \sum_{l=0}^{\infty} \sum_{m=-l}^{l} \tilde{q}_{lm} a^{l+1} \partial_{\bar{w}}^m \partial_z^{l-m} \frac{1}{r}, \end{aligned} \tag{3.6}$$

where $Y_l^m : S^2 \to \mathbb{C}$ are the spherical harmonics, the q_{lm} and $\tilde{q}_{lm}$ are complex coefficients and a is a characteristic length of the multipole, as might be set by the radius of a colloid. For compactness of notation it is to be understood that when m is negative in the second equation $\partial_{\bar{w}}^m$ represents $\partial_w^{|m|}$. The index m denotes the topological charge of the phase winding of the spherical harmonic. This gives the spin of the corresponding vector field as $1 - m$, where the 1 is due to a vector being a spin-1 object. Although the director $\mathbf{n}$ has spin-2 symmetry it is simplest to treat it as an oriented vector with the understanding that all results must be invariant under the global change $\mathbf{n} \to -\mathbf{n}$. The multipoles at order l therefore have spins that range from $1 - l$ to $1 + l$. They are illustrated up to quadrupole order in Figure 3.1, along with a representation in terms

of topological defects which we shall elaborate upon shortly. The structure of Figure 3.1 is such that differentiation maps the distortions of one order to the next, with ∂_z leaving the distortion in the same spin class, $\partial_{\bar{w}}$ moving it one column to the left and ∂_w moving it one column to the right. The operators ∂_w and $\partial_{\bar{w}}$ therefore play the same role as the raising and lowering operators in quantum mechanics and the shift by one in the spin values simply results from the object on which they act being a spin-1 director as opposed to a spin-0 wavefunction.

We shall predominantly follow Maxwell [45; 233; 234] and use the latter of the two harmonic representations in (3.6), describing the nematic distortions as derivatives of $1/r$. This will allow us to express the active flow response as the same set of derivatives acting on an analogous fundamental flow. The $1/r$ monopole distortion itself results from a rotation by an angle θ_0 of the nematic in a sphere of radius a. For this the equilibrium director field is [230]

$$\mathbf{n} = \cos\left(\frac{\theta_0 a}{r}\right)\mathbf{e}_z + \sin\left(\frac{\theta_0 a}{r}\right)\mathbf{e}_x, \tag{3.7}$$

and has the far-field character of a monopole distortion, $\mathbf{n} \approx \mathbf{e}_z + \frac{\theta_0 a}{r}\,\mathbf{e}_x$. Such distortions are shown at the top of Figure 3.1 and can be controllably created using platelet inclusions [235] by employing optical torques to balance the elastic torques associated with monopolar distortions [21] which preclude their existence in equilibrium. In the active case the response will be different because the active stresses associated with the distortion (3.7) will drive fluid flows.

At order l the nematic distortions form a 2(2l+1)-dimensional vector space. We are now in a position to see that the action of SO(2) provides a natural basis for that vector space. The dipolar distortion tensor $\mathbf{p}$ has $2(2+1) = 6$ dimensions and a basis is given by

$$\begin{aligned}
\mathbf{p}^0 &= \left\{\partial_{\bar{w}}\frac{1}{r}, \mathrm{i}\partial_{\bar{w}}\frac{1}{r}\right\} \sim -\frac{1}{2r^3}\left\{x\mathbf{e}_x + y\mathbf{e}_y, -y\mathbf{e}_x + x\mathbf{e}_y\right\} \sim \frac{1}{r^2}\left\{Y_1^1, \mathrm{i}Y_1^1\right\}, \\
\mathbf{p}^1 &= \left\{\partial_z\frac{1}{r}, \mathrm{i}\partial_z\frac{1}{r}\right\} \sim -\frac{1}{r^3}\left\{z\mathbf{e}_x, z\mathbf{e}_y\right\} \sim \frac{1}{r^2}\left\{Y_1^0, \mathrm{i}Y_1^0\right\}, \\
\mathbf{p}^2 &= \left\{\partial_w\frac{1}{r}, \mathrm{i}\partial_w\frac{1}{r}\right\} \sim -\frac{1}{2r^3}\left\{x\mathbf{e}_x - y\mathbf{e}_y, y\mathbf{e}_x + x\mathbf{e}_y\right\} \sim \frac{1}{r^2}\left\{Y_1^{-1}, \mathrm{i}Y_1^{-1}\right\},
\end{aligned} \tag{3.8}$$

where we have presented three representations for the distortions of each spin class: in terms of complex derivatives of $1/r$, two-component vectors whose coefficients are homogenous polynomials of degree 1 and complex spherical harmonics. In the interest of

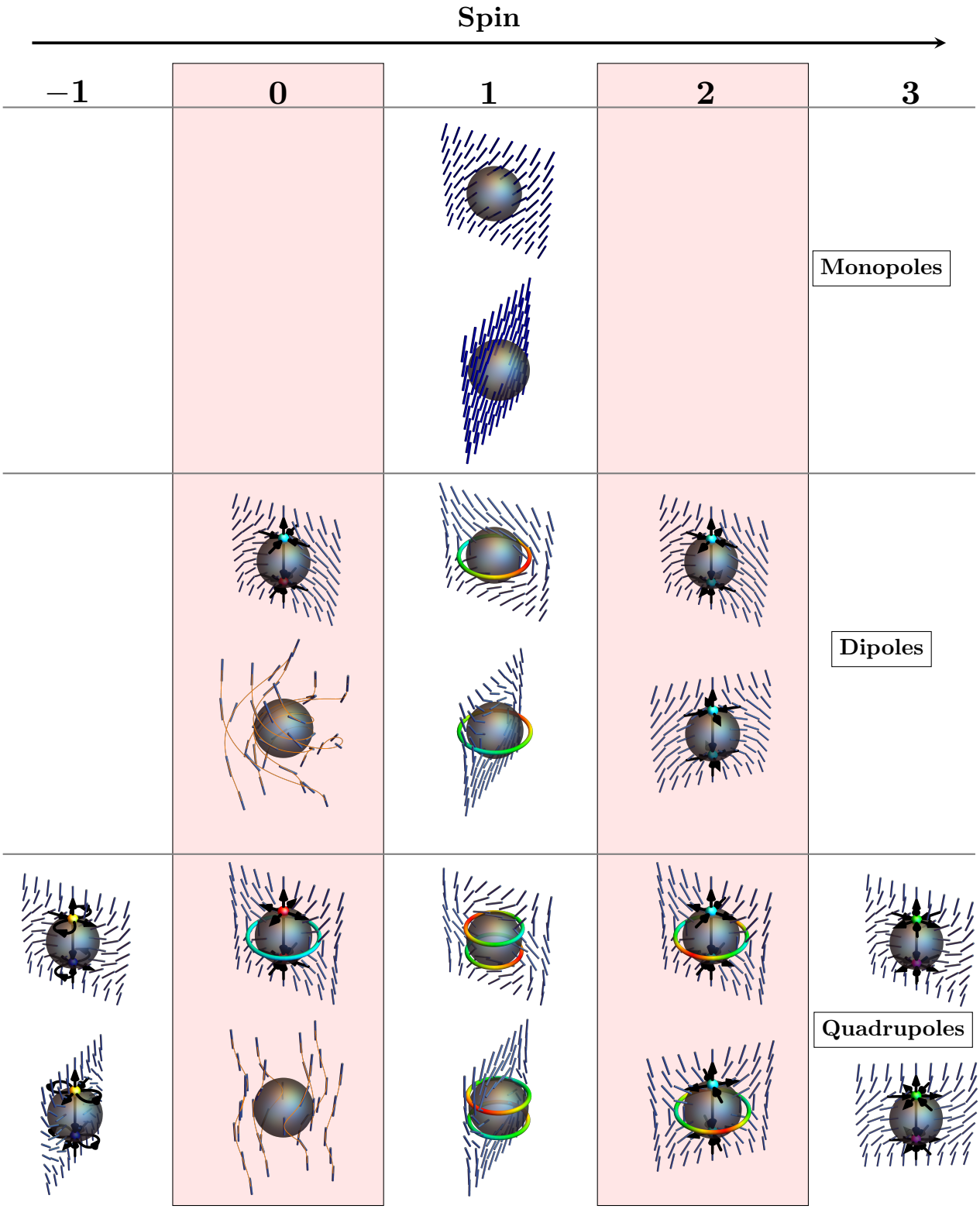
Spin
−1
0
1
2
3
Monopoles
Dipoles
Quadrupoles

space we have suppressed certain prefactors in the last of these, but note the difference in sign, and in some cases normalisation, between our representation as complex derivatives and the standard form of the harmonic distortions as two-component vectors [181]. The two basis functions of any spin class are related by a factor of i, which corresponds to a local rotation of the transverse director distortion by $\frac{\pi}{2}$. For a spin-s distortion this is equivalent to a global rotation by $\frac{\pi}{2s}$, with the pair of distortions having the same character and simply providing a basis for all possible orientations. The exception is when $s = 0$, such distortions lack an orientation and the local rotation produces two distinct states that transform under rotations as a scalar and pseudoscalar. In the dipole case the first is the isotropic distortion recognisable as the UPenn dipole [205], the second is an axisymmetric chiral distortion with the far-field character of left-handed double twist. This is equivalent to the transition between an aster and a vortex in two dimensions, both of which constitute spin-0 point defects. The non-singular nature of the chiral distortion is simply a result of the distortion sitting in a uniform background which tilts the director out of the plane and renders the vortical pattern helical. The full dipole distortion tensor can be represented as the direct sum $\mathbf{p} = \bigoplus_i \mathbf{p}^i$, by which it is meant that any element $\mathbf{v} \in \mathbf{p}$ can be expressed via its coordinates in the $\mathbf{p}^i$, with addition defined coordinate-wise and any distinct pair of the $\mathbf{p}^i$ having intersection $\{0\}$. Separating $\mathbf{p}^0$ into its isotropic and chiral components allows a full decomposition of the dipole tensor as

$$\mathbf{p} = p^I \oplus p^C \oplus \mathbf{p}^1 \oplus \mathbf{p}^2. \tag{3.9}$$

Figure 3.1 *(preceding page)*: The multipolar director distortions up to quadrupole order. The director is shown as blue rods along with a topological skeleton corresponding to the spherical harmonic, as elaborated upon in Figure 3.2, where appropriate. The defect loops are coloured according to the local winding of the director as in Figure 2.8 and the charge of any point defect is indicated through the use of opposing colour pairs: red (+1) and cyan (−1), yellow (+2) and blue (−2) and green (+3) and magenta (−3). Their charge is further indicated by a local decoration of the director with an orientation, indicated by black arrows. Each multipole order is classified into vertical pairs according to the spin of the distortion, with distortions within a pair related by multiplying the complex harmonic by i, that is rotating the director by $\pi/2$. Typically this results in a global rotation by $\pi/2s$, save for the spin-0 modes, for which it converts an isotropic distortion to a chiral one. For most distortions the director is shown in a planar cross-section in which the distortion is radial. For the chiral distortions there is no such plane but the integral curves are shown in orange to emphasise that these are of pure bend type.

This decomposition of the dipolar tensor was presented in [236].

Similarly, the 10-dimensional quadrupolar distortions may be given a basis

$$
\begin{aligned}
\mathbf{Q}^{-1} &= \left\{\partial_{\bar{w}}^2\frac{1}{r}, \mathrm{i}\partial_{\bar{w}}^2\frac{1}{r}\right\} \sim \frac{3}{4r^5}\left\{(x^2-y^2)\mathbf{e}_x + 2xy\mathbf{e}_y, -2xy\mathbf{e}_x + (x^2-y^2)\mathbf{e}_y\right\} \sim \frac{1}{r^3}\left\{Y_2^2, \mathrm{i}Y_2^2\right\},\\
\mathbf{Q}^{0} &= \left\{\partial_{\bar{w}z}^2\frac{1}{r}, \mathrm{i}\partial_{\bar{w}z}^2\frac{1}{r}\right\} \sim \frac{3}{2r^5}\left\{xz\mathbf{e}_x + yz\mathbf{e}_y, -yz\mathbf{e}_x + xz\mathbf{e}_y\right\} \sim \frac{1}{r^3}\left\{Y_2^1, \mathrm{i}Y_2^1\right\},\\
\mathbf{Q}^{1} &= \left\{\partial_{z}^2\frac{1}{r}, \mathrm{i}\partial_{z}^2\frac{1}{r}\right\} \sim \frac{1}{r^5}\left\{(2z^2-x^2-y^2)\mathbf{e}_x, (2z^2-x^2-y^2)\mathbf{e}_y\right\} \sim \frac{1}{r^3}\left\{Y_2^0, \mathrm{i}Y_2^0\right\},\\
\mathbf{Q}^{2} &= \left\{\partial_{wz}^2\frac{1}{r}, \mathrm{i}\partial_{wz}^2\frac{1}{r}\right\} \sim \frac{3}{2r^5}\left\{xz\mathbf{e}_x - yz\mathbf{e}_y, yz\mathbf{e}_x + xz\mathbf{e}_y\right\} \sim \frac{1}{r^3}\left\{Y_2^{-1}, \mathrm{i}Y_2^{-1}\right\},\\
\mathbf{Q}^{3} &= \left\{\partial_{w}^2\frac{1}{r}, \mathrm{i}\partial_{w}^2\frac{1}{r}\right\} \sim \frac{3}{4r^5}\left\{(x^2-y^2)\mathbf{e}_x - 2xy\mathbf{e}_y, 2xy\mathbf{e}_x + (x^2-y^2)\mathbf{e}_y\right\} \sim \frac{1}{r^3}\left\{Y_2^{-2}, \mathrm{i}Y_2^{-2}\right\}.
\end{aligned}
\tag{3.10}
$$

Once again the spin-0 distortions can be further partitioned into those that transform as a scalar and pseudoscalar, these being the Saturn's ring distortion [208] and a chiral quadrupole with opposing chirality in the two hemispheres respectively. As such the quadrupolar tensor can be decomposed as the direct sum

$$\mathbf{Q} = \mathbf{Q}^{-1} \oplus Q^I \oplus Q^C \oplus \mathbf{Q}^1 \oplus \mathbf{Q}^2 \oplus \mathbf{Q}^3. \tag{3.11}$$

Before embarking upon a full description of the basis nematic multipole distortions that we have identified it will be helpful to discuss how such harmonics might be associated with a configuration of topological defects. The nature of the derivatives of a field directly relates to the structures that can arise in the neighbourhoods of its zeros and hence to the types of topological defects that it can exhibit. Indeed, if we restrict to the case $m = \pm l$ then the classification of derivatives according to their spin in (3.6) mirrors that of point defects of a vector field in two dimensions. While it is typically not possible to establish a one-to-one correspondence between topological defects and harmonics, we can associate a harmonic with an arrangement of topological defects which would be expected to produce it in the far field on the basis of commensurate symmetries and defects of a type and location corresponding to the nodal set of the harmonic. This connection will allow us to condense the visualisation of complicated three-dimensional fields into a few discrete elements, suggests means by which such distortions might be induced and enables us to build an intuition for their behaviour in active systems through established results for defects [44].

Examples of this association are shown in Figure 3.2. On the left is the harmonic

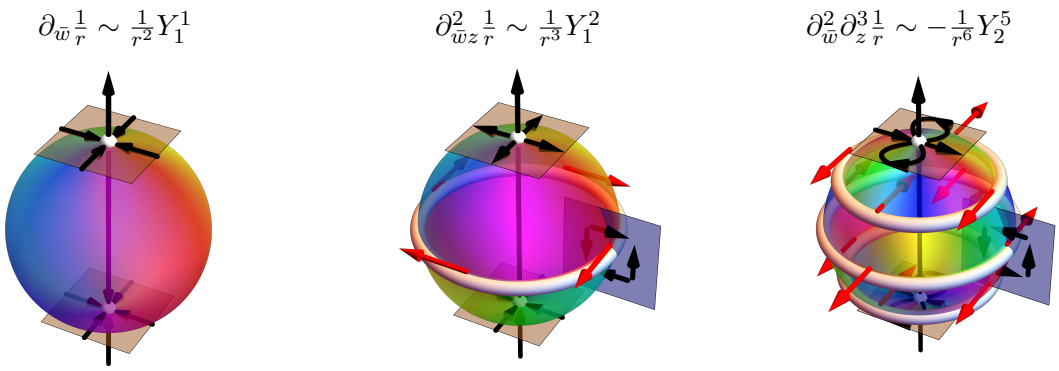

Figure 3.2: The connection between spherical harmonics and nematic topological defects. The coloured spheres indicate the phase of the complex spherical harmonics with the nodal set shown in white for simplicity. A representative skeleton of the corresponding nematic distortion is shown in black and the red arrows indicate the winding vector of the director.

that describes the UPenn dipole, with the form $-e^{i\phi}\sin\theta$. This has nodes at the two poles about which the phase has -1 winding and so we can infer similar winding of the director in the transverse plane, shown in brown. Supplementing with the far-field alignment along $\mathbf{e}_z$ yields the familiar picture of a pair of oppositely charged hedgehog defects.

Similarly, the Saturn ring quadrupole, described by $e^{i\phi}\sin 2\theta$, has zeros at the poles and around the equator. The winding about the poles is still $+1$, but the sign change in the lower hemisphere means that in the transverse plane around the south pole the vector points inwards, resulting in both point defects having topological charge $+1$. With regards to the equatorial line, since the director is everywhere radial the winding vector must be tangential to the defect loop, shown by the red arrows in Figure 3.2. As the phase changes by π on passing from one hemisphere to the other the winding must be ± 1 and the far-field alignment allows us to determine it to be -1.

For a general multipole distortion of the form $\partial_{\bar{w}}^m\partial_z^{l-m}(1/r)$ the nodal set is the poles along with $l-m$ lines of latitude. The phase winding of the spherical harmonic dictates the transverse winding of the director and, when supplemented with the far-field alignment, allows us to associate topological point defects with the poles. Similarly, nodal lines may be connected with defect loops with integer winding and a winding vector that rotates according to $e^{im\phi}$. In Figure 3.2 we illustrate this for the case $\partial^2_{\bar{w}}\partial^3_z(1/r) \sim -Y_2^5/r^6$.

We now apply this to the dipolar and quadrupolar distortions we have identified. As already stated, the isotropic scalar in $\mathbf{p}^0$ is the UPenn dipole, its pseudoscalar counterpart a chiral pure bend distortion whose integral curves are shown in orange in Figure 3.1. As a pure bend mode it may be of particular relevance to extensional systems given their instability to bend distortions. The two dipoles of $\mathbf{p}^1$ are transverse to the far-field alignment, they are related to those resulting from a defect loop of wedge-twist type [43] and will be discussed further in the following chapter. The distortions of $\mathbf{p}^2$ have a hyperbolic character; they describe the far field of a pair of point defects both of which have a hyperbolic structure. Such hyperbolic defect pairs arise in toron configurations in frustrated chiral nematics [77; 237].

Similarly, $\mathbf{Q}^0$ contains the Saturn ring quadrupole as the scalar, with the pseudoscalar a pure bend chiral distortion. For the latter, the integral curves of the director possess opposing chirality in the two hemispheres, which could be generated by an appropriately coated Janus particle. The director distortion exhibits a helical perversion in the $z = 0$ plane and, being a local rotation of the Saturn ring distortion, may be viewed as resulting from a pair of vortex point defects along with a pure twist defect loop with integer winding. This is similar to the bubble-gum defect lines [238] that appear between a colloidal dyad with normal anchoring, suggesting that this chiral quadrupole could be formed by two colloids with opposing chiral tangential anchoring.

The spin-1 quadrupoles consist of pairs of wedge-twist defect loops. The distortions of $\mathbf{Q}^2$ may be associated with a pair of hyperbolic defects along with a defect ring with the appropriate symmetry. The harmonics of spin -1 and 3 contain no z-derivatives and so are associated with pairs of point defects only.

Having established the appropriate basis of distortions we now move our attention to the response they induce in an active nematic. Just as the distortions could be derived from monopoles, we shall see that the active flows can be derived from corresponding fundamental flows.

3.3 Flows from multipole distortions

A note before we proceed. The construction for calculating active flow responses that we develop in this section requires knowledge of the multipole as a specified set of derivatives of $1/r$. As the multipoles are harmonic there are cases, for distortions of quadrupole order and higher, where there is potential ambiguity in the choice of derivatives, for example between $\partial_z^2 1/r$ and $-4\partial_{w\bar{w}}^2 1/r$. As the flow responses do not share the harmonicity of the nematic distortions these derivatives produce distinct active flows, neither of which

is *a priori* 'more correct' than the other. Accordingly we highlight this multiplicity of solutions when it arises and will show both solutions. However, in the following section we show that the non-equilibrium phenomena that result from certain distortions, as characterised by net active forces and torques, correspond to integrals of the director components and so do not suffer from this ambiguity. Additionally, the following chapter on defects loops will serve to illustrate that when a specific context is given a particular set of derivatives can naturally be determined and any apparent ambiguity resolved.

We turn now to calculating the active response to the elastic multipoles described above. As our description is linear the responses due to the two components of $\delta\mathbf{n}$ are independent and so to simplify the derivation of the active response we consider only distortions in the x-component for now; we will present a combined formulation shortly. Within this restriction to a single component a generic distortion at order l may be written as

$$\delta\mathbf{n} = a^{l+1}\mathbf{e}_x\nabla_{\mathbf{v}_1}\cdots\nabla_{\mathbf{v}_l}\frac{1}{r}, \tag{3.12}$$

valid for $r >> a$ where $\nabla_{\mathbf{v}} \equiv \mathbf{v}\cdot\nabla$, the directional derivative [239]. For brevity we suppress the factor of a^{l+1} while discussing the general solution and reinstate it when we come to discussing particular examples. Substituting (3.12) into (3.4) gives the Stokes equation the form

$$-\nabla p^x + \mu\nabla^2\mathbf{u}^x = \zeta\nabla_{\mathbf{v}_1}\cdots\nabla_{\mathbf{v}_l}\Big[\mathbf{e}_x\,\partial_z + \mathbf{e}_z\,\partial_x\Big]\frac{1}{r}, \tag{3.13}$$

where the use of superscripts is to emphasise that we are only treating the response to distortions in the x-component of the director. We do not impose any particular boundary condition at short distances, but seek flow solutions that decay to zero for large distances, with the pressure tending to a constant. Although well-behaved decaying solutions enter at dipole order in 3D, and at quadrupole order in 2D, in a manner reminiscent of the Stokes paradox, we still find it useful to present lower orders.

Taking the divergence of both sides of (3.13) we have

$$-\nabla^2 p^x + \mu\nabla^2\nabla\cdot\mathbf{u}^x = \zeta\nabla_{\mathbf{v}_1}\cdots\nabla_{\mathbf{v}_l}\partial^2_{xz}\frac{2}{r}. \tag{3.14}$$

Making use of the continuity equation $\nabla\cdot\mathbf{u}^x = 0$ in conjunction with the general result $\nabla^2 r = \frac{2}{r}$ we arrive at the pressure solution

$$p^x = -\zeta\nabla_{\mathbf{v}_1}\cdots\nabla_{\mathbf{v}_l}\,\partial_x\partial_z r = \zeta\nabla_{\mathbf{v}_1}\cdots\nabla_{\mathbf{v}_l}\,\frac{xz}{r^3}. \tag{3.15}$$

Substituting this solution back into the Stokes equation in (3.12) we obtain

$$\mu\nabla^2\mathbf{u}^x = \zeta\nabla_{\mathbf{v}_1}\cdots\nabla_{\mathbf{v}_l}\left\{\mathbf{e}_x\,\partial_z\left[\frac{1}{r}-\partial_x\partial_x r\right]-\mathbf{e}_y\,\partial_x\partial_y\partial_z r+\mathbf{e}_z\,\partial_x\left[\frac{1}{r}-\partial_z\partial_z r\right]\right\}. \quad (3.16)$$

We again integrate, this time using the addition relation $\nabla^2 r^3 = 12r$. This yields

$$\mathbf{u}^x = \frac{\zeta}{4\mu}\nabla_{\mathbf{v}_1}\cdots\nabla_{\mathbf{v}_l}\left\{\mathbf{e}_x\left[\frac{z}{r}+\frac{x^2z}{r^3}\right]+\mathbf{e}_y\,\frac{xyz}{r^3}+\mathbf{e}_z\left[\frac{x}{r}+\frac{xz^2}{r^3}\right]\right\}. \quad (3.17)$$

We can see that both the pressure and flow solutions for a generic multipole distortion may be expressed through derivatives of a fundamental response to a monopole deformation, namely

$$p^x = \zeta\frac{xz}{r^3}, \quad (3.18)$$

$$\mathbf{u}^x = \frac{\zeta}{4\mu}\left\{\mathbf{e}_x\left[\frac{z}{r}+\frac{x^2z}{r^3}\right]+\mathbf{e}_y\,\frac{xyz}{r^3}+\mathbf{e}_z\left[\frac{x}{r}+\frac{xz^2}{r^3}\right]\right\}. \quad (3.19)$$

This flow response, shown as the top panel in Figure 3.3, is primarily extensional in the xz-plane; its lack of decay with distance reflects the generic hydrodynamic instability of active nematics [25]. However, the response to any higher multipole does decay and vanishes at large distances.

The pressure and flow solutions in (3.18) and (3.19) are of course complemented by analogous ones resulting from distortions in the y-component of the director. By interchanging x and y these are found to be

$$p^y = \zeta\frac{yz}{r^3}, \quad (3.20)$$

$$\mathbf{u}^y = \frac{\zeta}{4\mu}\left\{\mathbf{e}_x\,\frac{xyz}{r^3}+\mathbf{e}_y\left[\frac{z}{r}+\frac{y^2z}{r^3}\right]+\mathbf{e}_z\left[\frac{y}{r}+\frac{yz^2}{r^3}\right]\right\}. \quad (3.21)$$

As illustrated in our derivation of the flow response to a generic distortion in the x-component (3.17), the linearity of our calculation makes these fundamental responses sufficient to derive the active flow induced by an arbitrary multipole distortion through the separate action on (3.19) and (3.21) of the derivatives appropriate to describe the x and y components of the director respectively.

However, in light of our previous description of nematic multipoles as complex derivatives and its use in identifying pairs of basis distortions in distinct spin classes it is natural to formulate the calculation in terms of a single fundamental response from which the response to a given distortion can be attained through application of a complex

derivative. This is achieved by taking the combinations $p = p^x - \mathrm{i}p^y$ and $\mathbf{u} = \mathbf{u}^x - \mathrm{i}\mathbf{u}^y$. To see this consider the multipole distortion $\delta n = (\mathcal{L}_x + \mathrm{i}\mathcal{L}_y)1/r$, where the $\mathcal{L}_i$ are generic real differential operators which generate the i-component of the director by acting on $1/r$. This distortion has a conjugate partner in the same spin class, given by $\mathrm{i}(\mathcal{L}_x + \mathrm{i}\mathcal{L}_y)1/r = (-\mathcal{L}_y + \mathrm{i}\mathcal{L}_x)1/r$. Acting with this same operator on $\mathbf{u}^x - \mathrm{i}\mathbf{u}^y$ we have

$$(\mathcal{L}_x + \mathrm{i}\mathcal{L}_y)(\mathbf{u}^x - \mathrm{i}\mathbf{u}^y) = (\mathcal{L}_x\mathbf{u}^x + \mathcal{L}_y\mathbf{u}^y) - \mathrm{i}(-\mathcal{L}_y\mathbf{u}^x + \mathcal{L}_x\mathbf{u}^y) \tag{3.22}$$

and can see that the flow response for our original distortion forms the real part and that for its conjugate partner the coefficient of $-i$ and the same holds for the pressure response. This leads us to a complex fundamental pressure response

$$\tilde{p} = \zeta\frac{\bar{w}z}{r^3} \tag{3.23}$$

and, introducing complex basis vectors $\mathbf{e}_w = \mathbf{e}_x + \mathrm{i}\mathbf{e}_y$ and $\mathbf{e}_{\bar{w}} = \mathbf{e}_x - \mathrm{i}\mathbf{e}_y$, a complex-valued fundamental flow vector

$$\tilde{\mathbf{u}} = \frac{\zeta}{4\mu}\left\{\mathbf{e}_w\,\frac{\bar{w}^2 z}{2r^3} + \mathbf{e}_{\bar{w}}\left[\frac{z}{r} + \frac{w\bar{w}z}{r^3}\right] + \mathbf{e}_z\,\frac{\bar{w}}{r}\left(1 + \frac{z^2}{r^2}\right)\right\}. \tag{3.24}$$

We use a tilde to distinguish these fundamental responses from those that result due to a generic distortion and which may be found by appropriate differentiation. This provides a unified framework in which the active response to a generic nematic multipole can be calculated through the application of the same complex derivatives that we have used to describe the distortion. The resulting active flows for distortions up to quadrupole order are shown in Figure 3.3, with their layout corresponding to that of the nematic distortions in Figure 3.1 which induce them.

Typically the active responses induced by the two distortions in a spin class will, like the distortions themselves, be related by a global rotation such that while both are needed to form a sufficient basis, the real part essentially serves as a proxy for the pair. This is not true for the spin-0 distortions and so in providing an explicit illustration of this calculation we use the case of the UPenn dipole [205] and its partner the chiral dipole. The far-field transverse director is

$$\delta n \approx \alpha a^2 \partial_{\bar{w}}\frac{1}{r}, \tag{3.25}$$

with α is a dimensionless coefficient, and the corresponding derivative of the fundamental

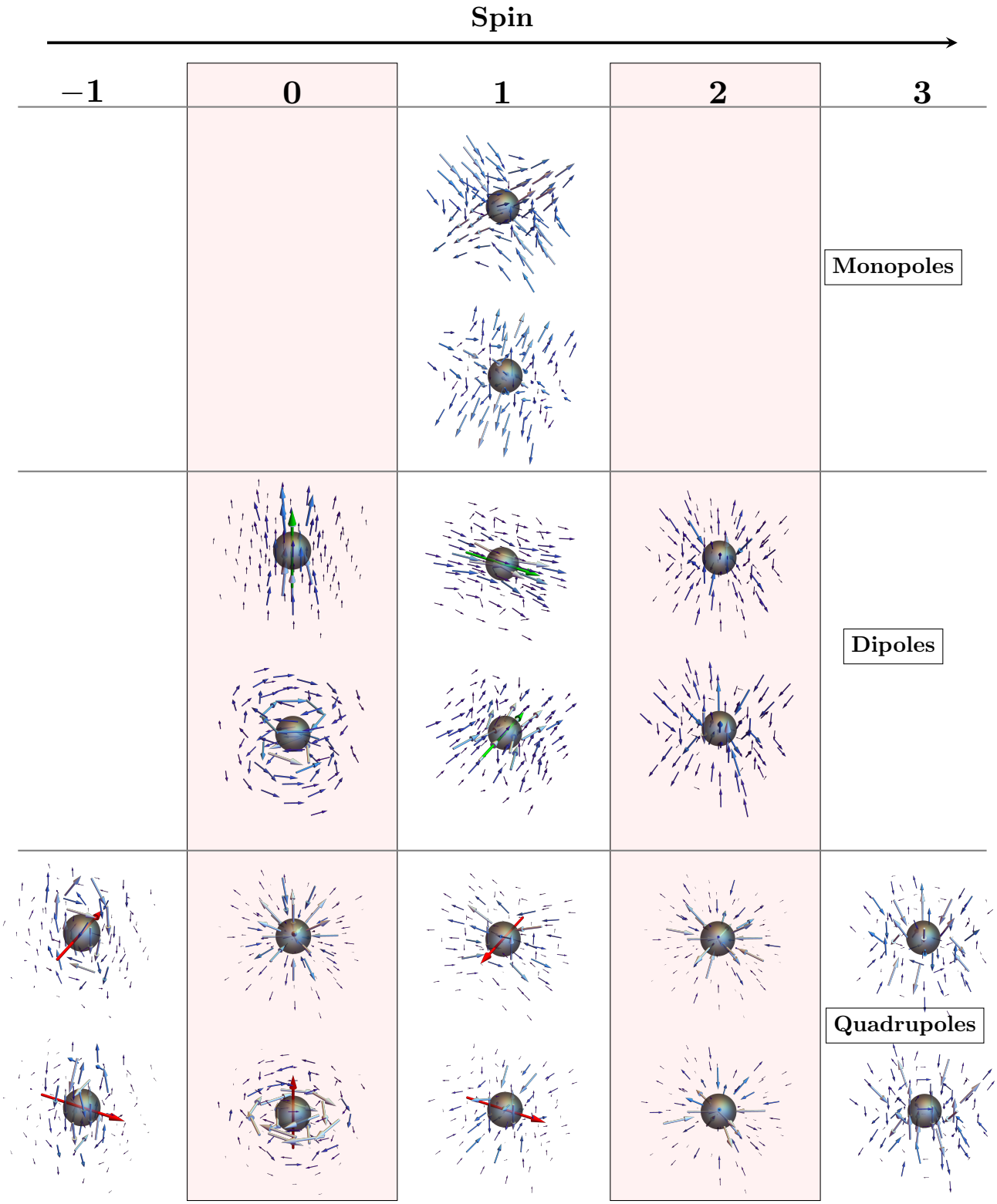
Spin
−1
0
1
2
3
Monopoles
Dipoles
Quadrupoles

flow solution in (3.24) gives

$$\alpha a^2 \partial_{\bar{w}} \tilde{\mathbf{u}} = \frac{\alpha a^2}{4r^5} \left\{ \mathbf{e}_w \, z\bar{w}(4z^2 + w\bar{w}) - \mathbf{e}_{\bar{w}} \, 3zw^2\bar{w} + \mathbf{e}_z \, 2\left[3z^4 + (z^2 + w\bar{w})^2\right] \right\}. \tag{3.26}$$

Taking the real part gives, after some manipulation, the flow induced by the UPenn dipole as

$$\mathbf{u} = \alpha a^2 \Re \partial_{\bar{w}} \tilde{\mathbf{u}} = \frac{\zeta \alpha a^2}{8\mu} \left\{ \mathbf{e}_z \left(\frac{1}{r} + \frac{z^2}{r^3} \right) + \mathbf{e}_r \frac{z}{r^2} \left(\frac{3z^2}{r^2} - 1 \right) \right\}, \tag{3.27}$$

where $\mathbf{e}_r$ is the unit vector in the radial direction. The flow response to the conjugate distortion, the isotropic chiral dipole is given by

$$\mathbf{u} = -\alpha a^2 \Im \partial_{\bar{w}} \tilde{\mathbf{u}} = -\frac{\zeta \alpha a^2}{4\mu} \frac{z}{r^2} \mathbf{e}_\phi, \tag{3.28}$$

with $\mathbf{e}_\phi$ the azimuthal unit vector. Both flows decay at large distances like $1/r$, with the UPenn flow having a striking net flow directed along the z-axis, as shown in Figure 3.3. The flow is reminiscent of that of the Stokeslet flow [240; 241] associated with a point force along $\mathbf{e}_z$. The chiral dipole generates an axisymmetric flow composed of two counter-rotating vortices aligned along $\mathbf{e}_z$, mirroring the circulating flows produced by spiral defects in two dimensions [88]. The $1/r$ decay of these active vortex flows is unusually slow, slower than the decay of a point torque in Stokesian hydrodynamics [241].

Despite the similarity between the active flow induced by the UPenn dipole and a Stokeslet, there is a key difference in their angular dependence. In a Stokeslet, and all related squirming swimmer flows [242; 243] that result from derivatives of it, the terms with higher angular dependence decay more quickly such that the lowest order terms dominate the far field. By contrast, distortions in active nematics produce asymptotic flow fields in which all terms decay at the same rate regardless of their angular dependence as they all result from the same derivative of the fundamental flow. Thus, even if the same angular terms are present in both systems, the lowest order ones will dominate

Figure 3.3 *(preceding page)*: The active flows due to three-dimensional nematic multipole distortions up to quadrupole order. The flows are grouped according to their spin, in correspondence with the distortions in Figure 3.1. Green and red arrows indicate the net active force and torque for the relevant dipoles and quadrupoles respectively. The flow solutions shown for spin-1 quadrupoles correspond to the operators ∂_z^2 and $\mathrm{i}\partial_z^2$, additional solutions for spin-1 quadrupoles corresponding to $\partial_{w\bar{w}}^2$ and $\mathrm{i}\partial_{w\bar{w}}^2$ are shown in Figure 3.4.

in the squirming case while the far field will bear the signature of the highest order in the active nematics.

A closer point of comparison comes from the flows induced by active colloids within a passive nematic [244; 228]. Calculation of the relevant Green's functions [245] has shown that the anisotropy of the medium leads to a difference in effective viscosities such that a Stokeslet aligned along the director pumps more fluid in this direction. This fits with the anisotropy displayed in (3.27), reaffirming the similarity between the flow induced by the UPenn dipole and the Stokeslet.

Considering the pressure response for these distortions in the same way we have

$$\begin{aligned} \alpha a^2 \partial_{\bar{w}} p &= \frac{\zeta \alpha a^2}{2r^5} z(2z^2 - w\bar{w}) \\ &= \frac{\zeta \alpha a^2 z}{2r^3}\left(\frac{3z^2}{r^2} - 1\right). \end{aligned} \tag{3.29}$$

As this expression is purely real it comprises the response due to the UPenn dipole in its entirety; the vanishing of the imaginary part shows that the chiral dipole is compatible with a zero-pressure solution. Our complexified construction allows this property to be read off immediately, since $\partial_{\bar{w}}(\bar{w}z^m/r^n)$ will be real for any m and n, with this also resulting in the vanishing z-component of flow for the chiral dipole. Indeed, this property of pure realness is unchanged by the action of ∂_z, it being real itself, and so extends to higher order distortions.

For the remaining multipoles up to quadrupole order we do not provide the same explicit calculation but instead highlight the key features of the active flows they induce. In full we find that half of the dipole distortions contain directed components in their active flow responses. Along with the isotropic UPenn dipole which produces flow along $\mathbf{e}_z$ the two spin-1 dipoles produce directed flows transverse to it. These directed flows indicated that were the source of the distortion free to move it would exhibit active self-propulsion. The net transverse flows for the dipoles of $\mathbf{p}^1$ is in accordance with the previously established motile nature of such defect loops [44]. We shall give them greater consideration in Chapter 4 when we present a description of the active dynamics of defect loops through their multipole distortions

Along with the chiral dipole, the two additional dipoles which do not generate directed flows are those with spin 2. These produce active flows which are extensional with the expected two-fold rotational symmetry about the z-axis. Direct calculation shows that the flows resulting from spin-2 distortions have zero azimuthal component. Once again, this observation is unaffected by z-derivatives and so holds true for the

$\partial^2_{w\bar{w}}\frac{1}{r}$ $\quad$ $\mathrm{i}\partial^2_{w\bar{w}}\frac{1}{r}$

Figure 3.4: Additional flow solutions induced by spin-1 nematic multipoles. The nematic multipoles which induce the flows are shown below them as complex derivatives of $1/r$. The red arrows indicate the net active torque.

higher-order multipoles of the form $\partial_z^n\partial_w(1/r)$.

Similarly, there are ten linearly independent quadrupoles, five of which can be seen from Figure 3.3 to generate rotational flows. As expected, it is the four modes of $\mathbf{Q}^{\pm 1}$ that generate rotations about transverse directions and Q^C that produces rotation around $\mathbf{e}_z$. For two of these, namely those in $\mathbf{Q}^1$, the director distortions are planar, suggesting a two-dimensional analogue and the potential to generate them with cogs or gears, something we shall investigate in Section 3.5 and Chapter 5. These distortions may be associated with a pair of opposingly oriented charge-neutral defect loops and so the rotational flow generated by these distortions is in accordance with their antiparallel self-propulsion. As highlighted at the beginning of this section there are two distinct flow solutions for the multipoles of $\mathbf{Q}^1$, according to whether the derivative taken is $\partial_z^2(1/r)$ or $-4\partial^2_{w\bar{w}}(1/r)$. The flows induced by the former are shown in Figure 3.3, those of $\partial^2_{w\bar{w}}(1/r)$ in Figure 3.4. The predominately horizontal form of the flows induced by $\partial_z^2(1/r)$ fits with the interpretation as a pair of defect loops; double transverse derivatives such as in $-\partial^2_{w\bar{w}}(1/r)$ will naturally arise when we consider buckling of defect loops in the following chapter and the vertical nature of the quadrupole flow will reappear in the context of non-planar splay loops. While the exact form of the flows differ, they both generate a rotational component about the same axis.

The quadrupoles of $\mathbf{Q}^{-1}$ are composed of pairs of point defects with topological charge $+2$. Using $\partial^2_{\bar{w}}\frac{1}{r}$ as an example, the rotation can be understood by considering the splay distortions in the xz plane. The splay changes sign for positive and negative x, leading to antiparallel forces. The active forces are greatest in this plane, as this is where the transverse distortion is radial resulting in splay and bend distortions. Along

$\mathbf{e}_y$ the distortions are of twist type and so do not contribute to the active force. This results in the rotational flow shown in Figure 3.3. The stretching of the flow along $\mathbf{e}_z$ is as observed for a rotlet in a nematic environment [245]. Finally, rotation about the z-axis results from Q^C. As for the chiral dipole the induced flow is purely azimuthal and compatible with zero pressure.

The Saturn ring distortion produces a purely radial flow reminiscent of a stresslet along $\mathbf{e}_z$. The purely radial nature is a result of the divergencelessness of the flow, combined with the $1/r^2$ decay and rotational invariance about $\mathbf{e}_z$. Working in spherical coordinates we have

$$\nabla \cdot \mathbf{u} = \frac{1}{r^2}\partial_r(r^2 u_r) + \frac{1}{r\sin\theta}\left[\partial_\theta(u_\theta \sin\theta) + \partial_\phi u_\phi\right] = 0 \tag{3.30}$$

All active flows induced by quadrupole distortions decay as $1/r^2$ and so $\partial_r(r^2 u_r) = 0$. The distortion is rotationally symmetric and achiral, meaning $u_\phi = 0$ and the condition of zero divergence reduces to

$$\frac{1}{r\sin\theta}\partial_\theta(u_\theta \sin\theta) = 0. \tag{3.31}$$

The only non-singular solution is $u_\theta = 0$, resulting in u_r being the only non-zero flow component. Although they lack the rotational symmetry of a stresslet, the flows produced by the quadrupoles of $\mathbf{Q}^2$ are also purely radial. The argument is largely the same as before, except that the vanishing of u_ϕ is not due to rotational invariance but a property inherited from the spin-2 dipoles.

The quadrupoles of $\mathbf{Q}^3$ produce extensional flows whose spin-3 behaviour under rotations about $\mathbf{e}_z$ is commensurate with that of the distortions. Although they visually resemble the similarly extensional flows produced by the dipoles of $\mathbf{p}^2$, they do not share the property of a vanishing azimuthal flow component.

3.4 Active forces and torques

The directed and rotational active flow components highlighted above result in viscous stresses whose net effect must be balanced by their active counterparts, since the net force and torque must be zero. Consequently, these generic aspects of the response of an active nematic can be identified by considering the contribution that the active stresses

make to the force and torque

$$\mathbf{f}^a = \int \zeta \mathbf{n}\mathbf{n} \cdot \mathrm{d}\mathbf{A} \approx \int \zeta \left\{ \mathbf{e}_x \frac{z\,\delta n_x}{r} + \mathbf{e}_y \frac{z\,\delta n_y}{r} + \mathbf{e}_z \frac{x\,\delta n_x + y\,\delta n_y}{r} \right\} \mathrm{d}A, \tag{3.32}$$

$$\begin{aligned} \tau^a &= \int \mathbf{x} \times \zeta \mathbf{n}\mathbf{n} \cdot \mathrm{d}\mathbf{A} \\ &\approx \int \zeta \left\{ \mathbf{e}_x \left[\frac{xy\,\delta n_x}{r} + \frac{(y^2 - z^2)\delta n_y}{r} \right] + \mathbf{e}_y \left[\frac{(z^2 - x^2)\delta n_x}{r} - \frac{xy\,\delta n_y}{r} \right] \right. \\ &\qquad \left. + \mathbf{e}_z \frac{z(-y\,\delta n_x + x\,\delta n_y)}{r} \right\} \mathrm{d}A, \end{aligned} \tag{3.33}$$

integrating over a large sphere of radius r. Formally the multipole approximation underlying these relations holds for $r >> a$, although it holds approximately for $r \gtrsim a$, see Figure 4.1. These integrals depend on the surface of integration, as the active stresses are neither divergenceless nor compactly supported. However, a spherical surface is concordant with the multipole approach we are taking and the results are then independent of the radius. From these expressions we can read off the multipole that will generate any desired active force or torque; dipoles generate forces and quadrupoles generate torques. When the active torque is non-zero, the compensating viscous torque will drive a persistent rotation of the multipole, creating an active ratchet; similarly, a non-zero active force will generate directed fluid flow.

If the multipole is free to move it will self-propel and rotate. The translational and rotational velocities are related to the viscous forces and torques by a general mobility matrix [99]; using the simplest expressions corresponding to a sphere of radius a in ordinary Stokes flow gives

$$\mathbf{U} = \frac{-1}{6\pi\mu a} \mathbf{f}^a, \tag{3.34}$$

$$\mathbf{\Omega} = \frac{-1}{8\pi\mu a^3} \tau^a. \tag{3.35}$$

We again use the UPenn dipole as an example. Integrating the active stresses over a spherical surface of radius r we find an active force

$$\begin{aligned} \int \zeta \mathbf{n}\mathbf{n} \cdot \mathrm{d}\mathbf{A} &\approx -\frac{\zeta \alpha a^2}{2} \int \left\{ \mathbf{e}_x \frac{xz}{r^4} + \mathbf{e}_y \frac{yz}{r^4} + \mathbf{e}_z \left[\frac{z}{r} + \frac{x^2 + y^2}{r^4} \right] \right\} \mathrm{d}A, \\ &= -\frac{4\pi\zeta\alpha a^2}{3}\, \mathbf{e}_z. \end{aligned} \tag{3.36}$$

Balancing this against Stokes drag predicts a 'self-propulsion' velocity for the active

dipole of

$$\mathbf{U} = \frac{2\zeta\alpha a}{9\mu}\,\mathbf{e}_z. \tag{3.37}$$

For extensile activity ($\zeta > 0$) the dipole moves 'hyperbolic hedgehog first' and with a speed that increases linearly with the core size a. The same self-propulsion speed along $\mathbf{e}_x$ and $\mathbf{e}_y$ is found for the transverse dipoles of $\mathbf{p}^1$. The same behaviour has been observed in a related system of an active droplet within a passive nematic [228], with the droplet inducing a UPenn dipole in the nematic and moving in the direction of the hedgehog defect at a speed that grew with the droplet radius. The mechanism at play is different however; the motion results from directional differences in viscosity resulting from the anisotropic environment.

To illustrate the rotational behaviour we use a member of $\mathbf{Q}^1$, $\partial_z^2(1/r)$, as an example. We find an active torque

$$\begin{aligned}\int \zeta\mathbf{x}\times\mathbf{nn}\cdot\mathrm{d}\mathbf{A} &\approx \zeta\alpha a^3\int\frac{1}{r^6}(2z^2-x^2-y^2)\left\{xy\mathbf{e}_x+(z^2-x^2)\mathbf{e}_y-yz\mathbf{e}_z\right\}\mathrm{d}A\\ &= \frac{8\pi\zeta\alpha a^3}{5}\mathbf{e}_y.\end{aligned} \tag{3.38}$$

Balancing against Stokes drag as was done in the dipole case gives an angular velocity

$$\mathbf{\Omega} = -\frac{\zeta\alpha}{5\mu}\mathbf{e}_y. \tag{3.39}$$

We note that for this and all other distortions which result in net torques the angular velocity is independent of the colloid size. In accordance with the relation $\partial_z^2+4\partial_{w\bar{w}}^2(1/r)=0$, the torque resulting from $\partial_{w\bar{w}}^2(1/r)$ is of the opposite sign and a quarter the strength. The net active torques due to harmonics of $\mathbf{Q}^0$ and $\mathbf{Q}^{-1}$ have the directions indicated in Figure 3.3 and half the magnitude of (3.38).

Let us consider the approximate magnitude of the effects we have described. Beginning with the self-propulsion speed, the fluid viscosity is roughly 10^{-2}Pa s [150], although effects due to the elongated form of the nematogens could increase this by a factor of 30 or so [246; 247]. Both the activity [40] and the dipole moment constant [181] are of order unity, meaning the colloid would approximately cover its radius in a second. Similar approximations for the quadrupole give an angular velocity of about 2/3rad s^{-1}. For a colloid of radius 10μm this has an associated power of the order of femtowatts, the same as predicted for bacterial ratchets [23].

3.5 Two-dimensional systems and ratchets

As noted above, the planar nature of the rotational distortions in $\mathbf{Q}^1$ suggests the existence of two-dimensional analogues. In part motivated by this we now discuss the active response of multipolar distortions in two dimensions, again beginning with the connection between these multipoles and topological defect configurations.

3.5.1 Multipoles as topological defects

The categorisation of the harmonic distortions in two dimensions is much simpler, but we provide it here for completeness. The symmetry of the far-field director is now described by the order 2 group $\{1, R_z\}$, with R_z reflection with axis $\mathbf{e}_z$, under which the monopole distortion $n_x \sim A\log(r/R)$ is antisymmetric. The higher-order distortions are once again generated via differentiation of the monopole, with ∂_z leaving the symmetry under R_z unchanged and ∂_x inverting it. The basis at any order of derivative can be reduced to $\left\{\partial_z^{n-1}\partial_x n_x, \partial_z^n n_x\right\}$, modulo a similar caveat relating to a multiplicity of flow solutions as in three dimensions. These two distortions are symmetric and anti-symmetric under R_z respectively and of course correspond to the two harmonic functions $\cos n\theta/r^n$ and $\sin n\theta/r^n$.

In two dimensions the connection between defect configurations and far-field multipole distortions can be made concrete. The director for a two-dimensional nematic can, under the one-elastic-constant approximation, be represented by a meromorphic function such that the angle that the director makes to $\mathbf{e}_x$ is given by

$$\phi = \phi_0 + \sum_j s_j \Im\left\{\ln(z - z_j)\right\}, \tag{3.40}$$

which, upon performing a series expansion, gives

$$\phi = \phi_0 + \sum_j s_j \Im\left\{\ln(z)\right\} - \sum_{n=1}^{\infty} \frac{\Im\left\{\sum_j s_j z_j^n \bar{z}^n\right\}}{n|z|^{2n}}, \tag{3.41}$$

where the s_j denote the topological charges of the defects and the z_j their locations. Provided the total topological charge is zero the winding term proportional to $\ln z$ vanishes and ϕ_0 is the far-field alignment. The distortions are given as a series of harmonics in which the coefficient of the n^{th} harmonic is determined by a sum of z_j^n weighted by the defect charges.

We would like to have a basis of representative defect configurations for each

harmonic distortion. However, it can be seen from (3.41) that the correspondence between arrangements of topological defects and the leading order nematic multipole is not one-to-one. Two defect-based representations of harmonic will prove particularly useful to us. The first, which we develop in this chapter, provides a representation in terms of half-integer defects on the disc and allows an intuition for the response to multipole distortions in active nematics through known results for such defects [39; 40]. The second uses the method of images to construct defect arrangements corresponding to a specific anchoring condition on the disc, with the same multipoles dominating the nematic distortion in the far field. This representation naturally lends itself to the control of induced multipoles through colloidal geometry and we shall present it fully in Chapter 5. Nonetheless, both of these representations will be of use to us in the remainder of this chapter and as they are equally valid near-field representations for the asymptotic distortions that we are considering we will pass fairly freely between them.

With this aforementioned half-integer representation in mind, let us consider sets of $2m$ defects sitting on the unit circle, with $-1/2$ defects at the m^{th} roots of unity and $+1/2$ defects at the intermediate points. A useful formula here is the following for the sum of a given power of these roots of unity, after first rotating them all by a given angle θ

$$\sum_{k=0}^{m-1}\left(e^{i\theta}e^{i\frac{2\pi}{m}k}\right)^n=\begin{cases}me^{in\theta}, & \text{if } m|n\\ 0, & \text{otherwise}\end{cases}. \tag{3.42}$$

The vanishing of this sum for values of n that are not multiples of m comes directly from the expression for the geometric sum and is a consequence of the cyclic group structure of the roots of unity. It means that the lowest order multipole distortion induced by such an arrangement of defects is order m and so allows a desired multipole distortion to be selected as the dominant far-field contribution. Explicitly, the director angle is given by

$$\phi=\phi_0+\sum_{k\text{ odd}}\frac{\Im\left\{\bar{z}^{mk}\right\}}{k|z|^{2mk}}=\phi_0+\frac{\Im\left\{\bar{z}^{m}\right\}}{|z|^{2m}}+O\left(\frac{1}{z^{3m}}\right), \tag{3.43}$$

with the approximation becoming rapidly better for higher-order multipoles due to the condition that n must be an odd multiple of the number of defects. Rotating the entire set of defects rigidly by an angle $-\pi/(2m)$ generates the conjugate multipole as the dominant far-field contribution

$$\phi=\phi_0+\sum_{k\text{ odd}}\frac{\Im\left\{(-i)^k\bar{z}^{mk}\right\}}{k|z|^{2mk}}=\phi_0-\frac{\Re\left\{\bar{z}^{m}\right\}}{|z|^{2m}}+O\left(\frac{1}{z^{3m}}\right), \tag{3.44}$$

with the natural interpolation between these two harmonics as the defect configuration is rigidly rotated.

Hence we can interchange between a given harmonic distortion and a defect arrangement which has this harmonic as its dominant far-field contribution, with the correspondence becoming rapidly more accurate for higher orders, allowing us to relate the existing results for the behaviour of active defects [39; 40] to ours and vice versa. This correspondence is illustrated in Figure 3.5. The locations of $+1/2$ and $-1/2$ defects are indicated with red and cyan dots respectively and the background colouring denotes the phase of the complex function $\sum s_j \ln(z - z_j)$, whose imaginary part provides the director angle for the given defect arrangement. The integral curves of this director field are shown in black and are remarkably well matched by those of the leading multipole, shown in white, despite the asymptotic nature of the approximation. In this context we are able to make precise the notion of a core region of a singular distortion, outside of which our multipole approach applies. The series in (3.41) is attained through a Taylor series of terms of the form $\ln(1 - 1/z)$, which are convergent for $|z| > 1$. More generally the greatest radial displacement of a defect defines a core radius, outside of which the multipole series converges onto the exact director angle.

3.5.2 Flows from multipole distortions

We can proceed analogously to our three-dimensional calculation in generating the active flows from a fundamental response in two dimensions, provided we are mindful of the logarithmic form that the monopole now has. A director rotation by θ_0 inside a disc of radius a results in an equilibrium texture given by

$$\mathbf{n} = \cos\left(\frac{\theta_0 \log(r/R)}{\log(a/R)}\right)\mathbf{e}_z + \sin\left(\frac{\theta_0 \log(r/R)}{\log(a/R)}\right)\mathbf{e}_x, \tag{3.45}$$

which in the far field tends to a monopole distortion $\mathbf{n} \approx \mathbf{e}_z + \frac{\theta_0 \log(r/R)}{\log(a/R)}\mathbf{e}_x$. Due to the logarithmic divergence of the fundamental harmonic in two dimensions it is necessary to normalise through a large length R such that a uniformly aligned far-field director is recovered.

Solving Stokes' equations as before the fundamental flow solution is now found

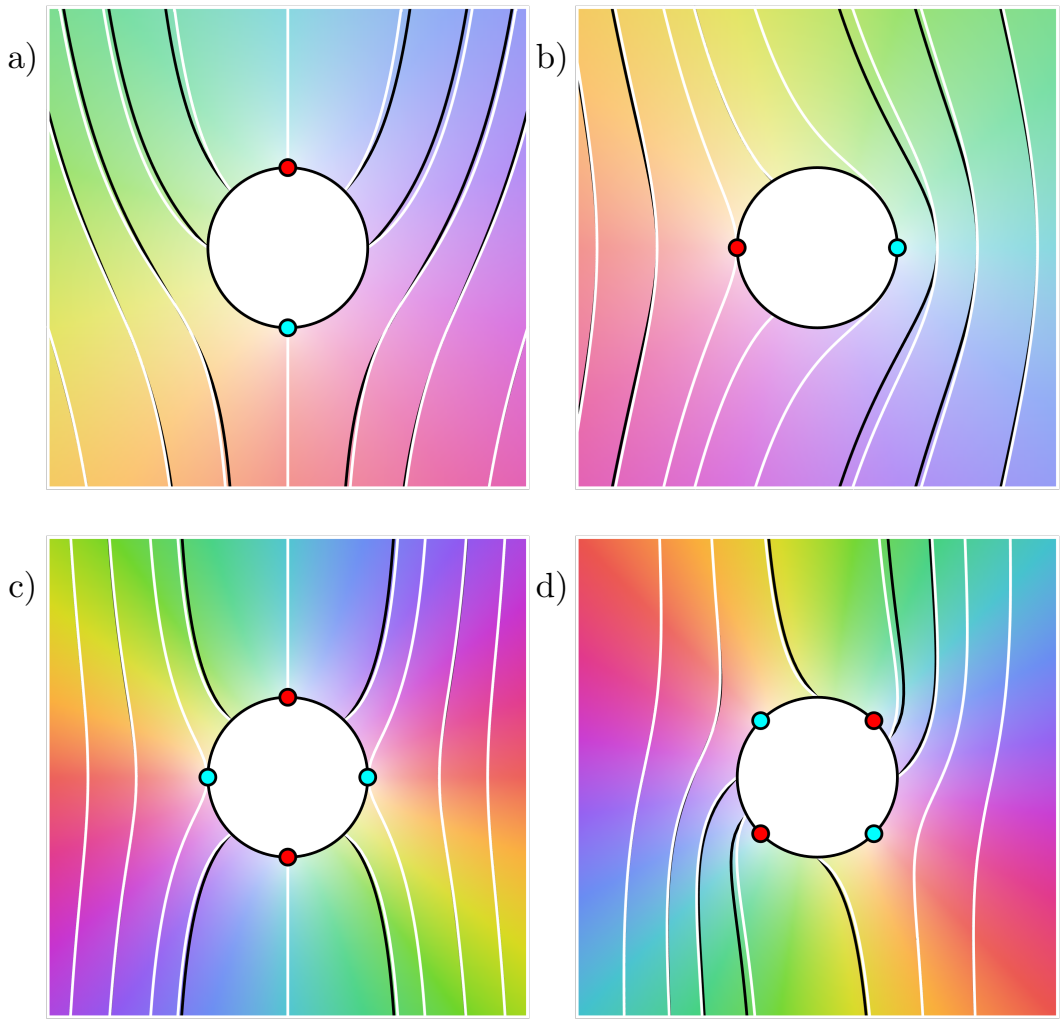

Figure 3.5: Representative defect configurations for nematic multipoles in two dimensions. The red and cyan dots indicate the locations of $+1/2$ and $-1/2$ defects respectively. The black curves are the integral curves of the corresponding director field and the background colour shows the phase of the complex function whose imaginary part gives the exact director angle, as in (3.40). The white lines are the integral curves of the dominant multipole, that is the leading term of (3.41). The multipole series converges onto the exact director angle outside a core region, shown as a white disc, and the leading multipole provides a remarkably good approximation in this region.

to be

$$\tilde{\mathbf{u}} = \frac{\zeta\theta_0}{4\mu\log(a/R)}\left[\mathbf{e}_x\left(z\log\left(\frac{r}{R}\right) - \frac{x^2 z}{r^2}\right) + \mathbf{e}_z\left(x\log\left(\frac{r}{R}\right) - \frac{xz^2}{r^2}\right)\right], \tag{3.46}$$

$$\tilde{p} = -\frac{\zeta\theta_0}{\log(a/R)}\frac{xz}{r^2}. \tag{3.47}$$

There is a clear similarity between these solutions and their three-dimensional counterparts, but while the fundamental flow response is still extensional it now grows linearly with distance from the distortion, with this change in scaling inherited by the subsequent harmonics.

As in the three-dimensional case we can gain general insight into the active response of a nematic by considering the net contribution of the active stresses to the force and torque when integrated over a large circle of radius r

$$\int \zeta\mathbf{nn}\cdot\mathbf{e}_r \mathrm{d}r \approx \int \zeta\left\{\frac{z\delta n_x}{r}\mathbf{e}_x + \frac{x\delta n_x}{r}\mathbf{e}_z\right\}\mathrm{d}r, \tag{3.48}$$

$$\int \mathbf{x}\times\zeta\mathbf{nn}\cdot\mathbf{e}_r \mathrm{d}r \approx \int \zeta\frac{(z^2-x^2)\delta n_x}{r}\mathrm{d}r. \tag{3.49}$$

We see that in two dimensions both dipoles will self-propel if free to move and there is a single chiral quadrupole which produces rotations.

The far-field flow solutions for distortions up to dipole order are illustrated in Figure 3.6, superposed over the nematic director. Both dipoles are now motile and as in the three-dimensional case they set up flows reminiscent of the Stokeslet. Vertical and horizontal self-propulsive modes may be viewed as resulting from normal and tangential anchoring respectively of the nematic on a disc. Interpolating between these orthogonal modes the angle of motility changes commensurately with the anchoring angle, such that sufficient control of the boundary conditions would allow for self-propulsion at an arbitrary angle with respect to the far-field alignment. This change in the dipole character can be represented by rigidly rotating the defect pair around the unit circle and the resulting motility is as would be expected from the position and orientation of the $+1/2$ defect [40; 130; 131]. Determining the motility induced by these dipolar modes is complicated by the Stokes paradox and although this can be circumvented by various means we do not pursue this here. If such dipolar colloids were fixed within the material they would pump the ambient fluid and so it should be possible to use them to produce the concentration, filtering and corralling effects observed previously by funneling motile bacteria [225].

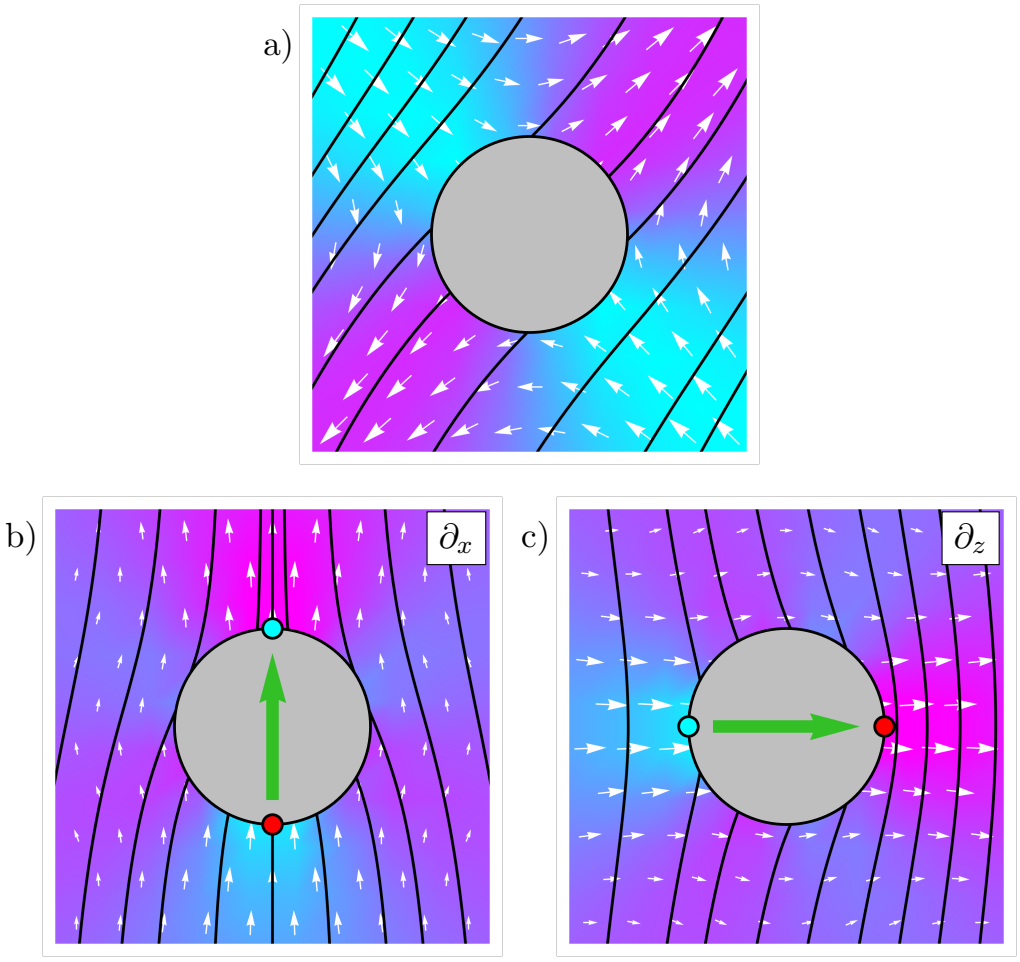

Figure 3.6: Monopole and dipole distortions in two-dimensional active nematics. The active flow in white is superposed on the pressure field, with the integral curves of the director shown in black. (a) The fundamental monopole response is extensional and grows linearly with distance from the distortion. (b) and (c) show the flows induced by dipole distortions, labelled by the appropriate derivative of the nematic monopole, with the green arrows indicating the direction of self-propulsion that would result from net active forces in extensile systems. The vertical and horizontal dipoles are the far-field director responses to normal and tangential anchoring respectively and may also be interpreted as arising from a pair of $+1/2$ (cyan) and $-1/2$ (red) defects. The self-propulsion matches that expected for the $+1/2$ defect.

The quadrupolar distortions and their corresponding flows are illustrated in Figure 3.7. We show both the flows that result from the three possible second derivatives as well as their negatives. Although the latter is redundant, it is intended to highlight

the connections between the location of defects, anchoring conditions on the disc and induced flows. The flow in Figure 3.7(a) is purely radial and resembles the stresslet flow, unsurprising as it results from differentiating the vertical dipole in the same way as the stresslet is related to the Stokeslet. It is produced by a quadrupole distortion which may be associated with normal anchoring on the disc – its counterpart with tangential anchoring, shown in Figure 3.7(b), has all the charges in its representative defect configuration inverted and a reversed flow response. Just as for the dipole distortions, the character of the quadrupole can be smoothly varied through adapting the boundary condition and the topological defects which represent the harmonic rotate rigidly in step with the changing anchoring angle.

The other four panels of Figure 3.7 show the active response to chiral quadrupoles. As was highlighted in our three-dimensional discussion, there are two distinct differential operators which produce the same nematic multipole; a comparison of the corresponding active responses is provided by panels (c) and (f) as well as by (d) and (e). Although the nature of the induced flows differs, being predominately horizontal and vertical respectively, the phenomenology of the active response, as characterised by the net active torque, is the same. It is tempting to ask if one of the flow solutions makes more sense in terms of the orientation of the motile $+1/2$ defects [130; 131]. This can be found in terms of Φ (2.8) as $\partial_z \left(\Phi/\bar{\Phi}\right)$, evaluated at the position of the defect. Fittingly, this reveals the orientation to be neither horizontal nor vertical but halfway in-between. For extensile activity the distortion shown in Figure 3.7(c) and (f) generates anticlockwise rotation, as can easily be justified via our representation of the far-field director structure as arising from a square arrangement of two $+1/2$ and two $-1/2$ defects – the dual mode rotates clockwise, see Figure 3.7(d) and (e). By choosing boundary conditions such that the defects are positioned closer to the mid-line of the colloid the strength of the active torque can be tuned.

This shows that suitable adaptation of the boundary conditions on a disc can in principle lead to all the self-propulsive and rotational modes in two dimensions. There is still interest in developing a purely geometric route to inducing these multipoles through modification of the colloidal shape, not least because while all the distortions in Figure 3.5 arise as formal solutions of a boundary value problem, some, such as the horizontal dipole in Figure 3.5(b), are not observed experimentally. Understanding the connection between colloidal shape and nematic distortion and applying this understanding to design colloids with desired properties will be the work of Chapter 5. In it we will show, amongst other things, how all the distinct active phenomena described here can be achieved geometrically, in particular producing ratchet effects with asymmetric cogs.

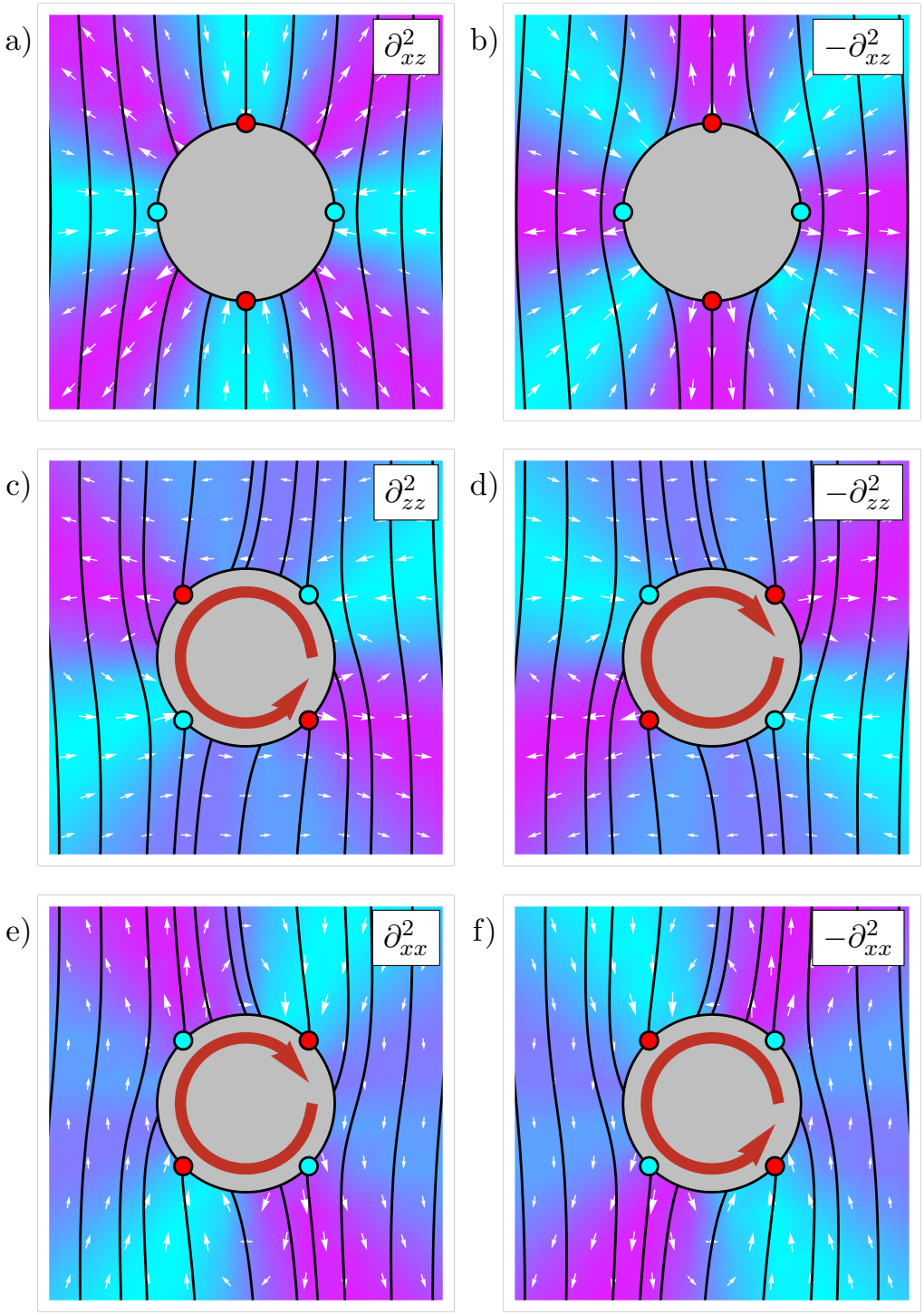
a)
∂^2_{xz}
b)
$-\partial^2_{xz}$
c)
∂^2_{zz}
d)
$-\partial^2_{zz}$
e)
∂^2_{xx}
f)
$-\partial^2_{xx}$

We end this section by commenting on the effect of chiral active stresses, which have been shown to be relevant in certain populations of eukaryotic cells [248; 249]. Such stresses cause the active force to be misaligned with the nematic director. The flow responses for purely chiral stresses are similar but with the monopole response rotated by $\frac{\pi}{4}$, leading to the roles of the two distinct dipole and quadrupole distortions being interchanged. A generic mixture of achiral and chiral stresses leads to a smooth interpolation of the behaviour of the multipole distortions, much as it causes a rotation of the flow profile of the $+1/2$ defect [248].

3.6 Discussion

We have presented a framework for understanding the far-field flow and pressure response to distortions in active nematics. These fit into a hierarchical structure such that the responses to all higher-order distortions may be derived from those for monopole distortions. The lack of decay exhibited in the monopole flow response is reflective of the fundamental hydrodynamic instability inherent to active nematics [220].

Particularly striking are those distortions for which the active response comprises a net active force or torque and we identified the dipole and quadrupole distortions which induce such responses. For unpinned distortions a net active force results in self-propulsion, mirroring the observed dynamics of biologically [228; 229; 250] or chemically

Figure 3.7 *(preceding page)*: Quadrupole distortions in two-dimensional active nematics. The active flow is shown in white superposed on the pressure field, with the integral curves of the director shown in black. The distortions are labelled by the derivative of the nematic monopole that produces them and the red arrows indicate the rotation that would result from net active torques in an extensile system. The character of the quadrupole distortion in a two-dimensional nematic can be determined through the anchoring conditions. Achiral quadrupoles arise from normal or tangential anchoring, shown in (a) and (b) respectively. Oblique anchoring leads to chiral quadrupoles which result in net rotations, shown in (c)-(f). In this case there are two distinct derivatives that produce the same nematic quadrupole and hence two distinct flow solutions, illustrated in the pairs (c) and (f) as well as (d) and (e). Although the flows differ, the net active torque does not. The sign and strength of the chiral mode can be tuned via the anchoring angle as seen by comparing the flows in (c) and (d) or (e) and (f). The quadrupoles may also be interpreted as the far-field distortion arising from configurations of $+1/2$ (cyan) and $-1/2$ (red) defects. A given change in anchoring angle corresponds to a commensurate but opposite rigid rotation of the defects and any rotational flow is in accordance with the self-propulsion of the $+1/2$ defects.

[251] active colloids in passive nematics. If the distortion is fixed then such forces will act as fluid pumps, such as have been used to maintain large concentration gradients in populations of bacteria [225]. Similarly, a net active torque will result in either rotation of the colloid or stirring of the fluid. The former response is similar to the behaviour of ratchets in bacterial baths [22; 23; 222], although the orientational order of the nematic environment impacts the chiral response due to a cog-shaped inclusion.

The addition of colloidal inclusions to nematic liquid crystals had a transformational effect, making possible metamaterials which are self-assembling and photo-responsive [176; 193]. Ultimately, these applications result from basic properties of the elastic response of the nematic director to local distortions [181] which result in interactions which are long-ranged and anisotropic. Our results on the active response to distortions suggests that there is the potential for colloids to have a similar impact on the behaviour of active nematics. The ability to produce self-propulsive and rotational inclusions is a key step towards being able to fashion micro-machines to extract work from such materials. Beyond this, it will be of interest to understand fully how the multi-particle behaviour will be affected by a combination of hydrodynamic and elastic interactions, along with whatever collective phenomena might result.

Our multipolar approach to the active behaviour of nematics mirrors the description of colloidal elastic interactions in passive nematics [90; 186]. Given the diversity of collective phenomena already present in these passive colloidal systems [177] it is natural to ask what dynamics would arise when this is combined with the active multipoles we have discussed. A detailed approach to the pair-wise interactions of active nematic inclusions would follow analogously that for isotropic active fluids [252], with the density fluctuations replaced by director distortions and the particle current replaced by the flow of the ambient fluid. Nonetheless, some basic points can be extracted from the flow solutions. The dominant contribution to the hydrodynamic interactions between two colloids is the advection of each by the flow of the other. All dipole distortions produce flows which are even under $\mathbf{r} \to -\mathbf{r}$ and so both colloids are advected with the same velocity. This means that even for dipoles which are not self-propulsive by themselves, they can acquire propulsion in pairs. This collective motility is reminiscent of that found for pairs of scallops or dumbbell swimmers [253; 254]. The direction of propulsion depends on the displacement of the two colloids. By contrast, the flows resulting from quadrupole distortions are all odd under $\mathbf{r} \to -\mathbf{r}$, meaning that the advection velocity is opposing for the two colloids. For the purely radial flows of the Saturn's ring quadrupole and those in $\mathbf{Q}^2$ this suggests that the dominant hydrodynamic interaction will be attractive or repulsive, depending on the angular separation of the colloids. Inherent to

this discussion of pairwise hydrodynamic interactions is their non-reciprocity. This is a hallmark of active matter which is observed across a wide range of systems [113].

Find out the cause of this effect,
Or rather say, the cause of this defect,
For this effect defective comes by cause.

Hamlet, Act 2, Scene 2. Polonius

4

Active Defect Loops as Active Multipoles

Active nematics are a class of materials combining self-driven, or motile, constituents with the orientational order of ordinary nematic liquid crystals [93; 57; 20]. Examples include bacterial suspensions [107], bacteria in a liquid crystal host [229], cell monolayers [156], tissues [30] and synthetic microtubule suspensions [61]. The main properties are well-established for two-dimensional active nematics, including their turbulent dynamics and self-motile topological defects [20]. Interest is now growing in three-dimensional active nematics, with initial results on the cross-over in behaviour of defect lines as a function of cell gap [175], the onset of the fundamental instability in channel geometry [255; 256], the dynamics and deformations of droplets [257; 147], the characterisation and dynamics of defect loops [62; 43; 44], and the statistical properties of the turbulent state [63]. Defect loops are fundamental objects in three-dimensional active nematics, analogous to $\pm 1/2$ point defects in two dimensions. They are created spontaneously and exhibit their own complex dynamics [62; 43], which a local analysis sheds light on by the determination of a self-propulsion velocity for each point of the loop [44].

The description of defects in two-dimensional active nematics as effective particles with their own dynamics has been influential in developing understanding [39; 40; 89; 150; 258; 42; 110] and it is natural to ask about the extent to which material properties

in three dimensions can similarly be reduced to an effective description in terms of defect loops. Although the problem is analogous to that in two dimensions, there are differences in the topological characterisation [178] and, more significantly, in the geometric diversity of defect loops. The geometry comes from both the shape of the defect loop and also the nature of the distortion in the director field around the loop. Exemplars of this come from cases where the director distortion through the middle of the loop is of pure splay, bend or twist type [43; 44] (see Figure 4.1). These have identical properties in passive nematics with one elastic constant [174] but behave distinctly in active systems, both in their self-propulsion dynamics [44] and in the abundances of different types, with twist defect loops found to be the most prevalent [43; 44].

An initial analysis of active defect loops has been developed in terms of the local profile and self-propulsion velocity assigned to each point [44]. Here, we construct a complementary global description based on an asymptotic multipole expansion for the director field. We show how the multipole structure of the active stresses generates a global self-dynamics for defect loops, involving both translational and rotational motion. The self-dynamics identifies twist loops as the only force- and torque-free states, suggesting a mechanism for the observed bias towards twist loops in three-dimensional active nematics [43]. Finally, we determine the fluid flows associated to defect loops; these are long range with a leading $1/r$ decay, such that the active hydrodynamics dominates the interactions between defect loops. We describe these qualitatively for the stable twist loops.

4.1 Multipole description of nematic defect loops

A minimal model for defect loops in nematics was introduced by Friedel & de Gennes [174], in which the director rotates within a single plane, which here we take to define the xz-plane, and the director field is

$$\mathbf{n} = \cos\theta\,\mathbf{e}_z + \sin\theta\,\mathbf{e}_x, \tag{4.1}$$

with θ increasing by π as you go once around the loop. In the one-elastic-constant approximation the Frank free energy is minimised whenever θ is a harmonic function, giving $\theta = \frac{1}{4}\omega$, where ω is the solid angle function for the loop [174; 45; 46; 44]. (In writing this we are taking the far-field orientation of the director to define the z-direction.) This construction is independent of the shape or relative orientation of the defect loop and varying the orientation, relative to the plane of the director field, gives different

geometries and local profiles for the defect loop. We illustrate this for splay, bend and twist type loops in Figure 4.1.

The global orientation of a defect loop, and hence its geometric type, is encoded in the structure of the multipole expansion for its solid angle function. The multipole expansion is known from applications in magnetostatics [259; 260] and vortex hydrodynamics [261]. Here we present a purely geometric formulation, dependent only on the form of the space curve K. By considering the asymptotics of this function we arrive at the multipole expansion used in this chapter.

The solid angle function $\omega(\mathbf{x})$ is the unique harmonic function on the complement of a curve K which winds by 4π about any segment and tends to 0 mod 4π for large distances. While $\omega(\mathbf{x})$ depends only on K it is perhaps most easily defined via an orientable surface Σ that spans K. In a natural extension of the definition of angle, $\omega(\mathbf{x})$ is then the projected area of Σ on a unit sphere centred on $\mathbf{x}$ [45; 46], that is

$$w(\mathbf{x}) = \int_{\Sigma} \frac{\mathbf{x}-\mathbf{y}}{|\mathbf{x}-\mathbf{y}|^3} \cdot \mathrm{d}\mathbf{S}, \tag{4.2}$$

with $\mathbf{y}$ parameterising Σ. There are several equivalent expressions for the solid angle function [46], for example it can be defined using only geometric properties of K as [46]

$$\omega(\mathbf{x}) = 2\pi\left(1 \pm \mathrm{Wr}(K)\right) - \int_K \frac{\mathbf{p}\cdot\mathbf{T}\times\mathrm{d}\mathbf{T}}{1\pm\mathbf{p}\cdot\mathbf{T}} \mod 4\pi, \tag{4.3}$$

where $\mathrm{Wr}(K)$ is the writhe of K [262; 263], $\mathbf{p} = \frac{\mathbf{y}-\mathbf{x}}{|\mathbf{y}-\mathbf{x}|}$ with $\mathbf{y}$ labelling points on the loop K and $\mathbf{T}$ is the unit tangent vector to K.

A formulation that facilitates the extraction of asymptotic behaviour is

$$\omega(\mathbf{x}) = \int_K \frac{\mathbf{p}_\infty \times \mathbf{p}}{1+\mathbf{p}_\infty\cdot\mathbf{p}} \cdot \mathrm{d}\mathbf{p} \mod 4\pi, \tag{4.4}$$

with $\mathbf{p}$ as in (4.3) and $\mathbf{p}_\infty$ an arbitrary constant vector. This relation can be arrived at from the projected area formula (4.2) by making an arbitrary choice of spherical coordinates (θ,ϕ) such that $\omega(\mathbf{x}) = \int(1-\cos\theta)\mathrm{d}\phi$ [45; 46] and then taking $\mathbf{p}_\infty$ as the direction $\theta = 0$ [46]. We seek an asymptotic expansion of $\omega(\mathbf{x})$ for $|\mathbf{x}| = r \gg |\mathbf{y}|$, for which it is convenient to take the choice $\mathbf{p}_\infty = -\frac{\mathbf{x}}{|\mathbf{x}|}$, and then make a general series

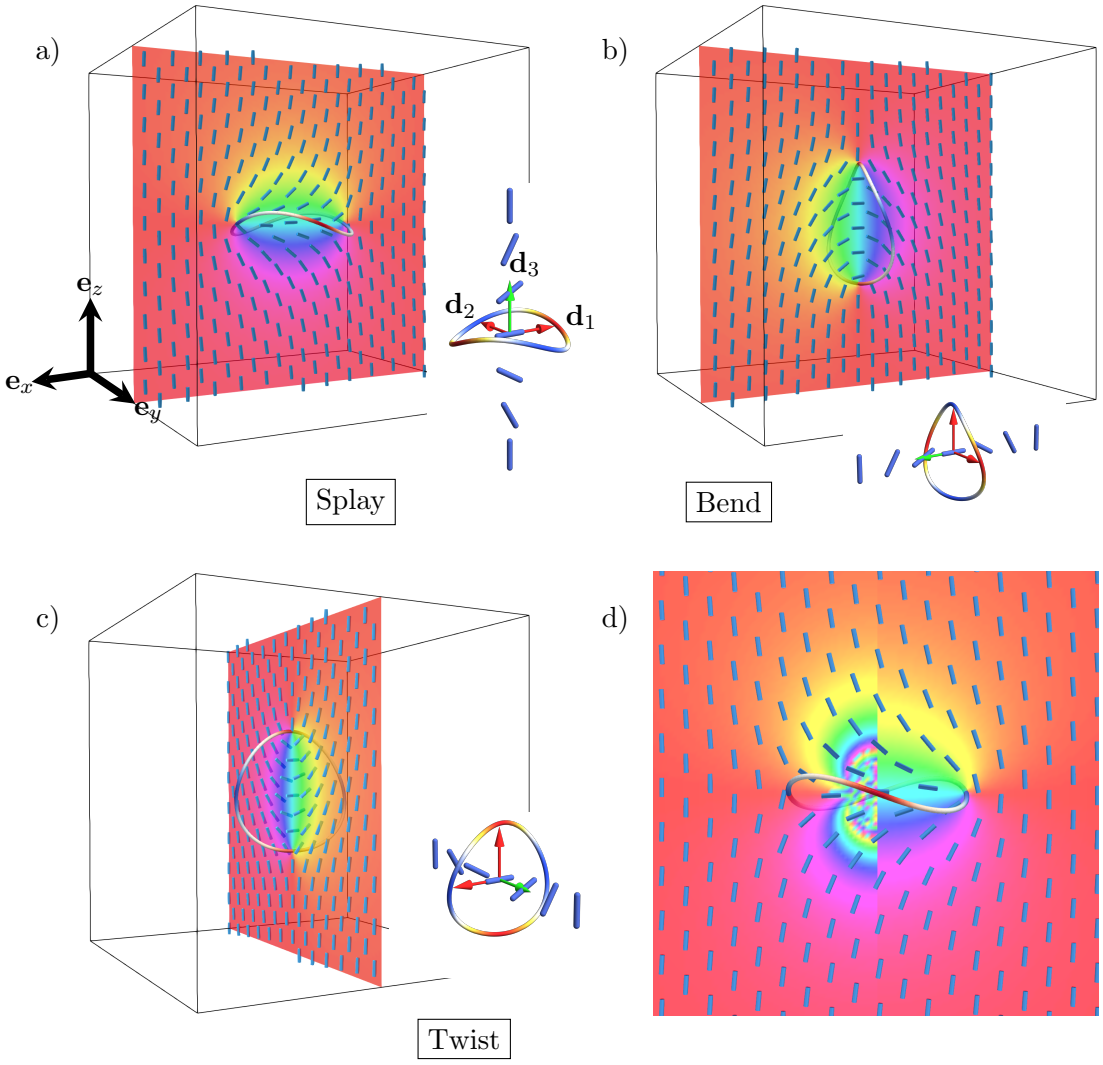

Figure 4.1: Defect loops of (a) splay, (b) bend, and (c) twist type. In each case the director field is shown (blue cylinders) on a slice through the defect loop; the colour map shows the structure of the solid angle function. The defect loop is coloured according to the torsion of the curve; red where it is maximally negative and blue where it is maximally positive. The insets give a simplified representation of the defect loops, showing only the variation of the director field through the centre of the loop. The arrows indicate the multipole frame – in green the $\mathbf{d}_3$ direction of the dipole vector and in red the $\mathbf{d}_1$ and $\mathbf{d}_2$ directions coming from the quadrupole tensor. (d) Comparison of the full solid angle function (right half) with the multipole approximation (4.24) (left half); the multipole approximation accurately captures the solid angle from distances only moderately larger than the loop size.

expansion of the terms in the integrand

$$\mathbf{p}_\infty \times \mathbf{p} \cdot \mathrm{d}\mathbf{p} = -\frac{\mathbf{x}}{r} \times \frac{\mathbf{y}}{|\mathbf{y}-\mathbf{x}|} \cdot \frac{\mathrm{d}\mathbf{y}}{|\mathbf{y}-\mathbf{x}|}, \tag{4.5}$$

$$= -\frac{\mathbf{x}}{r} \times \frac{\mathbf{y}}{r} \cdot \frac{\mathrm{d}\mathbf{y}}{r} \left[1 - \left(\frac{2\mathbf{x}\cdot\mathbf{y}}{r^2} - \frac{y^2}{r^2}\right)\right]^{-1}, \tag{4.6}$$

$$= -\frac{\mathbf{x}}{r} \times \frac{\mathbf{y}}{r} \cdot \frac{\mathrm{d}\mathbf{y}}{r} \sum_{n=0}^{\infty} \left(\frac{2\mathbf{x}\cdot\mathbf{y}}{r^2} - \frac{y^2}{r^2}\right)^n, \tag{4.7}$$

$$\frac{1}{1+\mathbf{p}_\infty\cdot\mathbf{p}} = \left[2 - \left(\frac{\mathbf{x}}{r}\cdot\frac{\mathbf{y}-\mathbf{x}}{|\mathbf{y}-\mathbf{x}|}+1\right)\right]^{-1}, \tag{4.8}$$

$$= \frac{1}{2}\sum_{n=0}^{\infty}\left[\frac{1}{2}\left(\frac{\mathbf{x}}{r}\cdot\frac{\mathbf{y}-\mathbf{x}}{|\mathbf{y}-\mathbf{x}|}+1\right)\right]^n, \tag{4.9}$$

$$= \frac{1}{2}\sum_{n=0}^{\infty}\frac{1}{2^n}\left[\frac{\mathbf{x}}{r}\cdot\frac{\mathbf{y}-\mathbf{x}}{r}\sum_{m=0}^{\infty}\frac{(-1)^m(2m)!}{2^{2m}(m!)^2}\left(-\frac{2\mathbf{x}\cdot\mathbf{y}}{r^2}+\frac{y^2}{r^2}\right)^m+1\right]^n. \tag{4.10}$$

We consider the expansion of the solid angle function up to quadrupole order. In doing so we first observe that the part in square brackets in (4.10) is already second order in $\mathbf{y}$, so that it is sufficient to retain only the leading $n=0$ term, $\frac{1}{1+\mathbf{p}_\infty\cdot\mathbf{p}} \approx \frac{1}{2}$. As a result we have

$$\omega(\mathbf{x}) = \int_K -\frac{\mathbf{x}}{r}\times\frac{\mathbf{y}}{r}\cdot\frac{\mathrm{d}\mathbf{y}}{r}\left(1+\frac{2\mathbf{x}\cdot\mathbf{y}}{r^2}+O(y^2)\right)\left(\frac{1}{2}+O(y^2)\right) \tag{4.11}$$

and so arrive at

$$\omega(\mathbf{x}) = \frac{1}{2}\int_K \epsilon_{ijk}y_j\mathrm{d}y_k\,\partial_i\frac{1}{r} - \frac{1}{3}\int_K \epsilon_{ikl}y_jy_k\mathrm{d}y_l\,\partial_i\partial_j\frac{1}{r}+\ldots, \tag{4.12}$$

where we have used that $\partial_i\frac{1}{r} = -\frac{x_i}{r^3}$ and $\partial_i\partial_j\frac{1}{r} = \frac{3x_ix_j}{r^5} - \frac{\delta_{ij}}{r^3}$. The position of the defect loop ($\mathbf{x}=0$) is taken to be the location of its 'centre of mass' (assuming a uniform density).

The dipole moment is a vector whose direction gives the principal orientation of the defect loop. As it has the form $\frac{1}{2}\int_K \mathbf{y}\times\mathrm{d}\mathbf{y}$ we can recognise it as a vector of projected areas. The i-component is the area of the loop when projected along $\mathbf{d}_i$. The dipole vector points in the direction of greatest projected area and its magnitude is this area. The quadrupole moment is a traceless, symmetric rank 2 tensor, giving a secondary orientation. Similarly, it is $-\frac{2}{3}$ times the first moment of area tensor, for which the ij-component is given by the j-moment of the area of the loop when projected

along $\mathbf{d}_i$. However, since $\partial_i \partial_j \frac{1}{r}$ is symmetric only the symmetric part contributes.

4.1.1 Generic perturbations of a circular loop

The expressions in (4.12) hold for any shape of defect loop, but for our current focus we calculate them explicitly only for the representative curve

$$\mathbf{y}(u) = (a_0 \cos u, a_0 \sin u, \frac{1}{6}\tau_0 a_0^2 \sin 2u) \tag{4.13}$$

corresponding to a loop that is approximately a circle of radius a_0. The parameter τ_0 captures the non-planarity of the loop and is the amplitude of its torsion. We justify this form of defect loop by describing general perturbations of a circular loop and calculating the dipole and quadrupole moments for its solid angle function.

We parameterise a generic loop using a Cartesian basis $\{\mathbf{d}_1, \mathbf{d}_2, \mathbf{d}_3\}$ as

$$\mathbf{y}(\theta) = r(\theta)\big[\cos\theta\, \mathbf{d}_1 + \sin\theta\, \mathbf{d}_2\big] + h(\theta)\, \mathbf{d}_3, \tag{4.14}$$

where $r(\theta)$ is the radius of the curve in the $\mathbf{d}_1\mathbf{d}_2$ plane, $r = y_1^2 + y_2^2$, and $h(\theta)$ is its height in the $\mathbf{d}_3$ direction. The generic perturbations of a loop about a planar circle of radius a_0 are captured by the Fourier series

$$r(\theta) = a_0 + \sum_{n=2}^{\infty} \big(a_n \sin n\theta + b_n \cos n\theta\big), \tag{4.15}$$

$$h(\theta) = A_2 \sin 2\theta + \sum_{n=3}^{\infty} \big(A_n \sin n\theta + B_n \cos n\theta\big). \tag{4.16}$$

In writing these, the low order Fourier modes have been fixed through the freedom in the choice of frame. Transformations of the frame under the Euclidean group afford six degrees of freedom, three translational and three rotational. The $n = 1$ terms of $r(\theta)$ correspond to translations of the loop's centre of mass and so we choose the origin such that these are zero, along with the $n = 0$ term of $h(\theta)$. Similarly, the $n = 1$ terms of $h(\theta)$ correspond to rigid rotations of the loop and so we orient the frame such that both these terms vanish. The remaining rotational degree of freedom is a gauge freedom in the choice of where $\theta = 0$, which we choose such that $B_2 = 0$ in $h(\theta)$.

With this generic form established we can evaluate the dipole vector and quadrupole

tensor. For the dipole vector we have

$$\begin{aligned}\frac{1}{2}\int_K \epsilon_{ijk} y_j \mathrm{d}y_k = \frac{1}{2}\Bigg[&\int (rh' - hr')(\sin\theta \mathbf{d}_1 - \cos\theta \mathbf{d}_2)\mathrm{d}\theta \\ &- \int hr(\cos\theta \mathbf{d}_1 + \sin\theta \mathbf{d}_2)\mathrm{d}\theta + \int r^2 \mathrm{d}\theta \mathbf{d}_3\Bigg].\end{aligned} \tag{4.17}$$

The explicit evaluation of these integrals is achieved through the orthogonality of the Fourier modes with the end result

$$\begin{aligned}\frac{1}{2}\int_K \epsilon_{ijk} y_j \mathrm{d}y_k = &\pi\left(a_0^2 + \frac{1}{2}\sum_{n=2}^{\infty}\left(a_n^2 + b_n^2\right)\right)\mathbf{d}_3 \\ &+ \pi\left(A_2 a_3 + \sum_{n=3}^{\infty}\frac{n}{2}\Big[A_n(a_{n+1} - a_{n-1}) + B_n(b_{n+1} - b_{n-1})\Big]\right)\mathbf{d}_1 \\ &+ \pi\left(-A_2 b_3 + \sum_{n=3}^{\infty}\frac{n}{2}\Big[B_n(a_{n+1} + a_{n-1}) - A_n(b_{n+1} + b_{n-1})\Big]\right)\mathbf{d}_2.\end{aligned} \tag{4.18}$$

The dominant contribution is $\pi a_0^2 \mathbf{d}_3$, with all other terms being second order in perturbations.

Proceeding similarly for the quadrupole tensor gives

$$\begin{aligned}-\frac{1}{3}\int_K \frac{1}{2}(\epsilon_{ikl} y_j + \epsilon_{jkl} y_i) y_k \mathrm{d}y_l = \frac{1}{6}\Bigg[&\int hr^2 \begin{pmatrix} 1+\cos 2\theta & \sin 2\theta & 0 \\ \sin 2\theta & 1-\cos 2\theta & 0 \\ 0 & 0 & -2 \end{pmatrix}\mathrm{d}\theta \\ &+ \int r(hr' - rh') \begin{pmatrix} \sin 2\theta & -\cos 2\theta & 0 \\ -\cos 2\theta & -\sin 2\theta & 0 \\ 0 & 0 & 0 \end{pmatrix}\mathrm{d}\theta \\ &+ \int r(h^2 - r^2) \begin{pmatrix} 0 & 0 & \cos\theta \\ 0 & 0 & \sin\theta \\ \cos\theta & \sin\theta & 0 \end{pmatrix}\mathrm{d}\theta \\ &+ \int h(hr' - rh') \begin{pmatrix} 0 & 0 & \sin\theta \\ 0 & 0 & -\cos\theta \\ \sin\theta & -\cos\theta & 0 \end{pmatrix}\mathrm{d}\theta\Bigg].\end{aligned} \tag{4.19}$$

The lowest order contribution comes from the first two terms and is given by

$$\frac{1}{6}\int r^2(h\sin 2\theta + h'\cos 2\theta)\mathrm{d}\theta(\mathbf{d}_1\mathbf{d}_2 + \mathbf{d}_2\mathbf{d}_1) = \frac{\pi a_0^2 A_2}{2}(\mathbf{d}_1\mathbf{d}_2 + \mathbf{d}_2\mathbf{d}_1). \tag{4.20}$$

As this is proportional to A_2, this term is only present for non-planar curves. It has an interpretation as the sum of two first moments of area of the curve, as was already mentioned. A second interpretation may be given in terms of the torsion of the curve. The torsion of a space curve is given by [264]

$$\tau = \frac{(\mathbf{y}' \times \mathbf{y}'') \cdot \mathbf{y}'''}{|\mathbf{y}' \times \mathbf{y}''|^2}. \tag{4.21}$$

Evaluating this for the curve $\mathbf{y} = (a_0 \cos\theta, a_0 \sin\theta, A_2 \sin 2\theta)$ gives

$$\tau = -\frac{6A_2 \cos 2\theta}{a_0^2 + A_2^2(10 - 6\cos 4\theta)} \approx -\frac{6A_2}{a_0^2} \cos 2\theta. \tag{4.22}$$

Hence we characterise the torsion of our perturbed loop as $\tau \approx -\tau_0 \cos 2\theta$, with $A_2 = \frac{a_0^2 \tau_0}{6}$. This identifies the minimal perturbation of a circular loop that captures non-zero dipole and quadrupole terms in the solid angle function; this minimal model being the one given in (4.13).

All other terms that arise in (4.19) are at least quadratic in the perturbations of a circle. In particular, in the case of a planar loop, corresponding to $h(\theta) = 0$, the leading contribution is

$$\frac{a_0}{12} \sum_{n=3}^{\infty} \Big[(a_n a_{n-1} + b_n b_{n-1})(\mathbf{d}_1\mathbf{d}_3 + \mathbf{d}_3\mathbf{d}_1) + (a_n b_{n-1} - b_n a_{n-1})(\mathbf{d}_2\mathbf{d}_3 + \mathbf{d}_3\mathbf{d}_2) \Big], \tag{4.23}$$

arising due to asymmetry of the loop with respect to the $\mathbf{d}_1$ or $\mathbf{d}_2$ axes. Therefore, while the quadrupole tensor for planar loops is not zero, it is an order higher in perturbations than that in (4.20) and so for generic perturbations about a circular shape the former non-planar term will be dominant.

Using (4.13) in (4.12) yields

$$\omega(\mathbf{x}) = \pi a_0^2 \nabla_{\mathbf{d}_3} \frac{1}{r} + \frac{\pi a_0^4 \tau_0}{6} \nabla_{\mathbf{d}_1} \nabla_{\mathbf{d}_2} \frac{1}{r} + \cdots, \tag{4.24}$$

where $\{\mathbf{d}_1, \mathbf{d}_2, \mathbf{d}_3\}$ are the Cartesian basis vectors for the coordinate system adapted to the defect loop. The direction of the dipole is the basis vector $\mathbf{d}_3$ and its magnitude is the 'area bound by the loop'. The quadrupole tensor is $\frac{\pi a_0^4 \tau_0}{12}[\mathbf{d}_1\mathbf{d}_2 + \mathbf{d}_2\mathbf{d}_1]$ and is proportional to τ_0 so that it vanishes for planar loops without torsion. The directions $\mathbf{d}_1, \mathbf{d}_2$ correspond to those of 'principal torsion'; specifically, the torsion is $\tau \approx -\tau_0 \cos 2u$ and takes its maximal negative value along the directions $\pm\mathbf{d}_1$ and its maximal positive value along $\pm\mathbf{d}_2$. This multipole frame is illustrated in Figure 4.1 and used in all figures

in this chapter.

4.2 Active forces and torques

In an active nematic, the activity imparts additional material stresses $-\zeta\mathbf{nn}$, where ζ is a phenomenological coefficient that is positive in extensile materials [93; 57; 20]. For simplicity of presentation we will assume $\zeta > 0$ in what follows, as is the case in the experimental system [43]. On large scales active nematics are unstable [25] and exhibit a state of active turbulence [107; 106; 111]. However, on intermediate scales a description can be given using the local nematic alignment. This is what is implied in the description of the local flows and self-propulsion velocities of topological defects and defect loops [40; 89; 258; 110; 44]. Our analysis similarly applies on these intermediate scales. Despite only working at moderate distances the multipole expansion still accurately captures the structure of the solid angle function, and hence of the director field. This is illustrated in Figure 4.1(d), where we see good agreement even at distances only moderately larger than the defect loop size.

The active stresses generate self-dynamics for the defect loop, which we characterise first by the contributions that they make to the force and torque on a spherical volume centred on the loop. At distances large compared to the size of the loop ($r \gtrsim a$) the active stress can be approximated by

$$-\zeta\mathbf{nn} = -\zeta\mathbf{e}_z\mathbf{e}_z - \frac{\zeta\omega}{4}\left[\mathbf{e}_z\mathbf{e}_x + \mathbf{e}_x\mathbf{e}_z\right] + \cdots, \tag{4.25}$$

and using this the contribution to the force is

$$\begin{aligned}\mathbf{F} &= \int -\zeta\mathbf{nn}\cdot d\mathbf{A},\\ &= -\zeta\int\left[\mathbf{e}_z z + \frac{\omega}{4}\left(\mathbf{e}_x z + \mathbf{e}_z x\right)\right]\frac{1}{r}\mathrm{d}A,\end{aligned} \tag{4.26}$$

with the integral taken over a spherical surface entirely enclosing, and centred on, the defect loop. Through the orthogonality of the spherical harmonics we can see that, for example, the only contribution along $\mathbf{e}_x$ will come from the part of ω proportional to the dipole $\frac{z}{r^3}$. In full the only terms which survive integration are

$$-\zeta\int\frac{\pi a^2}{4}\left[-\frac{(\mathbf{d}_3\cdot\mathbf{e}_z)z^2}{r^3}\mathbf{e}_x - \frac{(\mathbf{d}_3\cdot\mathbf{e}_x)x^2}{r^3}\mathbf{e}_z\right]\frac{1}{r}\mathrm{d}A, \tag{4.27}$$

which on integrating gives

$$\mathbf{F} = \frac{\zeta\pi^2 a^2}{3}\Big[\big(\mathbf{e}_z\cdot\mathbf{d}_3\big)\mathbf{e}_x + \big(\mathbf{e}_x\cdot\mathbf{d}_3\big)\mathbf{e}_z\Big]. \tag{4.28}$$

This force depends on the surface over which the integral is taken, since the active stress is neither compactly supported nor divergence-free, but for the multipole analysis a spherical surface is natural and the result (4.28) is then independent of the radius and determined by the dipole part of the solid angle (4.24).

Similarly, the active stress contribution to the total torque acting on the defect loop is given by

$$\begin{aligned}\mathbf{T} &= \int \mathbf{x}\times\big(-\zeta\mathbf{nn}\big)\cdot d\mathbf{A},\\ &= -\zeta\int\Big[-xz\mathbf{e}_y + yz\mathbf{e}_x + \frac{\omega}{4}\left(yx\mathbf{e}_x + \left(z^2-x^2\right)\mathbf{e}_y - yz\mathbf{e}_z\right)\Big]\frac{1}{r}\mathrm{d}A,\end{aligned} \tag{4.29}$$

where again the integral is taken over a spherical surface enclosing the entire loop and is independent of its radius. Once more the orthogonality of the spherical harmonics ensures that the only surviving terms are

$$\begin{aligned}-\zeta\int\frac{\pi a^4\tau_0}{24}\Big\{&\mathbf{e}_x\left[\mathbf{d}_1\cdot\left(\mathbf{e}_x\mathbf{e}_y+\mathbf{e}_y\mathbf{e}_x\right)\cdot\mathbf{d}_2\right]xy\partial^2_{xy}\frac{1}{r}\\ &+\mathbf{e}_y\left[\mathbf{d}_1\cdot\left(\mathbf{e}_z\mathbf{e}_z-\mathbf{e}_x\mathbf{e}_x\right)\cdot\mathbf{d}_2\right]\left(z^2-x^2\right)(\partial^2_z-\partial^2_x)\frac{1}{r}\\ &-\mathbf{e}_z\left[\mathbf{d}_1\cdot\left(\mathbf{e}_y\mathbf{e}_z+\mathbf{e}_z\mathbf{e}_y\right)\cdot\mathbf{d}_2\right]yz\partial^2_{yz}\frac{1}{r}\Big\}\frac{1}{r}\mathrm{d}A,\end{aligned} \tag{4.30}$$

such that

$$\begin{aligned}\mathbf{T} = \frac{-\zeta\pi^2 a_0^4\tau_0}{30}\Big\{&\mathbf{e}_x\Big[\mathbf{d}_1\cdot\big(\mathbf{e}_x\mathbf{e}_y+\mathbf{e}_y\mathbf{e}_x\big)\cdot\mathbf{d}_2\Big] + 2\mathbf{e}_y\Big[\mathbf{d}_1\cdot\big(\mathbf{e}_z\mathbf{e}_z-\mathbf{e}_x\mathbf{e}_x\big)\cdot\mathbf{d}_2\Big]\\ &-\mathbf{e}_z\Big[\mathbf{d}_1\cdot\big(\mathbf{e}_y\mathbf{e}_z+\mathbf{e}_z\mathbf{e}_y\big)\cdot\mathbf{d}_2\Big]\Big\},\end{aligned} \tag{4.31}$$

determined by the quadrupole part of the solid angle (4.24). We reiterate that the torque is proportional to the magnitude of the torsion of the loop and hence dependent on its non-planar shape.

If the defect loop was a rigid body, its self-dynamics would follow from the resistance matrix relating the force and torque to the translational and rotational velocities. However, we can also expect internal dynamics affecting its shape and form, which in

turn control the dipole and quadrupole moments. Nonetheless, even without knowledge of the internal dynamics, qualitative features of the global dynamics can be extracted from the structure of the force and torque and, in particular, the defect loop geometries for which they vanish. We consider the force first for the three representative loops of splay, bend and twist type.

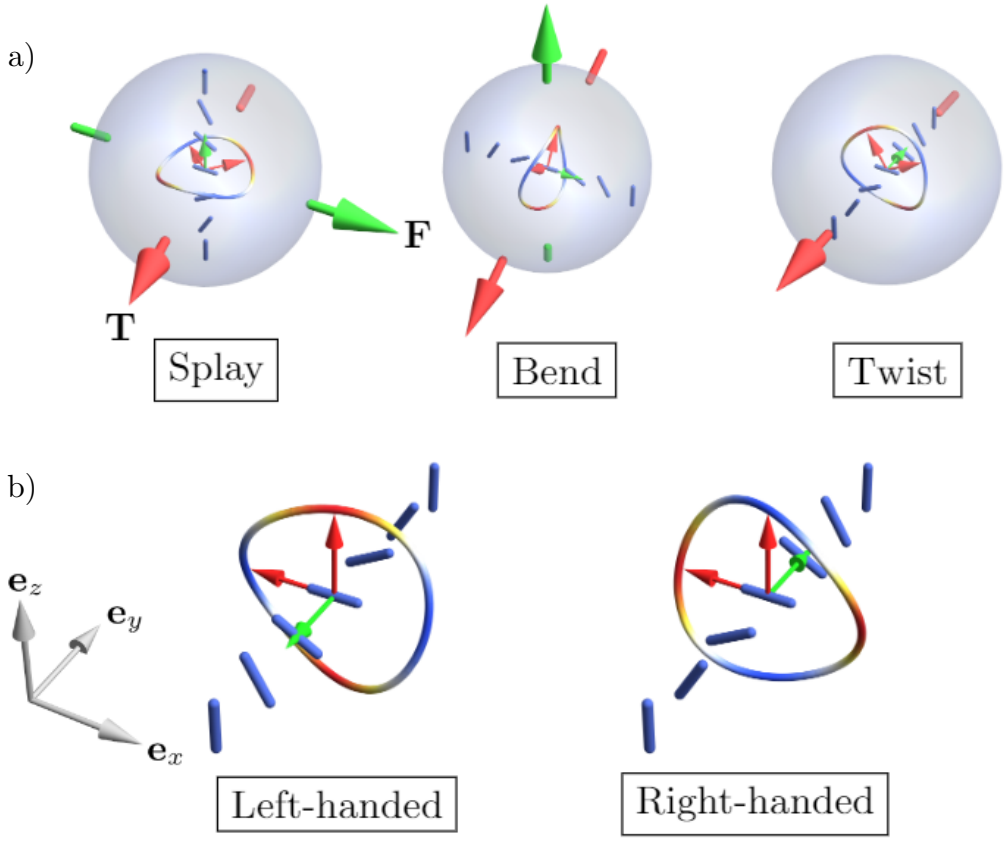

Figure 4.2: (a) Active forces and torques experienced by generic splay, bend and twist defect loops. The external green and red arrows indicate the force $\mathbf{F}$ (4.28) and torque $\mathbf{T}$ (4.31), respectively. The torque depends on the structure of the quadrupole tensor and is shown here for representative cases. (b) Stable left- and right-handed twist loops. Note that the principal torsion directions are oppositely oriented in the two cases.

For the splay loop ($\mathbf{d}_3 = \mathbf{e}_z$) the force is directed along $\mathbf{e}_x$; for the bend loop ($\mathbf{d}_3 = \mathbf{e}_x$) it is directed along $\mathbf{e}_z$; and for the twist loop ($\mathbf{d}_3 = \mathbf{e}_y$) it vanishes. This is illustrated by the large green arrows in Figure 4.2(a). Assuming a leading diagonal response, we expect the splay loop to move along x, the bend loop to move along z

and the twist loop to remain stationary. On dimensional grounds the magnitude of the resistance should scale as μa_0, where μ is the viscosity, so that the defect loop velocity scales as $\zeta a_0/\mu$ and therefore increases linearly with the size of the defect loop. In [44] the dynamics of these three geometries of defect loop were determined by assigning a local self-propulsion velocity to each point of the loop on the basis of its local director profile and exactly the same predictions obtained and confirmed by numerical solution of the full hydrodynamic equations.

We turn now to the torque (4.31) and the rotational motion of the defect loop. The torque is illustrated for the splay, bend and twist loops by the large red arrows in Figure 4.2(a). For the splay loop ($\mathbf{d}_3 = \mathbf{e}_z$), taking the general orientation $\mathbf{d}_1 = \cos\gamma\,\mathbf{e}_x + \sin\gamma\,\mathbf{e}_y$ for the quadrupole moment (out-of-plane buckling) the torque is

$$\mathbf{T} = -\frac{\zeta\pi^2 a_0^4 \tau_0}{30}\big[\mathbf{e}_x\cos 2\gamma + \mathbf{e}_y \sin 2\gamma\big], \tag{4.32}$$

and acts to reorient the defect loop from splay type to either bend or twist type. If we take the frictional resistance to scale as μa_0^3 on dimensional grounds, then the rotational velocity will scale as $\zeta a_0\tau_0/\mu$ and again increases linearly with the size of the defect loop. The situation is entirely analogous for bend loops ($\mathbf{d}_3 = \mathbf{e}_x$), which experience a torque reorienting them into twist or splay geometry. For twist loops ($\mathbf{d}_3 = \mathbf{e}_y$), taking a general orientation $\mathbf{d}_1 = \cos\gamma\,\mathbf{e}_z + \sin\gamma\,\mathbf{e}_x$ the torque is

$$\mathbf{T} = \frac{\zeta\pi^2 a_0^4\tau_0}{15}\,\sin 2\gamma\,\mathbf{e}_y, \tag{4.33}$$

and is purely about $\mathbf{e}_y$ so that they retain their twist character. The torque vanishes when $\gamma = 0, \frac{\pi}{2}$ and is restorative around $\gamma = \frac{\pi}{2}$, identifying this as a stable orientation for the defect loop. Of course, there are also twist loops with $\mathbf{d}_3 = -\mathbf{e}_y$; the torque they experience has a parallel description except that now the stable orientation corresponds to $\gamma = 0$ ($\mathbf{d}_1$ parallel to $\mathbf{e}_z$). These two stable states differ in the handedness of the twist rotation in the director passing through the defect loop; the case $\mathbf{d}_3 = \mathbf{e}_y$ corresponds to right-handed twist (dextro twist loop), while $\mathbf{d}_3 = -\mathbf{e}_y$ corresponds to left-handed twist (laevo twist loop). They are illustrated in Figure 4.2(b).

The existence of stable states and a general drive to convert other geometries towards these suggests that the self-dynamics will create a bias in the occurrence of different types of loops, favouring the stable twist forms. Observations in experiments and simulations [43] have found a prevalence of twist loops and it is natural to speculate that the active dynamics we have described may contribute to explaining this. In the

absence of chirality (as in our analysis) one expects equal numbers of right- and left-handed twist loops, although statistics for this from experiment or simulation are not currently available. However, as the biopolymers that go into active nematics are chiral it is possible there will be an imbalance in the proportion the two types.

4.3 Active flows

We now determine the far-field structure of the fluid flows generated by defect loops and show that they confirm the self-dynamics described above. To do so, we adopt the strategy of seeking a solution of the Stokes equations with active nematic force term given by the director field of a defect loop [44]. These are $\nabla \cdot \mathbf{u} = 0$ and

$$-\nabla p + \mu \nabla^2 \mathbf{u} = \zeta \nabla \cdot (\mathbf{nn}) = \frac{\zeta}{4} \big[\mathbf{e}_x \, \partial_z + \mathbf{e}_z \, \partial_x \big] \omega, \tag{4.34}$$

taking the linearised form of the active stresses. We seek solutions with $\mathbf{u}$ tending to zero and p tending to a constant for large r. No boundary condition is imposed at short distances, although a more complete approach would involve a matched asymptotics with the solution in [44]. The multipole expansion for the solid angle (4.24) is given in terms of derivatives of the generating monopole $1/r$ and the resulting flow is therefore the same derivatives of the fundamental flow in response to this monopole, which provides a convenient representation for the solution, as laid out in the previous chapter,

$$p = \frac{\zeta}{4} \left(\pi a_0^2 \nabla_{\mathbf{d}_3} + \frac{\pi a_0^4 \tau_0}{6} \nabla_{\mathbf{d}_1} \nabla_{\mathbf{d}_2} + \cdots \right) \frac{xz}{r^3}, \tag{4.35}$$

$$\begin{aligned} \mathbf{u} = \frac{\zeta}{16\mu} & \left(\pi a_0^2 \nabla_{\mathbf{d}_3} + \frac{\pi a_0^4 \tau_0}{6} \nabla_{\mathbf{d}_1} \nabla_{\mathbf{d}_2} + \cdots \right) \\ & \times \left\{ \mathbf{e}_x \left[\frac{z}{r} + \frac{x^2 z}{r^3} \right] + \mathbf{e}_y \, \frac{xyz}{r^3} + \mathbf{e}_z \left[\frac{x}{r} + \frac{xz^2}{r^3} \right] \right\}. \end{aligned} \tag{4.36}$$

We remark that the fundamental solution – the part in curly braces in (4.36) – does not decay with distance; this is the active flow that would result from a localised (monopole) reorientation of the director field in an otherwise uniformly aligned nematic and the non-decay may be viewed as a signature of the fundamental instability of active nematics [25]. The flow generated by a defect loop does decay but only slowly, with the leading dipole contribution falling off as $1/r$. These flows are shown in Figure 4.3 for splay, bend and twist type loops. For the splay and bend loops there is a clear directed flow, consistent both with the non-zero force (4.28) and with the global self-propulsion of

these loops found previously [44]. The bottom row of Figure 4.3 shows the quadrupole contributions to the flow; again, for the splay and bend loops there is a rotational character consistent with the non-zero torque (4.31) and indicating a corresponding rotation of the defect loop. The flow generated by the stable twist loop, Figure 4.3(c), is predominantly extensional in the xz-plane of the director and shows neither a directed nor a rotational component. In each Cartesian plane the flow is normal to the plane and with an alternating sign in each quadrant. In the xz-plane this amounts to the buckling flow found in [44]. Along the x- and z-axes the flow shows local circulations, while along the y-axis it has a hyperbolic structure.

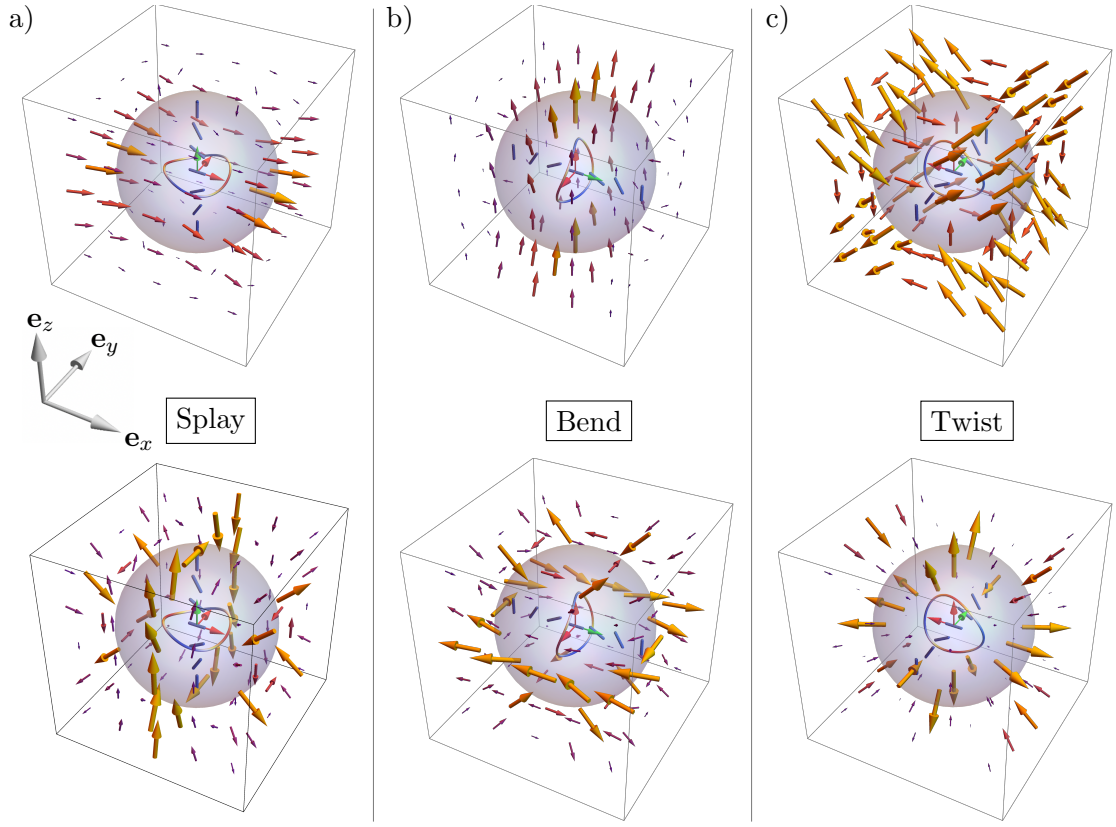

Figure 4.3: The asymptotic flows induced by defect loops. The dipole contribution for each defect loop geometry is shown in the top row, with the quadrupole flows shown below. For splay (a) and bend (b) loops the dipole and quadrupole flows show directed and rotational flows respectively, corresponding to the net active forces and torques experienced by the defect loops. (c) A stably-oriented right-handed twist loop. The stability of this configuration is reflected by the lack of propulsive or rotational flows; the dipole flow is predominantly extensional as described in the text.

By considering a generic perturbation of a defect loop the analysis in this chapter reveals the connection between non-planarity and active self-rotation, a dynamical feature that was not apparent from the results of [44] as it only considered planar loops. The multipole flow captures the global self-propulsion and rotation; however, it does not reproduce the detailed variation in local self-propulsion velocity at each point of the loop associated with the varying director profile [44]. This suggests that a matched asymptotics between the multipole and local calculations may yield a more complete analysis. Such an approach should also allow for the back effects of active stresses and flows on the shape of the defect loop (size a_0 and torsion τ_0) to be included, for instance through an overdamped curve dynamics.

The slow decay ($\sim 1/r$) of the active flows generated by defect loops suggests that hydrodynamic interactions may be particularly strong and important. The strength can be compared with the elastic dipole-dipole interactions mediated by the director field [181], which fall off more rapidly as $1/r^3$. The leading character of the hydrodynamic interactions is that each loop is advected and rotated by the flow(s) generated by the other(s). As an example, we consider qualitatively the advective interactions between stable twist loops ($\mathbf{d}_3 = \pm\mathbf{e}_y$). The dipole part of the flow (4.36) is even under $\mathbf{x} \to -\mathbf{x}$ and has different signs for the right- and left-handed loops. As a result, two twist loops of the same handedness advect each other with the same velocity, creating a collective motility reminiscent of that for pairs of scallops or dumbbells [254; 253]. In contrast, two loops with opposite handedness advect each other with equal but opposite velocities. The integral curves of the dipole part of (4.36) form closed loops that do not visit the origin, suggesting that this contribution to the hydrodynamic interaction may lead to a periodic motion of two loops of opposite handedness – a type of 'waltzing' – rather than simple attraction or repulsion, although it is likely that the actual dynamics will be far less regular than this heuristic picture and may be significantly affected by any large scale turbulence.

We conclude our discussion of defect loop hydrodynamics with an intriguing consequence for global nematic topology. Consider a pair of defect loops that form a Hopf link. There are two distinct compatible textures, corresponding to giving the loops a circulation in the same or opposing direction [75; 178]. These circulations relate to the dipole vector via the right-hand rule and, within our linear description, result in the two textures inducing active propulsion in perpendicular directions. While this prediction is not likely to be testable experimentally, it does provide a striking example of the ramifications topology can have for active dynamics.

4.4 Discussion

We have provided a global description of nematic defect loops in terms of a multipole decomposition of the director field. This complements the previous local analysis [44] and also shows the importance of non-planarity of defect loops in leading to net active torques. We find that twist loops are the only geometry with vanishing force and torque, providing a possible explanation of their preponderance in active nematics [43]. There are many immediate directions for development, including extending the analysis to more general shapes of defect loops, or multiple loops, and connecting this global description with the local analysis of [44] to incorporate the change in internal structure, or shape, of the defect loop to potentially develop a form of matched asymptotics. Also of interest will be to consider defect loops with non-zero topological charge and in confinement [62], and the effects of chiral active stresses [265].

'Here is an ordinary square.'
'Woah, woah, slow down egghead!'

Professor Frink explaining the cube (or 'Frinkahedron') to Chief Wiggum, The Simpsons, S07E06, Homer[3]

5

Polygonal Colloids in Two-Dimensional Nematics

Although the generation of defects due to colloidal inclusions is topological in origin, with the total charge of the defects compensating the degree of the director boundary condition on the surface of the colloid, the way in which this is realised is determined by the colloidal geometry. There is a great richness in the distortions that can arise even from genus 0 colloids, allowing specific deformations to be selected through appropriate variation of the colloidal shape. As discussed in Section 2.5 this has profound consequences for the elastic interactions between colloids and the behaviour of the colloidal nematic system and this, along with recent techniques allowing the production of intricately shaped colloids [266] makes this area ripe with potential. Better understanding the relationship between colloidal shape and the induced nematic distortion will open up new avenues for the design of soft metamaterials and photonic crystals [193]. In light of our results in Chapter 3 we are also motivated to understand how we might achieve geometric control of self-propulsive and rotational deformations and realise a nematic analogue of the bacterial ratchets. In service of these twin aims we shall, in this chapter, track a course through polygonal colloidal geometry from the square to the Koch fractal [266; 267].

Such shape-dependency of distortions has been realised through the use of 'gourd' colloids to induce high-order multipoles [186], tuning the equilibrium orientation of el-

lipsoids through variation of their aspect ratio [268; 269] and using spherocylindrical colloids to determine the form of ring defects [270]. A particularly effective route is to use sharp edges and vertices to determine the placement of topological defects since there is an energetic benefit in the nematic melting to the isotropic phase at the locations where the greatest director distortion would be required [271]. This has been exploited to control the equilibrium orientation, pair-wise interactions or tilings of truncated polygonal pyramids [272; 273], cylinders [274; 275], microbullets [275], cubes [275; 276], concave and convex polygonal prisms [277] and spirals [278].

Our focus in this chapter is on polygonal colloids in two-dimensional nematics. Of key importance in this context is the 2009 experimental study of the distortions induced by lithographically fabricated regular polygonal platelets [279]. This showed that the nature of the distortion was dependent on the number of sides of the polygon, being dipolar for odd-sided polygons and quadrupolar for even-sided ones, as illustrated in Figure 5.1(a)-(d). Numerical simulation of polygonal platelets in thin three-dimensional nematics confirmed these results and also demonstrated the impact this has on colloidal assembly into chains and lattices [280]. The lattices formed by pentagons are particularly intricate due to the voids that arise [280] and these can be used to form quasicrystalline Penrose tilings [281; 282], shown in Figure 5.1(e). The effects on concavity were investigated via simulations of stars formed of radial arms, with a similar odd-even effect arising and distinct ground and metastable states being observed [283], as shown in Figure 5.1(f)-(k). A particularly striking example of the richness of distortions that can arise from genus 0 colloids is provided by iterations of the Koch snowflake fractal [267]. Experiments and numerical simulations, shown in Figure 5.1(l) and (m) respectively, demonstrated a proliferation of topological defects that was exponential in the iteration of the fractal [266].

In this chapter we provide an analytical description for the distortions of a two-dimensional nematic due to polygonal colloids. Such deformations are captured by harmonic functions and our restriction to two dimensions allows us to construct these through the use of conformal maps from the circle to the boundary of the colloid. The use of conformal maps in physics is wide ranging; they are of relevance whenever Laplace's equation is being solved in a two-dimensional domain. Liquid crystalline examples include the modelling of both passive [121] and active [164] nematics on the sphere via stereographic projection but conformal symmetries also underpin the description of critical phenomena in statistical mechanics [285] and have been used to posit a cyclic model of the history of the universe [286]. Central to the latter two examples is that conformal mappings do not preserve lengths, only angles, as illustrated beautifully in much

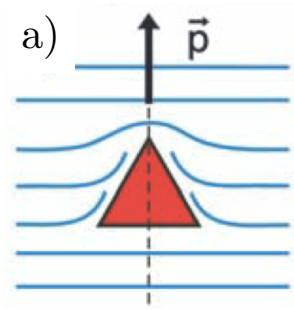
a)
$\vec{p}$

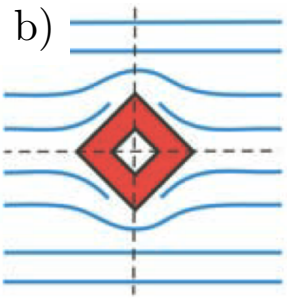
b)

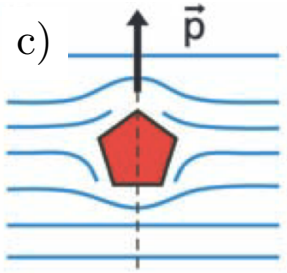
c)
$\vec{p}$

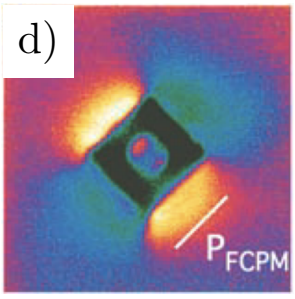
d)
P_{FCPM}

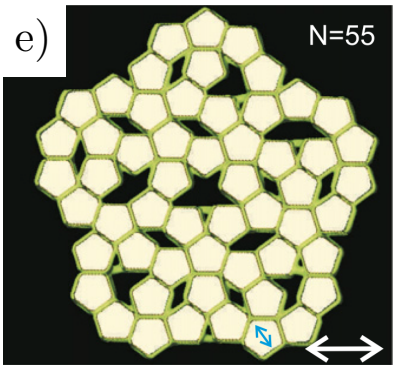
e)
N=55

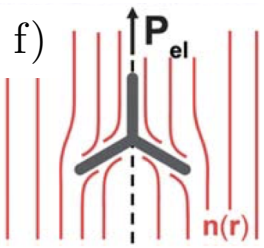
f)
P_{el}
n(r)

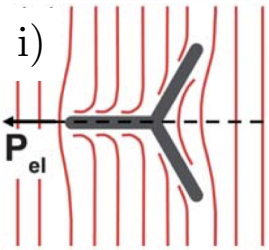
i)
P_{el}

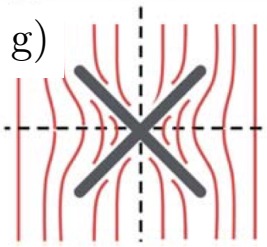
g)

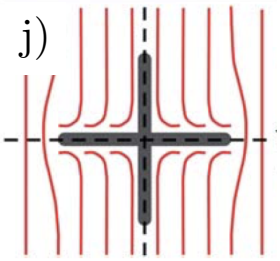
j)

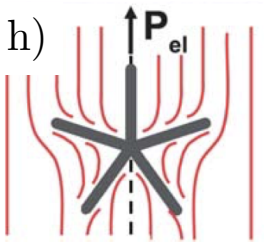
h)
P_{el}

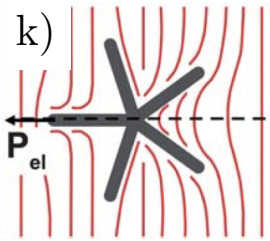
k)
P_{el}

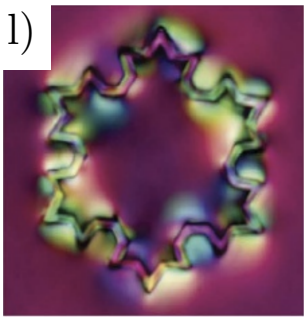
l)

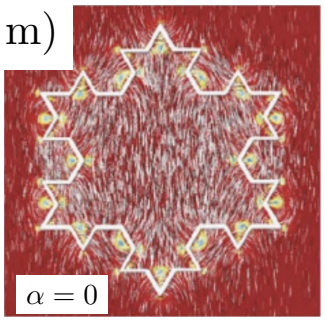
m)
$\alpha = 0$

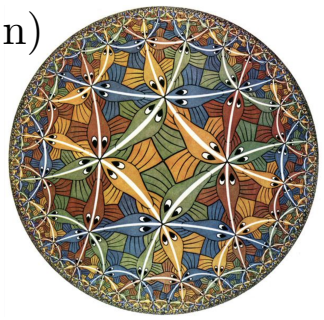
n)

of the artwork of M.C. Escher [287; 288], see Figure 5.1(n). We will employ a particular class of conformal transformation known as Schwarz-Christoffel maps [289], which are particularly well-suited for providing maps to polygonal domains. There has been some prior use of these mappings in describing nematics, for example in characterising the textures that arise due to a sawtooth substrate [290], or on the interior of regular polygons [291], with some of these applications reviewed in [292]. More broadly they may be utilised to address problems of potential flow, as laid out in Lamb's classic text on hydrodynamics [293]. A distinction between describing the nematic director in the interior of a polygonal boundary compared to on the exterior of a polygonal colloidal is that in the former case specification of the boundary condition requires knowledge of the charges and locations of all topological defects, whereas in the latter we may assume a defect-free bulk, as justified by experiments [279; 266] and simulations [280; 283].

Having set up the necessary machinery, we begin with calculating the nematic distortions due to regular polygons. This enables us to quantify their experimental description and will form the basis for our subsequent investigations. We follow this with a modified form of star polygons that allow the effects of concavity to be tuned. Next we investigate the behaviour of chiral cog-shaped colloids and find that depending on

Figure 5.1 *(preceding page)*: Shape-controlled nematic distortions with polygonal colloids. (a), (b) and (c) Schematic representations of experimentally observed distortions induced by polygons in 5CB with tangential anchoring, with the dashed lines denoting the mirror lines of the director. (a) and (c) Polygons with an odd number of sides align with one side parallel to the far-field alignment, $\mathbf{n}_0$, and induce a dipole moment perpendicular to $\mathbf{n}_0$. The square in (b) aligns with one of its diagonals along $\mathbf{n}_0$ and induces a quadrupole distortion. From [279]. These schematics for the director orientation are inferred from measurements of fluorescent confocal polarising microscopy, as shown for the square colloid in (d). From [279]. (e) A quasicrystalline tiling formed in a nematic from 55 pentagonal colloids, from [281]. (f) - (k) Schematics of the director distortion for star colloids in their ground state ((f), (g) and (h)) and metastable orientation ((i), (j) and (k)). The dashed lines indicate mirror lines of the nematic director and the arrows denote the elastic dipole for stars with an odd number of arms. From [283]. (l) and (m) A colloid with the shape of the second iteration of the Koch fractal in a nematic with vertical far-field alignment. The experimental image in (l) shows the system viewed through crossed polarisers, (m) shows the result of Landau-de Gennes numerical simulation with the location of topological defects highlighted. (n) M.C. Escher's Circle Limit III highlights the conformal symmetry used in this chapter. It is based on a conformal map of a $(6, 4, 2)$ tessellation of the hyperbolic plane. The angles at which the fish meet is invariant, even as the fish themselves shrink ever smaller towards the boundary. From [284].

the parameters of the cog the chiral quadrupole can display either subtle orientation-dependency or have a consistent sign as the cog is rotated, allowing the engineering of active nematic ratchets. Lastly we apply the techniques we develop to design colloids capable of producing arbitrarily high-order multipoles as the dominant director distortion.

5.1 The Dirichlet problem and conformal mapping

From applying the Euler-Lagrange equations to the Frank free energy with one elastic constant, we see that in an energy minimising nematic texture the director angle ϕ should be a harmonic function, which is uniquely determined by the boundary conditions. In our problem we have Dirichlet conditions on the surface on the polygon and an asymptotic value for the director angle provided by the far-field alignment. It is inconvenient to solve this Dirichlet problem on the exterior of the polygon. However if we have an analytic map $f : z \to \zeta$ taking a domain Ω onto another domain Ω' then a function $\phi(z)$ solving the problem in Ω will provide $\phi(f(z))$ which solves the analogous problem in Ω'. This can be confirmed directly through application of the chain rule

$$\begin{aligned} \partial_{\bar{z}}\partial_z\phi(f(z)) &= \partial_{\bar{z}}\left[\partial_z\zeta\partial_\zeta\phi(\zeta)\right] \\ &= \left(\partial_{\bar{z}}\partial_z\zeta\right)\partial_z\phi(\zeta) + \partial_{\bar{z}}\bar{\zeta}\partial_z\zeta\partial_{\bar{\zeta}}\partial_\zeta\phi(\zeta). \end{aligned} \tag{5.1}$$

As ζ is an analytic function the first term vanishes, leaving us with the result

$$\partial_{\bar{z}}\partial_z\phi(f(z)) = |\partial_z\zeta|^2\partial_{\bar{\zeta}}\partial_\zeta\phi(\zeta). \tag{5.2}$$

These analytic or holomorphic maps possess the striking property of being conformal, that is they leave angles unchanged (or are isogonal) and preserve orientations. This is most readily seen by means of a Taylor expansion

$$f(z) = f(z_0) + (z - z_0)\frac{\mathrm{d}f}{\mathrm{d}z} + \ldots, \tag{5.3}$$

from which we see that the effect of the mapping on the local neighbourhood of z_0 is scaling and rotation by the complex number $\frac{\mathrm{d}f}{\mathrm{d}z}$. Indeed not only are all holomorphic maps conformal but the converse is also true, all conformal maps are provided by holomorphic functions. Their antiholomorphic counterparts, functions only of $\bar{z}$, correspond to mappings which preserve angles but reverse orientation.

5.1.1 The Riemann mapping theorem

The existence of such conformal maps is guaranteed by the Riemann mapping theorem. This states that for Ω, Ω' non-empty simply connected subsets of $\mathbb{C}$, neither of which is the whole of $\mathbb{C}$, there exists a three-parameter family of biholomorphic mappings $f : \Omega \to \Omega'$ [294; 295]. As the holomorphicity of maps is maintained in composition we can construct all desired maps via maps from the disc D. With $f_1 : D \to \Omega$ and $f_2 : D \to \Omega'$, we have $f_2 \circ f_1^{-1} : \Omega \to \Omega'$. Viewed this way the aforementioned three degrees of freedom reveal themselves as the three parameters of automorphisms of the disc, described by the Möbius transformations [296].

A physical argument for this statement is provided by the very problem we are addressing in this chapter. Consider two nematic systems, each containing a simply connected colloid with normal anchoring, a defect-free bulk and a consistent far-field alignment. The nematic textures that result from minimising the energy subject to these constraints will have a harmonic angle function the contours of which, along with those of the harmonic conjugate, form an orthogonal grid filling the domain. By appropriately associating these grids we can construct a conformal map between the domains. The three parameters of such maps arise as the freedom to choose the difference in far-field alignment between the two systems and which point in the bulk of one system is mapped to infinity in the other. Similar reasoning can be made in the context of fluid flow [296] and electrostatics [67]. Though such arguments are appealing, and indeed in the spirit of the one put forward by Riemann in his own PhD thesis [297], they are flawed due to presupposing a solution to the Dirichlet problem, an error that was identified by Weierstrass [298]. The fallibility of our physical intuition notwithstanding, the result holds and so we content ourselves with the knowledge that it has been subsequently proven, first by Osgood in 1900 [299] and subsequently by Carathéodory [300] and Koebe, the essence of whose proof is contained in the account of Hilbert [301]. A history of the theorem is provided in [302; 303] and a modern revisiting of Riemann's idea can be found in [304].

We can therefore separate our problem into two parts, finding conformal maps from the exterior of the disc onto the exterior of our colloid and solving the analogous Dirichlet problem for the director angle on the exterior of the disc.

5.1.2 The Dirichlet problem on the disc

The problem at hand amounts to the solving of

$$\partial_{\bar{z}}\partial_z\phi(z,\bar{z}) = 0 \tag{5.4}$$

subject to the boundary conditions

$$\begin{aligned} \phi = f(\theta) : S^1 \to \mathbb{R} \text{ for } |z| = 1, \\ \phi \to 0 \text{ as } z \to \infty. \end{aligned} \tag{5.5}$$

The generic solution of (5.4) consists of a holomorphic and antiholomorphic part

$$\phi(z,\bar{z}) = \phi_1(z) + \phi_2(\bar{z}). \tag{5.6}$$

Performing a Fourier expansion of the boundary condition we have

$$f(\theta) = \sum_{n\in\mathbb{Z}} a_n \mathrm{e}^{\mathrm{i}n\theta} = a_0 \frac{\log(|z|/R)}{\log(1/R)}\Big|_{|z|=1} + \sum_{n=1}^{\infty} a_n \bar{z}^{-n}\Big|_{|z|=1} + \sum_{n=1}^{\infty} a_{-n} z^{-n}\Big|_{|z|=1}. \tag{5.7}$$

Having expressed $f(\theta)$ in terms of negative powers of z and $\bar{z}$ we can readily extend this to a regular function on the whole disc exterior as

$$\phi(z,\bar{z}) = a_0 \frac{\log(|z|/R)}{\log(1/R)} + \sum_{n=1}^{\infty} (a_n \bar{z}^{-n} + a_{-n} z^{-n}). \tag{5.8}$$

We now give consideration to certain boundary value problems for which the dominant far-field distortion is dipolar or quadrupolar. These will provide insight into the distortions induced by polygonal colloids that we shall come to later.

Firstly, taking $\theta \in (-\pi, \pi)$ and $f(\theta) = \theta$ we find

$$a_n = \begin{cases} 0 & \text{if } n = 0 \\ \frac{\mathrm{i}}{n} & \text{if } n \neq 0 \end{cases}, \tag{5.9}$$

giving

$$\phi(z,\bar{z}) = \mathrm{i} \sum_{n=1}^{\infty} \frac{1}{n} (\bar{z}^{-n} - z^{-n}). \tag{5.10}$$

The boundary condition consists of a linear increase of ϕ with θ and a discontinuous drop by 2π. The latter results from passing through a charge -2 defect. The former is

associated with positive winding at the origin and so, invoking charge neutrality, we may conclude that there is a +2 defect there. In this way we are able to reason directly from the boundary condition to the standard UPenn dipole configuration [181], as shown in the top-left panel of Figure 5.2. Indeed this can be confirmed directly by setting

$$\begin{aligned}\phi(z,\bar{z}) &= \mathrm{Im}\left\{\log\left(\frac{z^2}{(z-1)^2}\right)\right\} \\ &= \mathrm{i}\left[\log\left(1-\frac{1}{z}\right)-\log\left(1-\frac{1}{\bar{z}}\right)\right]\end{aligned} \tag{5.11}$$

which, upon Taylor expansion, yields (5.10). We can generate solutions with arbitrary anchoring angle by noting that the transformation $f(\theta) \to f(\theta+\alpha)$, for some constant α, rotates the location of the surface defect clockwise by α while rotating the director anchoring anticlockwise the same amount, as illustrated along the top row of Figure 5.2. This corresponds to the substitution $z \to e^{i\alpha}z$ in (5.10), meaning the dipole character rotates commensurately with the defect, being vertical for normal anchoring when $\alpha = 0$ and horizontal for tangential anchoring when $\alpha = \pi/2$. As the nematic director is invariant to rotations by π there are two distinct energy minimisers for these equivalent boundary conditions in which the defect sits at antipodal points.

To transition from a dipole-dominated distortion to a quadrupole-dominated one we must introduce additional defects by reversing the direction of the director along sections of the boundary. The boundary condition

$$f(\theta) = \begin{cases} \theta+\pi & \text{if } -\pi \le \theta \le -\pi+\theta_{\mathrm{d}}, \\ \theta & \text{if } -\pi+\theta_{\mathrm{d}} \le \theta \le \pi-\theta_{\mathrm{d}}, \\ \theta-\pi & \text{if } \pi-\theta_{\mathrm{d}} \le \theta \le \pi, \end{cases} \tag{5.12}$$

splits the -2 point defect into two -1 defects with an opening angle of θ_{d}, giving

$$\phi(z,\bar{z}) = \mathrm{i}\sum_{n=1}^{\infty}\frac{(-1)^{n+1}}{n}\cos(n\theta_{\mathrm{d}})(z^{-n}-\bar{z}^{-n}). \tag{5.13}$$

The correspondence between the boundary condition and the defect configuration can be inferred via the same reasoning as for the dipole case and may be confirmed directly

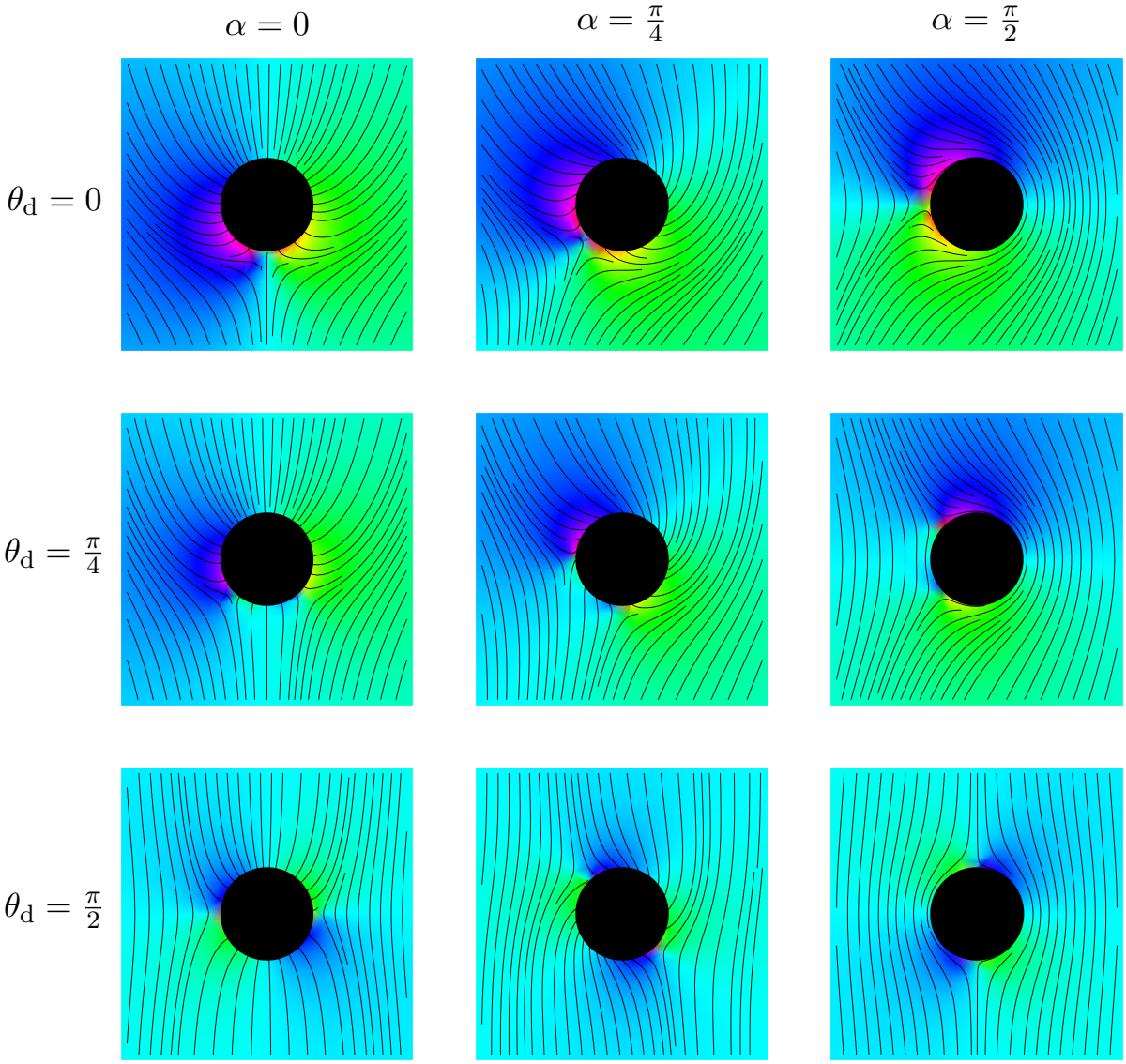

Figure 5.2: A two-dimensional nematic with varying anchoring conditions on a disc. The integral curves of the director are shown superposed on the phase field of its angle. As the director anchoring condition is changed from normal ($\alpha = 0$, left column) to tangential ($\alpha = \pi/2$, right column) the surface defects rotate around the disc commensurately but in the opposite sense. Also shown is the opening up of the -2 surface defect present in a dipole distortion (top row) into a pair of -1 defects with opening angle θ_d. When $\theta_\mathrm{d} = \pi/2$ the distortion is dominated by a quadrupole term (bottom row). The dipole character varies commensurately with the defect rotation, being vertical for normal anchoring ($\alpha = 0$) and horizontal for tangential anchoring ($\alpha = \pi/2$). The quadrupole character changes at twice this rate; it is achiral for normal anchoring, purely chiral for $\alpha = \pi/4$ and achiral but with reversed sign for tangential anchoring.

by comparison with

$$\begin{aligned}\phi(z,\bar{z}) &= \mathrm{Im}\left\{\log\left(\frac{z^2}{(z-e^{\mathrm{i}\theta_\mathrm{d}})(z-e^{-\mathrm{i}\theta_\mathrm{d}})}\right)\right\} \\ &= \frac{\mathrm{i}}{2}\left[\log\left(1-\frac{2\cos\theta_\mathrm{d}}{z}+\frac{1}{z^2}\right)-\log\left(1-\frac{2\cos\theta_\mathrm{d}}{\bar{z}}+\frac{1}{\bar{z}^2}\right)\right].\end{aligned} \tag{5.14}$$

When $\theta_\mathrm{d}=0$ (5.13) reduces to the previous dipole expression given in (5.10) and in general causes a reduction of the dipole term as shown in Figure 5.2. Once again we generate energy minimisers for generic anchoring via $f(\theta)\to f(\theta+\alpha)$, resulting in commensurate but opposing rotation of the surface defects and the director at the boundary, shown in the middle row of Figure 5.2. Of particular relevance is the case $\theta_\mathrm{d}=\pi/2$, for which the -1 defects sit at antipodal points and the dipole term vanishes, with (5.13) becoming

$$\phi(z,\bar{z}) = \mathrm{i}\sum_{n=1}^{\infty}\frac{(-1)^m}{2m}(\bar{z}^{-2m}-z^{-2m}), \tag{5.15}$$

this being the Saturn ring configuration [181], with the corresponding director distortions shown in the bottom row of Figure 5.2. The quadrupole character changes at twice the rate of the rotation of the defects; it is purely achiral for both normal and tangential anchoring, although with opposing sign and is purely chiral for $\alpha=\pi/4$.

These calculations show that in principle any dipole or quadrupole can be induced by controlling the anchoring conditions on the disc, solving the matter of inducing all the self-propulsive and rotational active responses that we described previously in Chapter 3, at least in two dimensions. However, we should emphasise that we have simply presented solutions to certain boundary value problems and there is no guarantee *a priori* that these will arise as the equilibrium state of a nematic system. The nature of the equilibrium distortion is affected by the type and strength of surface anchoring as well as the colloidal size [176]. In particular the configurations with generic opening angle shown in Figure 5.2(d)-(f) are never stable and for tangential anchoring only the quadrupole distortion in panel (f) is observed [176]. We should therefore not let this apparent resolution dissuade us from our polygonal inclusions and instead view these distortions as templates to inform our understanding of those induced by polygons. The investment we have made in describing the distortions around a disc will be justified by them serving as a 'classical limit' for the discretised polygonal distortions that follow.

This concludes the ideas which underpin the work of this chapter; the remainder of this section is devoted to the technicalities of their implementation. As such it is not needed in order to understand the results that follow and can be passed over on a first

reading.

5.1.3 Schwarz-Christoffel maps

For all its power the Riemann mapping theorem is not constructive. For explicit mappings we turn to the formulation introduced and developed in a series of papers by Christoffel [305; 306; 307; 308] beginning in 1867 and two years later, though independently, by Schwarz [309; 310; 311]. In a slight inversion of history these mappings are known as Schwarz-Christoffel transformations. An excellent review of their development, theory and applications can be found in the monograph by Driscoll and Trefethen [289]. Schwarz-Christoffel transformations are predicated on the notion that the desired mapping has a derivative expressible as the product of some set of canonical functions, that is [289]

$$f'(z) = \prod f_k(z). \tag{5.16}$$

It naturally follows that $\arg f' = \Sigma \arg f_k$ and so by choosing the f_k appropriately such that each is a step function we can contrive to make $\arg f'$ a piecewise constant function with prescribed jumps and hence map the real axis to a polygon. This faculty for producing conformal maps to polygons, along with the rich variety of nematic distortions they can induce, is why we focus on colloids of this form. Through additional modifications we can generate our desired transformations from the exterior of the disc to the exterior of polygons.

To make this precise, let us begin by setting out our notion for polygons. We define a polygonal colloid through a piecewise linear curve Γ comprised of n vertices $\zeta_1, \ldots, \zeta_n$ and bounding an interior region P, see the example in Figure 5.3. The vertices have interior angles $\mu_1\pi, \ldots, \mu_n\pi$. The corresponding exterior angles are $\nu_k\pi$, with $\nu_k = 1 - \mu_k$, and for Γ to form a closed curve we require $\sum_k \nu_k = 2$.

To determine the form of $f_k(z)$ in (5.16) we note that $(z - z_k)^{-\nu_k}$ has a constant argument on $\mathbb{R}$ save for a jump of $\nu_k\pi$ at z_k and is analytic in the upper half-plane H^+. It follows that a conformal transformation that maps $\mathbb{R}$ onto Γ and H^+ onto P is provided by

$$f(z) = A + C \int^z \prod_{k=1}^{n} (z' - z_k)^{-\nu_k} \mathrm{d}z'. \tag{5.17}$$

The z_k are the prevertices, preimages of the vertices under the map such that $\zeta_k = f(z_k)$. That these prevertices are well-defined is a consequence of the Carathéodory–Osgood theorem [289; 312]. The complex constants A and C allow for scaling, translation and rotation of the image. Together with the prevertices they form a set of parameters which

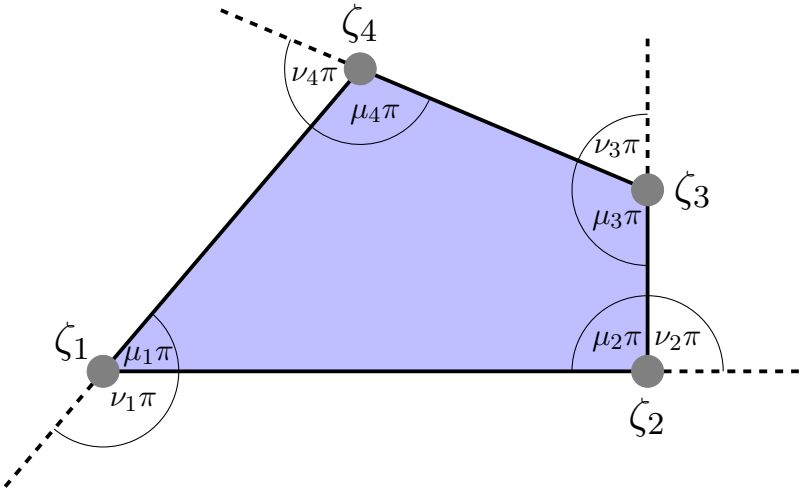

Figure 5.3: The notation for labelling polygons. The vertices ζ_i have interior angles $\mu_i\pi$ and exterior angles $\nu_i\pi$, with $\nu_i = 1 - \mu_i$.

are overdetermined to the tune of the three degrees of freedom inherent in Riemann's mapping theorem. The lower limit of integration is left unspecified as it only provides a constant that may be absorbed into A.

The proof that (5.17) truly is an analytic function as required goes as follows [289; 313]. By the Schwarz reflection principle [296] we may analytically continue f across $\mathbb{R}$ into the lower half-plane, H^-, as shown in Figure 5.4. The image of this continuation is found by reflecting P in one of the sides of Γ. Returning to the upper half-plane we reflect about a side of the new polygon, so that each branch of f in H^+ corresponds to an even number of such reflections. This results in the translation and rotation of P meaning each branch of f has the form $c_1 f + c_2$, for c_1 and c_2 complex constants. It follows that f''/f' is analytic in H^+, save perhaps at the prevertices of Γ. Indeed, we argued previously that in the neighbourhood of z_k we have $f' = (z - z_k)^{-\nu_k}$, up to multiplication by some analytic function and so f''/f' has a simple pole at z_k with residue $-\nu_k$. This can be regularised by subtraction of the appropriate pole and doing so for all prevertices leaves

$$\mathcal{F}(z) = \frac{f''(z)}{f'(z)} - \sum_k \frac{\nu_k}{z - z_k} \tag{5.18}$$

as an entire function. As all the prevertices are finite f is analytic at $z = \infty$ and a Laurent expansion shows that $f''/f' \to 0$ as $z \to \infty$. The same is clearly also true for $\nu_k/(z - z_k)$ and so by Liouville's theorem $\mathcal{F}(z)$ is constant and, as it vanishes at $z = \infty$

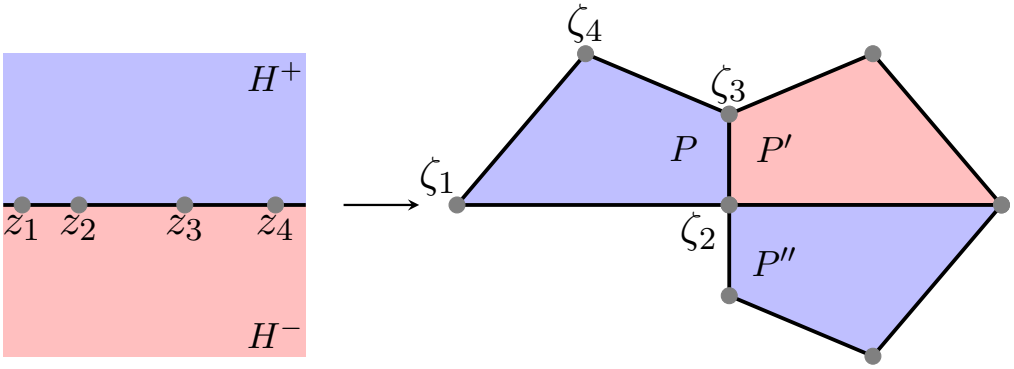

Figure 5.4: The argument for analyticity of the Schwarz-Christoffel map. The function in (5.17) takes the prevertices z_i to the vertices ζ_i and the upper half-plane H^+ to the polygon P. Successive reflection in edges of the image polygon gives branches of (5.17) on H^- or H^+, as indicated by the colour of the polygon, and shows that all branches are related by a translation and a rotation.

must be zero everywhere. Writing f''/f' as $(\log f')'$ and integrating produces (5.17).

There are two modifications we must make to (5.17) that we now consider in turn. The first is to change the domain of the map from the upper half-plane to the unit disc, D. This is achieved by composition of maps and application of the chain rule. For $h(z) : H^+ \to P$ and $g(z) : \Sigma \to H^+$ we have $f(z) = h(g(z)) : \Sigma \to P$ with [289]

$$\begin{aligned} f'(z) &= h'(g(z))g'(z) \\ &= Cg'(z)\prod_k [g(z) - g(z_k)]^{-\nu_k}\,. \end{aligned} \tag{5.19}$$

A map from the disc to the upper half-plane is provided by the Möbius transformation $g(z) = \mathrm{i}\frac{1+z}{1-z}$, giving

$$f'(z) = C\frac{2\mathrm{i}}{(1-z)^2}\prod_k \left[\frac{2\mathrm{i}(z-z_k)}{(1-z)(1-z_k)}\right]^{-\nu_k}. \tag{5.20}$$

Using that $\sum_k \nu_k = 2$ and absorbing various constants into C we integrate to obtain

$$f : D \to P, \qquad f(z) = A + C\int^z \prod_k \left(1 - \frac{z'}{z_k}\right)^{-\nu_k} \mathrm{d}z'. \tag{5.21}$$

Next we must consider mapping to the exterior region P'. The first change that this necessitates is reversing the sign of the exterior angles. In the same manner as before

this leads us to

$$\mathcal{F}(z) = \frac{f''(z)}{f'(z)} - \sum_k \frac{\nu_k}{z - z_k} \tag{5.22}$$

as an entire function. The difference now is that since the image of f contains the point at infinity it no longer follows that $\mathcal{F}(z)$ is constant. Taking $f(0) = \infty$ implies that f has a simple pole there and so at the origin $f''/f' = -2/z$ plus some analytic part. We therefore modify (5.22) to give

$$\mathcal{F}_2(z) = \frac{f''(z)}{f'(z)} - \sum_k \frac{\nu_k}{z - z_k} + \frac{2}{z} = 0. \tag{5.23}$$

Integrating we find

$$f : D \to P', \qquad f(z) = A + C \int^z z'^{-2} \prod_k \left(1 - \frac{z'}{z_k}\right)^{\nu_k} \mathrm{d}z'. \tag{5.24}$$

Finally, we may make the replacement $z \to 1/z$ in (5.24) to attain our desired conformal map from the exterior of the disc to the exterior of the polygon. With this general expression in our possession we now present the derivation of certain particular mappings that we shall make use of.

Despite its apparently explicit nature the Schwarz-Christoffel integral in (5.24) requires determination of the prevertices. This 'parameter problem' is highly non-linear and typically computationally expensive to solve [289]. In this chapter we primarily focus on polygons which are sufficiently symmetric as to constrain the locations of the prevertices. Here we derive mappings for three forms of polygon, namely regular polygons, star polygons and cog polygons, representative examples of which are shown in Figure 5.5 along with the notation that we employ. Those mappings for which the integral does not reduce to a closed form we do not present here but rather treat as they arise.

Regular polygons

In the case of regular polygons all exterior angles are $2/n$ and symmetry allows the prevertices to be taken as the n^{th} roots of unity and indeed to be fixed points of the map. Due to the cyclic nature of the roots of unity the product in the integrand of (5.24) reduces to $(1-t^n)^{2/n}$. In addition we can set $A = 0$ and determine C by requiring

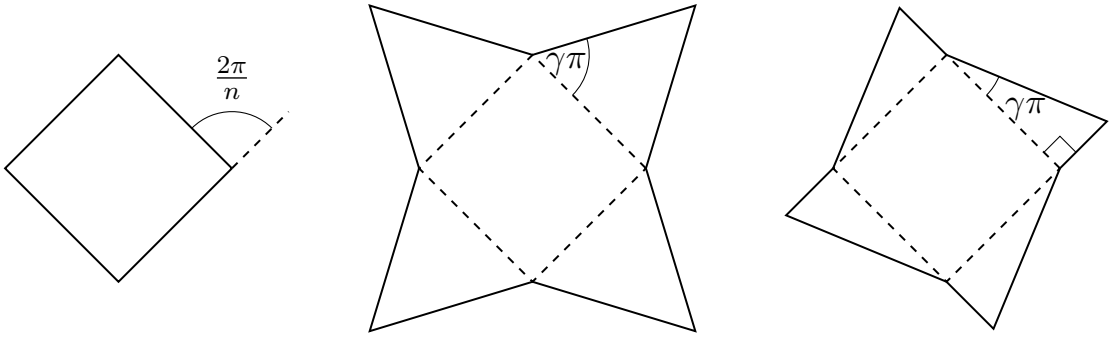

Figure 5.5: Representative examples of some of the families of polygonal colloids considered in this thesis. From left to right: regular polygons with exterior angle $2\pi/n$, star polygons and cog polygons formed by attaching isosceles and right-angled triangles respectively to each side of a regular polygon.

$f(1) = 1$ such that

$$f(z) = \frac{\int^z z'^{-2}(1 - z'^n)^{\frac{2}{n}} \mathrm{d}z'}{\int^1 z'^{-2}(1 - z'^n)^{\frac{2}{n}} \mathrm{d}z'}. \tag{5.25}$$

Making the transformation $t = z'^n/z^n$ brings the numerator to

$$\frac{1}{nz} \int^1 t^{-\frac{1}{n}-1} (1 - z^n t)^{\frac{2}{n}} \, \mathrm{d}t. \tag{5.26}$$

This has the form of Euler's integral representation of the hypergeometric function [314, Eq. 15.3.1]

$${}_2F_1(a, b; c; x) = \frac{1}{B(b, c-b)} \int_0^1 t^{b-1}(1-t)^{c-b-1}(1-xt)^{-a}\mathrm{d}t, \tag{5.27}$$

with the beta function $B(u, v) = \frac{\Gamma(u)\Gamma(v)}{\Gamma(u+v)}$ [314, Eq. 6.2.2]. However this integral is only applicable for $\Re c > \Re b > 0$ and comparing (5.26) and (5.27) we have $b = -1/n < 0$. The singularity at $t = 0$ can be handled through various adaptations of the integration contour, such as changing the lower limit to 0^+ [315, Eq. 15.6.4]. In light of the arbitrary nature of the lower limit in our case we find it cleaner to utilise the Pochhammer contour, shown in Figure 5.6, where the integration may be defined in terms of a generic point $\mathbf{p} \in (0, 1)$. Topologically this path is the commutator of the two generators of the (non-abelian) fundamental homotopy group of the twice-punctured plane. It is therefore homotopically non-contractable while being homologous to zero, as it has no net winding around either 0 or 1. This yields the following identity [315, Eq. 15.6.5]

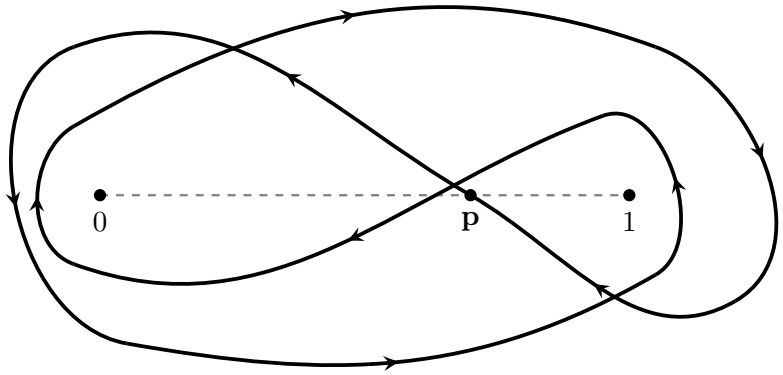

Figure 5.6: The Pochhammer integration contour. This is the contour used in (5.28) to circumvent the singularity at $t = 0$.

$$ {}_2F_1(a,b;c;x) = \mathrm{e}^{-\mathrm{i}c\pi}\Gamma(1-b)\Gamma(1+b-c)\frac{1}{4\pi^2}\int_C t^{b-1}(1-t)^{c-b-1}(1-xt)^{-a}\mathrm{d}t, \quad (5.28) $$

such that we may write the numerator of (5.25) as

$$ \frac{4\pi^2\mathrm{e}^{\mathrm{i}c\pi}}{\Gamma(1-b)\Gamma(1+b-c)}\frac{1}{nz}{}_2F_1\left(-\frac{2}{n},-\frac{1}{n};1-\frac{1}{n};z^n\right). \quad (5.29) $$

For the denominator we set $z = 1$, using Gauss's summation theorem [314, Eq. 15.1.20]

$$ {}_2F_1(a,b;c;1) = \frac{\Gamma(c)\Gamma(c-a-b)}{\Gamma(c-a)\Gamma(c-b)} \quad (5.30) $$

to give

$$ f(z) = \frac{\Gamma\left(1+\frac{1}{n}\right){}_2F_1\left(-\frac{2}{n},-\frac{1}{n};1-\frac{1}{n};z^n\right)}{\Gamma\left(1-\frac{1}{n}\right)\Gamma\left(1+\frac{2}{n}\right)z}. \quad (5.31) $$

This we tidy by applying the Legendre duplication formula for the gamma function [314, Eq. 6.1.18]

$$ \Gamma(2s) = \frac{\Gamma(s)\Gamma(s+\frac{1}{2})}{2^{1-2s}\sqrt{\pi}} \quad (5.32) $$

to $\Gamma(1+2/n)$. Additionally making the substitution $z \to 1/z$ and allowing for a rotation of the image polygon from the roots of unity by an angle α we arrive at our desired map from the disc exterior to the exterior of a regular polygon

$$ f(z) = \frac{4^{-\frac{1}{n}}\sqrt{\pi}z{}_2F_1(-\frac{2}{n},-\frac{1}{n};1-\frac{1}{n};\mathrm{e}^{\mathrm{i}n\alpha}z^{-n})}{\Gamma(1-\frac{1}{n})\Gamma(\frac{1}{2}+\frac{1}{n})}. \quad (5.33) $$

Star polygons

The star polygons are a perturbation of the regular polygons and the calculation follows in the same fashion. We take the vertices of the base regular polygon to still be at the n^{th} roots of unity, the newly introduced prevertices sit at the intermediate points. Consequently, referring to Figure 5.5, we have

$$f(z) = \frac{\int^z z'^{-2}(1-z'^n)^{\frac{2}{n}-2\gamma}(1+z'^n)^{2\gamma}\mathrm{d}z'}{\int^1 z'^{-2}(1-z'^n)^{\frac{2}{n}-2\gamma}(1+z'^n)^{2\gamma}\mathrm{d}z'}. \tag{5.34}$$

Again making the substitution $t = z'^n/z^n$ brings the numerator to the form

$$\frac{1}{nz}\int^1 t^{-\frac{1}{n}-1}\,(1-z^n t)^{\frac{2}{n}-2\gamma}\,(1+z^n t)^{2\gamma}\,\mathrm{d}t. \tag{5.35}$$

Comparing with Picard's single integral representation of Appell's F_1 function [315, Eq. 16.15.1]

$$F_1(a,b_1,b_2,c;x,y) = \frac{\Gamma(c)}{\Gamma(a)\Gamma(c-a)}\int_0^1 t^{a-1}(1-t)^{c-a-1}(1-xt)^{-b_1}(1-yt)^{-b_2}\mathrm{d}t, \tag{5.36}$$

we find that the numerator of (5.34) is given by [1]

$$\frac{1}{nz}\frac{\Gamma\left(-\frac{1}{n}\right)}{\Gamma\left(1-\frac{1}{n}\right)}F_1\left(-\frac{1}{n},2\gamma-\frac{2}{n},-2\gamma,1-\frac{1}{n};z^n,-z^n\right). \tag{5.37}$$

To normalise we use [316, Eq. 5.10.10]

$$\begin{aligned} F_1(a,b_1,b_2,c;1,z) &= {}_2F_1(a,b_1;c;1)\,{}_2F_1(a,b_2;c-b_1;z) \\ &= \frac{\Gamma(c)\,\Gamma(c-a-b_1)}{\Gamma(c-a)\,\Gamma(c-b_1)}\,{}_2F_1(a,b_2;c-b_1;z). \end{aligned} \tag{5.38}$$

[1] Similarly to the derivation of the conformal map for regular polygons, this representation is valid only for $\Re a > 0$ and our value of $a = -1/n$ lies outside this range. An adaptation of the integration contour as employed in (5.28) is needed to make this intermediate step valid. While integral representations of the Appell F_1 function using adapted integration contours can be derived, they are not presented in standard reference texts, such as [316], and we have not yet derived the suitable variation fit for our parameter values. The error is only in the intermediate integral since, just as in the derivation of the mapping for regular polygons, the modified integration contour will introduce a prefactor common to both the numerator and denominator of (5.34), leaving our conformal map in (5.39) unchanged.

Again replacing z with $1/z$ and including rotations of the image polygon we come to

$$f(z) = \frac{\Gamma\left(1+\frac{1}{n}-2\gamma\right) z F_1\left(-\frac{1}{n}, 2\gamma-\frac{2}{n}, -2\gamma, 1-\frac{1}{n}; \mathrm{e}^{\mathrm{i}n\alpha}z^{-n}, -\mathrm{e}^{\mathrm{i}n\alpha}z^{-n}\right)}{\Gamma\left(1-\frac{1}{n}\right)\Gamma\left(1+\frac{2}{n}-2\gamma\right)}. \tag{5.39}$$

Cog polygons

The derivation of the Schwarz-Christoffel map for the cog shapes shown in Figure 5.5 follows the same path as for the star polygons; having introduced n vertices to a regular n-gon the desired mapping is again given by the Appell F_1 function. However, the asymmetry of the shape means that the preimages of the new vertices do not simply interlace evenly the existing ones and their location must be determined numerically. Denoting the first such preimage anticlockwise from 1 by $\mathrm{e}^{\mathrm{i}\chi}$ we have

$$f(z) = \frac{\int^z z'^{-2}(1-z'^n)^{\frac{4-n}{2n}-\gamma}\left(1-\frac{z'^n}{\mathrm{e}^{\mathrm{i}n\chi}}\right)^{\frac{1}{2}+\gamma}\mathrm{d}z'}{\int^1 z'^{-2}(1-z'^n)^{\frac{4-n}{2n}-\gamma}\left(1-\frac{z'^n}{\mathrm{e}^{\mathrm{i}n\chi}}\right)^{\frac{1}{2}+\gamma}\mathrm{d}z'}. \tag{5.40}$$

Continuing as in the case of star polygons we reach the conformal transformation

$$f(z) = \frac{\Gamma\left(\frac{1}{2}+\frac{1}{n}-\gamma\right) z F_1\left(-\frac{1}{n}, \gamma+\frac{n-4}{2n}, -\frac{1}{2}-\gamma, 1-\frac{1}{n}; \mathrm{e}^{\mathrm{i}n\alpha}z^{-n}, \mathrm{e}^{\mathrm{i}n(\alpha+\chi)}z^{-n}\right)}{\Gamma\left(1-\frac{1}{n}\right)\Gamma\left(\frac{1}{2}+\frac{2}{n}-\gamma\right){}_2F_1\left(-\frac{1}{n}, -\frac{1}{2}-\gamma, 1-\frac{1}{n}-\frac{n-4}{2n}-\gamma, \mathrm{e}^{\mathrm{i}n\chi}\right)}. \tag{5.41}$$

5.2 Regular polygons

When analysing the director fields around regular polygons we shall find that their behaviour mirrors the above templates of dipole and quadrupole distortions according to whether their number of sides is odd or even [279]. We therefore treat these two cases in turn, in each case focusing initially on the simplest examples of triangles and squares as these will provide some key insights that can be applied first to regular polygons with arbitrary side number and later to more complex polygonal shapes. Ultimately it will emerge that all regular polygons produce a modification of the quadrupole distortion. The compatibility of the polygon with quadrupolar symmetry is dependent on the number of sides modulo four, prompting us to further subdivide our analysis. Some of the formulae and arguments that arise are simpler for even-sided polygons, so we lead with them.

5.2.1 Even-sided polygons

Our description of how the induced distortions change with the orientation of the colloid will be rooted in understanding the director profile when the colloid is in a symmetric configuration. For a square there are two such states - a 'compass' one in which the vertices are positioned along the cardinal directions and an orthogonal one, corresponding to a rotation of the former by $\frac{\pi}{4}$. In both of these the nematic has two lines of mirror symmetry, namely the far-field alignment direction and its perpendicular. However, the position of the vertices relative to these mirror lines means that the two squares must be differently decorated with topological defects to produce a distortion of the same multipole character. In order to maintain normal anchoring around the square there must be a half-integer defect at each vertex and to have a unique far-field director alignment we require charge-neutrality of these defects. In the compass state, shown in Figure 5.7(a), each vertex sits on one of the mirror lines and so quadrupolar symmetry only constrains the charges of defects on opposing defects to be the same. This allows us to place $+1/2$ defects on the north and south vertices and $-1/2$ ones at the east and west, the opposing choice corresponding to tangential rather than normal anchoring. By contrast, in the orthogonal state shown in Figure 5.7(b) the displacement of the vertices from the mirror lines means that quadrupolar symmetry demands that all vertices carry the same topological charge. Thus a form of geometric frustration arises – an incompatibility between the symmetry and charge neutrality. To relieve this tension and keep the square charge-neutral we have to add charge -1 defects on the equator. This means that while a square in the compass alignment can generate an achiral quadrupole distortion with only the four $\pm 1/2$ defects necessary to turn the director at the vertices, in the orthogonal orientation eight such defects are needed.

We note that a similar frustration would arise when trying to form an achiral dipole distortion with a square colloid, although with the role of the two configurations reversed due to the dipole lacking horizontal mirror symmetry. In the orthogonal alignment four defects suffice, shown in Figure 5.7(c), $+1/2$ defects at the top vertices and $-1/2$ defects at the bottom ones. In the compass orientation the vertical symmetry and lack of horizontal symmetry means we wish to have the same charge at the east and west vertices and different charges at the north and south. This is satisfied by a $-1/2$ defect at the south vertex and $+1/2$ defects at the other three, but this leaves the total topological charge at $+1$. Inducing a dipole in the compass state therefore requires six half-integer defects, with a $-3/2$ defect at the south vertex, shown in Figure 5.7(d).

From the above arguments we can see that although these two alignments of

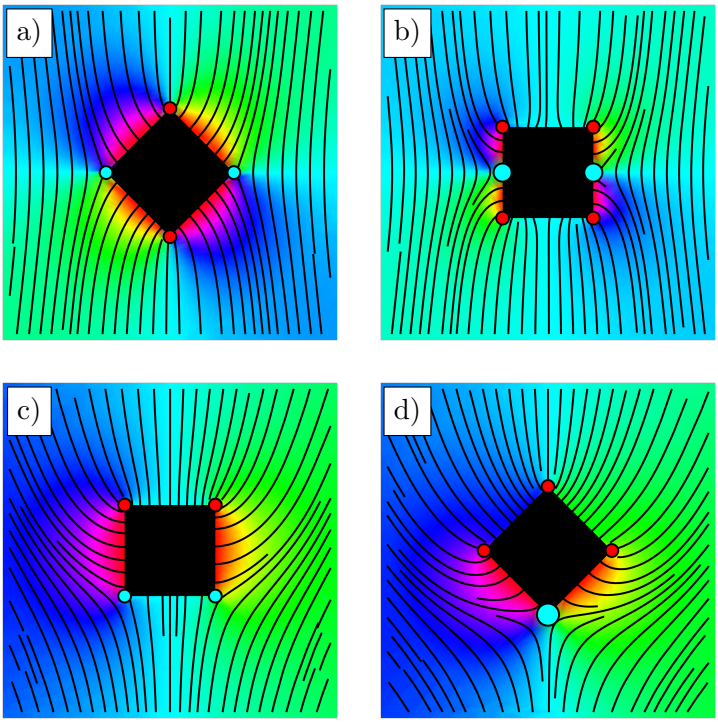

Figure 5.7: Geometric frustration due to symmetry of colloids. The integral curves of the director field are shown in black superposed on the phase field of its angle with normal anchoring on a square colloid. Topological defects are shown in red (positive) and cyan (negative) with areas scaled according to the magnitude of their charge. (a) and (b) For a quadrupolar distortion the four requisite half-integer vertex defects suffice when the square is in the 'compass' orientation, shown in (a). In (b) the square is in an orthogonal orientation and satisfying both quadrupolar symmetry and charge-neutrality requires four $+1/2$ defects and a pair of -1 defects. (c) and (d) A similar frustration arises when placing defects on a square to generate a dipole, although the roles of the two orientations are reversed. (c) Generating a dipolar distortion around a square in the orthogonal alignment needs only four half-integer defects, in the 'compass' state in (d) three $+1/2$ defects and a $-3/2$ defect are needed.

the square are ostensibly equal symmetry states, their differing compatibility with the symmetry of multipoles garners them different energies. Without calculation we can see that the energy is minimised by a quadrupole induced by the compass state, as has been demonstrated experimentally [279]. This both minimises the number of topological defects and arranges them so as to maximise the separation between like charges, producing a higher-order distortion with a more rapid radial decay.

Another insight provided by this reasoning is that we should not expect the number of topological defects to remain constant as the orientation of a colloid is varied. This orientation-dependent behaviour is what we now seek to determine.

Numerics

As was seen in our discussion of the Dirichlet problem on the disc exterior, although a harmonic function is fully determined by the boundary conditions, normal anchoring does not correspond to a unique condition. At any point on the boundary we are free to change the director angle ϕ by a multiple of π, corresponding to the placement of a topological defect. A colloid in a given orientation may therefore be associated with an endless array of boundary conditions.

To address this we employ numerical simulations, minimising the energy

$$F = \frac{K}{2}\int_{\Omega} |\nabla \mathbf{n}|^2 \mathrm{d}^2 A - \frac{W}{2}\int_{\partial\Omega} (\mathbf{n}\cdot\mathbf{v})^2 \mathrm{d}l. \tag{5.42}$$

The first of these terms is the familiar Frank free energy which acts to minimise elastic distortions in the bulk. The second is the Rapini-Papoular energy [194] which enforces normal anchoring on the colloidal boundary, but crucially does so without specifying a particular value of ϕ. We perform our simulations in the strong anchoring regime where $W >> K$. The energy minimisation is performed by iteratively updating the director according to the perpendicular component of the molecular field, $\mathbf{h}_\perp$, evaluated as

$$\begin{aligned} \mathbf{h} &= \frac{\delta F}{\delta \mathbf{n}}, \\ \mathbf{h}_\perp &= \mathbf{h} - (\mathbf{h}\cdot\mathbf{n})\mathbf{n}. \end{aligned} \tag{5.43}$$

To avoid numerical artifacts that might result from sharp corners we describe the boundary of the square colloid as a circle in a L_p norm, that is a function of the form

$$(x^p + y^p)^{\frac{1}{p}} = c. \tag{5.44}$$

This produces a circle for $p = 1$, a square for $p = \infty$ and for intermediate values provides an approximation of a square with smoothly rounded corners. A similar rounding has been employed to ameliorate the effects of sharp edges in the numerical simulation of polyhedral colloids in nematics [271; 275]. The simulation domain was a 200×200 square lattice with a uniform alignment imposed on a circle of radius 100 and the square colloid had a circumradius of 20.

A selection of the results is shown in Figure 5.8, taking $p = 6$ in (5.44), although other values were used to ensure robustness of the behaviour to the specifics of the smooth boundary. Here, and throughout the remainder of this chapter, we use α to denote the orientation of the colloid with respect to its equilibrium orientation. The reusing of this variable is intended to highlight the similar role played by the anchoring angle of the director on a disc and the orientational angle of a polygonal colloid with normal anchoring. We find that as the square's orientation is varied the defects remain pinned at the vertices such that a generic orientation can be described via a rigid rotation of the compass state. This pinning behaviour is akin to that observed for obliquely oriented hexagonal colloids [235]. The positive defects sit at the inside vertices, those with negative charges at the outside ones, with 'inside' and 'outside' defined via their position in the direction transverse to the far field. Rotating clockwise from the compass configuration the $+1/2$ defects are at the upper right and lower left vertices, when rotating anticlockwise they are at the upper left and lower right. These two branches of behaviour collide at the orthogonal alignment, in which there is no distinction between interior and exterior vertices. On passing through this orientation there is a discontinuous jumping of topological charge and an interchanging of the location of the $+1/2$ and $-1/2$ defects. This effective transfer of topological charge -1 from the outside vertices to the inside is mediated by the previously described orthogonal state in which the -1 defects sit in the middle of the vertical side.

Analytical Description

The behaviour described above in the case of the square follows *mutatis mutandis* for arbitrary side number and so in presenting an analytical description we generalise to any even-sided polygon. What has been referred to as the compass orientation is in general an alignment of the colloid such that its vertices lie at the roots of unity and the complementary symmetry state is given by a rotation of $\frac{\pi}{n}$.

Our first task is to determine the appropriate Dirichlet problem on the exterior of the disc. To establish the boundary conditions for the roots of unity configuration

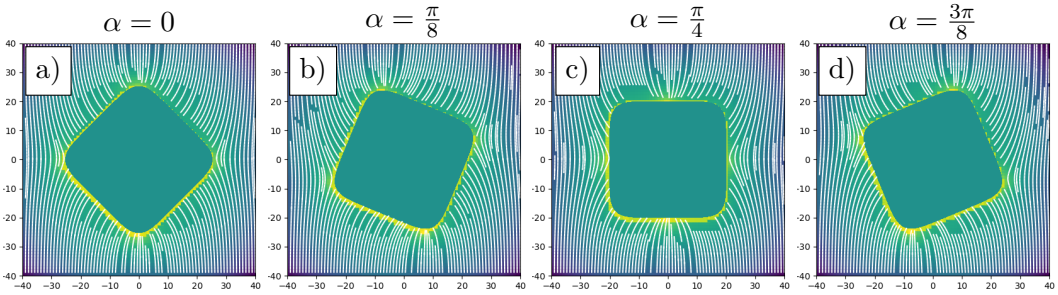

Figure 5.8: Numerical simulations of squares in a two-dimensional nematic. The integral curves of the director are shown in white, superposed on a colour plot of the Frank free energy density. Topological defects with charge $+1/2$ sit at 'inside' vertices; ones with charge $-1/2$ at 'outside' ones. The defects remain pinned at the vertices as the orientation of the square is varied, with additional defects arising when $\alpha = \pi/4$.

we note that as the director distortion is a quadrupole we might expect them to be a modification of the quadrupole boundary conditions for a disc. In fact it is clear that we need a discretisation of this function, which is achieved by the addition of a sawtooth wave with opposite gradient and periodicity determined by the number of sides, such that the director angle is constant along each side. This gives us

$$\phi(\theta) = \sum_{m=1}^{\infty} \frac{(-1)^{m+1}}{m} \sin 2m\theta + \sum_{m=1}^{\infty} \frac{2}{mn} \sin nm\theta \tag{5.45}$$

and through similar considerations we find that in the orthogonal configuration

$$\phi(\theta) = \sum_{m=1}^{\infty} \frac{(-1)^{m+1}}{m} \sin 2m\theta + \sum_{m=1}^{\infty} \frac{2(-1)^{m}}{mn} \sin nm\theta. \tag{5.46}$$

It should be noted that the symmetry arguments concerning the compass arrangement hinged on the number of sides being a multiple of four. When this is not the case the role of the above equations as providing the boundary conditions for the roots of unity and orthogonal configurations is switched.

In full therefore the director angle around an even-sided regular polygon rotated

from the roots of unity by an angle α is given by

$$\begin{aligned}\phi(z,\bar{z}) = &\sum_{m=1}^{\infty} \frac{\mathrm{i}(-1)^{m+1}\left[\left(\mathrm{e}^{-\mathrm{i}\alpha}z\right)^{-2m} - \left(\mathrm{e}^{\mathrm{i}\alpha}\bar{z}\right)^{-2m}\right]}{2m} \\ &+ \sum_{m=1}^{\infty} \frac{\mathrm{i}(\pm 1)^{m}\left[\left(\mathrm{e}^{-\mathrm{i}\alpha}z\right)^{-mn} - \left(\mathrm{e}^{\mathrm{i}\alpha}\bar{z}\right)^{-mn}\right]}{mn} + \frac{\alpha\log(\sqrt{z\bar{z}}/R)}{\log(1/R)}\end{aligned} \tag{5.47}$$

and in the orthogonal configuration by

$$\phi(z,\bar{z}) = \sum_{m=1}^{\infty} \frac{\mathrm{i}(-1)^{m+1}\left[z^{-2m} - \bar{z}^{-2m}\right]}{2m} + \sum_{m=1}^{\infty} \frac{\mathrm{i}(\mp 1)^{m}\left[z^{-mn} - \bar{z}^{-mn}\right]}{mn}, \tag{5.48}$$

where the choice of $\pm$ is made according to the number of sides mod four as described above. The monopole term in (5.47) is in accordance with the elastic torque that results from an orientation that doesn't minimise the energy [21] and has been observed experimentally using hexagonal colloids [235]. These formulae for the director angle on the exterior of the disc are supplemented by the conformal map from this region to the exterior of a regular polygon, derived in Section 5.1.3 to be

$$\zeta = \frac{4^{-\frac{1}{n}}\sqrt{\pi}z\,{}_2F_1(-\frac{2}{n},-\frac{1}{n};1-\frac{1}{n};\mathrm{e}^{\mathrm{i}n\alpha}z^{-n})}{\Gamma(1-\frac{1}{n})\Gamma(\frac{1}{2}+\frac{1}{n})}. \tag{5.49}$$

It should be noted that this map with $\alpha = 0$ always takes the disc to a polygon with its vertices sitting at the roots of unity. However, it is physically more meaningful to measure the rotation angle of a colloid with respect to its equilibrium orientation. When $n \equiv 2 \bmod 4$ these are orthogonal to each other and so a shift of π/n must be added to α. In later sections of this chapter we consider polygons which are constructed as a modification of regular polygons and the same shift is naturally required whenever the base polygon has side number 2 mod 4.

The resulting nematic textures, shown in Figure 5.9, manifestly match those of our numerical simulations for squares in Figure 5.8 and show the same pinning and jumping behaviour of defects. We see that in a generic alignment the interior vertices carry a topological charge of $+2/n$ with $-1+2/n$ at the equatorial ones. In the orthogonal state all vertices have a winding of $+2/n$ while two -1 defects sit at the equator. As such, both converge onto the disc quadrupole distortion discussed in 5.1.2, with continuous positive winding and two -1 surface defects. The director field defines an everywhere orthogonal field corresponding to $\phi \to \phi + \pi/2$. Making this transformation along

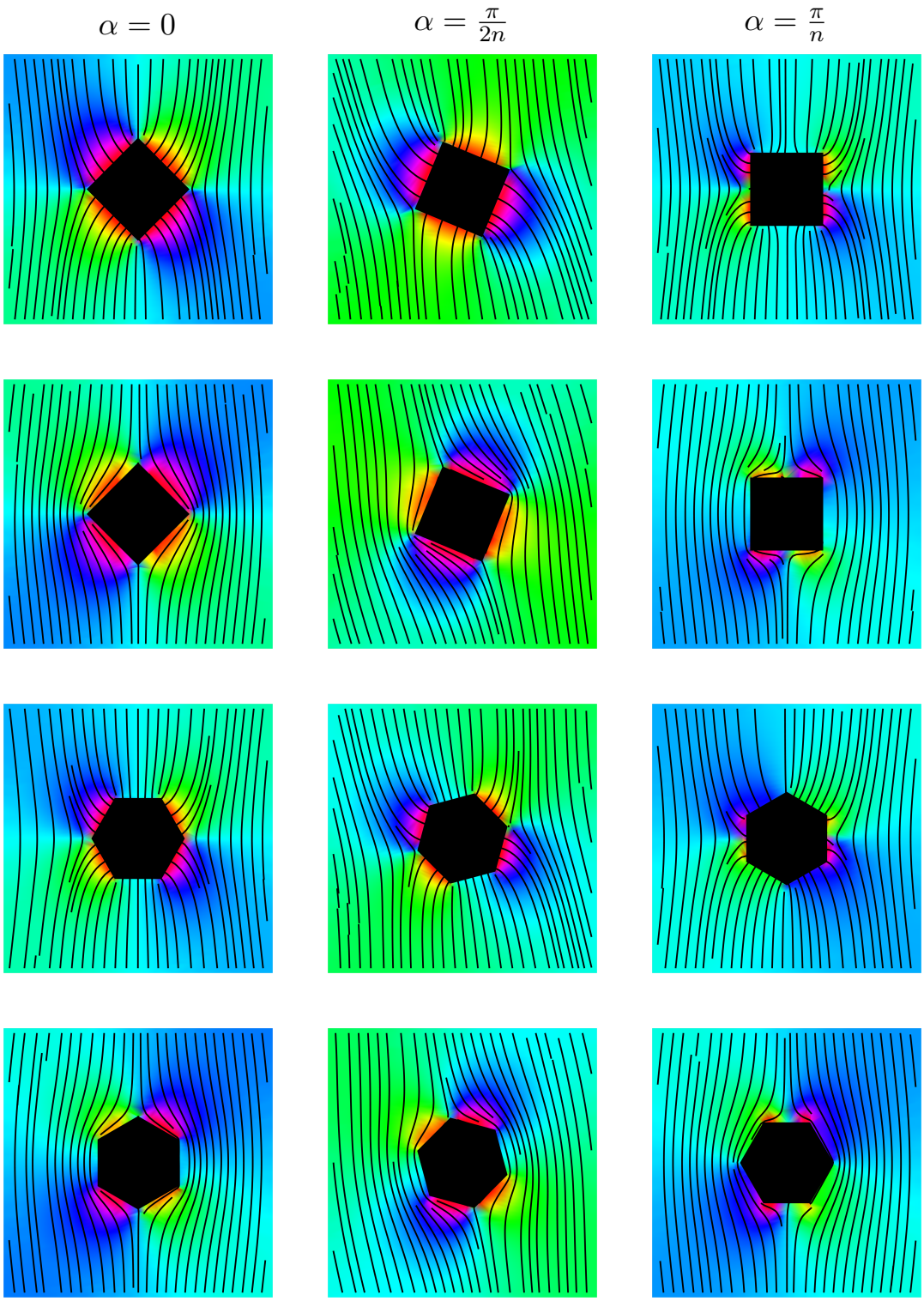
$\alpha = 0$
$\alpha = \frac{\pi}{2n}$
$\alpha = \frac{\pi}{n}$

with a global rotation to keep the far-field alignment fixed we see that our solution for normal anchoring provides a complementary solution for tangential anchoring in which the polygon has been rotated by $\pi/2$, with both these solutions having equal energy in a one-elastic-constant approximation. As normal and tangential anchoring produce distortions with predominantly splay and bend character respectively their deformation energies will differ if elastic anisotropy is present. With the exception of when $n \equiv 0 \mod 4$ this means that different orientations of the polygon result in equilibrium for normal and tangential anchoring. We present both solutions in this section but as it represents a degeneracy of information we restrict to showing just normal anchoring in later sections.

We now consider the role on the induced multipole distortions played by the discretisation of the disc space boundary conditions and the map to the polygon exterior. The first point to make is that from Taylor expanding the hypergeometric function we see that

$$\zeta = \frac{4^{-\frac{1}{n}}\sqrt{\pi}z}{\Gamma(1-\frac{1}{n})\Gamma(\frac{1}{2}+\frac{1}{n})} + O(z^{1-n}) \tag{5.50}$$

and so although the unit circle is strongly distorted to map onto the boundary of the polygon this angular dependence decays very rapidly and the conformal map tends to a radial rescaling. Consequently, the character of the far-field multipoles is determined by the boundary conditions on the disc space with the conformal map simply modifying the asymptotic strength of these multipoles. From (5.47) and (5.50) we can see that the strength of the induced quadrupole s_Q varies with the side number n as

$$s_Q = \frac{\pi}{8^{\frac{1}{n}}\Gamma^2(1-\frac{1}{n})\Gamma^2(\frac{1}{2}+\frac{1}{n})}. \tag{5.51}$$

Figure 5.9 *(preceding page)*: Analytic solutions for even-sided regular polygons in a two-dimensional nematic. The integral curves of the director are shown superposed on the phase field of its angle. The distortions induced by square and hexagonal colloids are shown for both normal and tangential anchoring with the colloid in the equilibrium orientation ($\alpha = 0$, left column), the metastable orthogonal state ($\alpha = \pi/n$, right column) and an intermediate alignment (middle). As the orientation of the polygon is changed any defects rotate rigidly with the colloid and remain fixed at the vertices. The orthogonal orientation represents a degenerate state in which additional defects arise. The distortions for normal and tangential anchoring are related by a local rotation of the director by $\pi/2$, along with a global $\pi/2$ rotation to keep the far-field orientation fixed.

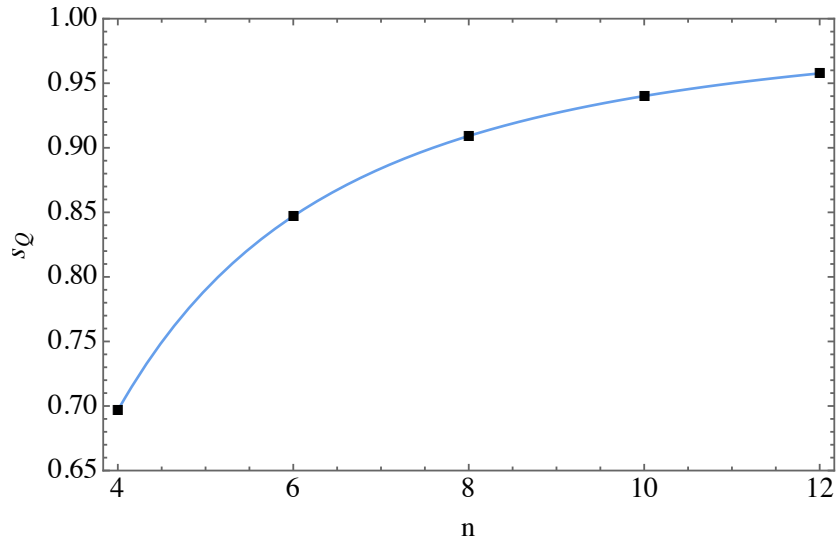

Figure 5.10: The dependence of quadrupole strength on side number for even-sided regular polygons. Convergence onto the disc in the large n limit is borne out by the asymptotic value of 1. The line is purely to guide the eye.

with this scaling with n shown in Figure 5.10. The far-field quadrupole strength increases with n, tending to 1 in the large n limit, in accordance with the convergence of the distortions induced by regular polygons onto those of the disc.

The change in multipole character as the polygon rotates can therefore be inferred directly from our knowledge that we rigidly rotate the roots of unity configuration. We focus our attention on the quadrupole distortions as they are of the greatest relevance for active systems; the behaviour of higher-order multipole follows analogously. Starting with a purely achiral configuration, the strengths of the achiral and chiral quadrupoles vary as $\cos 2\alpha$ and $\sin 2\alpha$ respectively, the same as the dependence on anchoring angle for colloidal discs. However, unlike in the disc case this smooth variation does not continue indefinitely, but instead holds only for $\alpha \in (-\pi/n, \pi/n)$, that is to say until the orthogonal configuration is reached, at which point the sudden change in which vertices are 'outside' causes the sign of the chiral quadrupole to flip and the strength of the achiral quadrupole to increase again. As expected, since the polygon is an achiral shape there is no net chiral quadrupole over a cycle of rotation, although it is possible for active stresses to act to stabilise the higher energy orthogonal state. The rate of change of a multipole with rotation is fixed by its order, but the period of change is a consequence of the number of sides of the polygon, meaning that as the number of sides increases the deviations from purely achiral multipoles decrease, again demonstrating convergence

onto the disc.

5.2.2 Odd-sided polygons

Let us now analyse odd-sided polygons in the same fashion, using the triangle as a concrete example. We again begin with numerical simulations before proceeding to an analytical description. The two key configurations now are the vertical one in which the triangle is symmetric in the far-field direction and the horizontal one where the vertices sit at the roots of unity, shown in Figure 5.11 (a) and (c) respectively. In the vertical state there is $+\frac{2}{3}$ winding at the inside vertex and $-\frac{1}{3}$ winding at the outside ones, similarly to before. From the simulation results shown in Figure 5.11 we see that just as before varying the triangle's orientation causes a rigid rotation of this pattern until a horizontal state is reached. At this point the vertical alignment of a side causes a degeneracy in which vertex is inside, resolved by the two aligned vertices both having $+\frac{2}{3}$ winding and a -1 defect being introduced between them. These two equatorial negative charges alter the dominant character of the distortion from a dipole to a quadrupole, matching experimental observations [266].

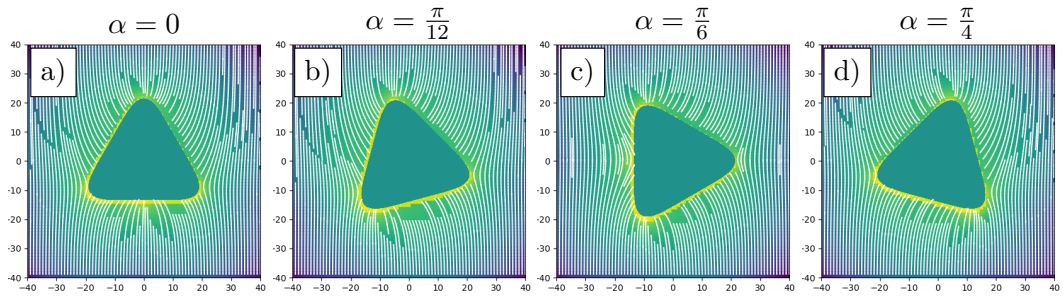

Figure 5.11: Numerical simulations of triangles in a two-dimensional nematic. The integral curves of the director are shown in white, superposed on a colour plot of the Frank free energy density. Positive winding occurs at the 'inside' vertex, negative winding at the 'outside' ones. The topological defects remain pinned at the vertices of the triangle as its orientation is varied, with an additional defect arising on the vertical edge when $\alpha = \pi/6$.

We are able to understand how the distortions will change with orientation just from these rotation and switching rules, without the need to find an explicit Fourier series for the boundary conditions. Here we restrict our attention to the dipoles, as they are the relevant distortions for self-propulsion in active nematics. Naively one might think that a triangular colloid could propel in any direction, depending on which

direction it points. In light of the three-fold symmetry of a triangle this then raises the question in which direction does a triangle point? The symmetry is of course broken by the far-field direction and the vertices are ascribed different windings according to the position relative to this alignment. The dipole induced by the triangle therefore points towards the positive winding at the inside vertex. It follows immediately that there is only a limited set of directions in which the triangle can self-propel, falling in two bands according to whether the inside vertex is at the top or at the bottom. Although these discontinuities act against the easy design of self-propelling colloids they provide an intriguing non-linear response to orientation. A triangular colloid placed in an active nematic with its orientation varying diffusively would seem to behave in a manner akin to run-and-tumble swimming [47] with the drastic change in propulsion direction caused by passing through the horizontal configuration acting as tumble events. As the number of sides is increased the width of the bands shrinks so that the self-propulsion direction is confined closer and closer to up and down. Unlike for even-sided polygons, the behaviour of the dipole with orientation does not map directly onto the disk case in the limit of large side number. The disk does not have an orientation and so the symmetry must be spontaneously broken in the selection of a sign for the vertical dipole and once this choice is made it is invariant to rotations of the disc. By contrast an odd-sided polygon always points up or down and rotating it results in rapid flipping of the sign of the vertical dipole.

We again combine generalising with providing an analytical description. The negative winding on a regular polygon occurs at the outside vertices, which, taking an anatomical viewpoint, may be termed the 'shoulders' of the polygon. For an even number of sides the equilibrium state corresponds to these shoulder vertices sitting at the equator and the boundary condition is simply a discretisation of the quadrupole boundary condition. When the side number is odd the shoulder vertices will always sit just above or below the equator and so an additional term is needed to reverse the director orientation in these two regions, giving the boundary condition in the vertical alignment as

$$\begin{aligned}\phi(\theta) = &\sum_{m=1}^{\infty} \frac{(-1)^{m+1}}{m} \sin(2m\theta) + \sum_{m=1}^{\infty} \frac{2}{mn} \sin(nm\theta) \\ &+ \sum_{m=1}^{\infty} \frac{2\left[\cos\left(\frac{m\pi}{2}\right) - \cos\left(\frac{m(n\pm1)\pi}{2}\right)\right]}{m} \sin(m\theta),\end{aligned} \tag{5.52}$$

the choice of sign being positive when $n \equiv 3 \bmod 4$ and negative when $n \equiv 1 \bmod 4$. The

dipole term that is introduced as a result is as we would expect for a pair of -1 defects with a generic opening angle (5.13). The -1 defects sit at the 'shoulders' of the polygon, that is the vertices at the horizontal extremes. As n varies the position shoulders tends to the equator, oscillating above and below it according to the value of n mod 4, with this 'shrugging' resulting in a weakening and alternating dipole coefficient.

In the horizontal configuration the boundary condition is given by a discretisation of the quadrupole boundary condition rotated by $\pi/2$ to account for the transverse orientation of the polygon

$$\phi(\theta) = \sum_{m=1}^{\infty} \frac{(-1)^{m+1}}{m} \sin(2m\theta) + \sum_{m=1}^{\infty} \frac{2(-1)^m}{mn} \sin\left[nm\left(\theta \pm \frac{\pi}{2}\right)\right]. \tag{5.53}$$

The sign choice is negative for $n \equiv 3$ mod 4 and positive when $n \equiv 1$ mod 4. This is because rotation of the vertical orientation may result in a polygon with its nose pointing either left or right. As this rotation turns a shoulder vertex into the nose this sign choice is also determined by whether the polygon's shoulders sit above or below the equator. Accordingly the director angle around an odd-sided regular polygon rotated an angle α from vertical is given by

$$\begin{aligned}\phi(z,\bar{z}) = &\sum_{m=1}^{\infty} \frac{\mathrm{i}(-1)^{-m+1}}{2m}\left[\left(\mathrm{e}^{-\mathrm{i}\alpha}z\right)^{-2m} - \left(\mathrm{e}^{\mathrm{i}\alpha}\bar{z}\right)^{-2m}\right] \\ &+ \sum_{m=1}^{\infty} \frac{\mathrm{i}}{mn}\left[\left(\mathrm{e}^{-\mathrm{i}\alpha}z\right)^{-mn} - \left(\mathrm{e}^{\mathrm{i}\alpha}\bar{z}\right)^{-mn}\right] \\ + \sum_{m=1}^{\infty} &\frac{\mathrm{i}\left[\cos\left(\frac{m\pi}{2}\right) - \cos\left(\frac{m(n\pm1)\pi}{2}\right)\right]}{m}\left[\left(\mathrm{e}^{-\mathrm{i}\alpha}z\right)^{-m} - \left(\mathrm{e}^{\mathrm{i}\alpha}\bar{z}\right)^{-m}\right] + \frac{\alpha\log(\sqrt{z\bar{z}}/R)}{\log(1/R)}\end{aligned} \tag{5.54}$$

and in the horizontal configuration by

$$\phi(z,\bar{z}) = \sum_{m=1}^{\infty} \frac{\mathrm{i}(-1)^{m+1}}{2m}\left[z^{-2m} - \bar{z}^{-2m}\right] + \sum_{m=1}^{\infty} \frac{\mathrm{i}(-1)^m}{mn}\left[(\mp\mathrm{i}z)^{-mn} - (\pm\mathrm{i}\bar{z})^{-mn}\right]. \tag{5.55}$$

The resulting nematic textures are shown for triangular and pentagonal colloids in Figure 5.12 and reproduce those observed in the numerical simulations of Figure 5.11 in the case of triangles with normal anchoring. The textures for tangential anchoring with the colloid in the equilibrium state ($\alpha = 0$) match those observed experimentally [279]. In considering the director winding at the vertices we see that generically there is a winding of $+2/n$ at $(n-2)$ vertices and of $-\frac{n-2}{n}$ at the remaining two. In the

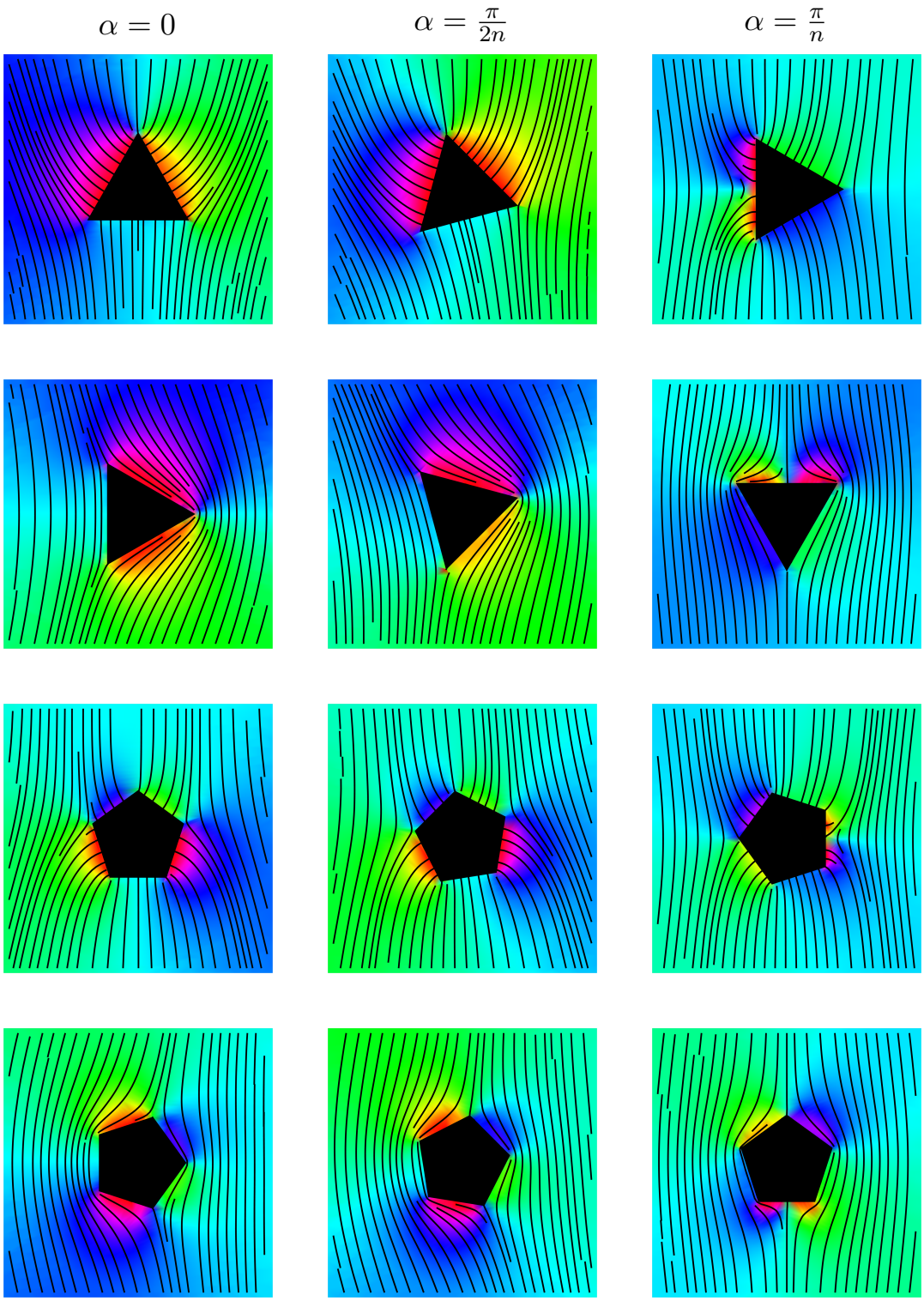
$\alpha = 0$
$\alpha = \frac{\pi}{2n}$
$\alpha = \frac{\pi}{n}$

horizontal alignment there is a -1 defect in the middle of the vertical edge, a winding of $-1+\frac{2}{n}$ at the opposing vertex and of $+\frac{2}{n}$ at all others. In both cases there is a clear convergence onto the distortions associated with the disc, as described in Section 5.1.2, in the large n limit.

Examining the asymptotic strength of the dominant multipoles as we did for even-sided polygons we see from (5.54) and (5.50) that the dipole and quadrupole strengths s_p and s_Q are given by

$$\begin{aligned} s_p &= \pm \frac{2\sqrt{\pi}}{4^{\frac{1}{n}}\Gamma\left(1-\frac{1}{n}\right)\Gamma\left(\frac{1}{2}+\frac{1}{n}\right)} \sin\left(\frac{\pi}{2n}\right), \\ s_Q &= \frac{\pi}{8^{\frac{1}{n}}\Gamma^2\left(1-\frac{1}{n}\right)\Gamma^2\left(\frac{1}{2}+\frac{1}{n}\right)} \cos\left(\frac{\pi}{n}\right), \end{aligned} \tag{5.56}$$

shown in Figure 5.13. The dipole coefficient decays in an oscillatory fashion, in accordance with the 'shrugging' identified above and quantifying the weakening strength of the dipole observed experimentally for triangles and pentagons [279]. The alternation in sign does not appear to have been noted before, see for example the same direction of elastic dipole shown in Figure 5.1(a) and (c), taken from [279]. As for even-sided polygons the quadrupole coefficient grows with n and asymptotes to 1, affirming once more the convergence onto the disc limit.

Figure 5.12 *(preceding page)*: Analytic solutions for odd-sided regular polygons in a two-dimensional nematic. The integral curves of the director are shown superposed on the phase field of its angle. The distortions induced by triangular and pentagonal colloids are shown for both normal and tangential anchoring with the colloid in the equilibrium orientation ($\alpha = 0$, left column), the metastable orthogonal state ($\alpha = \pi/n$, right column) and an intermediate alignment (middle). As the orientation of the polygon is changed any defects rotate rigidly with the colloid and remain fixed at the vertices. The orthogonal orientation represents a degenerate state in which additional defects arise. The distortions for normal and tangential anchoring are related by a local rotation of the director by $\pi/2$, along with a global $\pi/2$ rotation to keep the far-field orientation fixed.

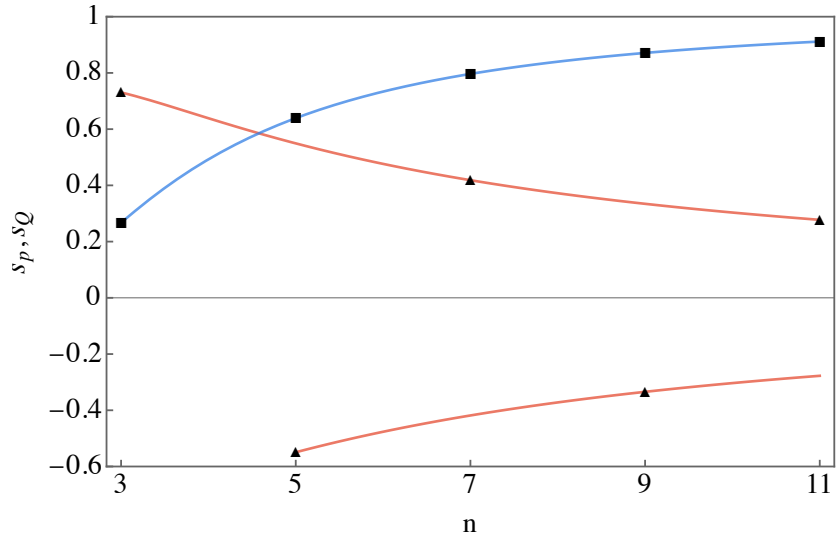

Figure 5.13: The dependence of multipole strengths on side number for odd-sided regular polygons. The dipole and quadrupole strengths s_p and s_Q are shown with triangular and square icons respectively, with red and blue lines to guide the eye. The dipole strength oscillates and decays to zero while the quadrupole strength tends to 1, demonstrating convergence onto the distortion due to a disc in the large n limit.

5.3 Principles of polygonal colloids in nematics

Before pressing on to the consideration of more intricate polygons we would do well to pause and consolidate the understanding we have acquired thus far. We have the following observations. The appropriate boundary condition is that where the director angle $\phi \in [-\pi/2, \pi/2]$. As the orientation of the colloid is varied the distortion is rigidly rotated, with the addition of a monopole term to maintain the anchoring condition, with the caveat that whenever an edge is moved through the vertical the director orientation is reversed so as to maintain the appropriate bounds on ϕ. We have also found negative winding to occur at the outside vertices of polygons and positive winding elsewhere.

Let us examine this last point more closely by considering the director winding that may be induced by a vertex. In this it will be beneficial to choose an orientation for the director, but all statements we make are of course independent of this choice. As illustrated in Figure 5.14, a vertex generically exists in one of two states, namely with the director on the two edges oriented in the same sense, either inwards or outwards, as in (a) and (c) or in opposing senses, as in (b) and (d). According to these circumstances we will have to rotate the director on one edge either clockwise or anticlockwise around the vertex to have it match that on the other side and hence the induced winding will

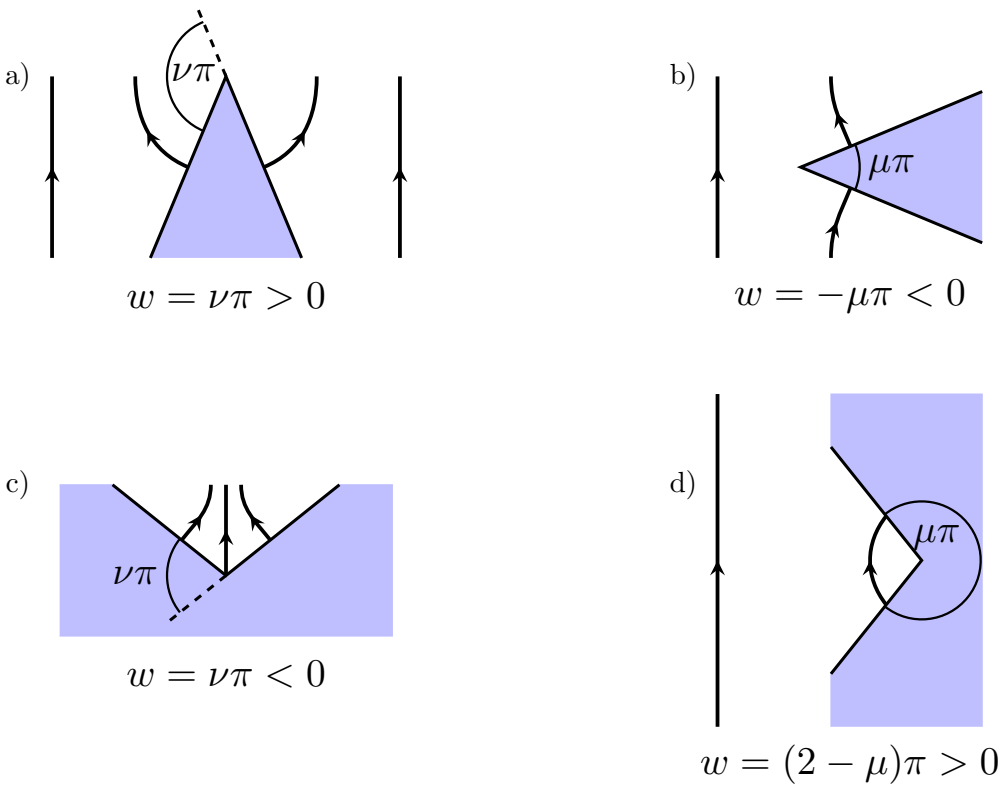

Figure 5.14: Local picture for director winding at a vertex. Schematics of the director, decorated with an orientation to aid our argument, around a vertex of a colloid with normal anchoring and vertical far-field alignment. a) and c) For a vertex aligned along the far-field orientation the induced director winding w is equal to the exterior angle for both convex and concave vertices. b) and d) For vertices which point 'into the flow' of the director field the winding at the vertex is determined by the interior angle and there is a discontinuous change in the induced winding for convex and concave vertices.

be given by either the exterior or interior angle. In the first case we see that the director winding is given by the exterior angle $\nu\pi$, positive for a convex vertex, shown in Figure 5.14(a), and negative for a concave one, shown in Figure 5.14(c). As $\nu \in [-1, 1]$ this always produces the minimal winding, commensurate with maintaining $\phi \in [-\pi/2, \pi/2]$. In the latter case a convex vertex produces negative winding determined by the interior angle as $-\mu\pi$, shown in Figure 5.14(b). The range of the interior angle differs from that of the exterior angle, with $\mu \in [0, 2]$ and so when $\mu > 1$, as for the concave vertex in Figure 5.14(d), the appropriate winding is not $-\mu\pi$ but rather $(2 - \mu)\pi$. When the director orientation was consistent across a vertex the winding varied smoothly from positive to negative as the vertex transitioned from convex to concave. With a reversal of orientation between the two edges there is instead a 'buckling', a discontinuous jump in winding as the vertex changes character.

The dividing line between these two regimes of behaviour is, in light of the bounds on ϕ, when one of the edges of the vertex is vertical, hence the discontinuous behaviour we have seen associated with this. Indeed a vertical line may, if desired, be viewed as containing a vertex with $\mu = 1$, at which a defect with topological charge ± 1 may be placed. If we restrict attention to convex polygons, as we have been considering so far, we recover our prior observation as to the locations of positive and negative windings. We note that as $\mu_k = 1 - \nu_k$ and $\sum_k \nu_k = 2$, associating two vertices with winding $-\mu_k\pi$ and the rest with $\nu_k\pi$ automatically satisfies topological charge neutrality.

This local description of the director winding at a vertex underpins the nature of the nematic distortions around all the colloids that we consider. As we shall see in the next section, the discontinuous change in winding associated with concave vertices leads to radically different distortions when concavity is introduced to a polygon. However, we shall also see that due to the orientation-dependent vertex behaviour laid out here any effects resulting from concavity or chirality of a shape are also subject to orientation dependence.

5.4 Star Polygons

We now consider star polygons formed by attaching an isosceles triangle of base angle $\gamma\pi$ to each side of a regular polygon, which we term the base polygon. This allows us to investigate the role of concavity on the induced nematic distortions. A point of comparison is provided by numerical simulations of star colloids composed of n radial lines emanating from a common centre and equidistributed in angle [283], corresponding to the $\gamma = \frac{1}{2}$ limit of our shapes. Our construction allows us to effectively tune the

degree of concavity and identify distinct regions of behaviour separated by discontinuous jumps as edges are pushed through vertical alignment. These bands of behaviour are of width $2/n$ in γ, $2\pi/n$ being the exterior angle of the base polygon. Here we restrict our focus to the orientations in which the director possesses lines of symmetry, although the distortions for generic alignment would follow from the arguments given previously. This gives us a stable and metastable state, as identified in [283], corresponding to the equilibrium and orthogonal orientations of the base polygon respectively. While the term star polygon is a natural fit for the shapes we consider here, it is also used for regular polygons described by the Schläfli symbol $\{\frac{p}{q}\}$ [317] in which of the p vertices every q^{th} is connected. When self-intersections are removed to form a concave polygon of the same geometry these form a subset of our family of polygons and correspond to particular values of γ. Although all of the stars have an even number of sides, they inherit many of their features from the regular polygon they are based on and so we classify them according to whether this has even or odd side number.

As was the case for regular polygons, the analytical description of the nematic distortions around star polygons is achieved through the combination of appropriate boundary conditions on the disc and conformal maps from the disc to the polygonal domain. The construction of the former will be laid out in this section, the latter is provided by

$$\zeta = \frac{\Gamma\left(1+\frac{1}{n}-2\gamma\right) zF_1\left(-\frac{1}{n}, 2\gamma-\frac{2}{n}, -2\gamma, 1-\frac{1}{n}; \mathrm{e}^{\mathrm{i}n\alpha}z^{-n}, -\mathrm{e}^{\mathrm{i}n\alpha}z^{-n}\right)}{\Gamma\left(1-\frac{1}{n}\right)\Gamma\left(1+\frac{2}{n}-2\gamma\right)}, \tag{5.57}$$

with α the angle of rotation of the base polygon from its roots-of-unity configuration. The derivation of this map is provided in Section 5.1.3.

Beginning with stars for which the base polygon has an even number of sides, we may surmise certain aspects of behaviour without explicit calculation by noting that $\gamma = \frac{1}{2n}$ produces a $2n$-gon and $\gamma = \frac{1}{n}$ the original n-gon rotated by $\frac{\pi}{n}$. As the $2n$-gon will be invariant under rotation by $\frac{\pi}{n}$ its alignment will be the same for both orientations of the base polygon and this degeneracy suggests that there should be no significant differences in the distortions induced for $\gamma < \frac{1}{2n}$. The second observation indicates that the star is still a convex polygon for $\gamma < \frac{1}{n}$ and so any effects of concavity only appear for γ above this threshold. Indeed, when the base polygon is in its equilibrium state the orthogonally aligned n-gon produced by $\gamma = \frac{1}{n}$ will contain vertical signs and herald inversion of the director. When the base polygon is in the orthogonal state director inversion is delayed until $\gamma = \frac{2}{n}$, provided this is less than $\frac{1}{2}$.

In constructing explicit solutions we start by observing that the initial mod-

ification to the boundary conditions is provided by a square wave of magnitude $\gamma\pi$ and period $\frac{\pi}{n}$. For the roots of unity orientation this has the Fourier series $-4\gamma\sum_{m=1}^{\infty}\frac{1}{2m-1}\sin\left[(2m-1)\,\theta\right]$ and so when combined with the boundary condition for the base polygon (5.45) we have

$$\begin{aligned}\phi(z,\bar{z}) = &\sum_{m=1}^{\infty}\frac{\mathrm{i}(-1)^{m+1}(z^{-2m}-\bar{z}^{-2m})}{2m} + \sum_{m=1}^{\infty}\frac{\mathrm{i}(z^{-mn}-\bar{z}^{-mn})}{mn}\\ &- 4\gamma\sum_{m=1}^{\infty}\frac{\mathrm{i}(z^{(1-2m)n}-\bar{z}^{(1-2m)n})}{2(2m-1)}.\end{aligned} \tag{5.58}$$

When the base polygon is in the orthogonal alignment this perturbing square wave must be rotated by $\frac{\pi}{n}$, reversing its sign, which is added to (5.46) to result in

$$\begin{aligned}\phi(z,\bar{z}) = &\sum_{m=1}^{\infty}\frac{\mathrm{i}(-1)^{m+1}(z^{-2m}-\bar{z}^{-2m})}{2m} + \sum_{m=1}^{\infty}\frac{\mathrm{i}(-1)^{m}(z^{-mn}-\bar{z}^{-mn})}{mn}\\ &+ 4\gamma\sum_{m=1}^{\infty}\frac{\mathrm{i}(z^{(1-2m)n}-\bar{z}^{(1-2m)n})}{2(2m-1)}.\end{aligned} \tag{5.59}$$

We reiterate at this point that whether the roots of unity or the orthogonal orientation is the equilibrium state is dependent on whether n is congruent to 0 or 2 modulo 4. The resulting nematic distortions for square- and hexagon-based stars are shown in the left-most panels of Figures 5.15 and 5.16. The modification of the boundary conditions only weakly perturb the distortions induced by the base polygon, regardless of orientation, since while γ is sufficiently small that no edges have moved through the vertical the modification must be n-fold periodic so the lowest order term introduced is $\sin(n\theta)$ which leaves the fundamental quadrupole nature of the distortion unaffected. The aforementioned degeneracy of the two orientations for $\gamma = \frac{1}{2n}$ is illustrated for the square.

This state of affairs is lost when concavity is introduced. For a square in the roots of unity alignment its four equatorial sides buckle through the vertical at $\gamma = \frac{1}{4}$, inverting the orientation of the nematic on these edges. This mandates the addition of

$$\sum_{m=1}^{\infty}\frac{2\mathrm{i}(-1)^{m}\sin^{2}\left(\frac{m\pi}{n}\right)}{m}(z^{-2m}-\bar{z}^{-2m}) \tag{5.60}$$

to (5.58), which flips the sign of the quadrupole term producing the markedly distinct distortion shown for $\gamma = \frac{3}{8}$ in Figure 5.15. Conversely, in the orthogonal alignment the

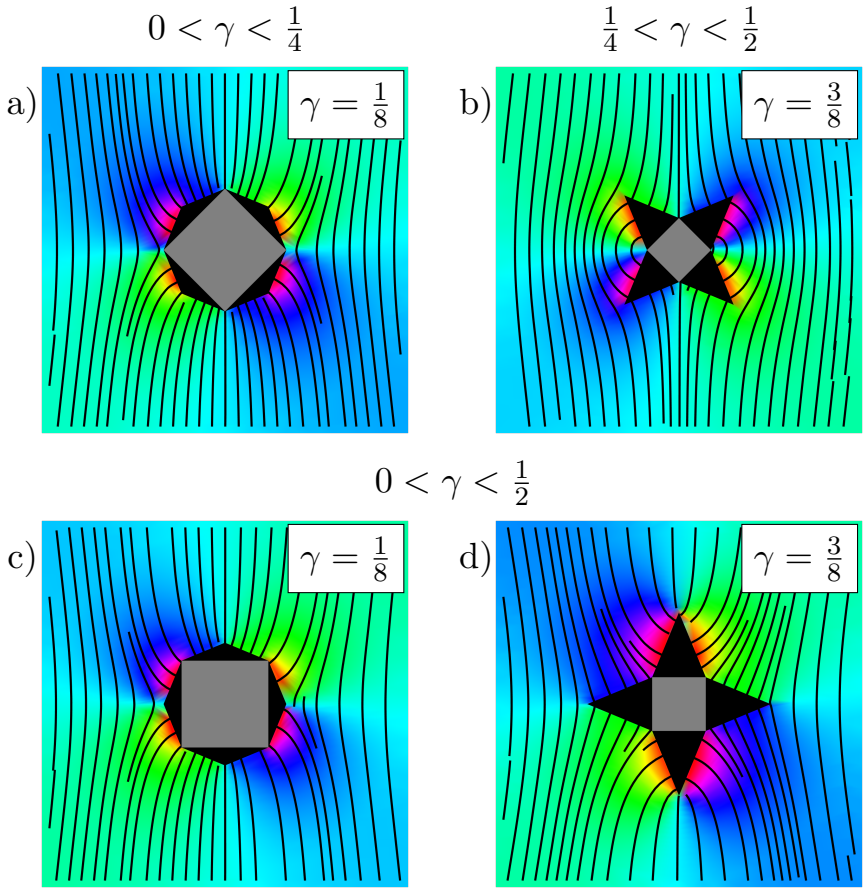

Figure 5.15: Square-based stars in a two-dimensional nematic. The integral curves of the director are shown superposed on the phase field of its angle. The base square is shown in grey inside the colloid to make its orientation clear. (a) and (b) When the base square is in the equilibrium configuration there are two distinct bands of behaviour. (a) A weak perturbation of the distortion around a square. (b) The quadrupole coefficient is reversed, brought about by the inversion of the director orientation along the four equatorial sides when concavity is introduced at $\gamma = 1/4$. (c) and (d) With the base square in the orthogonal alignment the distortion is always a weak perturbation of that for a square.

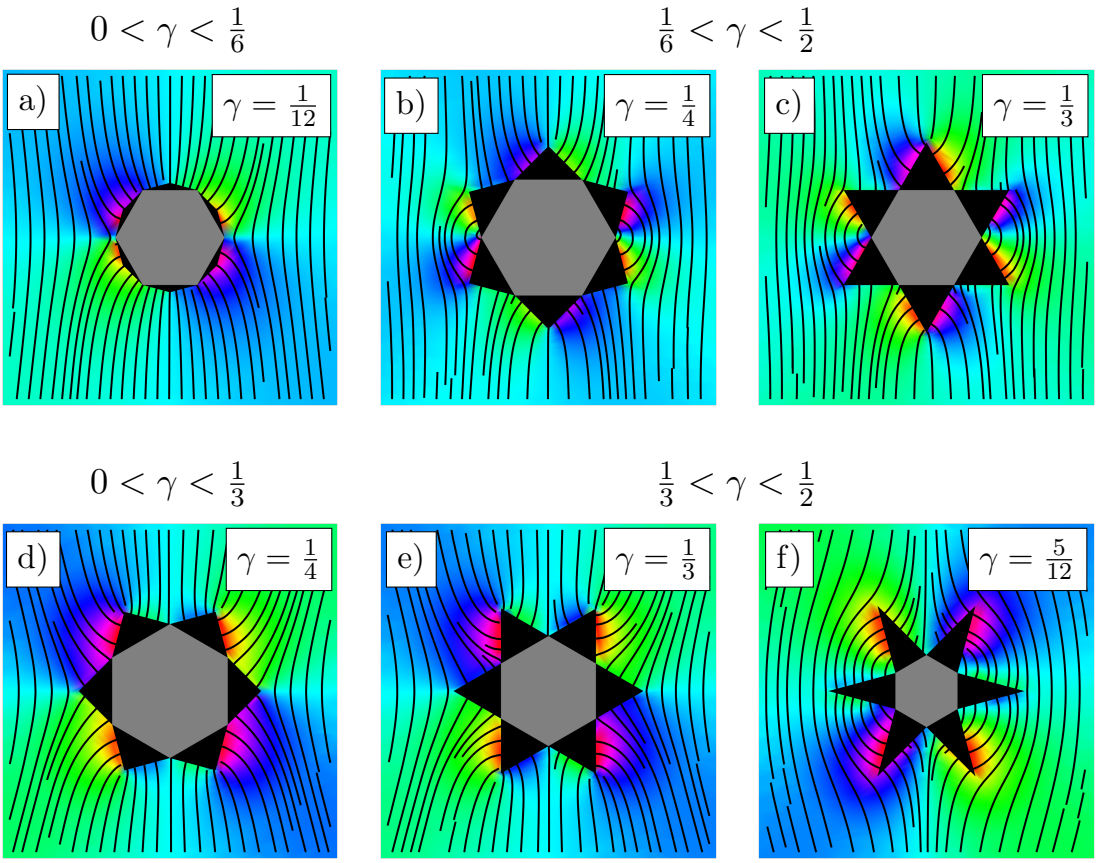

Figure 5.16: Hexagon-based stars in a two-dimensional nematic. The integral curves of the director are shown superposed on the phase field of its angle. The base hexagon is shown in grey inside the colloid to make its orientation clear. Two distinct bands of behaviour are displayed. (a), (b) and (c) When the base hexagon is in the equilibrium configuration there is a weak perturbation of the hexagon distortion, as shown in (a), until $\gamma = 1/6$ when director inversions cause the quadrupole term to vanish and the distortion to be dominated by a hexadecapole. (d), (e) and (f) With the base hexagon in the roots-of-unity configuration the weak perturbation band, shown in (d), persists until $\gamma = 1/3$. Compared to the equilibrium alignment the effect of the subsequent inversions is twice as pronounced at quadrupole order and so leads to a reversal of the quadrupole mode, shown in (f). We highlight the case of $\gamma = 1/3$, shown in (c) and (e), as its symmetry will be useful in later generalisations of high-order distortions.

concavity is not associated with any inversion of orientation and so (5.59) holds for all γ. The nematic distortion continues to be a small perturbation of that for the base polygon so that the two orientations of the same star produce distortions dominated by quadrupoles of opposing sign. This orientation-dependent effect of concavity is at its heart the orientation-dependent vertex behaviour we discussed previously. All the concave vertices in Figure 5.15(d) are inducing director winding according to their external angle, the equatorial pair in Figure 5.15(b) are causing winding determined by their internal angle.

A similar situation arises for the hexagonal stars. As the equilibrium state is provided by the base hexagon being in the orthogonal configuration the weakly perturbed director is described by (5.59), with a phase shift of π/n being applied to both the final square wave term and the Schwarz-Christoffel map in (5.57). Inversion on the four equatorial edges occurs for the equilibrium state at $\gamma = \frac{1}{6}$, with the director angle given by the addition of (5.59) and (5.60). As the number of sides on the base polygon increases, the effect of inversion on these four edges weakens. For the square-based stars the coefficient of the quadrupole term in (5.60) was -2 and so it reversed the sign of the quadrupole. For hexagon-based stars it is only half as strong and so leads to perfect cancellation of the quadrupole term and so for $\gamma > \frac{1}{6}$ the induced distortion is predominately hexadecapolar. A generic case is shown for $\gamma = \frac{1}{4}$ in Figure 5.16, but the nematic distortion for $\gamma = \frac{1}{3}$ is of particular interest due to its symmetry; the star has the geometry of the $\{\frac{6}{2}\}$ regular polygon. It is also the second iteration in a sequence converging on the Koch snowflake fractal [267] and the textures for its two orientations shown in Figure 5.16 replicate those achieved in the experimental study of such fractal colloids [266]. We will discuss this polygon further in Section 5.6, when we consider how it might be generalised in order to produce generic high-order nematic multipoles.

In the metastable state there is no possibility of inversion occurring on the four equatorial sides as the edges they originate from are already vertical. Accordingly, the nematic distortion is largely that of the base polygon until $\gamma = \frac{1}{3}$, resulting in the two distinct distortions for $\gamma = \frac{1}{4}$ shown in Figure 5.16. The inversion then occurs on the four next-most equatorial edges, captured by the addition of

$$\sum_{m=1}^{\infty} \frac{2\mathrm{i}(-1)^m \sin\left(\frac{m\pi}{n}\right) \sin\left(\frac{m\pi}{2}\right)}{m} (z^{-2m} - \bar{z}^{-2m}) \tag{5.61}$$

to (5.58). The positioning of these edges further from the mirror axis enhances their impact, doubling it when it comes to the quadrupole term, leading to the same reversal

in quadrupole character seen for the stable alignment of the square. This is illustrated for $\gamma = \frac{5}{12}$ in Figure 5.16(f).

Moving to stars based on odd-sided regular polygons insight is similarly gained by observing that, as before, $\gamma = \frac{1}{2n}$ results in a $2n$-gon while for $\gamma = \frac{1}{n}$ we recover the original polygon rotated by π. It is easy to see that these two conditions also correspond to the point at which pairs of sides become vertical when the base polygon is vertical and horizontal respectively and thus are the values of γ at which additional inversions of the director will need to be included.

The procedure for constructing the boundary conditions is much the same as in the even-sided case. When the base polygon is aligned vertically the initial modification is by the same square wave which, when added to (5.54) yields

$$\begin{aligned}\phi(z,\bar{z}) = &\sum_{m=1}^{\infty} \frac{\mathrm{i}(-1)^{m+1}(z^{-2m} - \bar{z}^{-2m})}{2m} + \sum_{m=1}^{\infty} \frac{\mathrm{i}(z^{-mn} - \bar{z}^{-mn})}{mn} \\ &+ \sum_{m=1}^{\infty} \frac{\mathrm{i}\left[\cos\left(\frac{m\pi}{2}\right) - \cos\left(\frac{m(n+1)\pi}{2n}\right)\right]}{m}(z^{-m} - \bar{z}^{-m}) \\ &- 4\gamma \sum_{m=1}^{\infty} \frac{\mathrm{i}(z^{(1-2m)n} - \bar{z}^{(1-2m)n})}{2(2m-1)}.\end{aligned} \tag{5.62}$$

In the horizontal alignment this additional contribution must be rotated by $\frac{\pi}{2n}$ resulting in

$$\begin{aligned}\phi(z,\bar{z}) = &\sum_{m=1}^{\infty} \frac{\mathrm{i}(-1)^{m+1}(z^{-2m} - \bar{z}^{-2m})}{2m} + \sum_{m=1}^{\infty} \frac{\mathrm{i}(-1)^{m}((-\mathrm{i}z)^{-mn} - (\mathrm{i}\bar{z})^{-mn})}{mn} \\ &- 4\gamma \sum_{m=1}^{\infty} \frac{\mathrm{i}\left(\left(\mathrm{e}^{-\mathrm{i}\frac{\pi}{2n}}z\right)^{(1-2m)n} - \left(\mathrm{e}^{\mathrm{i}\frac{\pi}{2n}}\bar{z}\right)^{(1-2m)n}\right)}{2(2m-1)}.\end{aligned} \tag{5.63}$$

As previously, this modification does not affect the fundamental mode of distortion and only constitutes a minor perturbation. This is illustrated for both orientations of triangle- and pentagon-based stars in the left-most panels of Figures 5.17 and 5.18.

Inversion occurs on pairs of edges rather than quartets, causing the leading effect to be at dipole rather than quadrupole order, and again at different values of γ according to the alignment of the base polygon. When the orientation is vertical the initial inversion

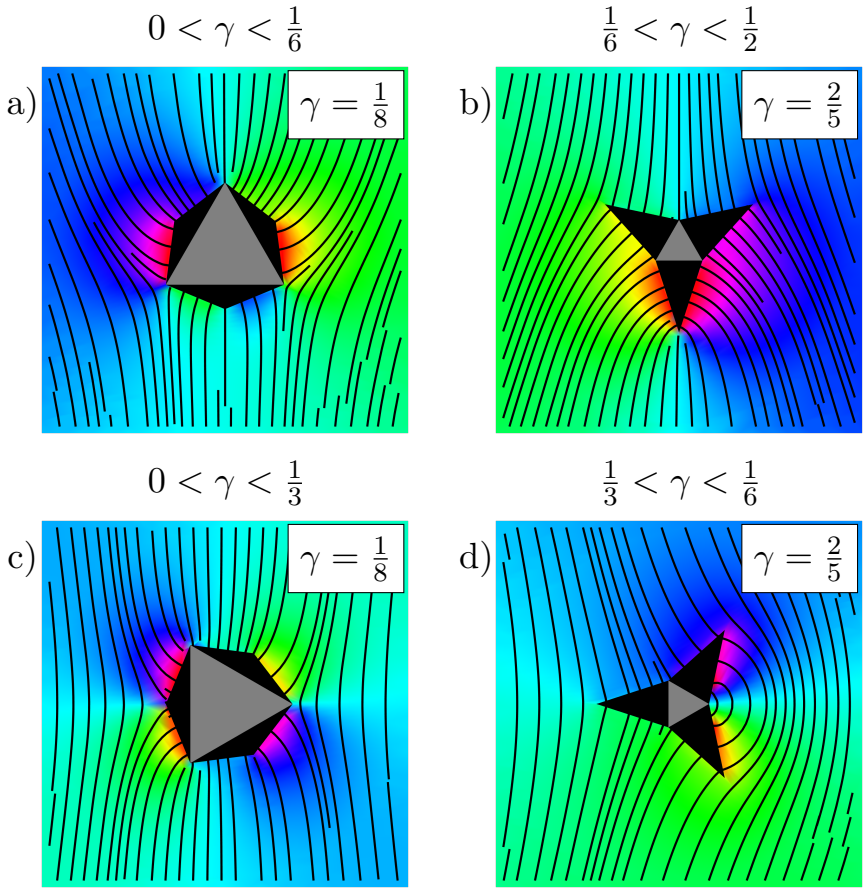

Figure 5.17: Triangle-based stars in a two-dimensional nematic. The integral curves of the director are shown superposed on the phase field of its angle. The base triangle is shown in grey inside the colloid to make its orientation clear. Two distinct bands of behaviour are displayed. (a) and (b) When the base triangle is vertical there is a weak perturbation of the triangle distortion, shown in (a), until $\gamma = 1/6$ when inversions of the director orientation flip the sign of the dipole, as shown in (b). (c) and (d) When the base triangle is horizontal a weak perturbation of the quadrupolar distortion around a triangle, shown in (c), persists until $\gamma = 1/3$, at which point inversions of the director orientation introduce a horizontal dipole, shown in (d).

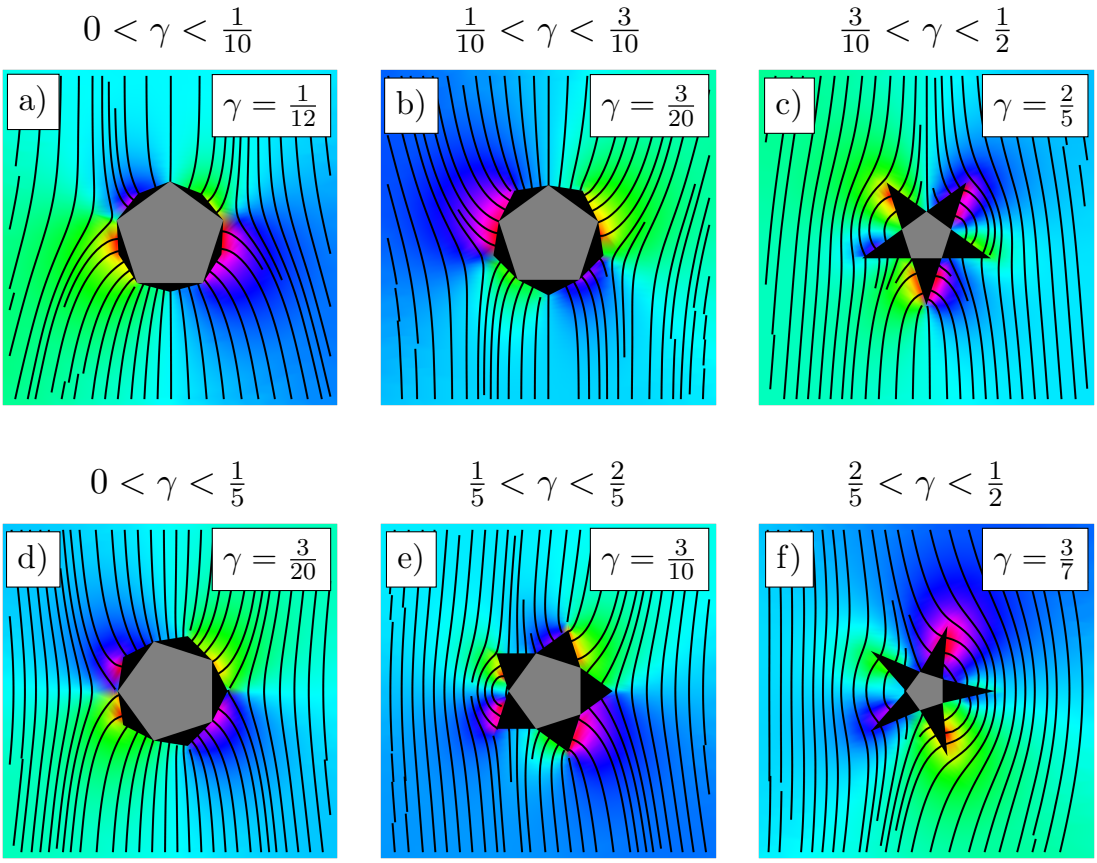

Figure 5.18: Pentagon-based stars in a two-dimensional nematic. The integral curves of the director are shown superposed on the phase field of its angle. The base pentagon is shown in grey inside the colloid to make its orientation clear. Three distinct bands of behaviour are displayed. (a), (b) and (c) When the base pentagon is vertical there is a weak perturbation of the pentagon distortion, as shown in (a), until $\gamma = 1/10$ when inversions of the director flip the sign of the dipole, illustrated in (b). Further inversions that arise at $\gamma = 3/10$ revert the dipole to its original character, shown in (c). (d), (e) and (f) When the base pentagon is horizontal a weak perturbation of the quadrupolar distortion around a pentagon, shown in (c), persists until $\gamma = 1/5$, at which point inversions of the director orientation introduce a horizontal dipole, shown in (e). As shown in (f), additional director inversions that occur for $\gamma = 2/5$ reverse the character of this dipole.

is on the equatorial sides at $\gamma = \frac{1}{2n}$, corresponding to the addition to (5.62) of

$$\pm \sum_{m=1}^{\infty} \frac{\mathrm{i}\left[\cos\left(\frac{m(n+1)\pi}{2n}\right) - \cos\left(\frac{m(n-1)\pi}{2n}\right)\right]}{m}(z^{-m} - \bar{z}^{-m}). \tag{5.64}$$

The overall sign is positive when $n \equiv 3 \bmod 4$ and negative when $n \equiv 1 \bmod 4$. This sign change has the same origin as arose for the sign of the dipole for regular polygons described earlier. According to whether the shoulders of the base polygon sit below or above the equator these new edges of the star will either be faced downwards or upwards when pushed through the vertical.

While the impact of this inversion weakens with increasing side number, so does the strength of the initial dipole due to the base polygon. The dipole term in (5.64) is double the magnitude of that in (5.54) and of opposite sign, resulting in a reversal of the dipole coefficient, as shown in Figures 5.17 and 5.18. The pentagonal star with $\gamma = \frac{3}{20}$ shows that concavity is not required for this change. Subsequent inversions occur at $\gamma = \frac{2k+1}{2n}$, provided this is less than $1/2$, implemented via

$$\pm \sum_{m=1}^{\infty} \frac{\mathrm{i}\left[\cos\left(\frac{m(n-(2k-1))\pi}{2n}\right) - \cos\left(\frac{m(n-(2k+1))\pi}{2n}\right)\right]}{m}(z^{-m} - \bar{z}^{-m}). \tag{5.65}$$

the sign dependent both on the value of n modulo 4 and the parity of k. This is shown for a pentagonal star in Figure 5.18(c), where it reverts the dipole back to its original sign.

For the horizontal orientation the first inversion is delayed until $\gamma = \frac{1}{n}$. For the same γ the vertically aligned star in Figure 5.17(a) produces a dipole distortion but when aligned horizontally the same star in Figure 5.17(c) produces a dominantly quadrupolar distortion, both distortions being a weak perturbation of that resulting from a triangle. Inversion occurs on the two edges on either side of the nose of the base polygon and requires adding

$$\sum_{m=1}^{\infty} \frac{2\mathrm{i}\sin^2\left(\frac{m\pi}{2n}\right)}{m}((\pm\mathrm{i}z)^{-m} - (\mp\mathrm{i}\bar{z})^{-m}) \tag{5.66}$$

to (5.63), with the top and bottom sign choices applying when $n \equiv 3 \bmod 4$ and $n \equiv 1 \bmod 4$ respectively. This is because rotation of the vertical orientation of an odd-sided regular polygon may result in a polygon with its nose pointing either right or left. As this rotation turns a shoulder vertex into the nose this sign choice is again determined by whether the shoulders of the base polygon sit above or below the equator. This

inversion introduces a dipole term where there previously was none, as shown in Figures 5.17(d) and 5.18(e), where the opposing signs of the dipole is in line with the preceding discussion.

Further inversions occur for $\gamma = \frac{k}{n}$, again with the proviso that this be less than 1/2, implemented by the addition of

$$\sum \frac{\mathrm{i}\left(\cos\left(\frac{(n-1)m\pi}{n}\right) - \cos\left(\frac{(n-2)m\pi}{n}\right)\right)}{m}((\pm \mathrm{i}z)^{-m} - (\mp \mathrm{i}\bar{z})^{-m}), \tag{5.67}$$

with the top and bottom sign choices again applying when $n \equiv 3 \bmod 4$ and $n \equiv 1 \bmod 4$ respectively. This has a larger dipole coefficient than (5.66) and so reverses the sign of the nematic dipole, as illustrated in Figure 5.18(f).

The results of this section show how a judicious introduction of concavity can cause inversion of the director orientation on certain edges of polygonal stars, leading to the modification, reversal or cancellation of fundamental multipole terms in the induced nematic distortion. In line with the discussion of Section 5.3 there is an orientation-dependence to these effects.

5.5 Cog Polygons

From concavity, we now turn our attention to the effect of colloidal chirality. In particular we seek to understand how active ratchet behaviour such as observed in bacterial baths [22; 23] might be generated in nematically ordered systems. In doing so we consider a 'weak activity' limit, in which the timescale for actively driven changes in the orientation of the cog is slower than that for director relaxation. This means we can always take the director to be in its equilibrium state and distinguishes the following results from those relating to sustained rotation in systems of mesoscale active turbulence [318]. Our work in Chapter 3 identified the chiral quadrupole as being responsible for the generation of a net active torque and so persistent actively-driven rotation will require a consistent sign of this multipole as the orientation of the colloid is varied.

We construct our cogs from regular n-gons by adding a right-angled triangle with base angle $\gamma\pi$ to each edge, as shown in Figure 5.5. As with regular polygons we begin with numerical simulations, shown in Figure 5.19 for square-based cogs with $\gamma = 1/8$. We find that the distortions follow from the principles we laid out in Section 5.3; rigid rotation along with a reversal of the director orientation along an edge as it rotates through the vertical. The orientation-dependent effect of concavity observed in

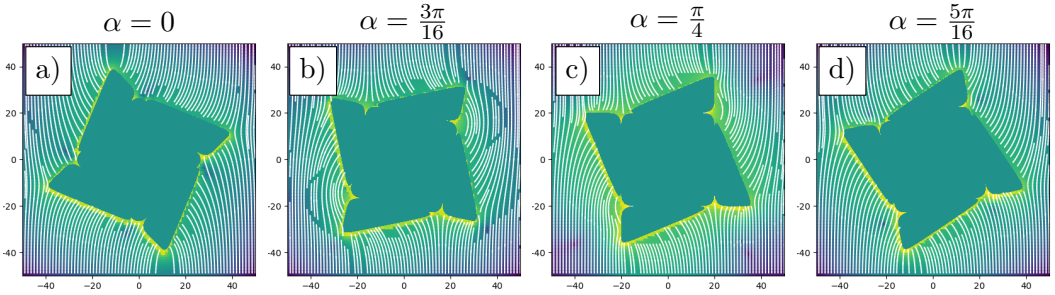

Figure 5.19: Numerical simulations of square-based cogs in a two-dimensional nematic. The integral curves of the director are shown in white, superposed on a colour plot of the Frank free energy density. The base angle for each cog tooth is $\pi/8$. As the orientation of the cog is varied the director winding remains pinned at the vertices, with the orientation of the director being reversed along an edge when it passes through the vertical, illustrated for a pair of long edges in (b). This leads to a changing in the sign of the chiral quadrupole between (a) and (d).

the previous section is also evident, with the concave vertices of the cog only inducing positive winding in Figure 5.19(b).

As always the first step in providing an analytical description of this behaviour is construction of the appropriate boundary condition on the circle. The boundary condition for cogs is more intricate than for the prior families of polygons and not particularly illuminating. Rather than presenting it for each cog that we consider we give the algorithmic process for its construction. Taking the boundary condition for the base regular polygon as a starting point, the addition of the cog teeth is captured by a square wave alternating between the values $\gamma\pi$ and $-\pi/2$. Unlike for previous polygons where the locations of all prevertices were constrained by symmetry, the preimage of the apex of each cog tooth must be determined numerically and will be dependent both on γ and n. We denote the first such prevertex anticlockwise from 1 by $\mathrm{e}^{\mathrm{i}\chi}$. This will typically result in a boundary condition where the director angle ϕ lies outside $[-\pi/2, \pi/2]$ in places and so the director orientation will need to be reversed along these segments to bring ϕ back within this range. Using the case $n \equiv 0 \bmod 4$ as a partial example, the first step gives

$$\begin{aligned}\phi(\theta) = &\sum_{m=1}^{\infty} \frac{(-1)^m}{m} \sin(2m\theta) + \sum_{m=1}^{\infty} \frac{2}{mn} \sin(nm\theta) + \gamma\pi - \frac{(1+2\gamma)n\chi}{4} \\ &+ \sum_{m=1}^{\infty} \frac{\left(\frac{1}{2}+\gamma\right)\left(1+(-1)^m\right)}{m} \left[\sin\left[\frac{nm}{2}\left(\theta - \frac{n\chi}{2}\right)\right] - \sin\left(\frac{nm}{2}\theta\right)\right].\end{aligned} \tag{5.68}$$

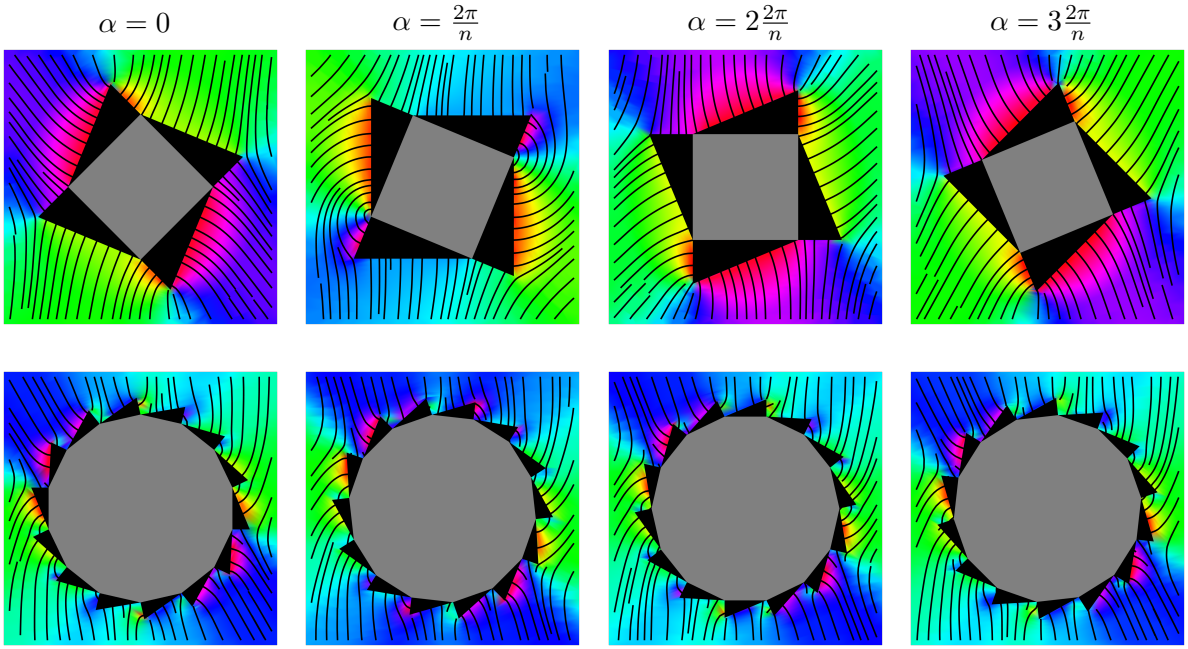

Figure 5.20: Analytical solutions for cog polygons in a two-dimensional nematic. The integral curves of the director are shown superposed on the phase field of its angle and the base regular polygon is shown inside the cog in grey. Four equally spaced orientations are shown. In the top row the square-based cog displays orientation-dependent chirality; the sign of the chiral quadrupole changes as the cog is rotated. In the bottom row a cog with 14 teeth produces a consistently signed chiral quadrupole, corresponding to a consistent direction of active torque in an active system. The angle of the cog teeth is $\pi/8$ in both cases, only the number of teeth is changed.

Any requisite reversal of director orientation may be achieved by using that

$$\frac{\theta_2 - \theta_1}{2} + \sum_{m=1}^{\infty} \frac{\sin(m(\theta - \theta_1)) - \sin(m(\theta - \theta_2))}{m} \tag{5.69}$$

increases ϕ by π between θ_1 and θ_2.

A striking feature of both the numerical simulations of square-based cogs shown in Figure 5.19 and their analytical companions in Figure 5.20 is the reversal in sign of the chiral quadrupole, $\cos 2\theta$. This is the multipole associated with net active torques and so this change in its sign hinders the ability to use cogs to generate persistent rotations in active nematics. It does, however, provide an instance of orientation-dependent chirality [319; 320]. As defined by Lord Kelvin an object is chiral if it lacks mirror symmetry [321; 322] and we may associate with it a handedness to distinguish it from its mirror

image. This definition is intuitive and useful in, for example, labelling the different enantiomers of molecules, but the situation here is more subtle. The induced distortion is a function of the orientation of the colloid in the nematic environment and by simply rotating the cog the surrounding director field can be transformed into its mirror image.

There are two factors behind the variation of the chiral mode: the rigid rotation of the distortion as the cog is rotated and inversions of the director orientation along certain edges. Both of these can be reduced by increasing the number of teeth. With n teeth the cog returns to its original state after a rotation of $2\pi/n$, so the smooth variation of the chiral mode can be made arbitrarily small. Sticking with the case $n \equiv 0 \bmod 4$ for concreteness there will generically be two inversion events, each affecting a pair of antipodal edges. The exact length of the arc of the circle corresponding to each edge depends on χ but is at most $2\pi/n$ and so from (5.68) we can see that the modification to the boundary conditions necessitated by such an inversion is bounded by

$$\frac{2\pi}{n} + \sum_{m=1}^{\infty} \frac{1+(-1)^m}{m} \left[\left(1 - \cos\left(\frac{2m\pi}{n}\right) \right) \sin(m(\theta-\theta_1)) + \sin\left(\frac{2m\pi}{n}\right) \cos(m(\theta-\theta_1)) \right], \quad (5.70)$$

with θ_1 varying according to the location of the edges on which the inversion is occurring. The discontinuous change brought about by these inversions can therefore also be made arbitrarily small. In short, as for regular polygons, the distortions induced by a cog converge onto the rotationally invariant disc distortion, this time with anchoring angle $\gamma\pi$. The orientational dependence of the chiral quadrupole is much like the dipole induced by odd-sided polygons, they are signatures of discretisation which grow ever fainter with increasing side number.

This smoothing out of distortion variations means that the persistent rotation of cogs observed in bacterial ratchets [22; 23] is achievable in orientationally-ordered active matter. An explicit demonstration of the consistent chirality of the induced distortion is given in Figure 5.20 for a cog with 14 teeth. The correspondence with the disc limit is confirmed by noting that the negative winding is situated on the first teeth to be tilted through the vertical, that is at $2\pi k/n$ where k is the smallest integer such that $\pi/n + \gamma\pi + 2\pi k/n > \pi/2$. In the large n limit we may take equality and find that the displacement of the negative winding from the equatorial points tends to $\gamma\pi$, in accordance with the quadrupole distortion for anchoring angle of $\gamma\pi$ on the disc.

Having identified these two distinct modes of behaviour, let us investigate more closely the relationship between the chiral response of the nematic and the parameters of the cog. Figure 5.21 shows the phase space for the coefficient of the chiral quadrupole

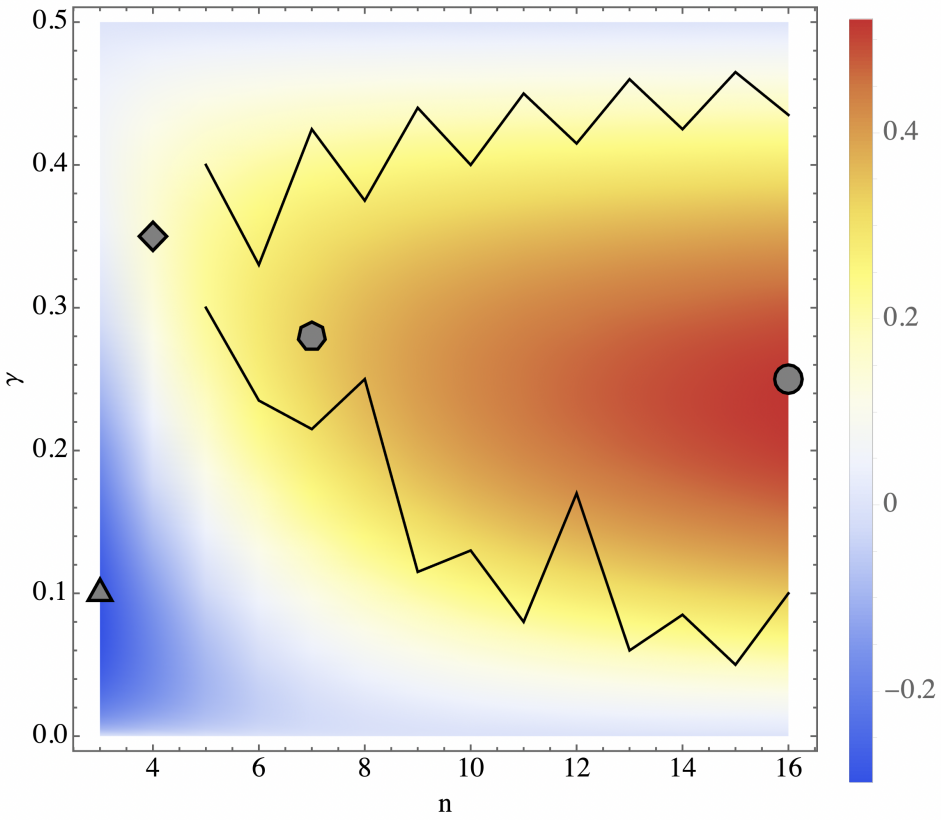

Figure 5.21: The phase space of the chirality of distortions induced by cogs in two-dimensional nematics. The temperature map represents the strength of the chiral quadrupole when averaged over all orientations of the cog as a function of the number of cog teeth n and the tooth angle γ. The two black lines form the boundaries of the region for which the chiral quadrupole has a consistent sign under rotation, corresponding to a consistent active torque in active nematics. The polygonal icons correspond to the locations in phase space of the cogs shown in Figure 5.22.

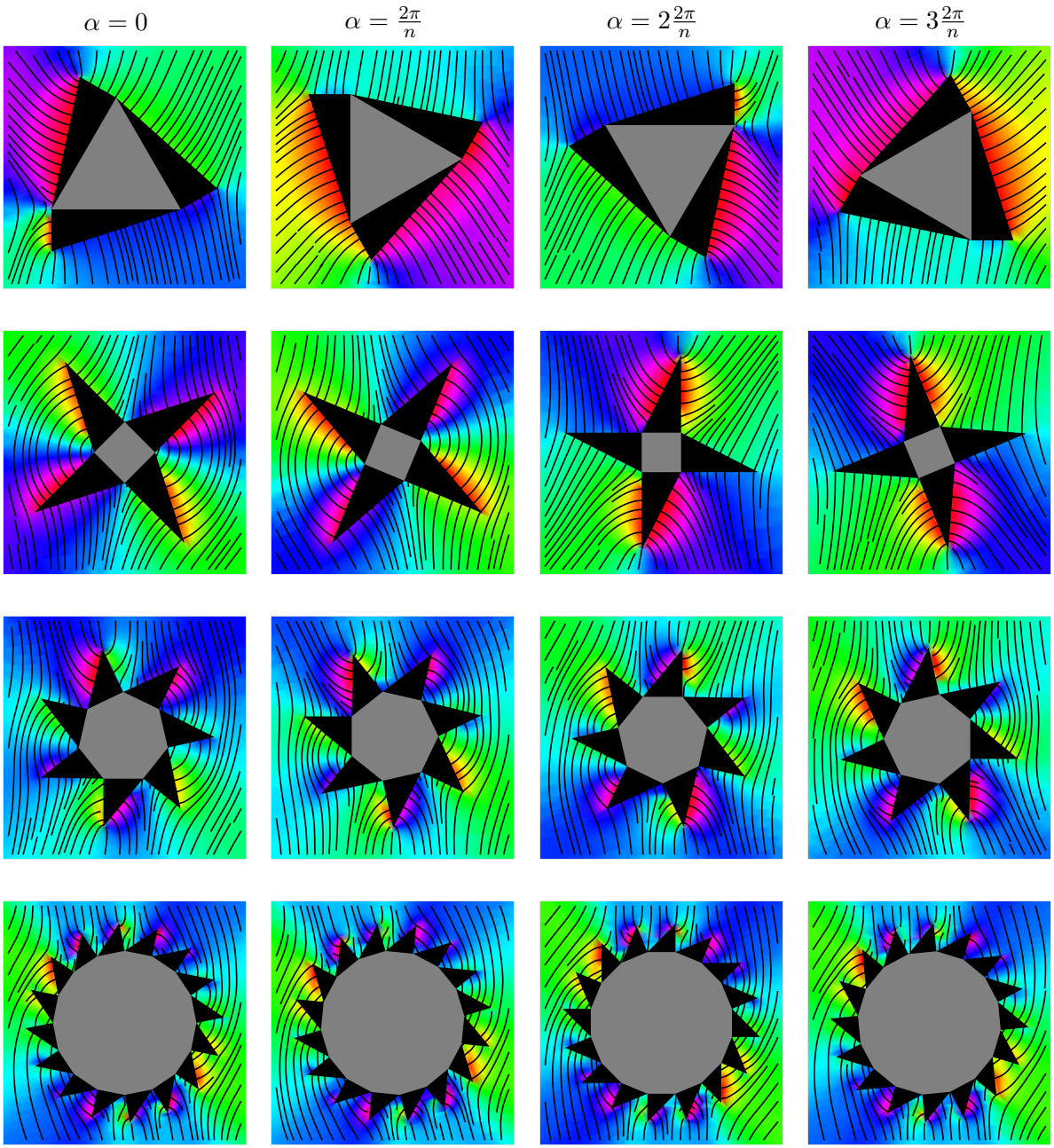
$\alpha = 0$
$\alpha = \frac{2\pi}{n}$
$\alpha = 2\frac{2\pi}{n}$
$\alpha = 3\frac{2\pi}{n}$

as a function of both the number of teeth n and the tooth angle $\gamma\pi$. It was generated by constructing the boundary condition for a cog and then averaging the chiral quadrupole coefficient over a full rotation. For each n from 3 to 16 100 evenly-spaced values of γ were used. The distortions produced by the cogs which sit at the locations of the polygonal icons are shown in Figure 5.22. Between the two black lines is the region for which the chiral quadrupole has a consistent sign under rotation, allowing for active nematic ratchets. There are several regions we can identify. When n is small (3 or 4) there is no value of γ which will produce a consistent chiral response. The square icon denotes a typical example, shown in the second row of Figure 5.22; there is a modest net chiral quadrupole but its sign changes from the first two panels to the last two. The region in the bottom-left of Figure 5.21 is even more extreme, as despite the angle of the cog teeth being such as to ostensibly induce a positive chiral quadrupole, the averaged coefficient is actually negative. This counter-intuitive state of affairs is illustrated by the triangle-based cog in the first row of Figure 5.22. The cog shown there is also convex, something that is possible only for triangle-based cogs with $\gamma < 1/6$, but this is not necessary for the net chiral quadrupole to be negative. For $n \geq 5$ a band of γ values develops for which the chiral response is of a consistent sign, with this band opening up with increasing n. The heptagon-based cog in the third row of Figure 5.22 provides an example of the behaviour typical for intermediate values of n; the chiral quadrupole is of a consistent sign but there is still significant variation in the nematic distortion as the orientation of the cog is changed. Lastly, in the high n limit we can understand the chiral response of the nematic to the cog by modelling it as a disc with anchoring angle $\gamma\pi$. Our discussion in Section 5.1.2 predicts the dependence of the chiral quadrupole

Figure 5.22 *(preceding page)*: Further analytical solutions for cog polygons in a two-dimensional nematic. The integral curves of the director are shown superposed on the phase field of its angle and the base regular polygon is shown inside in grey. Four equally-spaced orientations are shown for each cog, which sit at the locations of the polygonal icons in the phase space in Figure 5.21. 1^{st} row ($n = 3, \gamma = 0.1$): the chiral quadrupole changes sign with rotation but is net negative, despite the teeth angle γ being positive. 2^{nd} row ($n = 4, \gamma = 0.35$): the chiral quadrupole is positive on average but is not consistent in its sign. 3^{rd} row ($n = 7, \gamma = 0.28$): the chiral quadrupole is consistently positive. This value of γ gives the greatest average chirality for a cog with seven teeth, but there is still considerable variation as the cog rotates. 4^{th} row ($n = 16, \gamma = 0.25$): as the number of teeth increases the variation of the distortion due to rotation becomes smaller and smoother, the average chirality is maximised for $\gamma = 0.25$ and this maximum value tends to $1/2$.

coefficient, s_Q^C, on γ to be

$$s_Q^C = \frac{1}{2}\sin(2\pi\gamma) \tag{5.71}$$

and this is an increasingly good approximation for the behaviour in the high-n region of parameter space. As demonstrated by the hexadecagon-based cog in the fourth row of Figure 5.22, the variation of the distortion with cog orientation grows smaller and smoother with increasing n, the maximum value of the average chiral quadrupole tends to $1/2$ and the value of γ for which this is achieved tends to $1/4$. As far as using cogs to generate active nematic ratchets the optimal design is therefore to have as many teeth as feasible, in order to maximise the smoothness of the net active torque and the range of γ which can be utilised. The strength of the active torque can then be tuned using (5.71).

It should come as no surprise that the cogs which are 'most chiral', at least in the sense of our definition, are those with intermediate values of γ. Both $\gamma = 0$ and the limit $\gamma \to 1/2$ correspond to achiral shapes, the former regular polygons the latter tending to star-shaped polygons (although the $\gamma = 1/2$ limit itself does not yield a bounded polygon, as the two edges of the cog teeth become parallel). The black lines in Figure 5.21 are intriguingly non-monotonic and display sizeable jumps. The upper boundary exhibits an odd-even effect and is given by the largest fraction with denominator n that is less than $1/2$. The lower boundary is less regular and seems to display a mod 4 effect. Neither of these is particularly surprising, given the dependence on n mod 4 that we have encountered throughout this chapter due to the compatibility of discrete boundaries with the symmetry of a quadrupole. We do not discuss the specifics of these threshold values any further since they are tied to the precise cog construction that we have employed in this chapter and are thus of secondary interest compared to the qualitative phenomenology we have described, which applies to the chiral response of a nematic regardless of the exact geometry of the colloid.

We have shown that the same active ratchet behaviour achieved in bacterial suspensions lacking orientational ordering [22; 23] can be achieved in an active nematic. It is worth emphasising however that although the rotational effects seem similar, and even share the property of becoming smoother with increasing teeth number [23], their origin is not the same. The previously observed bacterial ratchets resulted from rectification of the swimming direction of the bacteria to produce coherent motion from an incoherent, isotropic environment and the mechanism for generating rotation is unchanged by rotation of the cog. The orientational order of a nematic gives meaning to the orientation of the cog relative to a far-field alignment and it was by no means guaranteed

that the ratchet behaviour would be replicable in this context, particularly given the orientation-dependence of the chiral distortions that drive the rotation of the cog. It is gratifying then that these effects melt away with increasing tooth number, allowing the active ratchet effect to be recovered.

5.6 High-order multipoles

We conclude this chapter with the most striking illustration of the diversity of distortions that can result from a genus 0 colloid; tailoring the colloidal geometry so as to produce a prescribed multipole as the dominant term in the distortion. As laid out in the introduction, this has been a major aim in the study of nematic colloids [187; 186; 188; 90], motivated both by the intricate collective structures that result from the highly anisotropic interactions and, inspired by the colloidal atom paradigm, a general desire to investigate the physics that results from high-order multipole structures. In this section we shall demonstrate that the techniques we have developed can be used to design a colloid whose far-field distortion is dominated by a multipole of arbitrarily high order.

To illustrate how the shape of a polygonal colloid relates to the multipoles that it induces we return to the example of the $\{\frac{6}{2}\}$ hexagonal star identified in Section 5.4. That the dominant multipole is fourth-order rests on two facts. Firstly, the twelve edges of the polygon exist in only three orientations which are cycled through in the same order four times. Secondly, by symmetry the prevertices are equally distributed on the circle. Together these constrain the boundary condition on the circle to have four-fold periodicity and preclude any harmonic below fourth order. In this light we can see that the dipoles and quadrupoles that dominate the distortions of regular polygons result from every odd-sided one consisting of a 1-cycle of n orientations while the even-sided ones provide a 2-cycle of $n/2$ orientations, the same director orientation arising on pairs of opposite sides.

The path ahead is clear. To have a colloidal distortion be dominated by an order l multipole that colloid should comprise an l-cycle of some set of orientations and have equidistributed prevertices. The first of these tasks is straightforwardly achieved, but the second is more subtle, for while we can input evenly-spaced prevertices to the Schwarz-Christoffel integral (5.24) and specify the exterior angle at each we are not free to separately choose the edge lengths. In our pursuit of high-order multipoles we must accept whatever side lengths stem from equally-spaced prevertices and there is no guarantee *a priori* that the resulting polygon is simple, that is free from self-intersections. As noted in [289], there is no elementary expression in terms of the polygon parameters

corresponding to the condition of being simple. Our best strategy is to maintain as much symmetry in the polygonal colloid as possible.

Inspired by the form of the hexagonal star, let us consider colloids formed of a triangle with k additional triangles attached to each edge. This gives us the family of polygons shown in Figure 5.23 in which the k^{th} member induces a dominant $(1+3k)$-pole. We start with a 1-cycle and increase the order of the cycle by one with each adjoined triangle. In full the director angle follows directly from (5.54), with $\alpha = 0$, by modifying the exponents of z and $\bar{z}$ according to the order of the cycle and is given by

$$\phi(z,\bar{z}) = \sum_{m=1}^{\infty} \frac{\mathrm{i}\left(z^{-(1+3k)m} - \bar{z}^{-(1+3k)m}\right)}{2m} - \sum_{m=1}^{\infty} \frac{\mathrm{i}\left(z^{-3(1+3k)m} - \bar{z}^{-3(1+3k)m}\right)}{6m}. \tag{5.72}$$

The form of the Schwarz-Christoffel map follows directly from our construction, but to provide an explicit example, when $k = 2$ we take the mapping to have the form

$$\zeta(z) = 1 - C\int_1^{1/z} \frac{\left[\left(1-z'^3\right)\left(1-\mathrm{e}^{\frac{4\mathrm{i}\pi}{7}}z'^3\right)\left(1-\mathrm{e}^{-\frac{4\mathrm{i}\pi}{7}}z'^3\right)\right]^{2/3}}{z'^2\left[\left(1-\mathrm{e}^{\frac{2\mathrm{i}\pi}{7}}z'^3\right)\left(1-\mathrm{e}^{-\frac{2\mathrm{i}\pi}{7}}z'^3\right)\left(1-\mathrm{e}^{\frac{6\mathrm{i}\pi}{7}}z'^3\right)\left(1-\mathrm{e}^{-\frac{6\mathrm{i}\pi}{7}}z'^3\right)\right]^{\frac{1}{3}}}\mathrm{d}z', \tag{5.73}$$

with the complex constant C determined numerically by requiring the vertices of the base triangle to be fixed points of the map. We might hope that we could extend this method of attaching copies of a shape onto each of its sides to arbitrary regular polygons, but as the number of sides is increased the exterior angle at the fusion points becomes increasingly negative and self-intersections arise.

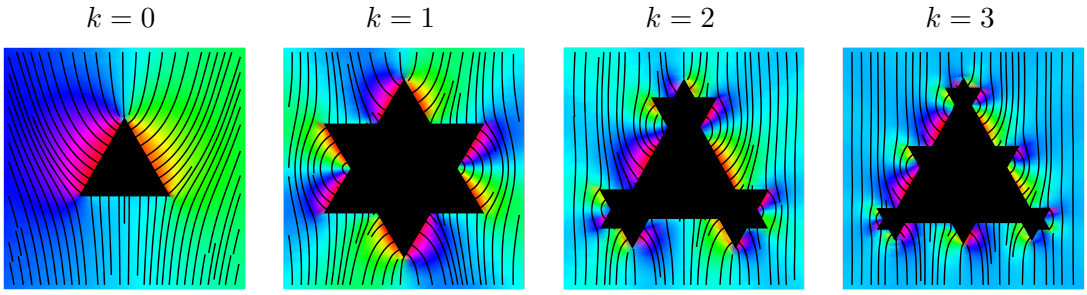

Figure 5.23: A one parameter family of polygonal colloids based on a triangular motif. The integral curves of the director are shown superposed on the phase field of its angle. Starting with a base triangle the k^{th} member of the family has k triangles on each edge of the base triangle and induces a $(1+3k)$-pole as the dominant far-field distortion.

However, as even-sided polygons already represent a 2-cycle of orientations they allow us to modify this construction by not attaching copies of the full polygon but instead (approximately) half of it. To be exact, from a regular polygon with $2q$ sides we construct a 'petal' motif from $q+1$ edges, giving us a series of edges with a pair of parallel sides at its ends. Replacing each edge of the $2q$-gon with this motif forms a 'flower' polygon whose edges provide a $(2+2q)$-cycle of q orientations. We may also choose to place more than one copy of this motif on each side and so have a two-parameter family of polygons constructed by placing k petals on each edge of a $2q$-gon. The director angle that results is again, by construction, an iterated version of that for the regular polygons (5.47) giving

$$\phi(z,\bar{z}) = \sum_{m=1}^{\infty} \frac{\mathrm{i}(-1)^{m+1}\left(z^{-m(2+2qk)} - \bar{z}^{-m(2+2qk)}\right)}{2m} + \sum_{m=1}^{\infty} \frac{\mathrm{i}\left(z^{-mq(2+2qk)} - \bar{z}^{-mq(2+2qk)}\right)}{2mq}, \quad (5.74)$$

with the parameters of the Schwarz-Christoffel map determined as described previously. The nematic distortions are shown in Figure 5.24 for squares, hexagons, octagons and decagons with up to three petals replacing each edge. We only show the case where the base polygon is in its equilibrium alignment as this is sufficient to demonstrate the idea, as for regular polygons, for odd q the fact that the equilibrium orientation does not correspond to the roots of unity requires a rotation to be incorporated into the Schwarz-Christoffel map and the boundary condition. The rapid decay of the nematic distortion means that the bulk is screened from the presence of the colloid, creating a form of 'elastic invisibility', analogous to optical cloaking [323].

The proliferation of topological defects that arises due to the colloids in Figure 5.24 is similar to that observed for colloids taking the form of iterations of the Koch snowflake [266]. The difference is that while the Koch colloids are equilateral in real space, the flower colloids we present here are equilateral (or should that be equi*arc*al) in the preimage space. Both families of colloids have intricate structure which requires high-order multipoles to be induced in the nematic and hence many places of director winding on the boundaries, but in the flower colloids the locations of these defects are tuned so as to perfectly cancel all but the highest harmonics, whereas in the Koch colloids there is no such destructive interference and more fundamental modes still dominate. The intricacy of the Koch colloids suggests that the same direct laser writing methods should be able to manufacture at least the simpler of the colloids in Figures 5.23 and 5.24 and their multipole character may be probed through the same video microscopy techniques used to study regular polygonal colloids [279].

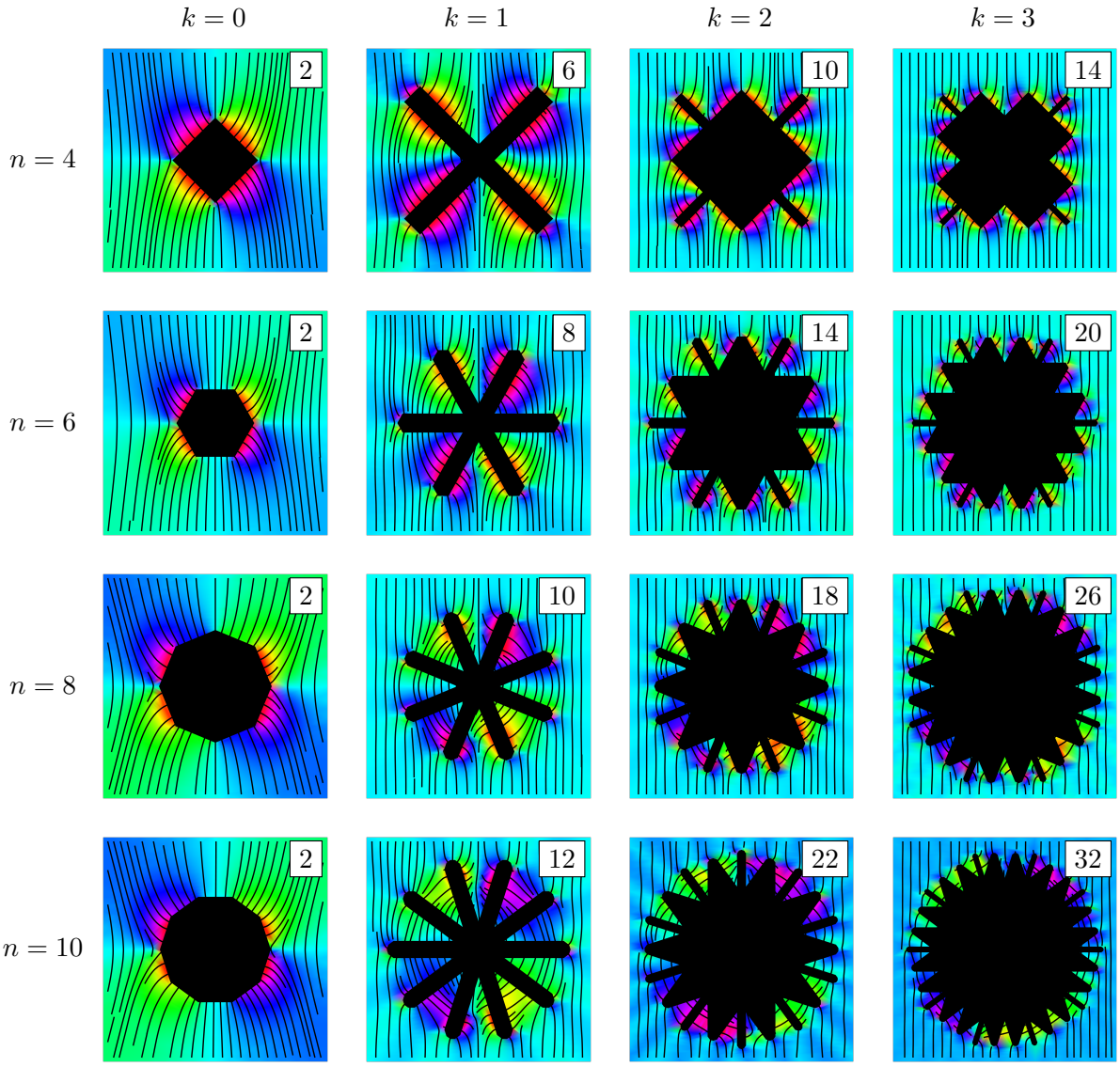

Figure 5.24: A two parameter family of polygonal 'flower' colloids based on a 'petal' motif from even-sided regular polygons. The integral curves of the director are shown superposed on the phase field of its angle. For each base even-sided n-gon a family is formed by adding to each side k 'petals' formed from $n/2+1$ sides of the base n-gon. The (n, k) polygon induces a $(2 + nk)$-pole as the dominant far-field distortion, as indicated by the numbers in the upper-right corner of each panel.

The construction we have presented allows for arbitrarily high multipoles to be induced in nematics. We must remember though that while our continuum description is able to respond perfectly to satisfy the boundary anchoring no matter how intricately we crenelate the colloid, the responsiveness of a nematic is governed by the correlation length, which is $\sim$ 10nm. Features smaller than this scale will result in regions where the nematic preferentially melts into the isotropic phase [266] and this is what ultimately limits the order of multipole that we can induce. What we have presented here merely serves as a demonstration of the method and is by no means an exhaustive set of all the colloids that might be designed to produce high-order distortions. There are many different colloidal geometries that produce the same multipole as the leading contribution to the nematic distortion, raising the question of which design is optimal. Such optimisation may be based on the 'purity' of the dominant multipole, that is its separation from the next-leading term, the practicality of construction, which is likely to be determined by the ratio of the smallest to largest edge lengths of the colloid and the sensitivity of the distortion to imperfections in manufacturing, such as incorrect side lengths. The balance of factors will probably be context-dependent and so we do not delve into this matter further, save to say that our construction provides us the tools for such differentiation of colloidal designs.

5.7 Discussion

We have provided a method for constructing harmonic nematic textures which minimise the one-elastic-constant free energy subject to normal anchoring on the boundary of a polygonal colloid. This has allowed us to quantify previous experimental observations [279; 283] and also make experimentally testable predictions for the behaviour of certain polygonal colloids in both active and passive nematics. There are various directions for further development of this work, centred on either widening the class of colloidal shape we consider or extracting additional results from the constructed director fields.

Taking the first of these, we have focused our attention here on relatively symmetric polygons for which the parameters of the Schwarz-Christoffel transformation were (largely) constrained, allowing the maps to be expressed analytically in closed form, but there is no need for this restriction. To the extent that any domain may be approximated by a polygon, the Schwarz-Christoffel mapping provides a constructive proof of Riemann's mapping theorem and the methods of this chapter may be extended to any colloid. In a more general approach one might determine the locations of the prevertices numerically, for example using [324], greatly expanding the scope of this chapter's

methods. As an illustration of this we offer the second iteration of the Koch snowflake, shown in Figure 5.25. The nematic distortion reproduces that found experimentally and numerically, see Figure 5.1(l) and (m), but is arrived at via the approach of this chapter: determination of the appropriate boundary condition on the disc along with the requisite conformal map. Furthering the investigation of the relationship between nematic ordering and fractal geometry initiated in [266] is just one avenue that this broader approach opens up. Various adaptations of the Schwarz-Christoffel transformation exist [289] and could be utilised to further extend the applicability of our methods, such as to include curvilinear polygons [289; 313] or multiply connected domains [289; 313; 325], based on the Schwarzian derivative and the Schottky-Klein prime function respectively.

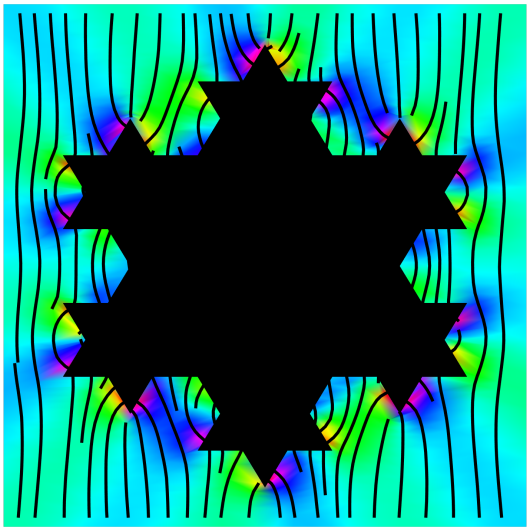

Figure 5.25: The second iteration of the Koch snowflake in a two-dimensional nematic. The nematic texture is calculated by determining the appropriate boundary condition on a disc, along with the conformal map from the disc to the Koch colloid and agrees with those found experimentally and numerically, shown in Figure 5.1(l) and (m).

As to the second point, it should be possible to calculate both the elastic deformation energy and the net active force and torque for a colloid through an appropriate contour integral. The asymptotic form of the Schwarz-Christoffel mapping, as illustrated in (5.50), allows them to serve as a reasonable proxy for conformal maps for a polygon in a finite, circular domain and the explicit solutions for the director field we have provided then allow the elastic energy to be calculated directly. Using Green's first identity the bulk integral may be transformed into one over the boundary of the polygon, with the integration contour being deformed to avoid the vertices. Such calculations have

been employed to find the total elastic deformation energy of a nematic confined to a polygonal domain [326]. As the net active force and torque are given by integrals of the stress tensor they should also be expressible as integrals over a similarly deformed contour, providing a second canonical expression for these properties, complementing the asymptotic integration approach utilised in this thesis.

Art is limitation;
the essence of every picture is the frame.

G.K. Chesterton, Orthodoxy

6 Envoi

Our threefold exploration of nematic harmonics now concluded, we have seen the power they have to illuminate the non-equilibrium behaviour of active nematics, as well as how they may be controllably induced in all their diversity through colloidal geometry.

Whether it be capturing the flow response to generic distortions and yielding predictions for activity-driven self-propulsive and ratchet behaviour of colloids (Chapter 3) or providing a description of the dynamics of fundamental topological excitations (Chapter 4), our linear, far-field approach has been successful both in matching existing results on active nematics and providing new predictions.

This asymptotic perspective is balanced by our work in Chapter 5, where in the name of understanding the connection between the shape of a colloid and the induced nematic distortion our attention was focused on the near field, in fact the boundary of the colloid itself. As always with conformal maps, where the boundary leads the bulk follows. Our results revealed not just how to induce those multipoles that we had previously identified as being relevant to active phenomenology, but also a geometric route to near-arbitrary control of the multipole structure of a nematic.

In addition to the specific avenues for continuation laid out at the end of each chapter there are two broad areas for extension of the multipole approach of this thesis:

chirality and boundaries. The pairing of parity and time-reversal symmetry breaking has dramatic consequences for the behaviour of chiral active matter [113] and active cholesterics provide a natural setting in which to study this [327; 265]. Distortions of the phase field that captures the cholesteric twist can be described in the same manner as those of the layer structure of a smectic. Using existing results in the latter context [328; 329] to provide a far-field picture of such cholesteric distortions could both have application to the response of passive cholesterics to colloidal inclusions [330] and provide the same insight into the active response as has been achieved for nematics. Boundaries have a similarly striking effect on the behaviour of microswimmers [331], including attraction to the boundary [332] and circular swimming [333], and their effect in rectifying the turbulent dynamics of active nematics is a rich and ongoing area of study, as described in Section 2.4.1. Just as a boundary-adapted Stokeslet allows a description of the behaviour of microswimmers near boundaries, an adaptation of the calculations in Chapter 3 to provide the fundamental active response to nematic distortions in the presence of a boundary, will potentially allow greater understanding of the effect of the role of confinement in the behaviour of active nematics.

The intent of this work was not to study active nematics in a specific realisation, but to provide a general framework for understanding the dynamics of the class of such systems. The results contained herein provide experimentally testable predictions applicable to a broad range of active and passive nematics. It is hoped that they constitute a useful contribution, however modest, to the attempt to understand and control nematically-ordered matter in all its forms.

Bibliography

[1] Erwin Schrödinger. *What is life?* Cambridge University Press, 1944.

[2] J. Watson. *The double helix.* Weidenfeld & Nicolson, 1968.

[3] P.W. Anderson. More is different. *Science*, 177(4047):393–396, 1972.

[4] M.V. Berry. Asymptotics, singularities and the reduction of theories. In *Studies in Logic and the Foundations of Mathematics*, volume 134, pages 597–607. Elsevier, 1995.

[5] Ichiro A. A simulation study on the schooling mechanism in fish. *Bulletin of the Japanese Society of Scientific Fisheries*, 48(8):1081–1088, 1982.

[6] B.L. Partridge. The structure and function of fish schools. *Scientific american*, 246(6):114–123, 1982.

[7] I. Stewart. *Life's other secret: The new mathematics of the living world.* John Wiley Nueva York, 1998.

[8] M.J. Bowick and L. Giomi. Two-dimensional matter: order, curvature and defects. *Advances in Physics*, 58(5):449–563, 2009.

[9] T. Vicsek, A. Czirók, E. Ben-Jacob, I. Cohen, and O. Shochet. Novel type of phase transition in a system of self-driven particles. *Physical review letters*, 75(6):1226, 1995.

[10] J. Toner and Y. Tu. Long-range order in a two-dimensional dynamical xy model: how birds fly together. *Physical review letters*, 75(23):4326, 1995.

[11] M. Ballerini, N. Cabibbo, R. Candelier, A. Cavagna, E. Cisbani, I. Giardina, A. Orlandi, G. Parisi, A. Procaccini, M. Viale, et al. Empirical investigation of starling flocks: a benchmark study in collective animal behaviour. *Animal behaviour*, 76(1):201–215, 2008.

[12] D.J.G. Pearce, A.M. Miller, G. Rowlands, and M.S. Turner. Role of projection in the control of bird flocks. *Proceedings of the National Academy of Sciences*, 111(29):10422–10426, 2014.

[13] D. Dell'Arciprete, M.L. Blow, A.T. Brown, F.D.C. Farrell, J.S. Lintuvuori, A.F. McVey, D. Marenduzzo, and W.C.K. Poon. A growing bacterial colony in two dimensions as an active nematic. *Nature communications*, 9(1):1–9, 2018.

[14] H. Li, X. Shi, M. Huang, X. Chen, M. Xiao, C. Liu, H. Chaté, and H.P. Zhang. Data-driven quantitative modeling of bacterial active nematics. *Proceedings of the National Academy of Sciences*, 116(3):777–785, 2019.

[15] M. Başaran, Y.I. Yaman, T.C. Yuce, R. Vetter, and A. Kocabas. Large-scale orientational order in bacterial colonies during inward growth. *arXiv preprint arXiv:2008.05545*, 2020.

[16] V. Narayan, S. Ramaswamy, and N. Menon. Long-lived giant number fluctuations in a swarming granular nematic. *Science*, 317(5834):105–108, 2007.

[17] A. Kudrolli, G. Lumay, D. Volfson, and L.S. Tsimring. Swarming and swirling in self-propelled polar granular rods. *Physical review letters*, 100(5):058001, 2008.

[18] W.F. Paxton, K.C. Kistler, C.C. Olmeda, A. Sen, S.K. St. Angelo, Y. Cao, T.E. Mallouk, P.E. Lammert, and V.H. Crespi. Catalytic nanomotors: autonomous movement of striped nanorods. *Journal of the American Chemical Society*, 126(41):13424–13431, 2004.

[19] J. Palacci, B. Abécassis, C. Cottin-Bizonne, C. Ybert, and L. Bocquet. Colloidal motility and pattern formation under rectified diffusiophoresis. *Physical review letters*, 104(13):138302, 2010.

[20] A. Doostmohammadi, J. Ignés-Mullol, J.M. Yeomans, and F. Sagués. Active nematics. *Nature communications*, 9(1):1–13, 2018.

[21] P.-G. De Gennes and J. Prost. *The physics of liquid crystals*. Number 83. Oxford University Press, 1993.

[22] R. Di Leonardo, L. Angelani, D. Dell'Arciprete, G. Ruocco, V. Iebba, S. Schippa, M.P. Conte, F. Mecarini, F. De Angelis, and E. Di Fabrizio. Bacterial ratchet motors. *Proceedings of the National Academy of Sciences*, 107(21):9541–9545, 2010.

[23] A. Sokolov, M.M. Apodaca, B.A. Grzybowski, and I.S. Aranson. Swimming bacteria power microscopic gears. *Proceedings of the National Academy of Sciences*, 107(3):969–974, 2010.

[24] R.P. Feynman, R.B. Leighton, and M. Sands. *The Feynman lectures on physics, Vol. I: The new millennium edition: mainly mechanics, radiation, and heat*, volume 1. Basic books, 2011.

[25] R.A. Simha and S. Ramaswamy. Hydrodynamic fluctuations and instabilities in ordered suspensions of self-propelled particles. *Physical review letters*, 89(5):058101, 2002.

[26] A. Ahmadi, T.B. Liverpool, and M.C. Marchetti. Nematic and polar order in active filament solutions. *Physical Review E*, 72(6):060901, 2005.

[27] A. Ahmadi, M.C. Marchetti, and T.B. Liverpool. Hydrodynamics of isotropic and liquid crystalline active polymer solutions. *Physical Review E*, 74(6):061913, 2006.

[28] H. Gruler, U. Dewald, and M. Eberhardt. Nematic liquid crystals formed by living amoeboid cells. *The European Physical Journal B-Condensed Matter and Complex Systems*, 11(1):187–192, 1999.

[29] G. Duclos, S. Garcia, H.G. Yevick, and P. Silberzan. Perfect nematic order in confined monolayers of spindle-shaped cells. *Soft matter*, 10(14):2346–2353, 2014.

[30] T.B. Saw, A. Doostmohammadi, V. Nier, L. Kocgozlu, S.P. Thampi, Y. Toyama, P. Marcq, C.T. Lim, J.M. Yeomans, and B. Ladoux. Topological defects in epithelia govern cell death and extrusion. *Nature*, 544(7649):212–216, 2017.

[31] W. Whewell. Xi. Essay towards a first approximation to a map of cotidal lines. *Philosophical Transactions of the Royal Society of London*, (123):147–236, 1833.

[32] W. Whewell. Researches on the tides; Sixth series. On the results of an extensive system of tide observations, made on the coasts of Europe and America, in June 1835. *Philosophical Transactions of the Royal Society of London*, (126):289–341, 1836.

[33] M.B. Hindmarsh and T.W.B. Kibble. Cosmic strings. *Reports on Progress in Physics*, 58(5):477, 1995.

[34] D.R. Tilley and J. Tilley. *Superfluidity and superconductivity*. Routledge, 2019.

[35] M.V. Berry and M.R. Dennis. Phase singularities in isotropic random waves. *Proceedings of the Royal Society of London. Series A: Mathematical, Physical and Engineering Sciences*, 456(2001):2059–2079, 2000.

[36] M.V. Berry and M.R. Dennis. Knotted and linked phase singularities in monochromatic waves. *Proceedings of the Royal Society of London. Series A: Mathematical, Physical and Engineering Sciences*, 457(2013):2251–2263, 2001.

[37] J. Leach, M.R. Dennis, J. Courtial, and M.J. Padgett. Knotted threads of darkness. *Nature*, 432(7014):165–165, 2004.

[38] S. Shankar, A. Souslov, M.J. Bowick, M.C. Marchetti, and V. Vitelli. Topological active matter. *arXiv preprint arXiv:2010.00364*, 2020.

[39] L. Giomi, M.J. Bowick, X. Ma, and M.C. Marchetti. Defect annihilation and proliferation in active nematics. *Physical review letters*, 110(22):228101, 2013.

[40] L. Giomi, M.J. Bowick, P. Mishra, R. Sknepnek, and M.C. Marchetti. Defect dynamics in active nematics. *Philosophical Transactions of the Royal Society A: Mathematical, Physical and Engineering Sciences*, 372(2029):20130365, 2014.

[41] S. Shankar, S. Ramaswamy, M.C. Marchetti, and M.J. Bowick. Defect unbinding in active nematics. *Physical review letters*, 121(10):108002, 2018.

[42] S. Shankar and M.C. Marchetti. Hydrodynamics of active defects: From order to chaos to defect ordering. *Physical Review X*, 9(4):041047, 2019.

[43] G. Duclos, R. Adkins, D. Banerjee, M.S.E. Peterson, M. Varghese, I. Kolvin, A. Baskaran, R.A. Pelcovits, T.R. Powers, A. Baskaran, et al. Topological structure and dynamics of three-dimensional active nematics. *Science*, 367(6482):1120–1124, 2020.

[44] J. Binysh, Ž. Kos, S. Čopar, M. Ravnik, and G.P. Alexander. Three-dimensional active defect loops. *Physical review letters*, 124(8):088001, 2020.

[45] J.C. Maxwell. *A treatise on electricity and magnetism*, volume 1. Clarendon press, 1873.

[46] J. Binysh and G.P. Alexander. Maxwell's theory of solid angle and the construction of knotted fields. *Journal of Physics A: Mathematical and Theoretical*, 51(38):385202, 2018.

[47] H.C. Berg. *E. coli in Motion*. Springer Science & Business Media, 2008.

[48] M.E. Cates and J. Tailleur. Motility-induced phase separation. *Annu. Rev. Condens. Matter Phys.*, 6(1):219–244, 2015.

[49] V. Soni, E.S. Bililign, S. Magkiriadou, S. Sacanna, D. Bartolo, M.J. Shelley, and W.T.M. Irvine. The odd free surface flows of a colloidal chiral fluid. *Nature Physics*, 15(11):1188–1194, 2019.

[50] B.C. van Zuiden, J. Paulose, W.T.M. Irvine, D. Bartolo, and V. Vitelli. Spatiotemporal order and emergent edge currents in active spinner materials. *Proceedings of the national academy of sciences*, 113(46):12919–12924, 2016.

[51] D. Banerjee, A. Souslov, A.G. Abanov, and V. Vitelli. Odd viscosity in chiral active fluids. *Nature communications*, 8(1):1–12, 2017.

[52] A. Souslov, K. Dasbiswas, M. Fruchart, S. Vaikuntanathan, and V. Vitelli. Topological waves in fluids with odd viscosity. *Physical review letters*, 122(12):128001, 2019.

[53] M.E. Cage, K.v Klitzing, A.M. Chang, F.D.M. Haldane, R.B. Laughlin, A.M.M. Pruisken, and D.J. Thouless. *The quantum Hall effect*. Springer Science & Business Media, 2012.

[54] J. Toner and Y. Tu. Flocks, herds, and schools: A quantitative theory of flocking. *Physical review E*, 58(4):4828, 1998.

[55] J.K. Parrish and W.M. Hamner. *Animal groups in three dimensions: how species aggregate*. Cambridge University Press, 1997.

[56] X. Serra-Picamal, V. Conte, R. Vincent, E. Anon, D.T. Tambe, E. Bazellieres, J.P. Butler, J.J. Fredberg, and X. Trepat. Mechanical waves during tissue expansion. *Nature Physics*, 8(8):628–634, 2012.

[57] M.C. Marchetti, J.-F. Joanny, S. Ramaswamy, T.B. Liverpool, J. Prost, M. Rao, and R.A. Simha. Hydrodynamics of soft active matter. *Reviews of Modern Physics*, 85(3):1143, 2013.

[58] P.M. Bendix, G.H. Koenderink, D. Cuvelier, Z. Dogic, B.N. Koeleman, W.M. Brieher, C.M. Field, L. Mahadevan, and D.A. Weitz. A quantitative analysis of contractility in active cytoskeletal protein networks. *Biophysical journal*, 94(8):3126–3136, 2008.

[59] C. Dombrowski, L. Cisneros, S. Chatkaew, R.E. Goldstein, and J.O. Kessler. Self-concentration and large-scale coherence in bacterial dynamics. *Physical review letters*, 93(9):098103, 2004.

[60] R. Kemkemer, D. Kling, D. Kaufmann, and H. Gruler. Elastic properties of nematoid arrangements formed by amoeboid cells. *The European Physical Journal E*, 1(2-3):215–225, 2000.

[61] T. Sanchez, D.T.N. Chen, S.J. DeCamp, M. Heymann, and Z. Dogic. Spontaneous motion in hierarchically assembled active matter. *Nature*, 491(7424):431–434, 2012.

[62] S. Čopar, J. Aplinc, Ž. Kos, S. Žumer, and M. Ravnik. Topology of three-dimensional active nematic turbulence confined to droplets. *Physical Review X*, 9(3):031051, 2019.

[63] Ž. Krajnik, Ž. Kos, and M. Ravnik. Spectral energy analysis of bulk three-dimensional active nematic turbulence. *Soft Matter*, 16(39):9059–9068, 2020.

[64] N.J. Mottram and C.J.P. Newton. Introduction to Q-tensor theory. *arXiv preprint arXiv:1409.3542*, 2014.

[65] F.C. Frank. I. liquid crystals. on the theory of liquid crystals. *Discussions of the Faraday Society*, 25:19–28, 1958.

[66] C.W. Oseen. The theory of liquid crystals. *Transactions of the Faraday Society*, 29(140):883–899, 1933.

[67] M. Stone and P. Goldbart. *Mathematics for physics: a guided tour for graduate students*. Cambridge University Press, 2009.

[68] T. Machon. Contact topology and the structure and dynamics of cholesterics. *New Journal of Physics*, 19(11):113030, 2017.

[69] L.D. Landau and E.M. Lifshitz. *Course of Theoretical Physics: Theory of Elasticity*. Butterworth Heinemann, 1995.

[70] M.P. Do Carmo. *Differential geometry of curves and surfaces: revised and updated second edition*. Courier Dover Publications, 2016.

[71] R.D. Kamien. The geometry of soft materials: a primer. *Reviews of Modern physics*, 74(4):953, 2002.

[72] J.P. Sethna, D.C. Wright, and N.D. Mermin. Relieving cholesteric frustration: the blue phase in a curved space. *Physical review letters*, 51(6):467, 1983.

[73] Ž. Kos and M. Ravnik. Relevance of saddle-splay elasticity in complex nematic geometries. *Soft Matter*, 12(4):1313–1323, 2016.

[74] L. Tran, M.O. Lavrentovich, D.A. Beller, N. Li, K.J. Stebe, and R.D. Kamien. Lassoing saddle splay and the geometrical control of topological defects. *Proceedings of the National Academy of Sciences*, 113(26):7106–7111, 2016.

[75] T. Machon. *Aspects of geometry and topology in liquid crystalline phases*. PhD thesis, University of Warwick, 2016.

[76] J.V. Selinger. Interpretation of saddle-splay and the Oseen-Frank free energy in liquid crystals. *Liquid Crystals Reviews*, 6(2):129–142, 2018.

[77] G.P. Alexander. Topology in liquid crystal phases. In *The Role of Topology in Materials*, pages 229–257. Springer, 2018.

[78] J. Binysh, J. Pollard, and G.P. Alexander. Geometry of bend: Singular lines and defects in twist-bend nematics. *Physical Review Letters*, 125(4):047801, 2020.

[79] T. Machon and G.P. Alexander. Umbilic lines in orientational order. *Physical Review X*, 6(1):011033, 2016.

[80] P.M. Chaikin and T.C. Lubensky. *Principles of condensed matter physics*. Cambridge University Press, 1995.

[81] I.E. Dzyaloshinskii. Theory of disinclinations in liquid crystals. *Soviet Journal of Experimental and Theoretical Physics*, 31:773, 1970.

[82] P.F. Byrd and M.D. Friedman. *Handbook of elliptic integrals for engineers and physicists*, volume 67. Springer, 2013.

[83] G.S. Ranganath. Energetics of disclinations in liquid crystals. *Molecular Crystals and Liquid Crystals*, 97(1):77–94, 1983.

[84] S. Chandrasekhar and G.S. Ranganath. The structure and energetics of defects in liquid crystals. *Advances in Physics*, 35(6):507–596, 1986.

[85] R. Zhang, N. Kumar, J.L. Ross, M.L. Gardel, and J.J. de Pablo. Interplay of structure, elasticity, and dynamics in actin-based nematic materials. *Proceedings of the National Academy of Sciences*, 115(2):E124–E133, 2018.

[86] N. Kumar, R. Zhang, J.J. de Pablo, and M.L. Gardel. Tunable structure and dynamics of active liquid crystals. *Science advances*, 4(10):eaat7779, 2018.

[87] A. Joshi, E. Putzig, A. Baskaran, and M.F. Hagan. The interplay between activity and filament flexibility determines the emergent properties of active nematics. *Soft matter*, 15(1):94–101, 2019.

[88] D. Khoromskaia and G.P. Alexander. Motility of active fluid drops on surfaces. *Physical Review E*, 92(6):062311, 2015.

[89] D. Khoromskaia and G.P. Alexander. Vortex formation and dynamics of defects in active nematic shells. *New Journal of Physics*, 19(10):103043, 2017.

[90] I.I. Smalyukh. Liquid crystal colloids. *Annual Review of Condensed Matter Physics*, 9:207–226, 2018.

[91] J. Goldstone. Field theories with superconductor solutions. *Il Nuovo Cimento (1955-1965)*, 19(1):154–164, 1961.

[92] P.C. Martin, O. Parodi, and P.S. Pershan. Unified hydrodynamic theory for crystals, liquid crystals, and normal fluids. *Physical Review A*, 6(6):2401, 1972.

[93] S. Ramaswamy. The mechanics and statistics of active matter. *Annu. Rev. Condens. Matter Phys.*, 1(1):323–345, 2010.

[94] G.K. Batchelor. *An introduction to fluid dynamics*. Cambridge University Press, 2000.

[95] L.D. Landau and E.M. Lifshitz. *Course of Theoretical Physics: Fluid Mechanics*. Butterworth Heinemann, 2000.

[96] A. Sokolov, I.S. Aranson, J.O. Kessler, and R.E. Goldstein. Concentration dependence of the collective dynamics of swimming bacteria. *Physical review letters*, 98(15):158102, 2007.

[97] J.P. Heller. An unmixing demonstration. *American Journal of Physics*, 28(4):348–353, 1960.

[98] E.M. Purcell. Life at low reynolds number. *American journal of physics*, 45(1):3–11, 1977.

[99] S. Kim and S.J. Karrila. Microhydrodynamics: Principles and selected applications, 1991.

[100] R. Di Leonardo, S. Keen, F. Ianni, J. Leach, M.J. Padgett, and G. Ruocco. Hydrodynamic interactions in two dimensions. *Physical Review E*, 78(3):031406, 2008.

[101] M. Lisicki. Four approaches to hydrodynamic Green's functions–the Oseen tensors. *arXiv preprint arXiv:1312.6231*, 2013.

[102] S. Sankararaman and S. Ramaswamy. Instabilities and waves in thin films of living fluids. *Physical review letters*, 102(11):118107, 2009.

[103] R. Alert, J. Casademunt, and J.-F. Joanny. Active turbulence. *Annual Review of Condensed Matter Physics*, 13, 2021.

[104] S.P. Thampi, R. Golestanian, and J.M. Yeomans. Vorticity, defects and correlations in active turbulence. *Philosophical Transactions of the Royal Society A: Mathematical, Physical and Engineering Sciences*, 372(2029):20130366, 2014.

[105] S.P. Thampi and J.M. Yeomans. Active turbulence in active nematics. *The European Physical Journal Special Topics*, 225(4):651–662, 2016.

[106] L. Giomi. Geometry and topology of turbulence in active nematics. *Physical Review X*, 5(3):031003, 2015.

[107] H.H. Wensink, J. Dunkel, S. Heidenreich, K. Drescher, R.E. Goldstein, H. Löwen, and J.M. Yeomans. Meso-scale turbulence in living fluids. *Proceedings of the national academy of sciences*, 109(36):14308–14313, 2012.

[108] J.M. Yeomans. The hydrodynamics of active systems. *La Rivista del Nuovo Cimento*, 40(1):1–31, 2017.

[109] R. Voituriez, J.-F. Joanny, and J. Prost. Spontaneous flow transition in active polar gels. *EPL (Europhysics Letters)*, 70(3):404, 2005.

[110] L. Angheluta, Z. Chen, M.C. Marchetti, and M.J. Bowick. The role of fluid flow in the dynamics of active nematic defects. *New Journal of Physics*, 23(3):033009, 2021.

[111] R. Alert, J.-F. Joanny, and J. Casademunt. Universal scaling of active nematic turbulence. *Nature Physics*, 16(6):682–688, 2020.

[112] https://commons.wikimedia.org/wiki/file:nematische_phase_schlierentextur.jpg.

[113] M.J. Bowick, N. Fakhri, M.C. Marchetti, and S. Ramaswamy. Symmetry, thermodynamics and topology in active matter. *arXiv preprint arXiv:2107.00724*, 2021.

[114] O.D. Lavrentovich and Y.A. Nastishin. Defects in degenerate hybrid aligned nematic liquid crystals. *EPL (Europhysics Letters)*, 12(2):135, 1990.

[115] D.L. Stein. Kosterlitz-thouless phase transitions in two-dimensional liquid crystals. *Physical Review B*, 18(5):2397, 1978.

[116] J.M. Kosterlitz and D.J. Thouless. Ordering, metastability and phase transitions in two-dimensional systems. *Journal of Physics C: Solid State Physics*, 6(7):1181, 1973.

[117] H. Hopf. *Differential geometry in the large*. Lecture Notes in Mathematics. Springer Berlin Heidelberg, 1989.

[118] V. Vitelli and A.M. Turner. Anomalous coupling between topological defects and curvature. *Physical review letters*, 93(21):215301, 2004.

[119] F. Serra. Curvature and defects in nematic liquid crystals. *Liquid Crystals*, 43(13-15):1920–1936, 2016.

[120] F.C. MacKintosh and T.C. Lubensky. Orientational order, topology, and vesicle shapes. *Physical review letters*, 67(9):1169, 1991.

[121] V. Vitelli and D.R. Nelson. Nematic textures in spherical shells. *Physical Review E*, 74(2):021711, 2006.

[122] D. Jesenek, S. Kralj, R. Rosso, and E.G. Virga. Defect unbinding on a toroidal nematic shell. *Soft matter*, 11(12):2434–2444, 2015.

[123] A. Hatcher. *Algebraic topology*. Cambridge University Press, 2002.

[124] N.D. Mermin. The topological theory of defects in ordered media. *Reviews of Modern Physics*, 51(3):591, 1979.

[125] B.G. Chen, G.P. Alexander, and R.D. Kamien. Symmetry breaking in smectics and surface models of their singularities. *Proceedings of the National Academy of Sciences*, 106(37):15577–15582, 2009.

[126] M.R. Dennis. *Topological singularities in wave fields*. PhD thesis, University of Bristol, 2001.

[127] J.F. Nye. Lines of circular polarization in electromagnetic wave fields. *Proceedings of the Royal Society of London. A. Mathematical and Physical Sciences*, 389(1797):279–290, 1983.

[128] G. Darboux. *Leçons sur la théorie générale des surfaces et les applications géométriques du calcul infinitésimal*, volume 4. Gauthiers-Villars, Paris, 1896.

[129] R. Penrose. The topology of ridge systems. *Annals of human genetics*, 42(4):435–444, 1979.

[130] A.J. Vromans and L. Giomi. Orientational properties of nematic disclinations. *Soft matter*, 12(30):6490–6495, 2016.

[131] X. Tang and J.V. Selinger. Orientation of topological defects in 2d nematic liquid crystals. *Soft matter*, 13(32):5481–5490, 2017.

[132] F. Vafa, M.J. Bowick, M.C. Marchetti, and B.I. Shraiman. Multi-defect dynamics in active nematics. *arXiv preprint arXiv:2007.02947*, 2020.

[133] T.R. Elsdale. Parallel orientation of fibroblasts in vitro. *Experimental cell research*, 51(2-3):439–450, 1968.

[134] T. Bonhoeffer and A. Grinvald. Iso-orientation domains in cat visual cortex are arranged in pinwheel-like patterns. *Nature*, 353(6343):429–431, 1991.

[135] F. Wolf and T. Geisel. Spontaneous pinwheel annihilation during visual development. *Nature*, 395(6697):73–78, 1998.

[136] H.Y. Lee, M. Yahyanejad, and M. Kardar. Symmetry considerations and development of pinwheels in visual maps. *Proceedings of the National Academy of Sciences*, 100(26):16036–16040, 2003.

[137] D. Volfson, S. Cookson, J. Hasty, and L.S. Tsimring. Biomechanical ordering of dense cell populations. *Proceedings of the National Academy of Sciences*, 105(40):15346–15351, 2008.

[138] A. Doostmohammadi, S.P. Thampi, and J.M. Yeomans. Defect-mediated morphologies in growing cell colonies. *Physical review letters*, 117(4):048102, 2016.

[139] Z. You, D.J.G. Pearce, A. Sengupta, and L. Giomi. Geometry and mechanics of microdomains in growing bacterial colonies. *Physical Review X*, 8(3):031065, 2018.

[140] K. Kawaguchi, R. Kageyama, and M. Sano. Topological defects control collective dynamics in neural progenitor cell cultures. *Nature*, 545(7654):327–331, 2017.

[141] Y.I. Yaman, E. Demir, R. Vetter, and A. Kocabas. Emergence of active nematics in chaining bacterial biofilms. *Nature communications*, 10(1):1–9, 2019.

[142] P. Guillamat, C. Blanch-Mercader, K. Kruse, and A. Roux. Integer topological defects organize stresses driving tissue morphogenesis. *bioRxiv*, 2020.

[143] C. Blanch-Mercader, P. Guillamat, A. Roux, and K. Kruse. Quantifying material properties of cell monolayers by analyzing integer topological defects. *Physical Review Letters*, 126(2):028101, 2021.

[144] L.A. Hoffmann, L.N. Carenza, J. Eckert, and L. Giomi. Defect-mediated morphogenesis. *arXiv preprint arXiv:2105.15200*, 2021.

[145] Y. Maroudas-Sacks, L. Garion, L. Shani-Zerbib, A. Livshits, E. Braun, and K. Keren. Topological defects in the nematic order of actin fibres as organization centres of hydra morphogenesis. *Nature Physics*, 17(2):251–259, 2021.

[146] L. Metselaar, J.M. Yeomans, and A. Doostmohammadi. Topology and morphology of self-deforming active shells. *Physical review letters*, 123(20):208001, 2019.

[147] L.J. Ruske and J.M. Yeomans. Morphology of active deformable 3D droplets. *Physical Review X*, 11(2):021001, 2021.

[148] D. Khoromskaia and G. Salbreux. Active morphogenesis of patterned epithelial shells. *arXiv preprint arXiv:2111.12820*, 2021.

[149] O.J. Meacock, A. Doostmohammadi, K.R. Foster, J.M. Yeomans, and W.M. Durham. Bacteria solve the problem of crowding by moving slowly. *Nature Physics*, 17(2):205–210, 2021.

[150] T.N. Shendruk, A. Doostmohammadi, K. Thijssen, and J.M. Yeomans. Dancing disclinations in confined active nematics. *Soft Matter*, 13(21):3853–3862, 2017.

[151] A. Doostmohammadi, T.N. Shendruk, K. Thijssen, and J.M. Yeomans. Onset of meso-scale turbulence in active nematics. *Nature communications*, 8(1):1–7, 2017.

[152] M.M. Norton, A. Baskaran, A. Opathalage, B. Langeslay, S. Fraden, A. Baskaran, and M.F. Hagan. Insensitivity of active nematic liquid crystal dynamics to topological constraints. *Physical Review E*, 97(1):012702, 2018.

[153] A. Opathalage, M.M. Norton, M.P.N. Juniper, B. Langeslay, S.A. Aghvami, S. Fraden, and Z. Dogic. Self-organized dynamics and the transition to turbulence of confined active nematics. *Proceedings of the National Academy of Sciences*, 116(11):4788–4797, 2019.

[154] A. Mozaffari, R. Zhang, N. Atzin, and J.J. de Pablo. Defect spirograph: Dynamical behavior of defects in spatially patterned active nematics. *Physical Review Letters*, 126(22):227801, 2021.

[155] G. Duclos, C. Blanch-Mercader, V. Yashunsky, G. Salbreux, J.-F. Joanny, J. Prost, and P. Silberzan. Spontaneous shear flow in confined cellular nematics. *Nature physics*, 14(7):728–732, 2018.

[156] G. Duclos, C. Erlenkämper, J.-F. Joanny, and P. Silberzan. Topological defects in confined populations of spindle-shaped cells. *Nature Physics*, 13(1):58–62, 2017.

[157] S.P. Thampi, R. Golestanian, and J.M. Yeomans. Active nematic materials with substrate friction. *Physical Review E*, 90(6):062307, 2014.

[158] A. Doostmohammadi, M.F. Adamer, S.P. Thampi, and J.M. Yeomans. Stabilization of active matter by flow-vortex lattices and defect ordering. *Nature communications*, 7(1):1–9, 2016.

[159] E. Putzig, G.S. Redner, A. Baskaran, and A. Baskaran. Instabilities, defects, and defect ordering in an overdamped active nematic. *Soft matter*, 12(17):3854–3859, 2016.

[160] P. Srivastava, P. Mishra, and M.C. Marchetti. Negative stiffness and modulated states in active nematics. *Soft matter*, 12(39):8214–8225, 2016.

[161] P. Guillamat, J. Ignés-Mullol, S. Shankar, M.C. Marchetti, and F. Sagués. Probing the shear viscosity of an active nematic film. *Physical review E*, 94(6):060602, 2016.

[162] P. Guillamat, J. Ignés-Mullol, and F. Sagués. Control of active liquid crystals with a magnetic field. *Proceedings of the National Academy of Sciences*, 113(20):5498–5502, 2016.

[163] P. Guillamat, J. Ignés-Mullol, and F. Sagués. Taming active turbulence with patterned soft interfaces. *Nature communications*, 8(1):1–8, 2017.

[164] F.C. Keber, E. Loiseau, T. Sanchez, S.J. DeCamp, L. Giomi, M.J. Bowick, M.C. Marchetti, Z. Dogic, and A.R. Bausch. Topology and dynamics of active nematic vesicles. *Science*, 345(6201):1135–1139, 2014.

[165] R. Zhang, Y. Zhou, M. Rahimi, and J.J. De Pablo. Dynamic structure of active nematic shells. *Nature communications*, 7(1):1–9, 2016.

[166] F. Alaimo, C. Köhler, and A. Voigt. Curvature controlled defect dynamics in topological active nematics. *Scientific reports*, 7(1):1–9, 2017.

[167] P.W. Ellis, D.J.G. Pearce, Y.-W. Chang, G. Goldsztein, L. Giomi, and A. Fernandez-Nieves. Curvature-induced defect unbinding and dynamics in active nematic toroids. *Nature Physics*, 14(1):85–90, 2018.

[168] G.P. Alexander, B.G. Chen, E.A. Matsumoto, and R.D. Kamien. Colloquium: Disclination loops, point defects, and all that in nematic liquid crystals. *Reviews of Modern Physics*, 84(2):497, 2012.

[169] R.B. Meyer. On the existence of even indexed disclinations in nematic liquid crystals. *The Philosophical Magazine: A Journal of Theoretical Experimental and Applied Physics*, 27(2):405–424, 1973.

[170] C. Williams and Y. Bouligand. Fils et disinclinaisons dans un nématique en tube capillaire. *Journal de Physique*, 35(7-8):589–593, 1974.

[171] M. Ravnik and J.M. Yeomans. Confined active nematic flow in cylindrical capillaries. *Physical review letters*, 110(2):026001, 2013.

[172] S. Čopar and S. Žumer. Nematic braids: topological invariants and rewiring of disclinations. *Physical review letters*, 106(17):177801, 2011.

[173] T. Machon and G.P. Alexander. Knotted defects in nematic liquid crystals. *Physical review letters*, 113(2):027801, 2014.

[174] J. Friedel and P.-G. De Gennes. Boucles de disclination dans les cristaux liquides. *CR Acad. Sc. Paris B*, 268:257–259, 1969.

[175] T.N. Shendruk, K. Thijssen, J.M. Yeomans, and A. Doostmohammadi. Twist-induced crossover from two-dimensional to three-dimensional turbulence in active nematics. *Physical Review E*, 98(1):010601, 2018.

[176] H. Stark. Physics of colloidal dispersions in nematic liquid crystals. *Physics Reports*, 351(6):387–474, 2001.

[177] I. Muševič. *Liquid crystal colloids*. Springer, 2017.

[178] T. Machon and G.P. Alexander. Global defect topology in nematic liquid crystals. *Proceedings of the Royal Society A: Mathematical, Physical and Engineering Sciences*, 472(2191):20160265, 2016.

[179] C.C. Adams. *The knot book*. American Mathematical Soc., 1994.

[180] I.I. Smalyukh. Knots and other new topological effects in liquid crystals and colloids. *Reports on Progress in Physics*, 83(10):106601, 2020.

[181] T.C. Lubensky, D. Pettey, N. Currier, and H. Stark. Topological defects and interactions in nematic emulsions. *Physical Review E*, 57(1):610, 1998.

[182] V.M. Pergamenshchik and V.A. Uzunova. Colloidal nematostatics. *Condensed Matter Physics*, 2010.

[183] V.N. Manoharan. Colloidal matter: Packing, geometry, and entropy. *Science*, 349(6251), 2015.

[184] V.J. Anderson and H.N.W. Lekkerkerker. Insights into phase transition kinetics from colloid science. *Nature*, 416(6883):811–815, 2002.

[185] R. Newburgh, J. Peidle, and W. Rueckner. Einstein, Perrin, and the reality of atoms: 1905 revisited. *American journal of physics*, 74(6):478–481, 2006.

[186] B. Senyuk, J. Aplinc, M. Ravnik, and I.I. Smalyukh. High-order elastic multipoles as colloidal atoms. *Nature communications*, 10(1):1–17, 2019.

[187] B. Senyuk, O. Puls, M. Tovkach, S.B. Chernyshuk, and I.I. Smalyukh. Hexadecapolar colloids. *Nature communications*, 7(1):1–7, 2016.

[188] Y. Yuan, M. Tasinkevych, and I.I. Smalyukh. Colloidal interactions and unusual crystallization versus de-mixing of elastic multipoles formed by gold mesoflowers. *Nature communications*, 11(1):1–14, 2020.

[189] M. Škarabot, M. Ravnik, S. Žumer, U. Tkalec, I. Poberaj, D. Babič, N. Osterman, and I. Muševič. Two-dimensional dipolar nematic colloidal crystals. *Physical Review E*, 76(5):051406, 2007.

[190] M. Škarabot, M. Ravnik, S. Žumer, U. Tkalec, I. Poberaj, D. Babič, N. Osterman, and I. Muševič. Interactions of quadrupolar nematic colloids. *Physical Review E*, 77(3):031705, 2008.

[191] U. Ognysta, A. Nych, V. Nazarenko, I. Muševič, M. Škarabot, M. Ravnik, S. Žumer, I. Poberaj, and D. Babič. 2D interactions and binary crystals of dipolar and quadrupolar nematic colloids. *Physical review letters*, 100(21):217803, 2008.

[192] U.M. Ognysta, A.B. Nych, V.A. Uzunova, V.M. Pergamenschik, V.G. Nazarenko, M. Škarabot, and I. Muševič. Square colloidal lattices and pair interaction in a binary system of quadrupolar nematic colloids. *Physical Review E*, 83(4):041709, 2011.

[193] I. Muševič. Nematic colloids, topology and photonics. *Philosophical Transactions of the Royal Society A: Mathematical, Physical and Engineering Sciences*, 371(1988):20120266, 2013.

[194] A. Rapini and M. Papoular. Distorsion d'une lamelle nématique sous champ magnétique conditions d'ancrage aux parois. *Le Journal de Physique Colloques*, 30(C4):C4–54, 1969.

[195] J. Milnor. Topology from the differentiable viewpoint. *University Press of Virginia, Charlottesville*, 1965.

[196] B. Senyuk, Q. Liu, S. He, R.D. Kamien, R.B. Kusner, T.C. Lubensky, and I.I. Smalyukh. Topological colloids. *Nature*, 493(7431):200–205, 2013.

[197] Q. Liu, B. Senyuk, M. Tasinkevych, and I.I. Smalyukh. Nematic liquid crystal boojums with handles on colloidal handlebodies. *Proceedings of the National Academy of Sciences*, 110(23):9231–9236, 2013.

[198] A. Martinez, M. Ravnik, B. Lucero, R. Visvanathan, S. Žumer, and I.I. Smalyukh. Mutually tangled colloidal knots and induced defect loops in nematic fields. *Nature materials*, 13(3):258–263, 2014.

[199] A. Martinez, L. Hermosillo, M. Tasinkevych, and I.I. Smalyukh. Linked topological colloids in a nematic host. *Proceedings of the National Academy of Sciences*, 112(15):4546–4551, 2015.

[200] U. Tkalec, M. Ravnik, S. Čopar, S. Žumer, and I. Muševič. Reconfigurable knots and links in chiral nematic colloids. *Science*, 333(6038):62–65, 2011.

[201] S. Čopar, U. Tkalec, I. Muševič, and S. Žumer. Knot theory realizations in nematic colloids. *Proceedings of the National Academy of Sciences*, 112(6):1675–1680, 2015.

[202] L. Carroll. *The Hunting of the Snark*. The Folio Society, London, 1976.

[203] N.D. Mermin. *Boojums all the way through: communicating science in a prosaic age*. Cambridge University Press, 1990.

[204] S.B. Chernyshuk. High-order elastic terms, boojums and general paradigm of the elastic interaction between colloidal particles in the nematic liquid crystals. *The European Physical Journal E*, 37(1):1–9, 2014.

[205] P. Poulin, H. Stark, T.C. Lubensky, and D.A. Weitz. Novel colloidal interactions in anisotropic fluids. *Science*, 275(5307):1770–1773, 1997.

[206] J.-F. Joanny. Nematic emulsions. *Science*, 275(5307):1751–1751, 1997.

[207] A. Nych, U. Ognysta, M. Škarabot, M. Ravnik, S. Žumer, and I. Muševič. Assembly and control of 3D nematic dipolar colloidal crystals. *Nature communications*, 4(1):1–8, 2013.

[208] E.M. Terentjev. Disclination loops, standing alone and around solid particles, in nematic liquid crystals. *Physical Review E*, 51(2):1330, 1995.

[209] O. Mondain-Monval, J.C. Dedieu, T. Gulik-Krzywicki, and P. Poulin. Weak surface energy in nematic dispersions: Saturn ring defects and quadrupolar interactions. *The European Physical Journal B-Condensed Matter and Complex Systems*, 12(2):167–170, 1999.

[210] C. Völtz, Y. Maeda, Y. Tabe, and H. Yokoyama. Director-configurational transitions around microbubbles of hydrostatically regulated size in liquid crystals. *Physical review letters*, 97(22):227801, 2006.

[211] Y. Gu and N.L. Abbott. Observation of Saturn-ring defects around solid microspheres in nematic liquid crystals. *Physical Review Letters*, 85(22):4719, 2000.

[212] P. Poulin, V. Cabuil, and D.A. Weitz. Direct measurement of colloidal forces in an anisotropic solvent. *Physical Review Letters*, 79(24):4862, 1997.

[213] K. Takahashi, M. Ichikawa, and Y. Kimura. Direct measurement of force between colloidal particles in a nematic liquid crystal. *Journal of Physics: Condensed Matter*, 20(7):075106, 2008.

[214] K. Takahashi, M. Ichikawa, and Y. Kimura. Force between colloidal particles in a nematic liquid crystal studied by optical tweezers. *Physical Review E*, 77(2):020703, 2008.

[215] N. Kondo, Y. Iwashita, and Y. Kimura. Dependence of interparticle force on temperature and cell thickness in nematic colloids. *Physical Review E*, 82(2):020701, 2010.

[216] K. Izaki and Y. Kimura. Hydrodynamic effects in the measurement of interparticle forces in nematic colloids. *Physical Review E*, 88(5):054501, 2013.

[217] I.I. Smalyukh, O.D. Lavrentovich, A.N. Kuzmin, A.V. Kachynski, and P.N. Prasad. Elasticity-mediated self-organization and colloidal interactions of solid spheres with tangential anchoring in a nematic liquid crystal. *Physical review letters*, 95(15):157801, 2005.

[218] S.B. Chernyshuk, O.M. Tovkach, and B.I. Lev. Elastic octopoles and colloidal structures in nematic liquid crystals. *Physical Review E*, 89(3):032505, 2014.

[219] J. Fukuda, H. Stark, M. Yoneya, and H. Yokoyama. Interaction between two spherical particles in a nematic liquid crystal. *Physical Review E*, 69(4):041706, 2004.

[220] S. Ramaswamy. Active matter. *Journal of Statistical Mechanics: Theory and Experiment*, 2017(5):054002, 2017.

[221] G. Gompper, R.G. Winkler, T. Speck, A. Solon, C. Nardini, F. Peruani, H. Löwen, R. Golestanian, U.B. Kaupp, L. Alvarez, et al. The 2020 motile active matter roadmap. *Journal of Physics: Condensed Matter*, 32(19):193001, 2020.

[222] L. Angelani, A. Costanzo, and R. Di Leonardo. Active ratchets. *EPL (Europhysics Letters)*, 96(6):68002, 2011.

[223] N. Nikola, A.P. Solon, Y. Kafri, M. Kardar, J. Tailleur, and R. Voituriez. Active particles with soft and curved walls: Equation of state, ratchets, and instabilities. *Physical review letters*, 117(9):098001, 2016.

[224] C.J.O. Reichhardt and C. Reichhardt. Ratchet effects in active matter systems. *Annual Review of Condensed Matter Physics*, 8:51–75, 2017.

[225] P. Galajda, J. Keymer, P. Chaikin, and R. Austin. A wall of funnels concentrates swimming bacteria. *Journal of bacteriology*, 189(23):8704–8707, 2007.

[226] O.D. Lavrentovich. Design of nematic liquid crystals to control microscale dynamics. *Liquid Crystals Reviews*, 8(2):59–129, 2020.

[227] T. Turiv, R. Koizumi, K. Thijssen, M.M. Genkin, H. Yu, C. Peng, Q.-H. Wei, J.M. Yeomans, I.S. Aranson, A. Doostmohammadi, et al. Polar jets of swimming bacteria condensed by a patterned liquid crystal. *Nature Physics*, 16(4):481–487, 2020.

[228] M. Rajabi, H. Baza, T. Turiv, and O.D. Lavrentovich. Directional self-locomotion of active droplets enabled by nematic environment. *Nature Physics*, pages 1–7, 2020.

[229] S. Zhou, A. Sokolov, O.D. Lavrentovich, and I.S. Aranson. Living liquid crystals. *Proceedings of the National Academy of Sciences*, 111(4):1265–1270, 2014.

[230] F. Brochard and P.-G. De Gennes. Theory of magnetic suspensions in liquid crystals. *Journal de Physique*, 31(7):691–708, 1970.

[231] S. Ramaswamy, R. Nityananda, V.A. Raghunathan, and J. Prost. Power-law forces between particles in a nematic. *Molecular Crystals and Liquid Crystals Science and Technology. Section A. Molecular Crystals and Liquid Crystals*, 288(1):175–180, 1996.

[232] C. Voisin. *Hodge Theory and Complex Algebraic Geometry II*. Cambridge University Press, 2003.

[233] M.R. Dennis. Canonical representation of spherical functions: Sylvester's theorem, Maxwell's multipoles and Majorana's sphere. *Journal of Physics A: Mathematical and General*, 37(40):9487, 2004.

[234] V.I. Arnold. Topological content of the Maxwell theorem on multiple representation of spherical functions. *Topological Methods in Nonlinear Analysis*, 7(2):205–217, 1996.

[235] Y. Yuan, Q. Liu, B. Senyuk, and I.I. Smalyukh. Elastic colloidal monopoles and reconfigurable self-assembly in liquid crystals. *Nature*, 570(7760):214–218, 2019.

[236] V.M. Pergamenshchik and V.A. Uzunova. Dipolar colloids in nematostatics: tensorial structure, symmetry, different types, and their interaction. *Physical Review E*, 83(2):021701, 2011.

[237] I.I. Smalyukh, Y. Lansac, N.A. Clark, and R.P. Trivedi. Three-dimensional structure and multistable optical switching of triple-twisted particle-like excitations in anisotropic fluids. *Nature materials*, 9(2):139–145, 2010.

[238] M. Ravnik and S. Žumer. Landau–de Gennes modelling of nematic liquid crystal colloids. *Liquid Crystals*, 36(10-11):1201–1214, 2009.

[239] C.H. Taubes. *Differential geometry: Bundles, connections, metrics and curvature*. OUP Oxford, 2011.

[240] J.R. Blake and A.T. Chwang. Fundamental singularities of viscous flow. *Journal of Engineering Mathematics*, 8(1):23–29, 1974.

[241] A.T. Chwang and T.Y. Wu. Hydromechanics of low-reynolds-number flow. part 2. singularity method for stokes flows. *Journal of Fluid mechanics*, 67(4):787–815, 1975.

[242] M.J. Lighthill. On the squirming motion of nearly spherical deformable bodies through liquids at very small reynolds numbers. *Communications on Pure and Applied Mathematics*, 5(2):109–118, 1952.

[243] O.S. Pak and E. Lauga. Generalized squirming motion of a sphere. *Journal of Engineering Mathematics*, 88(1):1–28, 2014.

[244] A. Daddi-Moussa-Ider and A.M. Menzel. Dynamics of a simple model microswimmer in an anisotropic fluid: Implications for alignment behavior and active transport in a nematic liquid crystal. *Physical Review Fluids*, 3(9):094102, 2018.

[245] Ž. Kos and M. Ravnik. Elementary flow field profiles of micro-swimmers in weakly anisotropic nematic fluids: Stokeslet, stresslet, rotlet and source flows. *Fluids*, 3(1):15, 2018.

[246] G.K. Batchelor. The stress generated in a non-dilute suspension of elongated particles by pure straining motion. *Journal of Fluid Mechanics*, 46(4):813–829, 1971.

[247] C. Lang, J. Hendricks, Z. Zhang, N.K. Reddy, J.P. Rothstein, M.P. Lettinga, J. Vermant, and C. Clasen. Effects of particle stiffness on the extensional rheology of model rod-like nanoparticle suspensions. *Soft matter*, 15(5):833–841, 2019.

[248] L.A. Hoffmann, K. Schakenraad, R.M.H. Merks, and L. Giomi. Chiral stresses in nematic cell monolayers. *Soft matter*, 16(3):764–774, 2020.

[249] V. Yashunsky, D.J.G. Pearce, C. Blanch-Mercader, F. Ascione, L. Giomi, and P. Silberzan. Chiral edge currents in confined fibrosarcoma cells. *arXiv preprint arXiv:2010.15555*, 2020.

[250] R. Zhang, A. Mozaffari, and J.J. de Pablo. Autonomous materials systems from active liquid crystals. *Nature Reviews Materials*, pages 1–17, 2021.

[251] D.K. Sahu, S. Kole, S. Ramaswamy, and S. Dhara. Omnidirectional transport and navigation of janus particles through a nematic liquid crystal film. *Physical Review Research*, 2(3):032009, 2020.

[252] Y. Baek, A.P. Solon, X. Xu, N. Nikola, and Y. Kafri. Generic long-range interactions between passive bodies in an active fluid. *Physical review letters*, 120(5):058002, 2018.

[253] E. Lauga and D. Bartolo. No many-scallop theorem: Collective locomotion of reciprocal swimmers. *Physical Review E*, 78(3):030901, 2008.

[254] G.P. Alexander and J.M. Yeomans. Dumb-bell swimmers. *EPL (Europhysics Letters)*, 83(3):34006, 2008.

[255] S. Chandragiri, A. Doostmohammadi, J.M. Yeomans, and S.P. Thampi. Flow states and transitions of an active nematic in a three-dimensional channel. *Physical Review Letters*, 125(14):148002, 2020.

[256] P. Chandrakar, M. Varghese, S.A. Aghvami, A. Baskaran, Z. Dogic, and G. Duclos. Confinement controls the bend instability of three-dimensional active liquid crystals. *Physical Review Letters*, 125(25):257801, 2020.

[257] L.N. Carenza, G. Gonnella, D. Marenduzzo, and G. Negro. Rotation and propulsion in 3D active chiral droplets. *Proceedings of the National Academy of Sciences*, 116(44):22065–22070, 2019.

[258] D. Cortese, J. Eggers, and T.B. Liverpool. Pair creation, motion, and annihilation of topological defects in two-dimensional nematic liquid crystals. *Physical Review E*, 97(2):022704, 2018.

[259] J.B. Bronzan. The magnetic scalar potential. *American Journal of Physics*, 39(11):1357–1359, 1971.

[260] C.G. Gray. Magnetic multipole expansions using the scalar potential. *American Journal of Physics*, 47(5):457–459, 1979.

[261] A. Powell. Theory of vortex sound. *The journal of the acoustical society of America*, 36(1):177–195, 1964.

[262] F.B. Fuller. Decomposition of the linking number of a closed ribbon: a problem from molecular biology. *Proceedings of the National Academy of Sciences*, 75(8):3557–3561, 1978.

[263] M.R. Dennis and J.H. Hannay. Geometry of Călugăreanu's theorem. *Proceedings of the Royal Society A: Mathematical, Physical and Engineering Sciences*, 461(2062):3245–3254, 2005.

[264] L.P. Eisenhart. *A treatise on the differential geometry of curves and surfaces*. Ginn, 1909.

[265] S.J. Kole, G.P. Alexander, S. Ramaswamy, and A. Maitra. Layered chiral active matter: Beyond odd elasticity. *Physical Review Letters*, 126(24):248001, 2021.

[266] S.M. Hashemi, U. Jagodič, M.R. Mozaffari, M.R. Ejtehadi, I. Muševič, and M. Ravnik. Fractal nematic colloids. *Nature communications*, 8(1):1–9, 2017.

[267] H.V. Koch. Sur une courbe continue sans tangente, obtenue par une construction géométrique élémentaire. *Arkiv for Matematik, Astronomi och Fysik*, 1:681–704, 1904.

[268] F. Mondiot, S.P. Chandran, O. Mondain-Monval, and J.-C. Loudet. Shape-induced dispersion of colloids in anisotropic fluids. *Physical review letters*, 103(23):238303, 2009.

[269] Y. Luo, T. Yao, D.A. Beller, F. Serra, and K.J. Stebe. Deck the walls with anisotropic colloids in nematic liquid crystals. *Langmuir*, 35(28):9274–9285, 2019.

[270] F.R. Hung. Quadrupolar particles in a nematic liquid crystal: Effects of particle size and shape. *Physical Review E*, 79(2):021705, 2009.

[271] D.A. Beller. *Controlling defects in nematic and smectic liquid crystals through boundary geometry*. University of Pennsylvania, 2014.

[272] B. Senyuk, Q. Liu, E. Bililign, P.D. Nystrom, and I.I. Smalyukh. Geometry-guided colloidal interactions and self-tiling of elastic dipoles formed by truncated pyramid particles in liquid crystals. *Physical Review E*, 91(4):040501, 2015.

[273] S.R. Seyednejad, M.R. Mozaffari, T. Araki, and E.N. Oskoee. Interactions between pentagonal truncated pyramids with homeotropic anchoring in a nematic liquid crystal. *Physical Review E*, 98(3):032701, 2018.

[274] S.M. Hashemi and M.R. Ejtehadi. Equilibrium state of a cylindrical particle with flat ends in nematic liquid crystals. *Physical Review E*, 91(1):012503, 2015.

[275] D.A. Beller, M.A. Gharbi, and I.B. Liu. Shape-controlled orientation and assembly of colloids with sharp edges in nematic liquid crystals. *Soft Matter*, 11(6):1078–1086, 2015.

[276] D.V. Sudhakaran, R.K. Pujala, and S. Dhara. Orientation dependent interaction and self-assembly of cubic magnetic colloids in a nematic liquid crystal. *Advanced Optical Materials*, 8(7):1901585, 2020.

[277] B. Senyuk, Q. Liu, P.D. Nystrom, and I.I. Smalyukh. Repulsion–attraction switching of nematic colloids formed by liquid crystal dispersions of polygonal prisms. *Soft Matter*, 13(40):7398–7405, 2017.

[278] B. Senyuk, M.B. Pandey, Q. Liu, M. Tasinkevych, and I.I. Smalyukh. Colloidal spirals in nematic liquid crystals. *Soft Matter*, 11(45):8758–8767, 2015.

[279] C.P. Lapointe, T.G. Mason, and I.I. Smalyukh. Shape-controlled colloidal interactions in nematic liquid crystals. *Science*, 326(5956):1083–1086, 2009.

[280] J. Dontabhaktuni, M. Ravnik, and S. Žumer. Shape-tuning the colloidal assemblies in nematic liquid crystals. *Soft Matter*, 8(5):1657–1663, 2012.

[281] J. Dontabhaktuni, M. Ravnik, and S. Žumer. Quasicrystalline tilings with nematic colloidal platelets. *Proceedings of the National Academy of Sciences*, 111(7):2464–2469, 2014.

[282] J. Dontabhaktuni, M. Ravnik, and S. Zumer. Quasicrystalline ordering in thin liquid crystal films. *Crystals*, 8(7):275, 2018.

[283] C.P. Lapointe, K. Mayoral, and T.G. Mason. Star colloids in nematic liquid crystals. *Soft Matter*, 9(32):7843–7854, 2013.

[284] https://www.wikiart.org/en/m-c-escher/circle-limit-iii.

[285] J. Cardy. *Scaling and renormalization in statistical physics*, volume 5. Cambridge University Press, 1996.

[286] R. Penrose. *Cycles of time: an extraordinary new view of the universe*. Random House, 2010.

[287] B. de Smit and H. W. Lenstra Jr. Artful mathematics: The heritage of M.C. Escher. *Notices of the AMS*, 50(4):446–451, 2003.

[288] D. Dunham. Creating repeating hyperbolic patterns—old and new. *Notices of the AMS*, 50(4):35–46, 2003.

[289] T.A. Driscoll and L.N. Trefethen. *Schwarz-Christoffel mapping*, volume 8. Cambridge University Press, 2002.

[290] O.A. Rojas-Gómez and J.M. Romero-Enrique. Generalized Berreman's model of the elastic surface free energy of a nematic liquid crystal on a sawtoothed substrate. *Physical Review E*, 86(4):041706, 2012.

[291] Y. Han, A. Majumdar, and L. Zhang. A reduced study for nematic equilibria on two-dimensional polygons. *SIAM Journal on Applied Mathematics*, 80(4):1678–1703, 2020.

[292] A.J. Davidson and N.J. Mottram. Conformal mapping techniques for the modelling of liquid crystal devices. *European Journal of Applied Mathematics*, 23(1):99–119, 2012.

[293] H. Lamb. *Hydrodynamics*. University Press, 1924.

[294] L.V. Ahlfors. *An Introduction to the Theory of Analytic Functions of One Complex Variable*. McGraw-Hill, 1979.

[295] R.E. Greene and S.G. Krantz. *Function theory of one complex variable*, volume 40. American Mathematical Soc., 2006.

[296] T. Needham. *Visual complex analysis*. Oxford University Press, 1998.

[297] B. Riemann. *Grundlagen fur eine allgemeine Theorie der Functionen einer veränderlichen complexen Grösse*. Adalbert Rente, 1867.

[298] K. Weierstrass. Über das sogenannte dirichlet'sche princip. In *Ausgewählte Kapitel aus der Funktionenlehre*, pages 184–189. Springer, 1988.

[299] W.F. Osgood. On the existence of the Green's function for the most general simply connected plane region. *Transactions of the American Mathematical Society*, 1(3):310–314, 1900.

[300] C. Carathéodory. Untersuchungen über die konformen abbildungen von festen und veränderlichen gebieten. *Mathematische Annalen*, 72(1):107–144, 1912.

[301] D. Hilbert and S. Cohn-Vossen. *Geometry and the Imagination*, volume 87. American Mathematical Soc., 2021.

[302] J.L. Walsh. History of the Riemann mapping theorem. *The American Mathematical Monthly*, 80(3):270–276, 1973.

[303] J. Gray. On the history of the Riemann mapping theorem. *Supp. di Rend*, 1994.

[304] R.E. Greene and K.-T. Kim. The Riemann mapping theorem from Riemann's viewpoint. *Complex Analysis and its Synergies*, 3(1):1–11, 2017.

[305] E.B. Christoffel. Sul problema delle temperature stazonarie e la rappresentazione di una data superficie. *Ann. Mat. Pura Appl. Serie II*, 1:89–103, 1867.

[306] E.B. Christoffel. Sopra un problema proposto da dirichlet. *Ann. Mat. Pura Appl. Serie II*, 4:1–9, 1870.

[307] E.B. Christoffel. Über die abbildung einer n-blattrigen einfach zusammenhängender ebenen fläche auf einen kreise. *Göttingen Nachrichten*, pages 359–69, 1870.

[308] E.B. Christoffel. Über die integration von zwei partiellen differentialgleichungen. *Nachr. Kgl. Ges. Wiss. Göttingen*, pages 435–53, 1871.

[309] H.A. Schwarz. Conforme abbildung der oberfläche eines tetraeders auf die oberfläche einer kugel. *J. Reine Ange. Math.*, 70:121–36, 1869.

[310] H.A. Schwarz. Über einige abbildungsaufgaben. *J. Reine Ange. Math.*, 70:105–20, 1869.

[311] H.A. Schwarz. *Gesammelte Mathematische Abhandlungen, volume II*. Springer, Berlin, 1890.

[312] P. Henrici. *Applied and Computational Complex Analysis, Volume 1: Power Series, Integration, Conformal Mapping, Location of Zeros*. Wiley, New York, 1974.

[313] Z. Nehari. *Conformal mapping*. Courier Corporation, 2012.

[314] M. Abramowitz and I.A. Stegun. *Handbook of mathematical functions with formulas, graphs, and mathematical tables*, volume 55. US Government printing office, 1972.

[315] *NIST Digital Library of Mathematical Functions*. http://dlmf.nist.gov/, Release 1.1.3 of 2021-09-15. F.W.J. Olver, A.B. Olde Daalhuis, D.W. Lozier, B.I. Schneider, R.F. Boisvert, C.W. Clark, B.R. Miller, B.V. Saunders, H.S. Cohl, and M.A. McClain, eds.

[316] H. Bateman. *Higher transcendental functions [volumes i-iii]*, volume 1. McGraw-Hill Book Company, 1953.

[317] H.S.M. Coxeter. *Regular polytopes*. Courier Corporation, 1973.

[318] S.P. Thampi, A. Doostmohammadi, T.N. Shendruk, R. Golestanian, and J.M. Yeomans. Active micromachines: Microfluidics powered by mesoscale turbulence. *Science advances*, 2(7):e1501854, 2016.

[319] E. Efrati and W.T.M. Irvine. Orientation-dependent handedness and chiral design. *Physical Review X*, 4(1):011003, 2014.

[320] G. Dietler, R. Kusner, W. Kusner, E. Rawdon, and P. Szymczak. Chirality for crooked curves. *arXiv preprint arXiv:2004.10338*, 2020.

[321] W.T. Kelvin. *The molecular tactics of a crystal*. Clarendon Press, 1894.

[322] L.L. Whyte. Chirality. *Nature*, 182(4629):198–198, 1958.

[323] O.D. Lavrentovich. Liquid crystals, photonic crystals, metamaterials, and transformation optics. *Proceedings of the National Academy of Sciences*, 108(13):5143–5144, 2011.

[324] T.A. Driscoll. Algorithm 756: A matlab toolbox for Schwarz-Christoffel mapping. *ACM Transactions on Mathematical Software (TOMS)*, 22(2):168–186, 1996.

[325] D. Crowdy. The Schottky-Klein prime function on the Schottky double of planar domains. *Computational Methods and Function Theory*, 10(2):501–517, 2011.

[326] A.H. Lewis, I. Garlea, J. Alvarado, O.J. Dammone, P.D. Howell, A. Majumdar, B.M. Mulder, M.P. Lettinga, G.H. Koenderink, and D.G.A.L. Aarts. Colloidal liquid crystals in rectangular confinement: theory and experiment. *Soft Matter*, 10(39):7865–7873, 2014.

[327] C.A. Whitfield, T.C. Adhyapak, A. Tiribocchi, G.P. Alexander, D. Marenduzzo, and S. Ramaswamy. Hydrodynamic instabilities in active cholesteric liquid crystals. *The European Physical Journal E*, 40(4):1–16, 2017.

[328] P. Sens, M.S. Turner, and P. Pincus. Particulate inclusions in a lamellar phase. *Physical Review E*, 55(4):4394, 1997.

[329] M.S. Turner and P. Sens. Multipole expansion for inclusions in a lamellar phase. *Physical Review E*, 57(1):823, 1998.

[330] R.P. Trivedi, M. Tasinkevych, and I.I. Smalyukh. Nonsingular defects and self-assembly of colloidal particles in cholesteric liquid crystals. *Physical Review E*, 94(6):062703, 2016.

[331] E. Lauga and T.R. Powers. The hydrodynamics of swimming microorganisms. *Reports on Progress in Physics*, 72(9):096601, 2009.

[332] A.P. Berke, L. Turner, H.C. Berg, and E. Lauga. Hydrodynamic attraction of swimming microorganisms by surfaces. *Physical Review Letters*, 101(3):038102, 2008.

[333] E. Lauga, W.R. DiLuzio, G.M. Whitesides, and H.A. Stone. Swimming in circles: motion of bacteria near solid boundaries. *Biophysical journal*, 90(2):400–412, 2006.